Approaching the design of novel oxygen-carrier materials for hydrogen production via the chemical looping water-gas shift process in a packed bed reactor

Mustafa Selim Ungut

A thesis submitted for the degree of Doctor of Philosophy (PhD) in Chemical Engineering at Newcastle University

School of Engineering

Supervisors: Prof. Ian. S. Metcalfe & Dr. Wenting Hu

Submitted: June 2022

Abstract

The work presented in this thesis focused on the use of a chemical looping process that uses novel oxygen carrier materials (OCMs) for the production of hydrogen. A methodology was presented for the selection of suitable OCMs based on the possible conversions and outlet product quality, with a focus on the non-stoichiometric materials $La_{0.4}Sr_{0.6}Fe_{0.67}Mn_{0.33}O_{3-\delta}$ (LSFM6473) and $Ce_{0.8}Zr_{0.2}O_{2-\delta}$ (CZ82), using $La_{0.4}Sr_{0.6}FeO_{3-\delta}$ (LSF641) as a comparative benchmark.

The chemical looping process used in this work was via the chemical looping water-gas shift process (CLWGS). In this process a solid OCM is repeatedly oxidised and reduced in two half cycles in a packed bed reactor flowing consecutive counter-current streams of carbon monoxide and water vapour as the reducing agent and the oxidising agent. Such a system can overcome the thermodynamic limitations of conventional mixed feed reactors with no need to separate the outlet hydrogen and carbon dioxide streams, thereby reducing plant costs.

The use of non-stoichiometric materials instead of phase changing materials allows for high conversions in both half cycles to be achieved during steady cycling. It was shown that the case for an optimal oxygen non-stoichiometry vs. chemical potential relationship exists for non-stoichiometric OCMs, and this was verified by use of a reactor model. This hypothesis was used to select LSFM6473 and CZ82 as OCMs, and during experimental studies in a packed bed reactor both achieved conversion and outlet product qualities in excess of OCMs with less optimal oxygen non-stoichiometry vs. chemical potential relationships such as LSF641, further verifying the hypothesis.

The oxygen non-stoichiometry and thermodynamics of the perovskite LSFM6473 was investigated using thermo-gravimetric analysis and iodometric titration. The substitution of 33% Mn onto the B-site of LSFM6473, when compared with no doping, resulted in an increase in the change in oxygen non-stoichiometry in the oxygen partial pressure range that sees the greatest extent of reaction of the water-gas shift reaction at constant temperature. The high oxygen capacity and stability of the material LSFM6473 was also verified by in-situ x-ray diffraction analysis of the reactor bed. Stable hydrogen production was seen for over 450 cycles with approximately 80% conversion of water vapour using 3 minute feed durations, indicating the viability of this OCM for industrial scale use.

Acknowledgements

I would firstly like to thank my supervisors Prof. Ian Metcalfe and Dr. Wenting Hu for all of their guidance and wisdom, which has proven invaluable throughout my PhD, and for enabling me to attend conferences to present my research. I am also grateful for funding from the EPSRC which made it possible for me to carry out this work.

The in-situ XRD experiments (MA4239) were carried out at ID22 at ESRF and were made possible thanks to Prof. Ian Metcalfe and Dr. Wenting Hu. Thanks go to the staff at ID22, especially Dr. Catherine Dejoie. I would also like to thank Dr. Evangelos Papioannou, Dr. Dragos Neagu, Dr. Kelly Kousi, Dr. Chris de Leeuwe and Leonidas Bekris for their help in setting up and running the plethora of equipment at the beamline. My thanks also go to Prof. John Evans and Dr. Stevin Pramana for their help with data analysis using TOPAS software. The XANES data was made possible thanks to the UK Catalysis Hub BAG allocation at B18 at Diamond Light Source. Special thanks to Dr. Nitya Ramanan, as well as Prof. Ian Metcalfe and Dr. Wenting Hu for guiding me through this process.

I would also like to thank the entire MatCoRE team for the good times and happy memories, and the support when the entire university was abruptly shut down for several months during the pandemic. I am grateful to Chris for showing me the ropes when I was still a novice, especially for teaching me the lengthy process of how to disassemble, reassemble and then run an integral reactor. My thanks also go to Stephen Johnston for teaching me how to use the TGA kit, to Leonidas for being a great colleague and always finding ways to keep things fun in the lab, and to Daniel Telford, Reinaldo Lee Pereira, Alex Martinez Martin and Matthew Guy for their camaraderie and giving a hand with running final laboratory experiments.

Thanks also go to the workshop staff and technicians at Merz Court for their assistance in testing and fixing equipment. Special shoutouts to electrical staff Stephen Mitchel and Roy Proud for their help in installing additional sockets which greatly assisted with the notorious cable management for the integral reactor. Thanks also go to the powder XRD staff at the Bedson building, especially Maggie White and Dr. Jamie Gould, for carrying out the ex-situ XRD scans.

Finally a very special thank you to my loving family for your support throughout these years, it has meant the world to me.

Table of contents

List of figures

List of tables

Nomenclature

A	Referring to site in perovskite structure (ABO_3)
ATR	Auto-thermal reformer
B	Referring to site in perovskite structure (ABO_3)
BET	Brunauer-Emmett-Teller
CLWGS	Chemical looping water-gas shift
CLC	Chemical looping combustion
CLR	Chemical looping reforming
CZ	Ceria-zirconia mixed metal oxide
FWHM	Full width at half maximum
LSF	Strontium doped lanthanum ferrite perovskite
LSM	Strontium doped lanthanum manganate perovskite
LSFM	Manganese doped lanthanum strontium ferrite perovskite
LSFCr	Chromium doped lanthanum strontium ferrite perovskite
OCM	Oxygen-carrier material
PEM	Proton exchange membrane
PSA	Pressure swing adsorption
QGA	Quantitative gas and vapour analysis

SMR	Steam methane reformer	
SOFC	Solid oxide fuel cell	
TGA	Thermo-gravimetric analysis	
TRCL	Three-reactor chemical looping	
TPO	Temperature programmed oxidation	
TPR	Temperature programmed reduction	
WGS	Water-gas shift	
XANES	X-ray absorption near edge structure spectroscopy	
XRD	X-ray powder diffraction	
a	Lattice cell parameter	Å
CF	Calibration factor	
F	Total volumetric flowrate	ml min^{-1}
H	Maximum degree of non-stoichiometry	
k_{grad}	Steepness of logistic function	
K_{WGS}	Equilibrium constant for WGS reaction	
K_{ox}	Equilibrium constant for water-splitting reaction	
K_{red}	Equilibrium constant for carbon monoxide oxidation reaction	
K_{dis}	Equilibrium constant for Eq. 2.16	
K_{inc}	Equilibrium constant for Eq. 2.14	

$\dot{N}$	Molar flowrate	mol s^{-1}
T	Temperature	K
P	Pressure	bar
p_{H_2}	H_2 partial pressure	bar
p_{H_2O}	H_2O partial pressure	bar
p_{CO_2}	CO_2 partial pressure	bar
p_{CO}	CO partial pressure	bar
pO_2	Oxygen partial pressure	bar
$pO_{2,mid}$	Midpoint of logistic function	bar
r	Rate of reaction	mol m^{-3} s^{-1}
SF	Splitting factor	
t	Time	s
y	Mole fraction	mol mol^{-1}
X	Conversion	
ΔH	Enthalpy change	kJ mol^{-1}
ΔG	Gibbs free energy change	kJ mol^{-1}
ΔS	Entropy change	kJ mol^{-1}
δ	Degree of non-stoichiometry	
ε	Voidage	
λ_O	Dimensionless number defined by ratio of solid phase oxygen capacity to gas phase oxygen capacity	

ρ_g	Molar density of gas phase	mol m^{-3}
ρ_s	Molar density of solid phase	mol m^{-3}

Chapter 1: Introduction

This introductory chapter summarises the various uses of hydrogen in industry and transportation and the various methods of hydrogen production. An explanation of the concept of chemical looping is given, as well as how chemical looping can be applied to the water-gas shift reaction for hydrogen production. A review of the nature of various chemical looping reactor configurations is given. Finally, a summary provides an overview of the chapter as well as an explanation of the purpose of this thesis.

1.1 Uses of hydrogen

1.1.1 Transportation

The use of hydrogen in transportation has the potential to diversify available energy sources and could provide one solution to help reducing the current dependence on finite fossil fuels. As of 2020 about 91% of the total energy used for passenger and commercial transportation is derived from oil (IEA, 2021). Hydrogen can be used to provide clean energy in contrast to traditional fossil fuels that produce CO_2 when combusted. Hydrogen forms only water when oxidised and generates heat in a highly exothermic reaction.

$$H_2 + 0.5O_2 \rightarrow H_2O \qquad \Delta\mathbf{H}^{\mathbf{0}}_{\mathbf{298K}}\ (\text{kJ/mol}) = -286 \qquad \text{(Eq. 1.1)}$$

Hydrogen can be used in either an internal combustion engine, or a fuel cell to provide energy for transportation. When used in an internal combustion engine, the cyclic motion of a piston due to the combustion of hydrogen and subsequent cooling allows for mechanical energy to be provided to run the car by operation of a crankshaft. While there is an advantage in that existing motor engines could be more easily retrofitted to operate with hydrogen, this technology is limited by the fact that there are significant heat losses associated with the heat engine due to practical considerations such as the maximum operating temperature of the engine and the lack of heat recovery from the exhaust gases (Hosseini et al, 2019). The production of hydrogen currently relies mainly on the use of steam methane reforming which has a large carbon footprint and depends on fossil fuels, so it would be important for the system of a hydrogen powered vehicle to be as efficient as possible.

An alternative way in which hydrogen may be used is by converting its chemical energy via the use of a fuel cell. A fuel cell is an electrochemical device in which hydrogen is combined with oxygen across an anode-cathode interface to produce electricity, with water and heat being generated as by-products. The 2020 second generation Toyota Mirai fuel cell powered vehicles have a stated hydrogen fuel consumption of 0.79 kg/100 km (Reuß et al, 2017), significantly better than that of the Hydrogen 7, a limited-edition automobile that utilised an internal combustion engine manufactured by BMW in 2005-2007 and had a hydrogen fuel consumption of 3.7 kg/100 km under city-driving conditions (Wallner et al, 2008).

Fuel cells may either be a proton exchange membrane (PEM) or solid oxide fuel cell (SOFC) depending on whether either hydrogen ions or oxygen ions are being transported through the electrolyte. The total cell reaction in either case is the same as given in Eq. 1.1 previously. The anode/cathode reactions for a PEM fuel cell or an SOFC fuel cell are as follows:

Type of fuel cell	**Anode**		**Cathode**	
PEM	$H_2 \rightarrow 2H^+ + 2e^-$	(Eq. 1.2)	$0.5O_2 + 2H^+ + 2e^- \rightarrow H_2O$	(Eq. 1.3)
SOFC	$H_2 + O^{2-} \rightarrow H_2O + 2e^-$	(Eq. 1.4)	$0.5O_2 + 2e^- \rightarrow O^{2-}$	(Eq. 1.5)

SOFCs are disadvantaged by high temperature requirements, operating at temperature ranges of 573 K to 1273 K, meaning that component materials may be thermally challenged - for example aluminium has a melting point of about 933 K (Sreedhar et al, 2020). PEM fuel cells operate at lower temperatures of 323 K to 373 K, but are more susceptible to deactivation due to poisoning and tend to use expensive catalysts like platinum (Shabani et al, 2019).

The transportation and storage of hydrogen represent significant challenges that currently prevent larger scale usage. The major limiting factor is the low energy per unit volume of hydrogen: in order to store a quantity of compressed hydrogen (70 MPa) with the same amount of energy as 70 L of petrol, a storage tank with a volume exceeding 770

L would be required which is impractical (Koike et al, 2012). This also poses an issue for transporting hydrogen from production plants in vehicles, and since hydrogen is normally stored as a compressed gas, this can be dangerous as well – hydrogen has a large volume range of flammability and explosivity in air (4-74% and 18-59% in air respectively). There is a lack of a dedicated pipeline distribution network for hydrogen which would incur large capital costs to build and depend on large volumes of hydrogen to financially break even. Some studies have suggested the use of existing natural gas infrastructure as a viable alternative, as in the H21 Leeds City Gate project report (Northern Gas Networks, 2016). As of the end of 2020, the National Grid plc In the UK has drawn up a £12.7 million plan to trial the safe use of hydrogen in existing natural gas network at a facility in Cumbria (Morison, 2020). Fig. 1.1 shows that as of the end of 2020 there were 553 hydrogen refuelling stations in operation worldwide which although is a roughly 260% increase since 2010, is still not sufficient for large numbers of users (H2stations press release 2020, H2stations press release 2021).

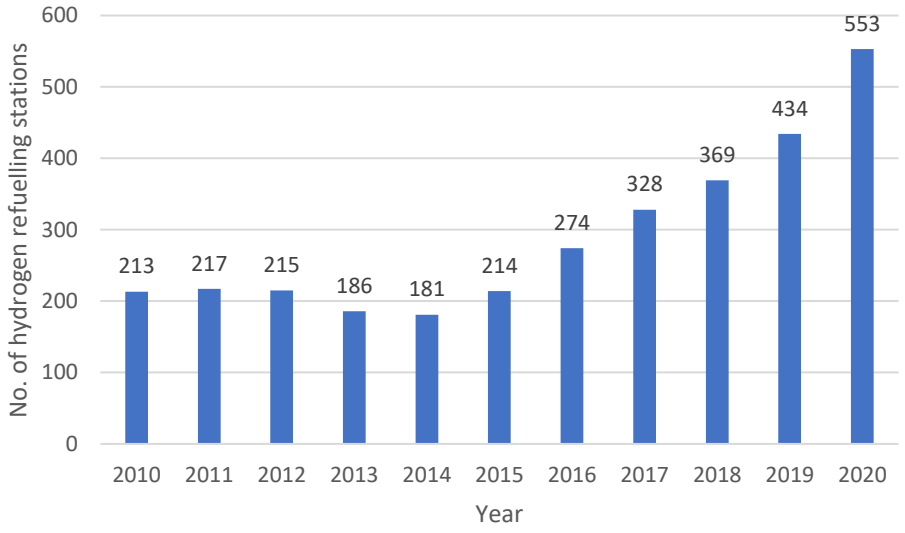

Figure 1.1: Global numbers of hydrogen refuelling stations per annum since 2010 (data from H2stations press release 2020 & H2stations press release 2021).

Fig. 1.2 gives an overview of the various methods of hydrogen storage. In its molecular form, pure hydrogen may be stored in either gas or liquid phases. As a gas hydrogen is stored in high pressure tanks of about 350-700 bar, while in liquid form cryogenic temperatures are needed since the boiling point of hydrogen at 1 bar is 20 K. Both of

these methods are disadvantaged by high costs – high pressure storage tanks require advanced materials such as carbon fibre, and cryogenic temperatures are energy intensive to maintain (Andersson & Grönkvist, 2019). Alternative methods of storage involve either adsorption onto a solid material surface, such as with the metal hydride sodium borohydride (Demirci, 2018) or absorption via chemical bonding.

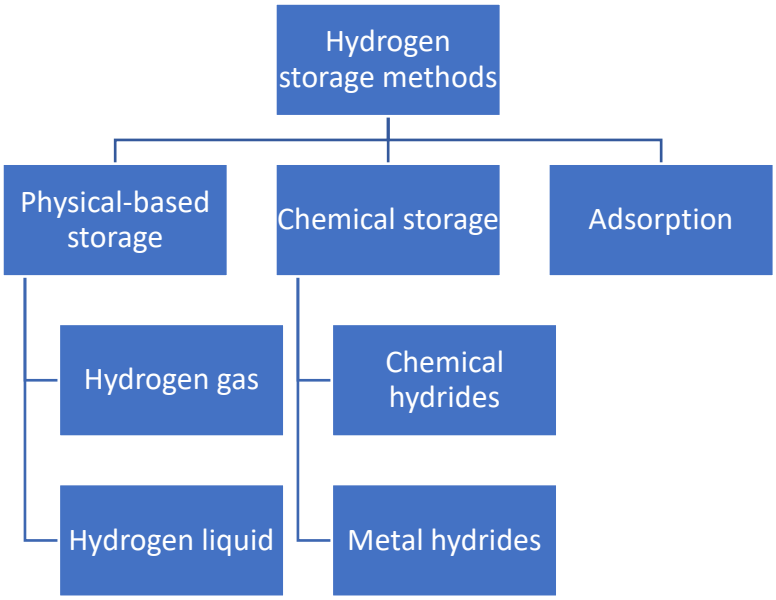

Figure 1.2: Summary of the various methods of hydrogen storage (Andersson & Grönkvist, 2019).

Hydrogen storage is not so much an issue with spacecraft however, where external fuel tanks may simply be jettisoned. Liquid hydrogen combined with liquid oxygen has been used as rocket fuel by NASA since the 1960s, and has the highest specific impulse of all known rocket propellants. The importance of hydrogen in spaceflight has prompted studies into the in-situ generation of hydrogen during missions, including harvesting hydrogen from Martian regolithic brine (Gayen et al, 2020). Further fringe uses of hydrogen have been highlighted by studies that have investigated using hydrogen-oxidising bacteria as a potential food source in space as opposed to pre-packaged food sent from Earth (Alvarado et al, 2020).

1.1.2 Industrial feedstock

Hydrogen plays an important role in a number of industrial processes. These include hydrogenation, where unsaturated hydrocarbons are saturated by hydrogen for foods

production such as margarine and butter, the Haber-Bosch process, where hydrogen derived from natural gas is fed in with nitrogen and reacts over an iron catalyst for ammonia synthesis, or for hydrocracking, where hydrogen reacts with high-boiling point long chain hydrocarbons to convert them into useful lower-boiling point products such as diesel, kerosene or jet fuel.

Table 1.1: Major processes using hydrogen and their products.

Process	**Products**
Hydrogenation ($C_nH_{2n} + H_2 \rightarrow C_nH_{2n+2}$) (Eq. 1.6)	Butter, margarine, various foods
Haber-Bosch ($N_2 + 3H_2 \rightarrow 2NH_3$) (Eq. 1.7)	Ammonia
Hydrocracking reactions	Diesel, kerosene, jet fuel, other petroleum products

Promising future uses of hydrogen are also in the steel, cement and shipping industries. For steel production, current processes involve the reaction of iron oxide with carbon monoxide derived from coke fuel heated in a blast furnace. This produces molten pig iron as well as significant quantities of carbon dioxide. The production of 1 tonne of steel results in the emission of about 1.9 tonnes of carbon dioxide (Bellona, 2019) and roughly 1869 million tonnes of steel were produced in 2019 alone (World Steel Association, 2020). As a result roughly 7-9 % of all direct fossil fuel greenhouse gas emissions are derived from steelmaking (Pooler, 2020). If hydrogen gas were to be used instead of coke the only by-product from the reaction with iron oxide would be water vapour, making the process emission-free if the hydrogen that is used is derived from renewable sources.

In the cement industry the production of clinker, the main component of cement, is a highly carbon dioxide and energy intensive process. Roughly 7% of global carbon dioxide emissions are derived from the cement industry (IEA, 2018). Most importantly,

about 50% of the carbon dioxide is process carbon dioxide rather than fuel carbon dioxide, i.e. from decomposition of limestone. Research is ongoing looking into ways to reduce the clinker to cement ratio, allow for the implementation of carbon capture and improve the energy efficiency. Less carbon intensive fuels are also being investigated, for example the use of hydrogen as a combustion fuel to reach the high temperatures required for cement manufacturing , which would tackle some part of the carbon dioxide emissions. In 2021 Hanson UK, a major cement manufacturing company, announced a recently installed hydrogen demonstration unit capable of using renewable energy generated on site through wind and solar to produce hydrogen via electrolysis. This hydrogen is then used as a replacement for natural gas in the burner, and thus avoids carbon emission from burning natural gas.

The generation of hydrogen for industrial use or as an energy source presents an interesting problem. Following the Big Bang, the first atoms to be formed were primarily those of hydrogen and helium, and as such hydrogen is a highly abundant element in the universe. On Earth however, pure un-combined hydrogen is relatively rare; it readily reacts with oxygen and in the atmosphere it is light enough to escape Earth's gravitational attraction. At standard conditions, hydrogen is present at about 5×10^{-5} % by volume air (Rumble, 2021). Hydrogen is primarily found as a component of water, as well as in hydrocarbons and organic compounds; there are no practical sources of hydrogen gas and it must be manufactured industrially from hydrogen containing compounds.

Unfortunately about 98% of the roughly 115 million tonnes of hydrogen used globally is manufactured from fossil fuels such as coal or natural gas, resulting in the emission of about 830 million tonnes of carbon dioxide on a yearly basis and constituting around 2% of all global greenhouse gas emissions (IEA, 2019). As such a complete overhaul of the hydrogen production industry is also required before expanded use can be considered.

1.2 Methods of hydrogen production

1.2.1 Overview

There are three general classifications of the main hydrogen production processes: electrolysis, where water molecules are split into oxygen and hydrogen using thermal or electrical energy, photolysis, which utilises the energy of light, and thermolysis, where a raw material from either renewable or fossil sources such as ethanol or methanol is transformed into hydrogen with heat and catalysts for triggering the chemical reactions. A summary of the various manufacturing processes for hydrogen is given in table 1.2 and section 1.2 will discuss these processes in more detail.

Of the manufacturing processes listed in table 1.2, the steam reforming process (particularly from natural gas) is the most efficient technology. Almost 50% of global hydrogen production is via this method and it has a high level of industrial maturity, being in use since the late 1920s. Other methods of hydrogen production based on photolysis, electrolysis and various bio-hydrogen routes such as fermentation are also present and some can potentially eliminate the need for carbon capture and storage. However they are generally still in various stages of research, and this currently prevents them from being a realistic method for industry-wide application.

Another method of hydrogen production is via the chemical looping water-gas shift (CLWGS) process, and will be the main focus in this thesis. This is a hydrogen production technique where a solid oxygen carrier material is continuously oxidised and reduced in a cyclic process carrying out two halves of a redox reaction, using carbon monoxide and water vapour as the reducing agent and the oxidising agent. Section 1.3 later in this chapter will focus specifically on describing the process of chemical looping as it is the technology which forms the basis of this thesis. Before that however, the following sections will give a description of the other processes, shown in table 1.2 before.

Table 1.2: Hydrogen manufacturing processes from numerous feedstocks, their energy efficiency and technological maturity.

Feedstock	Production Technology	Efficiency	Maturity	References
Hydrocarbons	Steam reforming	70 – 85%	Commercial	Pinsky et al (2020)
	Partial oxidation	60 – 75%	Commercial	Pinsky et al (2020)
	Auto-thermal reforming	60 – 75%	Near term	Kim et al (2021)
	Plasma reforming	9 – 85%	Long term	Nikolaidis et al (2017)
	Aqueous phase reforming	35 – 55%	Med. term	El-Shafie et al (2019)
Ammonia	Ammonia reforming	28.3%	Near term	El-Shafie et al (2019)
Biomass	Biomass gasification	35 – 50%	Commercial	Mah et al (2019)
	Dark fermentation	60 – 80%	Long term	Mah et al (2019)
H_2O + sunlight	Photo-electrolysis	0.5%	Long term	Pinsky et al (2020)
Biomass + sunlight	Photo fermentation	1.9%	Long term	Wu et al (2016)
Biomass + electricity	Microbial electrolysis cells	60 – 78%	Long term	Kadier et al (2016)
H_2O + electricity	Alkaline electrolyser	61 – 82% *	Commercial	Parra et al (2019)
	Proton exchange membrane electrolyser	67 – 84% *	Near term	Dawood et al (2020)
H_2O + electricity + heat	Solid oxide electrolysis cells	< 110% *	Med. term	Lehner et al (2014)
H_2O + heat	Thermochemical water splitting	20 – 45%	Long term	Pinsky et al (2020)
H_2O + sunlight	Photoelectrochemical water splitting	12.4%	Long term	Pinsky et al (2020)

* % Voltage efficiency based on higher heating value of hydrogen.

1.2.2 Steam methane reforming

A steam methane reformer (SMR) is essentially a multi-tubular fixed-bed reactor, where a plug flow reactor is incorporated with a heat exchanger. The typical reactions that occur in steam methane reforming are given in Eq. 1.8-1.10. Heat exchange is carried out around the tubes, where water gas shift and methane steam reforming reactions occur at high temperatures with an external hot gas source. Depending on the feedstock, various amounts of higher order hydrocarbons C_nH_m may also be present and will undergo reaction. Fig. 1.3 gives an overview of the various stages in a typical SMR plant.

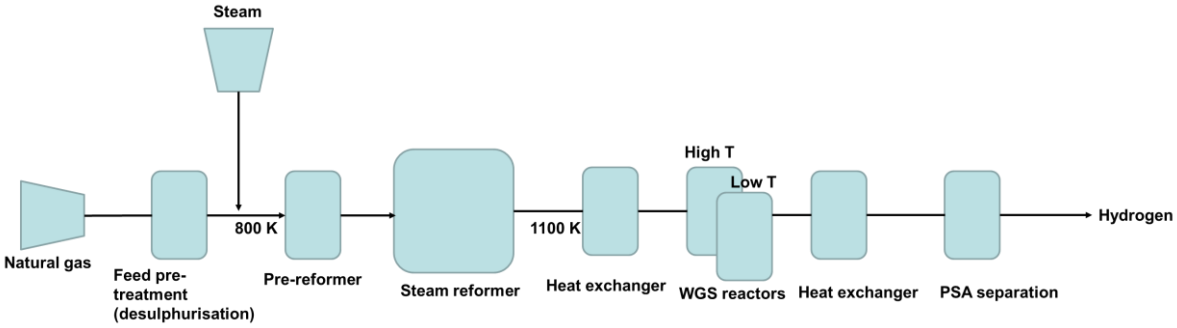

Figure 1.3: Basic flow diagram of a conventional SMR process for hydrogen production.

Many plants will have a feed treatment stage prior to the SMR, where a zinc-oxide sulphur extraction bed can remove most of the sulphur from the feed to avoid poisoning the catalyst (Lew et al 1989, Atimtay 2001, Hadi et al 2018). A pre-reformer may be integrated alongside an existing SMR in order to reduce the composition of higher order hydrocarbons (which can reduce soot formation) and produce higher SMR inlet feed temperatures.

The endothermic steam reforming reactions (Eq. 1.8 and Eq. 1.10) occur first, where the hydrocarbons are converted into carbon monoxide and hydrogen under a nickel-based catalyst. This is carried out at high temperatures (> 1073 K) and ideally with a high steam to carbon ratio in order to achieve optimal conversion. Subsequently, the gas mixture passes through to a second stage with two fixed bed adiabatic reactors carrying out the WGS reaction (Eq. 1.9) in series with a cooler in between them. The first reactor operates at higher temperatures (583-723 K, 25-35 bar) and uses a Fe/Cr catalyst, while the second reactor uses a Cu/Zn/Al catalyst and operates at lower temperatures (483-

513 K) to maximise the equilibrium conversion of CO since the WGS reaction (Eq. 1.9) is exothermic (Rhodes et al 1995, Luo et al 2017).

Methane Steam Reforming	$CH_4 + H_2O \rightleftharpoons CO + 3H_2$	(Eq. 1.8)
Water Gas Shift	$CO + H_2O \rightleftharpoons CO_2 + H_2$	(Eq. 1.9)
Higher Order Hydrocarbons Steam Reforming	$C_nH_m + n\ H_2O \rightleftharpoons n\ CO + (n + 0.5m)\ H_2$	(Eq. 1.10)

It has been estimated by that carbon dioxide accounts for up to 77.6% of the SMR system's global warming potential (Spath and Mann, 2000). The remainder is mainly from methane, followed by NO_x, SO_x, CO, particulates, and benzene derived from the production and distribution of natural gas. As much as 13.7 kg carbon dioxide may be produced per kg of net hydrogen produced. For production of pure hydrogen gas, the carbon dioxide by-product of the water-gas shift reaction must be removed by a separation process, usually pressure swing adsorption (PSA), which can add to the final production costs.

It is possible to replace the two-stage reforming process with an auto-thermal reformer (ATR). Fig. 1.4 shows an overview of an ATR, a complex piece of equipment that combines sub-stoichiometric combustion and the SMR reactions into a single unit. Partial combustion allows for the heat for steam reforming to be supplied internally using pure oxygen instead of air as the oxidant. Industrially it is possible for savings on investment at around 15-25% to be made using oxygen-fired reforming technologies in comparison to fired tubular reformers such as with SMR (Rostrup-Nielsen).

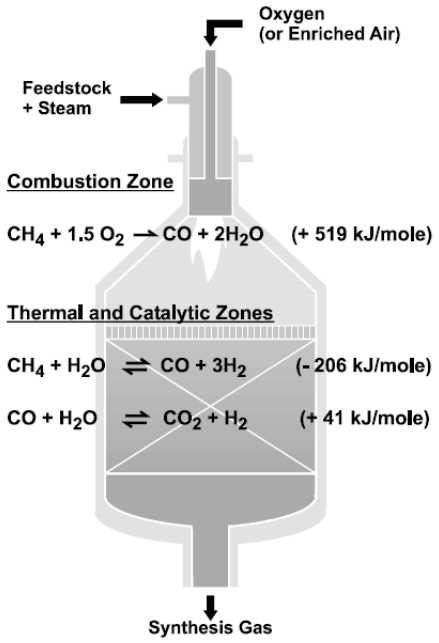

Figure 1.4: Overview of the auto-thermal reforming process with the different reaction zones indicated (Rostrup Nielsen).

1.2.3 Partial oxidation of hydrocarbons

Partial oxidation occurs when sub-stoichiometric fuel-air mixtures are partially combusted to produce a mixture of H_2 and CO (Speight 2015, Lee 2015). This process can accommodate high molecular-weight organic compounds such as petroleum residual and petroleum coke.

$$CH_4 + 0.5O_2 \rightarrow 2H_2 + CO \qquad \Delta\mathbf{H}^{\mathbf{0}}_{\mathbf{298K}}\ (\mathrm{kJ/mol}) = -43.6 \qquad \text{(Eq. 1.11)}$$

$$C_nH_m + (0.5n)\ O_2 \rightarrow (0.5m)\ H_2 + n\ CO \qquad \text{General form} \qquad \text{(Eq. 1.12)}$$

Partial oxidation has an exothermic heat of reaction and as such external heating is not required. The thermal efficiency of the process from methane is typically 60-75% in table 1.2. The process can be operated either non-catalytically at temperatures of 1423-1588 K where hydrocarbons including methane, heavy oil and coal can be used, or with a catalyst, typically nickel, which lowers the temperature to about 1223 K and can operate with feedstocks ranging from methane to naphtha (Nikolaidis & Poullikkas, 2017). Additional separation stages are also typically needed to achieve high purity hydrogen production.

1.2.4 Ammonia reforming

Ammonia cracking is given by the reverse of Eq. 1.7 and is an endothermic reaction. Ammonia reforming for hydrogen production has been investigated mainly for production of carbon free hydrogen for PEM fuel cells (Miyaoka et al, 2018). Ammonia is considered an environmentally benign molecule to store hydrogen and can carry higher quantities of hydrogen on a volumetric and gravimetric basis than liquid hydrogen (Ashik et al, 2018). Ammonia is extensively used in fertiliser production and is therefore cheap and there is an already existing extensive distribution system. The exposure of ammonia to the acidic PEM electrolyte can cause a severe performance loss and is one limiting factor of this method. In order to ensure longer life ammonia levels need to be kept to below part per billion levels. The study by Miyaoka et al in 2018 gives the ammonia conversion at the chemical equilibrium state of 773-823 K at 99.74-99.84% with ammonia concentration roughly 1300-800 ppm. In the study it was shown how a conventional Li-exchange X-type zeolite could be used to reduce the concentration of ammonia in a hydrogen stream from cracking ammonia from 1000 to <0.1 ppm.

1.2.5 Plasma reforming

While plasma reforming has the same overall reactions as conventional reforming, it is different in that a plasma is used with water or steam being injected into the fuel causing H, OH and O radicals and electrons to be formed, and thus creating conditions for the oxidative and reductive reactions to take place (Sekiguchi & Mori, 2003). It has been argued that the process can overcome most of the limitations of conventional methods (Nikolaidis & Poullikkas, 2017), and when no catalysts are used the process has a high tolerance to sulphur (Biniwale et al, 2004). The significant electrical requirements and electrode erosion at high pressures represent the main disadvantages of this process (Bromberg et al, 1999).

1.2.6 Electrolysis

An electrical current can be used to affect the dissociation of water and produce gaseous hydrogen and oxygen via the reaction given by the reverse of Eq. 1.1. This reaction is endothermic and the nature of the energy input for this electrical current determines how environmentally friendly the process is. The three most well-known electrolysis

technologies are alkaline, proton exchange membrane (PEM) and solid oxide electrolysis cells (SOEC). Of these alkaline electrolysers are the most developed technology with production rates of <760 Nm^3h^{-1} as opposed to <10 Nm^3h^{-1} for PEM electrolysers (Chisholm & Cronin, 2016). If the electrical energy needs to be generated from non-renewable sources, the high energy usage of the electrolysers does not make the process economically viable (Dönitz & Erdle, 1985), and can produce more overall CO_2 than steam methane reforming (Koroneos et al, 2004). However, if the electrical energy can be supplied from renewable energy sources such as hydroelectric, wind or solar then the process can be potentially carbon neutral and offers a sustainable and cost-effective option (Zeng & Zhang, 2010).

1.2.7 Thermochemical water splitting

At temperatures of about 4700 K the Gibbs function of the reaction where water decomposes to form hydrogen and oxygen without the presence of a catalyst (via the reverse of Eq. 1.1) tends to zero, and thereby becomes feasible (Funk, 2001). A major problem with this method however is the availability of stable materials at this high temperature and the considerable energy required to maintain the conditions. Chemical reagents have been used to significantly lower the temperatures of operation, but these also normally require higher pressures. Thermochemical water-splitting cycles have been proposed that can lower temperature and improve overall efficiency. Of these the lowest was a Cu-Cl cycle with maximum temperatures of 823 K, but efficiency of only 45% (Orhan et al, 2008). In addition, there is the issue of hydrogen and oxygen recombining if not separated prior to cooling down the system, making this process still far from successful commercialisation.

Photo-electrolysis is another related process which involves the decomposition of water into hydrogen and oxygen but differs in that it uses the energy of visible light instead. Semi-conducting materials are used to aid in the absorption of sunlight. This process has a low efficiency due to the high bandgap energy requirement for separation of electron from the hole (Aroutiounian et al, 2005).

1.2.8 Hydrocarbon pyrolysis

Hydrocarbon pyrolysis involves the decomposition of a hydrocarbon feed into elemental hydrogen and carbon in the absence of oxygen or water, and is given by the following general reaction which can be operating either by use of plasma or thermally:

$$C_nH_m \rightarrow (0.5m)H_2 + nC \qquad \text{(Eq. 1.13)}$$

In the case of heavy residual fractions which have a boiling point of > 623 K a two-stage scheme involving hydrogasification and cracking of methane is used to produce hydrogen (Muradov, 1993):

$$CH_{1.6} + 1.2H_2 \rightarrow CH_4 \qquad \text{Hydrogasification} \qquad \text{(Eq. 1.14)}$$

$$CH_4 \rightarrow C + 2H_2 \qquad \text{Methane cracking} \qquad \text{(Eq. 1.15)}$$

$$CH_{1.6} \rightarrow C + 0.8H_2 \qquad \text{Overall reaction} \qquad \text{(Eq. 1.16)}$$

This process has the potential to be environmentally friendly since no oxides of carbon are formed during the reaction in Eq. 1.13. The price of hydrogen could be reduced if a market for the produced carbon could be found (Muradov, 2001). In addition, there is no need for additional stages involving WGS and CO_2 removal, which could lower the costs of capital investment for large plants by 25-30% (Muradov, 1993). It is important that the feedstock is prepared carefully however, as significant CO and CO_2 emissions could still be produced if air or moisture is present. Deactivation of the metal catalyst is another issue that may limit the feasibility of this process (Holladay et al, 2009).

1.2.9 Biomass gasification and biological routes for hydrogen production

Biomass is organic matter that can be derived from plants and animals. Subject to regulated usage it could represent a more sustainable alternative to using fossil fuels as feedstock and is more readily available. Even though CO_2 is produced when the biomass is used, the amount of emission is equal to the amount absorbed by organisms during their lifetime (Flamos et al, 2011). Hydrogen production from biomass can be carried out in two main routes: either thermochemical or biological methods.

In thermochemical processes, hydrogen can be produced via gasification and pyrolysis techniques, and hydrogen-rich gas can be produced via synthesis gas obtained from these processes (Fremaux et al, 2014). In biomass gasification different gasification units can have different feed pre-treatment requirements and typically require large amounts of energy. Entrained flow gasifiers have strict requirements needing biomass feed to have a moisture content <15% and a particle size of < 1mm, while bubbling fluidised bed gasifiers can accept feed with moisture content of up to 55% and particle size up to 150 mm (E4Tech, 2009). Pyrolysis, where the biomass is rapidly heated at 773 K producing a slurry can allow for easier storage and transport in comparison to untreated biomass and increases the energy density of the material (Drift & Boerrigter, 2006). In the main gasification stage, the biomass is heated in the presence of an oxidising agent to produce lighter components that mainly comprise CO_2, CO and H_2. The decomposition of biomass into lighter components is an endothermic reaction and is given by Eq. 1.17.

$$C_6H_{11}O_5 \text{ (biomass)} \rightarrow CH_4 + CO_2 + CO + H_2O + H_2 + C \text{ (char)} + \text{tars} \qquad \text{(Eq. 1.17)}$$

The additional costs from feed pre-treatment stages and clean-up can make the process consume more energy than using natural gas, with additional units that may be required to convert the tars into volatile gas components as otherwise tar could cause downstream processing issues.

Biological processes to produce hydrogen involve the use of certain bacteria and algae that undergo photosynthesis to generate energy and use excess solar energy from this process to produce hydrogen via direct photolysis of water (Kovacs et al, 2006). Fermentation processes are particularly attractive as they can utilise waste materials and can provide inexpensive energy generation (Balthasar, 1984). Photo fermentation involves the use of photosynthetic bacteria, while dark fermentation uses anaerobic bacteria on carbohydrate rich substrates under anoxic dark conditions (Orhan et al, 2008). Current biological processes are limited by their low tolerance to temperature fluctuations and have lower rates and yields than thermochemical processes (Balat & Kırtay, 2010).

1.3 Chemical looping for hydrogen production

1.3.1 Principles of chemical looping

Chemical looping occurs when a reaction is broken down into several sub-reactions by use of an intermediate material which undergoes redox cycling (Thursfield et al, 2012). For example the generic reaction $A + B \rightarrow C + D$ can be split into the two sub-reactions $A \rightarrow C$ and $B \rightarrow D$, where A is converted to C by reacting with an intermediate material and likewise B is converted to D. The reactants and the products are not mixed and are in a different phase to the intermediate material.

This concept can be applied to the WGS process whereby the homogeneous gas-phase WGS reaction (Eq. 1.18) may be split into two heterogeneous reactions: an oxidation reaction (Eq. 1.19) where steam oxidises the OCM resulting in H_2 being produced, and a reduction reaction (Eq. 1.20) where CO reduces the OCM thereby producing high purity CO_2. Here, the OCM is represented as a generic oxide of the form MO_x.

Principle reaction:	$CO + H_2O \rightleftharpoons CO_2 + H_2$		(Eq. 1.18)
Split reactions with OCM:	$MO_{x-m} + m\ H_2O \rightleftharpoons MO_x + m\ H_2$	(Oxidation of OCM)	(Eq. 1.19)
	$MO_x + m\ CO \rightleftharpoons MO_{x-m} + m\ CO_2$	(Reduction of OCM)	(Eq. 1.20)

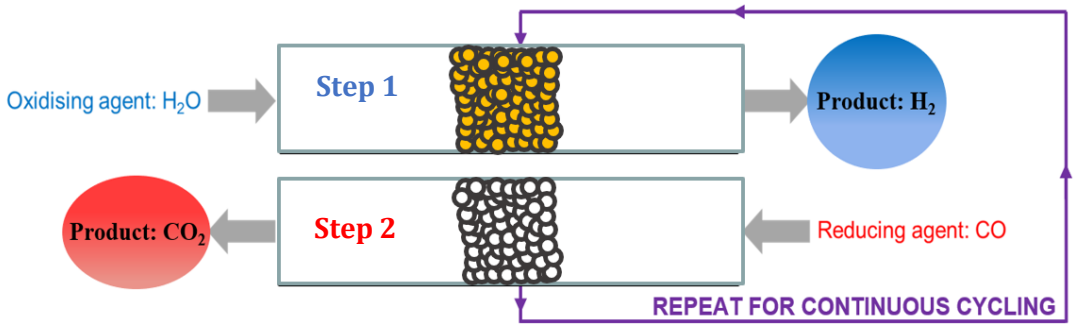

Figure 1.5: A typical cycle in the CLWGS process using a packed bed reactor with a solid OCM (represented by the circular particles in the diagram). The bed is first oxidised by flowing through H_2O, after which the bed is reduced by flowing CO, and thus completing a single cycle. In the figure, step 1 and step 2 (referred to as half cycles throughout this thesis) are both carried out on the same bed with the direction of flow switched.

This is a cyclic process as illustrated in Fig. 1.5, where the solid intermediate is being repeatedly oxidised and reduced by the passing gas-phase streams. In the context of hydrogen production in this thesis, this solid intermediate is referred to as an oxygen-carrier material (OCM), owing to its ability to donate or receive oxygen. The main advantage of this process is that it presents us with the potential to achieve a very high purity hydrogen product in just a single stage with no need to separate hydrogen from carbon dioxide, and overcomes the thermodynamic limitations of conventional mixed reactors (Metcalfe et al, 2019).

In comparison with most of the processes still in the research and development stage in table 1.2, the concept of chemical looping is fairly old with precedent dating back to the work of Howard Lane in 1903. His invention, known as the Lane Hydrogen Producer, is the earliest form of what is now more commonly referred to as the steam-iron process. In the steam-iron process, iron oxide, which acts as an OCM, is fixed in place in a bed and consecutively oxidised and reduced by alternately passing through counter-current streams of steam and a suitable carbon based fuel such as carbon monoxide. The splitting of the water molecules during the oxidation stage allows for the production of hydrogen, and pure carbon dioxide may be produced in the reduction stage – though hydrogen production is not continuous. Since the two streams are separate, this eliminates the need for any additional separation and the process for carbon capture and storage is more straightforward. In contrast, commonly used processes in industry

today such as steam methane reforming suffer from entropic losses due to the use of mixed feeds and can require multiple stages and a separation.

1.3.2 Reactor systems for hydrogen production via chemical looping

Chemical looping for hydrogen production may be carried out using one or more packed bed reactors, or for continuous production without multiple reactors a circulating fluidised bed system may be used. In the latter case, the OCM is transferred between multiple reactors, though the lifetime of the material can be reduced due to attrition.

The steam-iron process described in section 1.3.1 is an example of a typical single packed bed reactor process for hydrogen production. During the initial stage of the process a bed of fresh OCM is subject to a flow of water vapour. All the water vapour is converted to hydrogen initially but over time the oxygen vacancies in the OCM are filled up and so the concentration of water vapour increases. In the reduction half cycle carbon dioxide is produced by counter-current carbon monoxide gas passing through the oxidised section of the bed, but eventually the concentration of carbon dioxide decreases as more of the oxygen is removed from the bed. Heidebricht and Sundmacher (2009) demonstrated distinct phase changes in a packed bed reactor with iron oxide fixed as the OCM by development of a model assuming that a shock front passes through the bed. They also found that counter-current systems could achieve higher hydrogen productivity than co-current systems, because iron and wüstite could be oxidised simultaneously in counter-current systems (Heidebrecht et al, 2008).

The main limitation of packed bed reactors is their inability to produce hydrogen continuously without the use of multiple reactors, as the OCM must be regenerated during the reduction step to prevent a drop in hydrogen production, which may not be economically viable unless a suitable use can be found for the carbon dioxide. Packed bed reactors are also sensitive to particle size as this can cause pressure drops across the reactor bed due leading to fluidisation in which case the reactant gas can channel through the bed unreacted resulting in lower yields and the need for downstream separation.

The process can be expanded to two separate reactors for continuous hydrogen production by use of a single 4-way switching valve as in Fig. 1.6. In this scenario the direction of flow for oxidising and reducing agents can be switched from one reactor to another in order to maintain a high level of hydrogen production without having to wait for the bed to regenerate during the reduction stage.

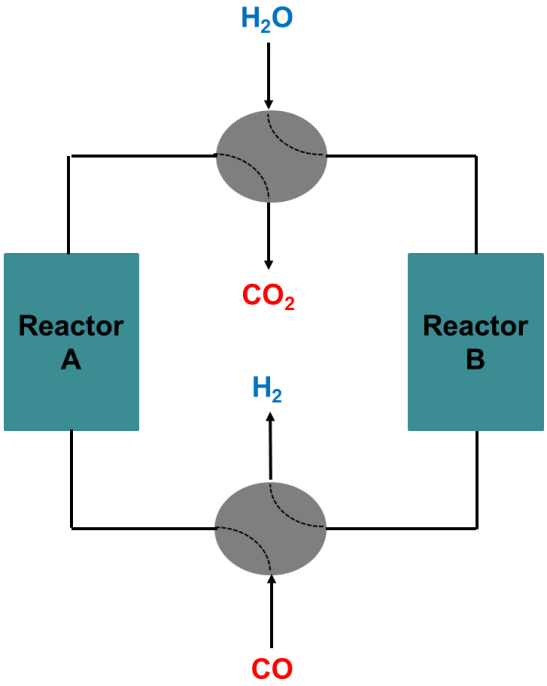

Figure 1.6: A parallel packed bed reactor system capable of carrying out continuous hydrogen production via CLWGS through simultaneous switching of 4-way valves.

The second type of reactor system commonly encountered is a circulating fluidised bed system illustrated in Fig. 1.7. In this scenario the solid OCM is fluidised using high flowrates of gas and circulated between multiple reactors that are dedicated for oxidation and reduction steps. The reactor where the reduction stage is carried out is a riser which has a low radial area to enable the OCM particles to be fluidised and carried upward. At the top of the reactor the area of the column increases so that the OCM particles are carried through into the oxidation stage reactor. The use of cyclone separators and loops seals have been studied as ways to ensure separation of particles and make sure that gas cross over does not occur, and the system usually needs to be flushed with an inert gas between each stage (Basu & Cheng 2000, Kim & Kim 2002, Basu 2006).

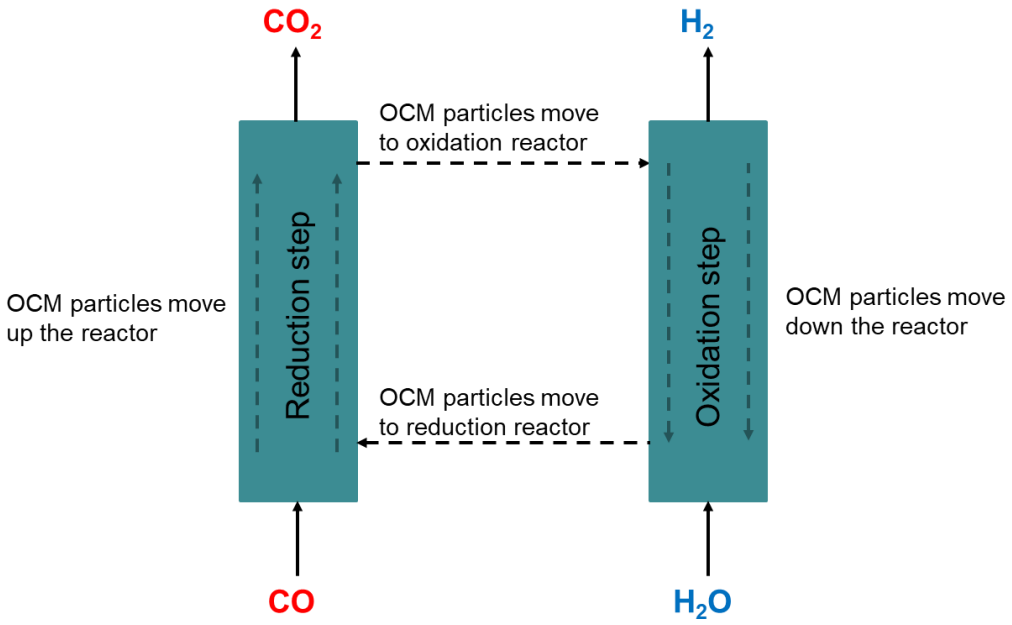

Figure 1.7: Circulating fluidised bed process using two reactor stages.

Mattisson and Lyngfel proposed an auto-thermal chemical looping reforming (CLR) process in 2001 that uses two interconnected fluidised beds, one as the fuel reactor where methane is partially oxidised to form a stream of carbon monoxide, carbon dioxide, hydrogen and water using a metal oxide OCM, and the other as an air-reactor where the OCM is regenerated by oxidation in air. The stream from the fuel reactor is taken to a shift reactor where the carbon monoxide and water in the stream react to form carbon dioxide and hydrogen.

A Three-Reactor Chemical Looping (TRCL) process, that involves the addition of a water splitting step and can use methane or syngas as the reducing agent, was introduced by Chiesa et al (2008) as a variation of the circulating fluidised system and uses iron oxide as the OCM. This process involves in order: a separate air reactor (AR), fuel reactor (FR) and steam reactor (SR) where an additional water splitting stage is carried out to produce hydrogen, and is shown in Fig. 1.8. The AR stage is carried out since steam is not a strong enough oxidising agent to fully oxidise iron oxide to haematite, and doing so can improve conversions. Reed et al (1953) devised one of the earliest set-ups for a TRCL system using iron oxide as the OCM and a hydrocarbon as the reducing agent, though this process included the air oxidation step before the SR stage with the

intention of using the air oxidation step to remove any carbon that had been deposited on the OCM during the reduction stage, though at the cost of lower hydrogen production.

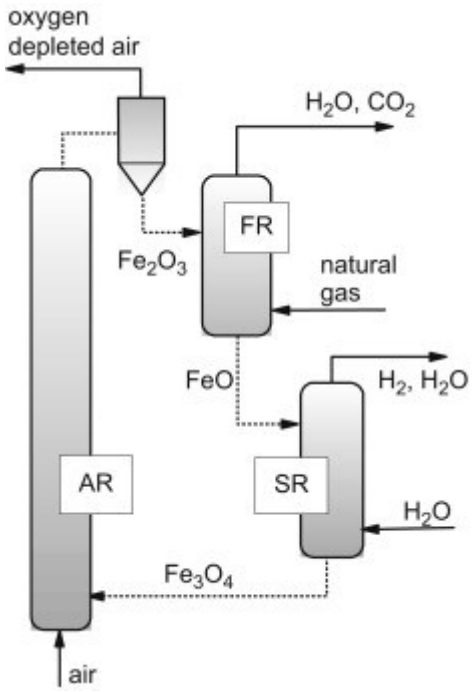

Figure 1.8: General process outline for TRCL (Chiesa et al, 2008). The two steps (FR and SR) are present in typical two-step CLWGS processes but with CO reducing agent. The air oxidation step is present in the TRCL process to oxidise magnetite back to haematite.

1.3.3 Reducing agents

Various alternative reducing agents other than carbon monoxide have been identified and reviewed in the literature. Carbon monoxide on its own is not a viable choice industrially since it must be produced from another source. This can typically be via separation of syngas which itself can be used as the reducing agent and would thus make more sense economically. Other possible fuels include coal, biomass and natural gas.

Methane

The use of methane as a reducing agent is an attractive option for industrial scale applications. It is the primary component of natural gas which is far easier to obtain than carbon monoxide and is used widely in industry for existing processes like methane steam reforming. For a circulating fluidised bed system the ratio of oxygen available to methane from the OCM can be controlled and set to a continuous value as shown by de

Diego et al (2009) – this is important since the products of the reduction stage can vary based on whether methane is partially oxidised (carbon monoxide and hydrogen) or fully oxidised (carbon dioxide and water). These reactions are given in Eq. 1.21 and Eq. 1.22.

Full methane oxidation	$CH_4 + 2O_2 \rightarrow CO_2 + 2H_2O$	(Eq. 1.21)
Partial methane oxidation	$CH_4 + 0.5O_2 \rightarrow CO + 2H_2$	(Eq. 1.22)

However the large endothermic heat of reaction seen in Eq. 1.23 when the OCM is reduced via oxidation of methane results in an energy deficit in two-step chemical looping systems, such as that proposed by Mattisson and Lyngfelt (2001), meaning that additional heat would be required to operate the process. The aforementioned TRCL process in section 1.3.2 with the air oxidation step could be used to cover this deficit, and this can be further optimised by increasing the air-to water ratio and finding a balance between lower hydrogen production and the generation of additional energy, ultimately allowing for the process to potentially be operated auto-thermally on an industrial scale and maintaining full oxidation of the OCM (Kang et al, 2010). To achieve auto-thermal operation there must be no extra energy added to the system other than the heat generated during the air oxidation step, and initial process start-up. Studies of the system efficiency using a steam compression and combustion turbine with metal-oxide OCMs have predicted that significant amounts of heat could be recovered from the gas streams to make the TRCL process near self-sufficient in terms of electrical power consumption (Chiesa et al, 2008).

Table 1.3: TRCL methane reduction, water oxidation and air oxidation stage reactions using iron oxide as the OCM. Note that the methane reduction stage is endothermic.

Reaction	**ΔH_{1023K} (kJ/mol)**
$3CH_4 + 3Fe_2O_3 \rightarrow 3CO + 6H_2 + 6FeO$ (Eq. 1.23)	760
$6Fe + 8H_2O \rightarrow 2Fe_3O_4 + 8H_2$ (Eq. 1.24)	-190.5
$½\ O_2 + 2Fe_3O_4 \rightarrow 3Fe_2O_3$ (Eq. 1.25)	-240

Another potential area of concern with the use of methane is the formation of carbon (Eq. 1.26 – 1.29) on the OCM surface which would reduce the lifetime of the material. Reactions in Eq. 1.27 – 1.29 may occur if traces of CO, H_2, or higher order hydrocarbons are present in the feedstock. Murugan (2011) investigated the perovskite-type material $La_{0.7}Sr_{0.3}FeO_{3-\delta}$ as an OCM and proposed that compounds of CH_x could be adsorbed onto the surface of the material, leading to the formation of carbon monoxide and/or carbon dioxide in the subsequent oxidation stages lowering the purity of the hydrogen product stream.

Table 1.4: Potential carbon formation reactions that may occur when using methane as reducing agent. If traces of carbon monoxide or higher order hydrocarbons are present in the feedstock, reactions in Eq. 1.27 – 1.29 may also take place.

Description	**Reaction**	**ΔH^0_{298K} (kJ/mol)**
Methane Decomposition	$CH_4(g) \rightleftharpoons C(s) + 2H_2(g)$ (Eq. 1.26)	74.86
Reverse Boudouard Reaction	$2CO(g) \rightleftharpoons C(s) + CO_2(g)$ (Eq. 1.27)	-172.53
Reverse Carbon Gasification	$CO(g) + H_2(g) \rightleftharpoons C(s) + H_2O(g)$ (Eq. 1.28)	-131.38
Polymerisation (Gum)	$C_nH_{m+2}(g) \rightarrow (CH_2)_n(g) \rightarrow gum(s)$ (Eq. 1.29)	-

Christensen and Rostrup-Nielsen (2011) described the different types of carbon that may be formed in various temperature ranges in methane steam reforming reactions on nickel surfaces. Gum carbon is prevalent in the temperature range of 693 – 803 K, while whisker carbon is formed in the range of 843 – 873 K. Reactions in Eq. 1.26 – 1.28 in table 1.4 indicate reactions where whisker carbon may be formed. Eq. 1.29 shows the polymerisation reaction from which gum may be formed. Although gum does not actually cause significant carbon build-up, it could lead to the gradual reversible deactivation of the OCM due to slow polymerisation of higher hydrocarbon radicals on the OCM surface through surface reactions. The rate of adsorption of hydrocarbons is higher than that of hydrocracking at lower temperatures, resulting in gum formation.

Go et al (2009) investigated the suitable temperature conditions to use for a steam-iron process using methane as the reducing agent. They found that the optimal reduction temperature range to use was between 1073 – 1148 K in order to avoid methane decomposition, and an oxidation temperature of 1173 K was suggested. It was also seen that carbon formation occurred much more rapidly in the presence of elemental iron, and could lead to contamination of the hydrogen product with carbon monoxide formed by reaction of deposited carbon with water vapour during the oxidation half cycle. Higher hydrocarbons are in general more prone to carbon formation than methane.

Carbon monoxide

Another option for the reducing agent is the use of carbon monoxide gas. It is an ideal reducing agent to use in laboratory-scale experiments involving chemical looping as it oxidises directly to carbon dioxide, thereby avoiding selectivity complications and simplifying the modelling involved. However carbon monoxide is not a realistic feed gas to use on an industrial scale since it does not naturally occur in large concentrations and its main production method is via the Boudouard reaction given by the reverse of Eq. 1.27 in table 1.4.

Carbon monoxide has a lower tendency for carbon formation owing to the fact that solid carbon can only be formed via the reverse Boudouard reaction in Eq. 1.27. Mondal et al (2004) produced an Ellingham diagram of the Gibbs free energies of the reactions of iron oxide with carbon monoxide and this is reproduced in Fig. 1.9.

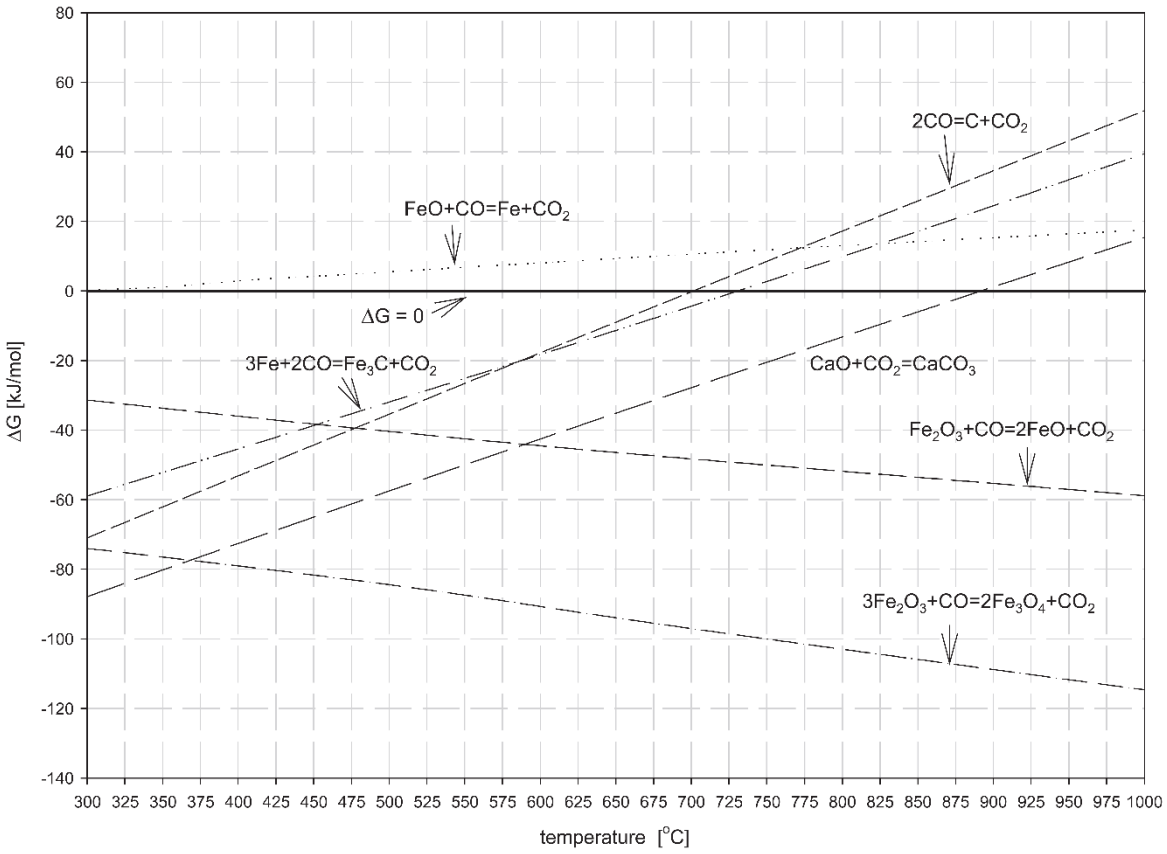

Figure 1.9: Ellingham diagram showing the Gibbs free energies of reactions of iron oxide with carbon monoxide at different temperatures (Mondal et al, 2004).

From Fig. 1.9 it can be seen that if the reactions are carried out at T > 1023 K (750 °C) the Gibbs free energy for the reverse Boudouard reaction and for the formation of iron carbide is greater than zero, meaning carbon formation will be reduced and the rate of reduction will be improved.

Syngas

Syngas is another possible reducing agent that can be used. It is an artificially produced mixture of fuel gases that typically consists of 30-60% carbon monoxide, 25-30% hydrogen, 5-15% carbon dioxide, 0-5% methane, and other hydrocarbons and condensable compounds, and may be produced from the gasification of coal or biomass.

Syngas is an important intermediate product in the chemical industry - ~ 6 EJ of syngas is manufactured globally per annum and this is roughly 2% of the current global primary energy consumption (El-Nagar & Ghanem, 2019).

The presence of impurities such as tar, sulphur and chlorine (Cleeton et al, 2009) in the syngas feed could lead to the pre-mature deactivation of the OCM, meaning potential feed pre-treatment processes such as a desulphurisation unit would need to be put in place if syngas were to be used as the reducing agent (Thursfield et al, 2012). Studies have been carried out that have looked into the limits of certain impurities in the feed that can hinder the cyclic stability of the OCM. Hacker et al (2000) and Müller et al (2011) both found that the presence of hydrogen sulphide did not adversely affect the kinetics of reaction and purities of CO < 8 ppm, HCl < 4 ppm and H_2S < 1 ppm were quoted by Hacker et al (2000), although the experiments were only carried out over 5 cycles in both cases.

Carbon deposition from the carbon-based fuels in the syngas can also lead to a reduction in hydrogen purity. Voitic et al (2016) carried out cyclic reduction experiments using a $Fe_2O_3/Al_2O_3/CeO_2$ OCM with syngas as the reducing agent, and found that there was no correlation between using an increased system pressure (up to 50 bar) and the hydrogen purity from the oxidation stage. They suggested that solid carbon was not being fully re-oxidised during steam-oxidation and was accumulating in the cyclic experiments. This would result in the purity of hydrogen to gradually decrease per cycle unless air oxidation was carried out to completely remove the carbon residues.

Syngas derived from coal

Coal may be used to produce syngas, and it can also be used directly in the process. Direct feed coal is relatively cheap and more abundant than natural gas alternatives (Li et al, 2009). The use of direct feed coal can eliminate the need for gasification reactors, although problems can arise relating to solid-solid mixing, impurities in the coal, and requirements for additional equipment for solid transportation. Yang et al (2008) carried out an investigation of the effect of potassium impregnated coal into fuel conversions, and found that this improved the carbon conversion rate and gave a higher concentration of CO_2, although they also caution this with an explanation that addition of

potassium would not be economically viable for industrial use. Gupta et al (2007) investigated the theoretical conversions possible with various metal oxides (Ni, Cu, Cd, Co, Mn, Sn, and Fe) for producing hydrogen from coal derived syngas and found that iron oxide (haematite) provided the best conversion of syngas to combustion products and the highest conversion of steam to hydrogen. An Aspen Plus reactor simulation by Zeng et al (2012) showed that even with a kinetically limited scenario using iron oxide it was possible to achieve overall energy conversion of 77.2% and 95% CO_2 removal. Liu et al (2018) investigated the characteristics of various $CaSO_4$ composite oxygen carriers composed of clay, cement, and ash for CLC using coal derived syngas as the reducing agent. While sulphurous gas generation was observed for all three types of OCM, it was found that the $CaSO_4$/clay composite OCM had good reactivity with the steam gasifying agent, and it was suggested that addition of CaO to the $CaSO_4$/clay could enhance its reaction rate with coal and restrain the release of SO_2.

Syngas derived from biomass

Like with coal, biomass can also be used to produce syngas for use of hydrogen production. Solid biomass first undergoes the process of fast pyrolysis where it is heated at high temperatures in an oxygen-free atmosphere followed by subsequent cooling to produce a liquid which is typically 65-75 wt.% pyrolysis oil, 15-35 wt.% water and remainder oxygenated hydrocarbons (Bleeker et al, 2007). The pyrolysis oil may then by injected into the reaction bed for steam reforming to produce hydrogen, and benefits from a high energy density and easier transport and storage than solid biomass (Rahimpour & Nategh, 2016). Impurities in the biomass, like with coal, can lead to deactivation for the OCM and/or lead to a decrease in reactivity. Bleeker et al (2010) explained that the presence of water in the pyrolysis oil could reduce the formation of carbon by preventing complete reduction of the OCM to metallic iron, but high losses of surface area were still observed.

1.4 Objectives

This chapter has provided a background to hydrogen and an explanation of the key concept of chemical looping that forms the basis of this thesis, focusing on the CLWGS process.

In the CLWGS process, temporally separate gaseous carbon monoxide and water feeds are passed over a suitable solid OCM to produce unmixed hydrogen and carbon dioxide product streams. Due to the high purity of hydrogen produced, CLWGS can reduce or eliminate the need for additional separation stages thereby reducing plant costs and lowering the carbon footprint compared to more conventional processes such as SMR.

The aim of this thesis is to investigate the thermodynamic principles behind the selection of non-stoichiometric OCMs (OCMs which can accommodate a variable amount of oxygen) for the CLWGS process. The case for a hypothetical material which arises from the thermodynamics of the WGS reaction is proposed. In conjunction with a mathematical reactor model this can be applied as a benchmark against which new OCMs may be measured, provided that they have sufficiently fast kinetics to make the process thermodynamically limited.

This benchmark will be used to justify the selection and subsequent investigation of the performance and stability of OCMs using a variety of experimental techniques. These involve a laboratory scale packed bed integral reactor carrying out the CWLGS process, using water vapour as the oxidising agent and carbon monoxide as the reducing agent. The performance of OCMs will be evaluated via gas analysis, and in-situ X-ray diffraction techniques will also be used to provide a better understanding of the internals of the reactor. Thermogravimetric analysis will be used to study the oxygen non-stoichiometry versus oxygen partial pressure behaviour of selected OCMs more closely. The screening and selection of OCMs is covered in chapters 3 and 4.

Ultimately the thesis aims to yield an approach to the selection of OCMs that can be used in practice to select higher conversion, higher usable oxygen capacity materials tailored for CLWGS. By taking advantage of the inherent carbon capture incorporated into the process due to the separation of product streams, the CLWGS process may in turn be used as a bridge on the path to future widespread environmentally friendly production of hydrogen and lower dependence on SMR technology.

Chapter 2: Oxygen-carrier materials and the advantage of non-stoichiometry for chemical looping water-gas shift

Critical for the success of the chemical looping process is the use of an appropriate OCM. Rydén et al (2008) suggested a number of parameters as being important to the selection of a good OCM. In order to achieve a high conversion towards the desired hydrogen product the OCM must demonstrate high reactivity towards the reducing and oxidising agents, and this is brought about through favourable thermodynamic properties and fast reaction kinetics. The OCM should have a high oxygen transfer capacity and show a low level of surface carbon formation during extensive cycling as this can lead to lower purity hydrogen. The OCM should also demonstrate a good degree of resistance to mechanical or thermal degeneration, especially towards fragmentation, attrition and agglomeration, in order to allow for longer lifetimes. It will also ideally be of a low price, toxicity and have minimal environmental impact.

In addition, there are specific OCM requirements which depend on the chemical looping reactor system in use. For circulating fluidised bed reactors the OCM must have a high resistance to attrition in order to maintain the particle size for such a duration as for the cost of material replacement to be economically viable. For packed bed reactors, the pressure drop across the bed must be minimised by use of OCM with appropriate particle sizes while still maintaining the reaction kinetics and avoiding agglomeration problems as well.

This chapter will provide a review of the various OCMs studied in the literature and explain how by using a suitable non-stoichiometric OCM within a packed bed reactor the thermodynamics will allow for higher reactor conversions than with other types of OCMs such as metal/metal oxides.

2.1 Phase changing oxygen carrier materials

Phase changing OCMs refer to OCMs that undergo phase changes and receive or donate oxygen at fixed chemical potentials. In this respect the oxides of the period 4 d-block transition metals have been studied for use as OCMs in CLWGS, where incomplete d-subshell allows for metals that can take various oxidation states. The greater the

difference in the oxidation states the cation can take, the greater the oxygen transfer potential. They are also more readily available and cheaper than transition elements in other periods such as Ag or Pd. Table 2.1 shows a summary of the abundance of the transition elements in periods 4 to 6, as well as indicating which elements can form oxides which are thermodynamically capable of being reduced and oxidised by carbon monoxide and steam in the CLWGS process (without the use of a support material such as alumina). Of the elements in table 2.1 iron is the most abundant, followed by titanium and then by manganese. Of the elements in period 5, only zirconium and niobium show abundances in similar orders of magnitude to those in period 4. The rest of the elements in period 5 and in period 6 are expensive to procure in large quantities due to low abundance.

Table 2.1: Abundance of transition metals in mg/kg of Earth's crust (Rumble et al, 2021). Elements which are realistically capable of forming unsupported oxides which can be reduced and oxidised with carbon monoxide and steam are indicated with blue text and underlined (determined using Ellingham diagram data available from the University of Cambridge DoITPoMS online resource).

22 **Ti** 5650	23 **V** 120	24 **Cr** 102	25 **Mn** 950	26 **Fe** 56300	27 **Co** 25	28 **Ni** 84	29 **Cu** 60
40 **Zr** 165	41 **Nb** 20	42 **Mo** 1.2	43 **Tc** 1.35×10^{-12}	44 **Ru** 0.001	46 **Rh** 0.001	47 **Pd** 0.015	48 **Ag** 0.075
72 **Hf** 3.0	73 **Ta** 2.0	74 **W** 1.25	75 **Re** 0.0007	76 **Os** 0.0015	77 **Ir** 0.001	78 **Pt** 0.005	79 **Au** 0.004

$<10^{-2}$	$10^{-2} - 10^{-1}$	1 – 10	$10 - 10^{2}$	$10^{2} - 10^{3}$	$>10^{3}$

2.1.1 Iron oxide

Iron oxide has long been seen as an attractive material to use as an OCM for CLWGS processes and has precedence as the material for the steam-iron process (Yang et al, 2008). It is relatively cheap - indeed iron oxide is the cheapest of all the metal oxides – although this cost can increase depending on whether it is obtained from a low cost source such as iron ore, which contains various impurities such as silica, alumina and calcia, or from a higher purity and more expensive source like sponge iron (U.S. Geological Survey, 2013). Iron oxide also benefits from favourable reaction kinetics with CO and its thermodynamics allows for a large potential oxygen capacity between oxidised and reduced states. The oxidation states which iron may typically exist in during reactions are given in table 2.2.

Table 2.2: The standard oxidation states of iron oxide.

Phase	**Formula**	**Oxidation state**
Iron	Fe	0
Wüstite	FeO	+2
Magnetite	Fe_3O_4	+2,+3
Haematite	Fe_2O_3	+3

Iron oxide can exist in 3 stable oxidation states: haematite (Fe_2O_3), where the Fe cations have an oxidation state of +3, magnetite (Fe_3O_4), where the Fe cations exist as a mixture of +2 and +3 oxidation states, and wüstite (FeO), where the Fe cations have a +2 oxidation state. Metallic iron with oxidation state 0 may be formed during reaction conditions if wüstite undergoes reduction. It should be noted that wüstite can have iron deficient composition with the iron/oxygen ratio in the range 0.83-0.95 (Hacker et al, 1998). However this thesis will consider wüstite to be in the form FeO in order to simplify thermodynamic analyses. Iron oxide may be reduced in reaction with carbon monoxide as in the following reactions:

$$CO + 3Fe_2O_3 \leftrightarrow CO_2 + 2Fe_3O_4 \qquad \text{Eq. 2.1}$$

$$CO + Fe_3O_4 \leftrightarrow CO_2 + 2FeO \qquad \text{Eq. 2.2}$$

$$CO + FeO \leftrightarrow CO_2 + Fe \qquad \text{Eq. 2.3}$$

Likewise, the reaction of iron oxide with steam and with air to oxidise to magnetite and to haematite are as follows:

$$H_2O + Fe \leftrightarrow H_2 + FeO \qquad \text{Eq. 2.4}$$

$$H_2O + 3FeO \leftrightarrow H_2 + Fe_3O_4 \qquad \text{Eq. 2.5}$$

$$0.5O_2 + 2Fe_3O_4 \leftrightarrow 3Fe_2O_3 \qquad \text{Eq. 2.6}$$

The reactions of iron-oxide with steam and carbon monoxide in the steam-iron process are shown in Eq. 2.7 and Eq. 2.8, where magnetite is reduced with carbon monoxide to form iron and carbon dioxide, before being oxidised back to magnetite.

Oxidation	$3Fe + 4H_2O \rightarrow Fe_3O_4 + 4H_2$	Eq. 2.7
Reduction	$Fe_3O_4 + 4CO \rightarrow 3Fe + 4CO_2$	Eq. 2.8

Although iron oxide may initially exist as haematite before the process is first started, steam is not a strong enough oxidiser to oxidise the metal back to haematite, hence magnetite has been used in the descriptions of the general reactions. The Baur-Glaessner diagram in Fig. 2.1 shows how iron oxide changes phase under different gas atmospheres and temperatures from 673 K to 1273 K (Bleeker et al, 2007).

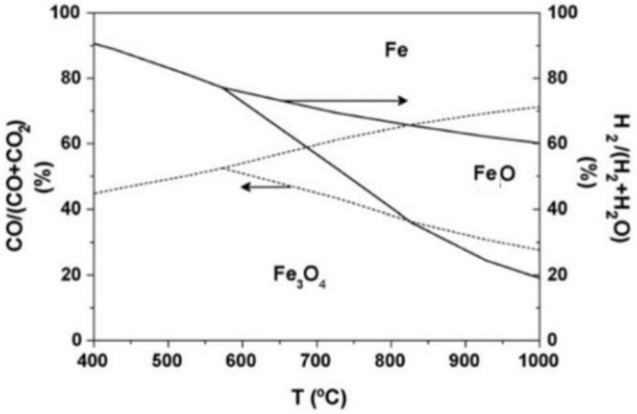

Figure 2.1: Baur - Glaessner diagram describing the phases of iron oxide under different atmospheric conditions (Bleeker et al, 2007).

At 1093 K iron oxide exhibits two phase changes: the first is from magnetite to wüstite at a $CO/(CO+CO_2)$ ratio of ~40%, and the second is from wüstite to metallic iron at a $CO/(CO+CO_2)$ ratio of ~67%. of oxygen that is available for reaction. In Fig. 2.1 it can be seen that the wüstite phase is only stable above a temperature of ~838 K (565 °C), and that steam cannot oxidise the material to haematite. The only way to do this would be to use air, though no hydrogen would be produced.

Since it is not possible to oxidise iron oxide to haematite with steam, the only way in which the oxygen capacity of the material may be increased therefore is by allowing the material to be reduced all the way to metallic iron before oxidising it. However this brings about a number of complications as Hertel et al (2012) showed that this can result in the formation of iron-wüstite and wüstite-magnetite reaction zones in the bed, with the metallic iron acting as a catalyst for carbon deposition via the Boudouard reaction thereby limiting the lifetime of the material. In addition the deposition of carbon can result in contamination of the hydrogen product with carbon dioxide and/or carbon monoxide during the oxidation half cycle due to the removal of the deposition carbon. If air were to be used to re-oxidise the material to haematite, an additional problem that can be encountered is thermal sintering due to the exothermic nature of the oxidation reactions for the deposited carbon as well as the OCM. This would also affect the activity of the material and reduce the potential lifetime, as well as the

conversion to hydrogen since some of the OCM oxygen capacity would be used up by reaction with air.

Bohn et al (2008) has also reported deactivation of iron oxide due to agglomeration and sintering. During ten cycles between the Fe_2O_3-Fe phase transition that were carried out using CO and CO_2 gas mixes using 10 minute feeds, the production of hydrogen dropped consistently each cycle for all of the three temperatures that were studied (873 K, 1023 K and 1173 K) to ~19% in the tenth cycle in comparison to the first cycle. However, when cycling was carried out between the Fe_2O_3-FeO transition consistent levels of hydrogen could be produced per cycle. It was noted that the production of hydrogen was greater for reduction to metallic iron (owing to the fact that most of the oxygen capacity for iron oxide is derived from the Fe-FeO transition) despite the increased rate of deactivation.

The effects of sulphur (which may be present in feeds such as biomass, natural gas or coal) were investigated by Wang et al (2008) who found that with syngas the oxidation effect of carbon dioxide (for hydrogen sulphide conversion to sulphur dioxide) was stronger than that of water vapour, while water vapour had a stronger inhibition effect against carbon deposition. Zhang (2014) found that the rate constants associated with the of reduction of haematite were adversely affected if the addition of hydrogen sulphide was prolonged after the reduction of haematite was completed, while this effect could be diminished if at higher temperatures (923 K) and hydrogen sulphide addition not prolonged.

The kinetics for CLWGS using packed-bed reactors with gas feeds (which is the primary focus of this thesis) relate to gas-solid interactions. The reduction of iron oxide was investigated by Bohn et al (2010) who found that the kinetics of the reduction steps for reduction from haematite to magnetite or to wüstite were first order in carbon monoxide. For non-catalytic gas-solid interactions, the reaction may be described in the following intermediate stages:

i) The gas phase reactants diffuse through the film surrounding the particle to the surface of the OCM.

ii) The penetration and diffusion of the gas phase reactant through the pores of the OCM to the surface of the unreacted core.

iii) The reaction of the gas phase reactants with the OCM at the surface.

iv) The diffusion of the gaseous product through the OCM pores and back to the surface of the OCM.

v) The gaseous product diffuse through the film surrounding the particle and return to the bulk gas phase stream.

The simplest kinetic model which approximates these steps and allows for prediction of the rate and conversion of the reaction is the shrinking core model as described by Levenspiel (1999). The shrinking core model for reduction of an iron oxide particle has been covered by Alamsari et al (2011) and Parisi & Laborde (2004) and is illustrated in Fig. 2.2. In the figure the model assumes the existence of several layers in the cross section of the material that consist of the different phases of iron oxide with sharply defined boundaries. The most oxidised form haematite exists at the centre, while the more reduced forms exist in progressive steps further out. At the outside the model assumes layers consisting of a gas film and ash (deposited carbon).

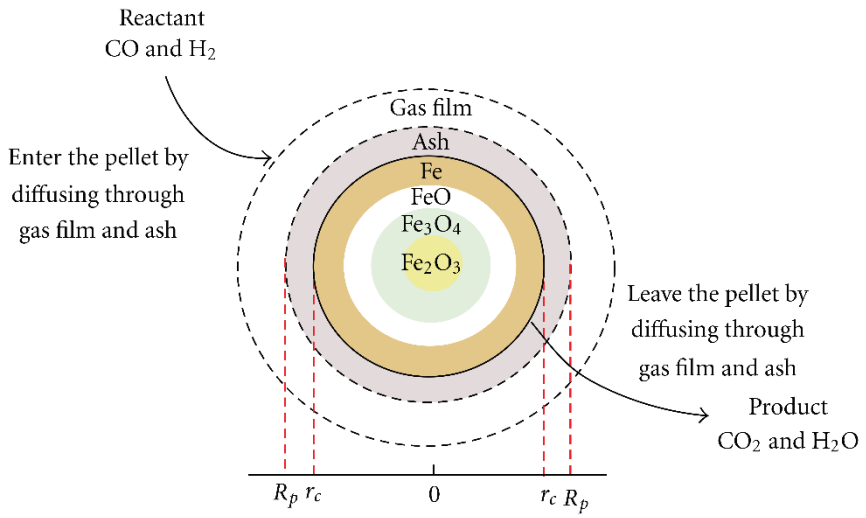

Figure 2.2: Cross-sectional schematic representing the different phases of iron oxide in the shrinking core model, from Alamsari et al (2011).

The shrinking core model presumes that the reaction is initiated by the gas phase reactants (CO, H_2) at the outer surface of the OCM and is restricted to a sharp front that moves towards the OCM core. Starting from a fully oxidised OCM, as the gas permeates towards the OCM core the various levels of oxidation states start to form. Assuming that the system is under isothermal conditions and the reactions are irreversible, the rate of the reaction is determined by steps *i-iii* as previously outlined. The step with the highest resistance will be the rate determining step; the thickness of each layer in the particle and therefore the rate of reduction depends on the OCM gas diffusion rate. Alamsari et al (2011) assume negligible quantities of wüstite and magnetite phases and that they do not affect the kinetics. This limits the use of the model in scenarios with high concentrations of wüstite and magnetite under strongly reducing atmospheres

A cracking core model was described by Park & Levenspiel (1977) which assumes an increase in the porosity and fragmentation of iron oxide as it becomes more reduced from haematite to magnetite etc. The gas diffusivity increases as a result of the increasing porosity thereby allowing for higher rates of reduction. While the cracking core model is more accurate, it is harder to use than the shrinking core model.

Sohn & Szekely (1972, 1973) proposed a grain model where a particle is assumed to consist of many small non-porous grains that each individually follow the shrinking core model while during reaction. While this is beneficial for describing the reactions between reduction gases and porous particles the model assumes that the size and shape of the grains do not change during the reaction, which is not true in reality as they would be effect by differences in molar volume between reactant and solid product. Georgakis et al (1979) and Bhatia & Perlmutter (1980) have described more complicated models which take into account structural changes of the particle by using a size distribution of randomly overlapping cylindrical surfaces to describe the surface of the particle as a function of time, although these have additional complexity and have several variables which are hard to accurately define. Hossain & Lasa (2010) describes the formation of nuclei at the active sites at the start of reaction, which then grow and proliferate through the particle resulting in the rate of reaction increasing. The nuclei continue to grow and eventually start to overlap and combine with each other.

Piotrowski et al (2005) used the Johnson–Mehl–Avrami–Erofe'ev equation describing nucleation and growth processes to suggest that the reduction was initially a surface-controlled process, but that after the reduction of the outer layer to magnetite and wüstite, the mechanism was controlled by diffusion. The reaction rate was found to increase with both increasing the temperature and the hydrogen concentration of the inlet gas. Comparison with reductions carried out at 973 K – 1173 K with a thermogravimetric analyser showed a better fit for the topochemical reaction model than the phase-boundary controlled model.

A combined approach was suggested by Peña et al (2006) where the shrinking core model is used for the initial reduction of the haematite to magnetite in the first stage, followed by using of the cracking core and nucleation models to describe later stages of the reduction involving the phase transition of magnetite to metallic iron.

Various studies have been carried out looking into the use of supports to increase the cyclability and lifetime of iron oxide OCM. Bohn et al (2010) used modified iron oxide with supports of alumina, magnesia, silica and chromium oxide added via wet impregnation in various loadings and subject to ten cycles with steam and either carbon monoxide or hydrogen. The alumina supported iron oxides gave the best performance, with authors attributing this to the formation of $FeO{\cdot}Al_2O_3$ spinels from the reaction of iron oxide with alumina which stabilises the OCM. An investigation by Kierzkowska et al (2010) carrying out cycles with carbon monoxide and steam found that 40 wt% alumina loading on iron oxide gave the greatest improvement compared to other levels (0, 10 and 20 wt%) irrespective of the degree to which the OCM was reduced. Murugan et al (2011) carried out a longer cycling campaign with iron oxide with 40 wt% alumina doping using carbon monoxide and steam and found that the reactivity of the reduction and oxidation steps started to decrease after ~40 cycles due to degradation of the material, and after ~80 cycles the material remained steady but with a lower reactivity.

An investigation by Yüzbasi et al (2017) assessed the influence of precursors of iron nitrate, iron chloride and iron acetylacetonate during synthesis via a sol gel technique (described by Kierzkowska et al (2010)) on the performance of OCM with 80 wt% Fe_2O_3 for 15 cycles between carbon monoxide and water vapour (plus an additional air

oxidation stage). They found that OCMs synthesised using iron nitrate or iron acetylacetonate gave high initial hydrogen yields before decreasing in later cycles due to loss of surface area from sintering, while the OCM synthesised using iron chloride gave low but stable hydrogen yields over the 15 cycles attributed to formation of spinel $FeO{\cdot}Al_2O_3$.

Several investigations have been carried out to assess the effect of doping small quantities of transition metals to iron oxide in order to improve the reaction rates with reactant gasses, and allow for lower temperatures and longer usable lifetime. The addition of 26 different metals (< 3 mol.%) to iron oxide was studied by Otsuka et al (2003) in redox cycles at temperatures of < 673 K where carbon deposition via the Boudouard reaction is more favourable, and it was found that additives of Al, Cr, Zr, Ga and V gave the best reaction rates. Brunauer-Emmett-Teller (BET) analysis of the samples indicated a decrease in surface area for all samples, although addition of Al and Cr gave the highest resistance to carbon deposition.

The effects of adding either Rh and Mo independently or at the same time were investigated by Takenaka et al (2004), who found that when added independently both resulted in faster rates of sintering than undoped Fe_2O_3. However addition of the two metals at the same time resulted in a high resistance to sintering and was also able to allow for a lower operating temperature. Urasaki et al (2005) investigated the addition of Pd and Zr to iron oxide and found that while only Pd improved the reduction rate, both reduced sintering and enhanced the reaction rate during oxidation. The best performance was seen with the addition of both metals suggesting a synergetic effect.

2.1.2 Nickel oxide

Nickel oxide has been investigated as an OCM for the CLWGS process, albeit less successfully than iron oxide. There is a thermodynamic limitation for reducing or oxidising nickel oxide using carbon monoxide or steam as indicated before in Fig. 2.1. One way to get around this problem is to lower the activity of NiO through the formation of a stable spinel which is more stable than NiO. A thermodynamic study by Svoboda et al (2008) analysed the redox reactions for the Ni-NiO system with steam. They found that the yield of hydrogen from the reaction of steam with Ni (Eq. 2.9) at lower

temperatures could be improved by 1-2 orders of magnitude if the activity of NiO were to be substantially reduced by reaction with another solid material or carrier such as spinel $NiO \cdot Al_2O_3$.

$$H_2O + Ni \leftrightarrow NiO + H_2 \qquad \Delta H_{1000K}\ (\text{kJ/mol}) = 43.48 \qquad \text{Eq. 2.9}$$

Mattisson et al (2001) found that the reactivity of nickel oxide with steam for hydrogen production was lower than systems using iron oxide OCMs. Murugan et al (2011) showed that thermodynamically nickel oxide exists as metallic Ni or NiO, which limits the number oxidation states this OCM can take in comparison to iron oxide and hence the oxygen capacity. They reported the presence of only one phase change when carrying out cyclic TPR and TPO experiments with supported 20% wt. NiO/Al_2O_3. In addition, carbon deposition was seen during the reduction half cycle with CO and this was attributed to the increase in hydrogen production that was seen in the later oxidation half cycles where carbon was removed during water oxidation. These problems, along with the thermodynamic limitations and its increased cost in comparison to iron oxide, make nickel oxide based OCMs less desirable for CLWGS.

On the other hand, OCMs based on nickel oxide have been used extensively in chemical looping combustion (CLC) processes at high temperatures (1173 – 1473 K) owing to its high redox reactivity, large oxygen capacity and high melting point (~2273 K) (Mattisson et al 2006, Corbella et al 2005, Corbella et al 2006). The selectivity of nickel oxide for the full oxidation of methane was found to decrease from 99% at 1173 K to 97.7% at 1473 K in a study by Cho et al (2004). In addition issues that would affect the operational lifetime of the OCM were also reported such as carbon deposition due to the material promoting methane cracking, sulphur poisoning and thermal sintering. García et al (2012) suggested that above a maximum concentration of H_2S of 100 ppmv the nickel oxide OCM would have too high a loss in redox activity to maintain good performance.

The use of an alumina support on nickel oxide has been investigated in CLC processes to get around issues of carbon deposition and sintering as well as to increase the rates of the oxidation and reduction reactions. The partial transformation of NiO to the spinel

compound $NiAl_2O_4$ during material preparation (> 1273 K) limits reduction, and studies have looked at different methods of sample preparation and support modification to minimise the interaction of the NiO with alumina. Ryu et al (2004, 2005) reported that a bentonite support with nickel oxide prepared by spray drying outperformed a 60 wt% NiO on bentonite OCM prepared by mechanical mixing, with good operational results for more than 50 hours. Shen et al (2010) investigated the performance of supported nickel oxide prepared by coprecipitation using coal as fuel and reported no significant change in morphology after 100 hours at fuel reactor temperature ≤ 1213 K but loss of surface area and porosity when the temperature exceeded 1233 K. Shen et al (2010) also investigated the redox reactivity of supported NiO when using sulphur containing CO and concluded that after 10 cycles the OCM was not significantly affected.

2.1.5 Manganese oxide

The development of Mn-based materials has been in the interest of literature; they are non-toxic and cheaper than nickel oxide, while having a higher oxygen transport capacity than iron oxides (Adánez et al, 2012). However as indicated previously in Fig. 2.1, the reduction and oxidation of manganese and its oxides using carbon monoxide and steam is thermodynamically limited, ruling this material out for use in CLWGS. A thermodynamic investigation by Svoboda et al (2007) found that between 400 K to 1000 K the reduction of Mn_3O_4 and Mn_2O_3 to MnO with carbon monoxide is thermodynamically favourable, however only the oxidation of MnO to Mn_3O_4 with steam is allowed and the resulting equilibrium conversions are very low. In addition, the melting point for the manganese oxides are at 808 K for MnO_2 (National Center for Biotechnology Information) and at 1213 K for Mn_2O_3 (American Elements), making this material more limited in the range of operating temperatures at which it could be used.

For CLC processes, a thermodynamic analysis of the oxide pair Mn_2O_3-Mn_3O_4 by Jerndal et al (2006) found than it was not possible to be used at higher temperatures due to the decomposition of the most oxidised phase. The equilibrium concentrations for oxygen release with manganese oxide occurs below 1073 K and the reoxidation of the material is slow at lower temperatures (Rydén et al, 2011); Shulman et al (2009) found that the reoxidation of a pure manganese oxide system by 10% O_2 in N_2 would be impossible at

1173 K. Zafar et al (2007) found that at temperatures above 1073 K only the presence of the Mn_2O_3 phase could be established, meaning that for CLC applications only the transition between Mn_3O_4 and MnO is considered.

Larring et al (2015) investigated the use of mixed Fe-Mn oxides for CLC application with methane and found that the addition of small amounts of Mn to iron based OCMs could improve the kinetics and capacity at lower temperatures, although decreasing the temperature also resulted in slowing the reaction and reduced the capacity, to which the authors suggest that a compromise would need to be reached. An investigation by Haidar et al (2016) using metal ores impregnated with manganese and iron oxides in a bench-scale fluidised bed found that unlike with methane, when using syngas the conversion to combustion products was not influenced significantly by faster kinetics associated with higher temperatures.

2.1.3 Copper oxide

Like with manganese oxide, the reduction and oxidation of copper oxide using carbon monoxide and steam is thermodynamically infeasible making it unsuitable for CLWGS, and it also has a lower melting point at 1573 K. Overall, this limits the suitability of this material for looping processes at elevated temperatures but is still acceptable for CLC at lower temperatures.

For CLC processes, OCMs based on copper oxide have a high redox activity even at low temperatures (973 K – 1173 K) (Tian et al, 2008) and was reported by Mattisson et al (2001) to have higher conversion of methane in comparison to either nickel oxide or iron oxide. A study by de Diego et al (2004) investigated the performance of copper oxide with and without using a support for CLC. When the unsupported copper oxide OCM was subjected to repeated cycling with methane and air there was a 90% decrease in the conversion levels over three cycles. When using carriers prepared by coprecipitation or mechanical mixing the carriers underwent degradation of mechanical properties during multicycle TGA tests but exhibited high reactivities and complete conversions. To reduce the effect of chemical and thermal stresses, CuO based carriers were prepared by wet impregnation using titania and silica as supports. These new carriers exhibited high reactivities and complete conversions for 100 redox cycles. In

addition, it was found that there was no influence of carbon deposition on the oxidations and reduction rates.

Forero et al (2009) studied the effect of variable amounts of light hydrocarbons such as ethane and propane in a CLC process using copper oxide with a γ-alumina support. One reactor was used for syngas combustion and one for methane combustion. They reported encountering no carbon deposition, agglomeration or any other type of operational problem, and the attrition rate was found to rapidly decrease after being high at the start of the experiment. Despite sulphur impurities in the feed gas full methane conversion could still be reached in the fuel reactor with no effect on the reactivity of the OCM (Forero et al, 2010). A similar study by de Diego et al (2007) using the same material suggested a particle lifetime of 2400 hours.

Another investigation by Son et al (2008) looked into the performance of copper oxide when using different types of inert support, with a synthetic syngas mixture as the reducing agent and a 20% water in nitrogen mixture as the oxidising agent. Alumina support resulted in higher methane conversions at 923 K than that achieved using silicon oxide. Higher temperatures lead to a drop in conversion due to the formation of the spinel compound $CuAl_2O_4$ and lower temperatures lead to a drop in the reaction kinetics. Although the oxidation reactivity using water were more favourable at lower temperatures, the kinetic limitations resulted in a water conversion of only 2% at 623 K. Imtiaz et al (2015) reported on using a co-precipitated ceria support for the copper oxide that demonstrated three times higher resistance to carbon deposition compared to alumina support at 1173 K and 1223 K, as well as improved oxygen capacity and redox cycling stability without phase intermixing.

2.1.3 Chromium oxide

Svoboda et al (2007) investigated the thermodynamic possibility of using chromium oxide as an OCM with various oxidising and reducing agents in the range 400-1000 K. For the reduction reactions of Cr_2O_3 with H_2, CO and CH_4, the reduction of Cr_2O_3 to metallic Cr was found to be thermodynamically exclusive, meaning that Cr_2O_3 was very stable in the range 400-1000 K. Likewise they found that the oxidation of Cr_2O_3 and CrO_2 by steam and CO_2 was thermodynamically excluded at lower temperatures. CrO_2 could

only be easily reduced to Cr_2O_3 and the reverse oxidation by steam or CO_2 was not possible thermodynamically. The authors suggest that the stability of Cr_2O_3 could make the material ideal for resistance to carbon deposition and utilised in mixed carrier materials. However as it stands the unsupported oxide is unsuitable for CLWGS applications.

2.1.4 Cobalt oxide

The high oxygen transport capacity of cobalt oxide has led to it being considered as a potential OCM. Thermodynamically Co_3O_4 is unstable at temperatures above 1173 K and is converted to CoO, this limits processes to only be able to utilise the phase transition from CoO to Co, which limits the maximum conversions possible when using this OCM (Adánez et al, 2012). A thermodynamic study by Svoboda et al (2008) found that Co-CoO could only achieve equilibrium hydrogen concentration in steam oxidation of metallic Co of < 2 vol.%, which is undesirable for CLWGS application. They suggested that complex systems with cobalt aluminium spinel and cobalt ferrite should be more thermodynamically advantaged to achieve higher yields of hydrogen in oxidation by steam.

Jin et al (1998, 1999) found that there was a strong interaction between CoO and various inert supports such as Al_2O_3, TiO_2 and MgO leading to the formation of unreactive spinel compounds such as $CoAl_2O_4$, $CoTiO_3$ and $Mg_{0.4}Co_{0.6}O$ which can lead to a decrease in conversion during operation. Ryu et al (2005) studied the operation of a CLC process using a Co-based material supported on $CoAl_2O_4$ and reported a 99.6% methane conversion during 25 hours of operation but noted limitations with respect to the attrition resistance of the material.

2.1.7 Tungsten oxide

Tungsten oxide is a promising material as it has four oxide states WO_2, $WO_{2.72}$, $WO_{2.96}$ and WO_3. A thermodynamic study was carried out by Villafan-Vidales et al (2016) looking into the use of the WO_3/W redox pair system for thermochemical production of solar fuels. They found that the formation of WC and W_2C phases was promoted when reducing WO_3 with methane at temperatures below 1000 K due to carbon deposition, making this material not suitable for long-term high purity hydrogen production. In

addition, Khan & Shamim (2017) showed with a thermodynamic investigation that the steam oxidation of WO_2 to either $WO_{2.72}$ or $WO_{2.96}$ and $WO_{2.72}$ to $WO_{2.96}$ was not possible in the investigated temperature range 1073 K - 1473 K which limits the number of usable phase changes for CLWGS at lower temperatures.

A study by Kodama et al (2000) carried out one redox cycle using zirconia supported tungsten oxide and suggested that syngas and hydrogen production could be carried out using methane reduction and water oxidation at 1273 K without formation of carbides, although no mention was made on whether oxides of carbon were present in the hydrogen product stream.

2.1.8 Niobium oxide

The reduction and oxidation of unsupported niobium oxide using carbon monoxide and steam is thermodynamically infeasible which prevents the use of this material for CLWGS. An investigation by dos Santos et al (2019) however has looked into the use of niobium oxide supported on alumina as an OCM for chemical looping reforming (CLR) processes. They found that the active phase was not Nb_2O_5 but the mixed oxide $AlNbO_4$ formed from the interaction between the metal oxide and the support. Using 10% methane as the reducing agent the authors claim that the process is entirely selective towards CLR products with no CO_2 being formed for the first few seconds of the reaction. This is a different behaviour from other transition metal oxides such as nickel oxide which start the reduction stage producing CO_2 and steam and only produce CO and H_2 after the oxidation of CH_4 to CO_2 is no longer total (Zafar et al, 2005). During the air oxidation stage a significant amount of CO is formed (Fig. 2.3), which suggests that during the reduction stage the methane was being converted to a carbon deposit on the material surface and hydrogen was released, confirmed by the high H_2/CO ratio during the first ten seconds of the reaction.

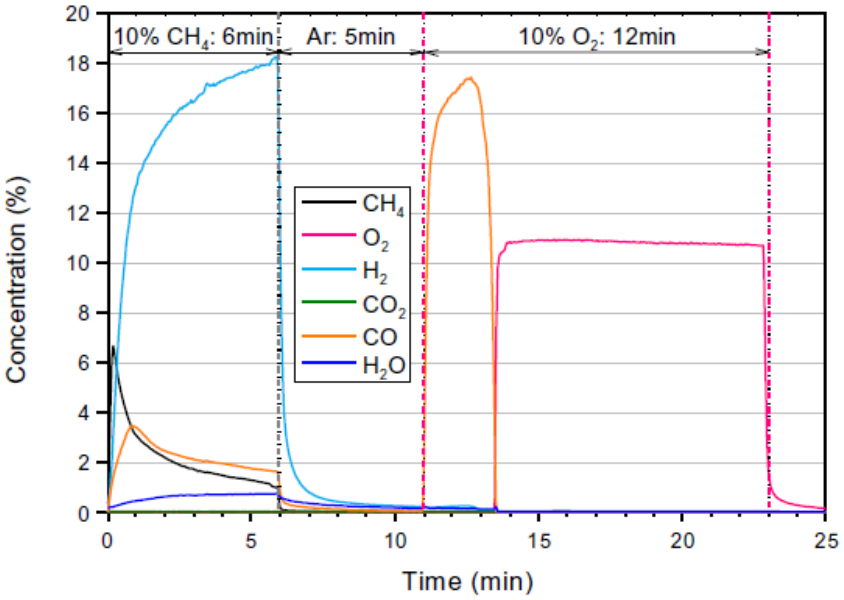

Figure 2.3: Concentration profile from the 5th redox cycle from investigation into niobium oxide by dos Santos et al (2019). Production of CO during the oxidation stage suggests the occurrence of carbon deposition during the reduction stage.

2.1.9 Non transition metal phase changing oxygen carrier materials

Słowiński & Smoliński (2016) investigated the thermodynamic feasibility of using germanium oxide in a CLWGS process for hydrogen production. The reaction of germanium oxide with steam and the resulting hydrogen is given in the following equation:

$$0.5Ge + H_2O \rightarrow 0.5GeO_2 + H_2 \qquad \text{Eq. 2.10}$$

Likewise the reduction reaction of germanium dioxide with carbon monoxide is given in Eq. 2.11:

$$0.5GeO_2 + CO \rightarrow 0.5Ge + CO_2 \qquad \text{Eq. 2.11}$$

The phase stability diagrams for a Ge/GeO_2 system are given in Fig. 2.4. For Ge oxidation, concentrated hydrogen may be generated at temperatures below 873 K (600 °C), while the maximum hydrogen concentration decreases to ~56 vol. % at 1073 K (800 °C). On the other hand, the concentration of carbon dioxide increases from ~30 vol.% at 373 K to ~58 vol.% at 1073 K, meaning that higher temperatures (873 K – 1073 K) would be more favourable for the reduction stage.

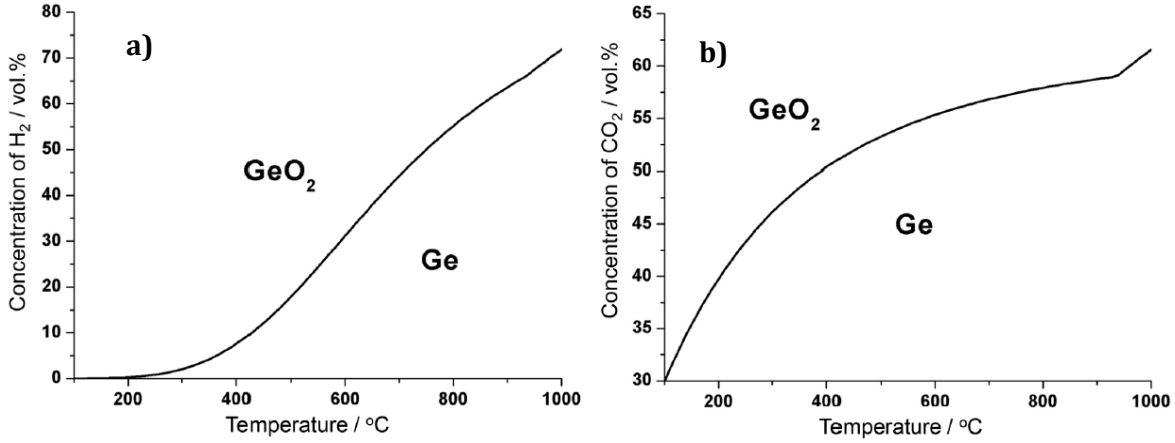

Figure 2.4: Phase stability diagrams for a Ge/GeO_2 system under: a) H_2O-H_2 atmosphere b) CO_2-CO atmosphere. (Słowiński & Smoliński, 2016).

Germanium oxide supported on alumina was investigated by Miyamoto et al (1984) who showed that it was able to provide higher hydrogen yields during water splitting in comparison to unsupported iron oxide which was attributed to interactions between the germanium oxide and the support.

Another non-transition metal OCM, cerium oxide, has been investigated by Otsuka (1983) for hydrogen production. They found that the surface area of the material decreased over 7 redox cycles though there was no reported reduction in the rate of reduction. The water oxidation rate was improved with the addition of palladium, platinum and nickel oxide, although there was only a very small increase in the reduction rate.

2.2 Non-stoichiometric oxygen carrier materials

2.2.1 Perovskite oxides

Suitable non-stoichiometric OCMs exist in the perovskite family of materials of the form ABX_3, where 'A' and 'B' are cations of differing radii and 'X' is an anion (typically oxygen 'O'). Size is the main differentiating factor between A and B sites. In the ideal cubic perovskite structure shown in Fig. 2.5, the A cations exist at the corners of the cube – the dodecahedral sites. The B cation exists in the centre surrounded by oxygen anions to form an octahedron. The A sites may be taken by a rare earth, alkali or alkaline earth metal, and the B cations are taken by a transition metal (Verma & Jindal, 2009). As an

example of doping, an atom M could be partially substituted for A to give the structure $A_{1-x}M_xBO_{3-\delta}$. The parameter δ represents the degree of non-stoichiometry of the material, essentially the number of deficient oxygen atoms per unit formula (Ishihara, 2009).

Perovskite-type non-stoichiometric OCMs benefit from being able to avoid any significant phase changes from occurring during oxidation and reduction reactions. This is due to the ease at which their oxygen storage capacity may be manipulated by forming oxygen vacancies through incorporating various cations of different valance states within their structure (Teraoka et al, 2006). Since the material does not change phase when exchanging oxygen (unlike transition metal oxides like iron oxide) this results in a decrease in the energy barrier stopping oxygen release from the material.

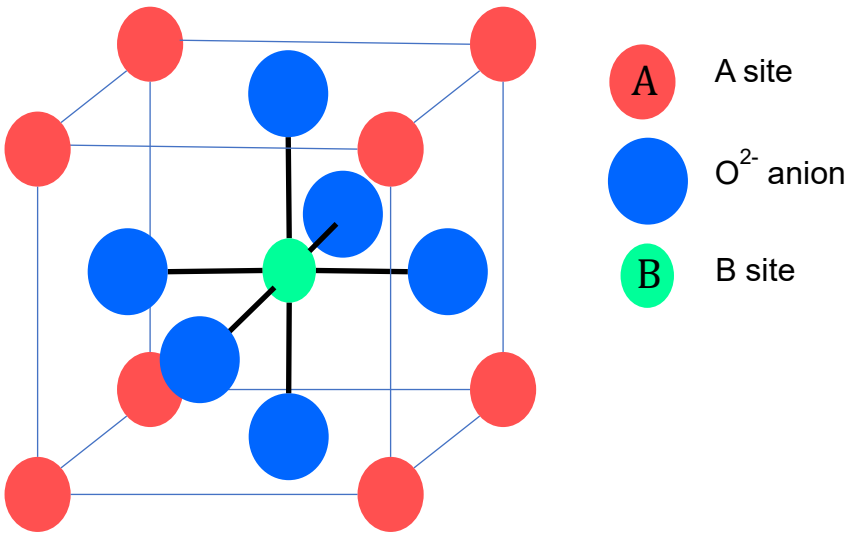

Figure 2.5: The ideal perovskite cubic structure with general stoichiometry ABO_3.

The tolerance factor *t*, introduced by Goldschmidt (1926), is a dimensionless number that can be used as a measure of the stability of a perovskite:

$$t = \frac{r_A + r_O}{\sqrt{2} \bullet (r_B + r_O)} \qquad \text{Eq. 2.12}$$

where r_A, r_O and r_B are the ionic radii of either the A, B or O ion.

For a stable perovskite the value of *t* will be in the range 0.8-1. This allows for an estimation of the extent to which the ionic radius of the perovskite may vary before it is no longer a perovskite.

Stoichiometric point defects may be classified as either Schottky or Frenkel defects (Kittel 1996, Fierro 2005). Frenkel defects occur when the difference between the size of anions and cations is very large, and involves the movement of a smaller ion in the matrix to occupy an interstitial site thereby creating a vacancy at the original position of the ion. The density of the solid is not changed as a result of this process. Schottky defects in the other hand occur when there are equal concentrations of cations and anions with the same charge and having similar sizes in the crystal structure of the material. In this scenario the charge neutrality is maintained, and the solid density increases. Singh et al (2012) indicated that the oxygen transport in perovskite materials is dependent on vacancy diffusion rather than interstitial diffusion.

Numerous studies have been conducted that have looked into the effects of various cations doped onto the A or B-sites of perovskites (Franca et al 2012, Benamira et al 2014, Feng et al 2014, Vasala et al 2014, Kim et al 2014). The choice of the dopant to employ on the perovskite is a key factor when trying to engineer certain properties into the material. They can change the relationship between the non-stoichiometry of the material and the equilibrium pO_2. Different dopants can increase or decrease rate constants as well as alter the materials sintering and attrition resistances. Ultimately the choice of the dopant will depend on the particular application in mind and choosing correctly can lead to a better performing OCM.

2.2.2 Strontium doped lanthanum ferrite perovskite

Strontium doped lanthanum ferrite oxides of the form $La_{1-x}Sr_xFeO_{3-\delta}$ have been identified as potential candidates as OCMs (Duduković 2009, Murugan et al 2011, Thursfield et al 2012, Dueso et al 2015, Nalbandian & Zaspalis 2015, De Vos et al 2020). Studies have shown that $La_{0.7}Sr_{0.3}FeO_{3-\delta}$ (LSF731) can give high material stability and steady hydrogen production under isothermal conditions at 1123 K for over 100 redox cycles (Murugan et al, 2011), although the production of hydrogen is less than for the same amount of iron oxide due to the higher oxygen capacity of iron oxide. 1 g of Fe_2O_3

has an oxygen molar content of 18.79 mmol, whereas 1 g of LSF731 only has an oxygen molar content of 13.19 mmol. Dueso et al (2015) found that composite perovskite-type materials (specifically Fe_2O_3 clusters within an LSF731 matrix) could bring together the desirable components of both materials to allow for both high oxygen capacity and stability of the OCM.

He et al (2013) suggests that there exists an optimal degree of strontium substitution in the range x=0.3-0.5 for the $La_{1-x}Sr_xFeO_{3-\delta}$ type perovskites in terms of reactivity, oxygen-donation ability and resistance to carbon formation, and $La_{0.6}Sr_{0.4}FeO_{3-\delta}$ (LSF641) falls in the middle of this range. An electronic imbalance of the perovskite structure is caused by the substitution of Sr2+ for La3+, and in order to preserve charge neutrality the valence state of Fe increases from 3+ to 4+/5+ (He et al, 2019). This in turns allows for oxygen transportation to occur through the material via diffusion, and the electrical and oxygen conductivity may be explained via point defect chemistry.

A defect model was first derived by Mizusaki et al (1985) which describes how the thermodynamics of LSF641 are effected by the interaction between the solid phase and the oxygen partial pressure of the gas phase. This was done by assuming a defect equilibrium exists where the incorporation of oxygen into the lattice and the annihilation of oxygen vacancies is accompanied by the disproportionation of Fe_{Fe}^{x} into $Fe_{Fe}^{\bullet}$ and Fe_{Fe}' (Kröger-Vink notation). In this notation system • indicates one positive charge, ′ indicates one negative charge, and x indicates null charge. The lattice site which a specie is on is given in the subscript. V represents a vacancy. Using the Kröger-Vink notation, the incorporation of $SrFeO_3$ in the $LaFeO_3$ lattice can be written as:

$$SrFeO_3 \xrightarrow{LaFeO_3} Sr_{La}' + Fe_{Fe}^{\bullet} + 3O_O^x \qquad \text{Eq. 2.13}$$

The overall reaction for point defect equilibrium can be written as:

$$1/2O_2 + 2Fe_{Fe}^{x} + V_O^{\bullet\bullet} \rightleftharpoons 2Fe_{Fe}^{\bullet} + O_O^x \qquad \text{Eq. 2.14}$$

where the equilibrium constant is given as:

$$K_{inc} = \frac{[Fe_{Fe}^{\bullet}]^2[O_O^x]}{[Fe_{Fe}^{x}]^2[V_O^{\bullet\bullet}]pO_2{}^{0.5}} \qquad \text{Eq.2.15}$$

The disproportionation of $[Fe_{Fe}^{x}]$ into $[Fe_{Fe}^{\bullet}]$ and $[Fe_{Fe}']$ is also assumed and is given by the following reaction:

$$2[Fe_{Fe}^{x}] \rightleftharpoons [Fe_{Fe}^{\bullet}] + [Fe_{Fe}'] \qquad \text{Eq. 2.16}$$

for which the equilibrium constant is given as:

$$K_{dis} = \frac{[Fe_{Fe}^{\bullet}][Fe_{Fe}']}{[Fe_{Fe}^{x}]^2} \qquad \text{Eq. 2.17}$$

It is taken that the charges for La and Sr on the A-site are constant as 3+ and 2+ respectively, while the Fe cation on the B-site may be in either 2+, 3+ or 4+ states ($[Fe_{Fe}']$, $[Fe_{Fe}^{x}]$ and $[Fe_{Fe}^{\bullet}]$ respectively). It is assumed that the A and B-sites are always fully occupied:

$$[La_{La}^{x}] + [Sr_{La}'] = 1 \qquad \text{Eq. 2.18}$$

$$[Fe_{Fe}'] + [Fe_{Fe}^{x}] + [Fe_{Fe}^{\bullet}] = 1 \qquad \text{Eq. 2.19}$$

The charge neutrality is maintained as follows:

$$[Fe_{Fe}'] + [Sr_{La}'] = 2[V_O^{\bullet\bullet}] + [Fe_{Fe}^{\bullet}] \qquad \text{Eq. 2.20}$$

The oxygen content is defined as:

$$[O_O^{x}] = 3 - [V_O^{\bullet\bullet}] \qquad \text{Eq. 2.21}$$

where $[V_O^{\bullet\bullet}] = \delta$.

Finally $[Sr_{La}']$ = 0.4 since the doping content of strontium is 0.4 mol for LSF641.

Based on this model, Kuhn et al (2011) correlated the oxygen partial pressure to the non-stoichiometry with Eq. 2.22. K_{dis} and K_{inc} are the equilibrium constants for the oxygen incorporation and iron disproportionation reactions respectively, given previously.

$$\frac{\delta^{\frac{1}{2}}(2\delta - x + 1)}{(3-\delta)^{\frac{1}{2}}(2\delta - x)} pO_2^{\frac{1}{4}} = \frac{K_{dis}}{K_{inc}} \frac{(1 + x - 2\delta)(3-\delta)^{\frac{1}{2}}}{\delta^{\frac{1}{2}}(2\delta - x)} pO_2^{\frac{-1}{4}} - K_{ox}^{-\frac{1}{2}} \qquad \text{Eq. 2.22}$$

Experimental studies by Mizusaki et al (1985), Søgaard et al (2007) and Kuhn et al (2011) have determined the values for the enthalpy and entropy of reaction of Eq. 2.14 and Eq. 2.16 which enables calculation of K_{dis} and K_{inc}. These values are given in table 2.3 as follows:

Table 2.3: Values of thermodynamic properties enthalpy and entropy for the defect model reactions. Data from Mizusaki et al (1985), Søgaard et al (2007) and Kuhn et al (2011) is presented.

	Søgaard et al (2007)	**Kuhn et al (2011)**	**Mizusaki et al (1985)**
ΔH°_{inc} **(kJ mol^{-1})**	-90.0 ± 9.5	-95.62 ± 4.18	98.79 ± 11.17
ΔS°_{inc} **(J mol^{-1} K^{-1})**	-57.7 ± 7.6	-54.27 ± 4.43	-65.39 ± 8.26
ΔH°_{dis} **(kJ mol^{-1})**	114.8 ± 13.4	95.75 ± 2.05	127.50 ± 24.76
ΔS°_{dis} **(J mol^{-1} K^{-1})**	-10.2 ± 10.8	-21.63 ± 2.13	-4.02 ± 16.52

Using the values from Kuhn et al (2011), the oxygen non-stoichiometry of $La_{0.6}Sr_{0.4}FeO_{3-\delta}$ material may be plotted vs. the log pO_2 as shown in Fig. 2.6 using Eq. 2.22. The material displays two plateaus in the relationship. At the plateau at δ=0 the composition is stoichiometry and all of the oxygen sites of the material are occupied. The second plateau is at δ=[Sr]/2=x/2 where the Fe cations have an average valence of 3+, where the electrons are strongly localised on the cation site and the equilibrium constant for Fe3+ disproportionation is very small.

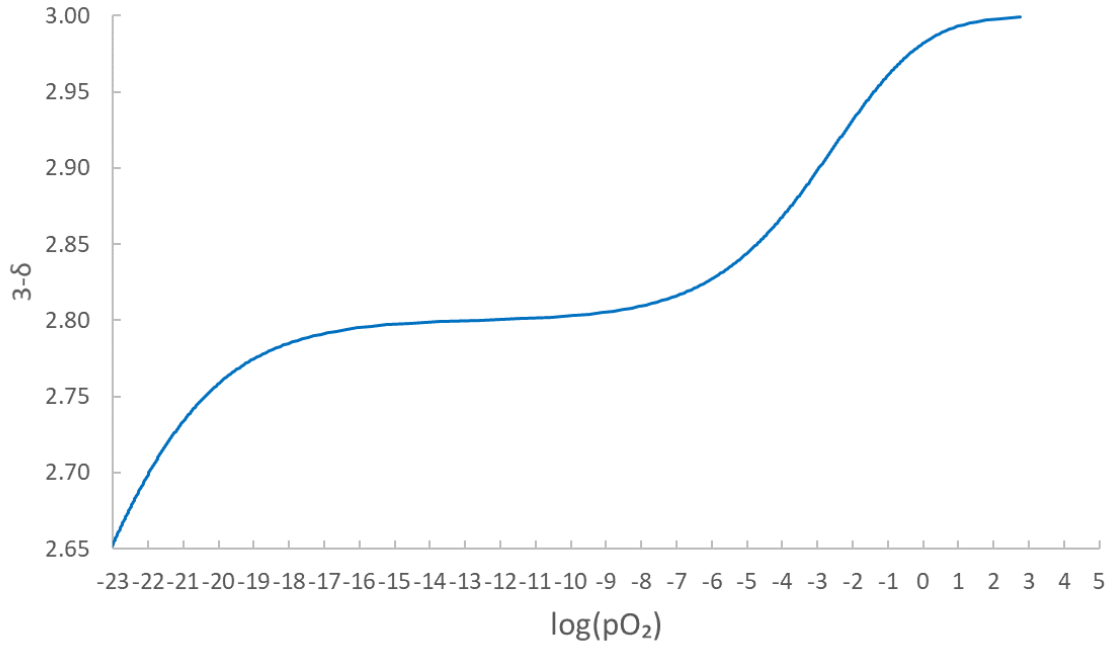

Figure 2.6: Oxygen non-stoichiometry versus oxygen partial pressure for LSF641 at 1093 K, derived using the defect model in Eq. 2.22 first described by Kuhn et al (2011). A plateau may be seen at δ = 0.2 between pO_2s of ~10^{-16} bar and ~10^{-9} bar which hinders oxygen exchange in the active WGS pO_2 range.

From Fig. 2.6 it can be clearly seen that the oxygen content of the material can vary continuously per step change in the oxygen partial pressure that it is in equilibrium with, unlike with transition metal oxides discussed in section 2.1 which are better represented as undergoing a phase change with step changes in oxygen content (see section 2.3 for more detailed discussion on this concept). The existence of a plateau at δ=0.2 limits the extent to which oxygen exchange can occur between the solid and the gas phase which can also limit the possible conversion and product quality possible in CLWGS. By minimising the effect of phase change, variations in the electrical and chemical activity may be prevented which can lead to longer usable lifetime for the OCM. de Leeuwe (2019) found that LSF641 could be used in CLWGS for > 1000 cycles switching between carbon monoxide and water vapour feeds for a steady production of hydrogen with no apparent degradation of the material, suggesting it has a much greater usable lifetime than iron oxide.

One of the main aims of this thesis is to investigate what kind of shapes to the oxygen non-stoichiometry vs. oxygen partial pressure plot in Fig. 2.6 could result in better performance during CLWGS, and to investigate a way in which the limiting plateau could

be removed by taking advantage of the easily manipulable structure of the perovskite through doping different cations onto the structure of the perovskite OCM.

2.2.3 Strontium doped lanthanum manganate perovskite

The $La_{1-x}Sr_xMnO_{3-\delta}$ family of perovskites with manganese doping on the B-site are another alternative perovskite OCM of interest. A study by Jiang et al (2005) investigated $(La_{0.8}Sr_{0.2})_xMnO_3$ electrodes of solid oxide fuel cells (SOFC) under polarisation and open circuit conditions at 1273 K for 1600 hours and reported good stability and long term performance. Since a SOFC works in a very similar fashion to CLWGS albeit at higher pO_2 values (an intermediate material is reduced by passing through hydrogen to produce water, and in the next stage the material is re-oxidised by passing through air), there is a case for arguing that the strontium doped lanthanum manganates could still be expected to benefit from a similar structural stability and kinetics as with $La_{1-x}Sr_xFeO_{3-\delta}$ type perovskites.

In particular, the oxygen non-stoichiometry vs pO_2 plot for these materials shown in Fig. 2.7 lacks the plateau that was seen for $La_{0.6}Sr_{0.4}FeO_{3-\delta}$ in Fig. 2.6 at $\delta=[Sr]/2=x/2$, which suggests a potentially larger oxygen capacity in the pO_2 range for CLWGS may be possible than with strontium doped lanthanum ferrite materials (Mizusaki et al 2000). It has also been shown that these materials may experience a positive deviation from the ideal defect structure at highly oxidising oxygen chemical potentials, which Mizusaki was able to explain by introducing an empirical factor α that represents the interactions among lattice ions and defects such that:

$$\Delta H^{xs} = \alpha\delta \qquad \text{Eq. 2.23}$$

where ΔH^{xs} refers to the excess enthalpy of oxidation reaction that involves oxygen vacancies $V_O^{\bullet\bullet}$ and holes $h^{\bullet}$:

$$1/2O_2 + V_O^{\bullet\bullet} \rightleftharpoons 2h^{\bullet} + O_O^x \qquad \text{Eq. 2.24}$$

The exact origins of this α factor are unclear, although recent work has suggested that it corresponds to a first-order approximation of the hole-degeneracy effect (Yoo, 2019).

Fig. 2.7 also indicates that $La_{1-x}Sr_xMnO_{3-\delta}$ materials may not be as resistant to harsher reducing conditions as $La_{1-x}Sr_xFeO_{3-\delta}$ type materials as they tends to decompose at a higher pO_2s. Interestingly Gokon et al (2019) found that the oxygen storage capacity of the related material $La_{0.5}Sr_{0.5}FeO_{3-\delta}$ was 6 times greater than that of $La_{0.5}Sr_{0.5}MnO_{3-\delta}$, however this observation was not for the specific log pO_2 range applicable to CLWGS but from the reduction of a fresh sample.

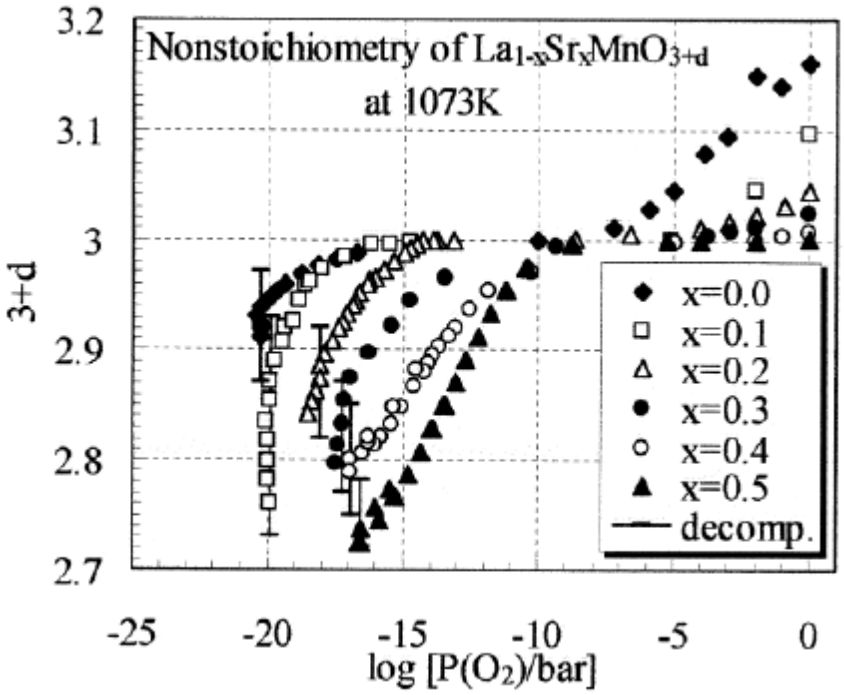

Figure 2.7: $La_{1-x}Sr_xMnO_{3-\delta}$ δ-pO_2 plot at 1073 K for different La and Sr doping ratios (Mizusaki et al, 2000). The black lines indicate the pO_2s at which decomposition occurs.

2.2.4 Strontium doped lanthanum cobaltite perovskite

Strontium doped lanthanum cobaltite perovskites are a promising other avenue for perovskite materials, especially due to the increased transport properties this can offer. However Martin (2003) suggests that these materials suffer from a decrease in OCM lifetime due to an increase in phase segregation at low pO_2s.

An investigation of the non-stoichiometry vs. pO_2 behaviour of $La_{0.6}Sr_{0.4}CoO_{3-\delta}$ was carried out by Kuhn et al (2013) which shows that the material would decompose at a much higher pO_2 than seen with either the $La_{1-x}Sr_xFeO_{3-\delta}$ or the $La_{1-x}Sr_xMnO_{3-\delta}$ type materials. This plot is shown in Fig. 2.8. This is much higher than the pO_2 range in which

the CLWGS process typically operates, meaning that the material should give poor conversions if used in the process.

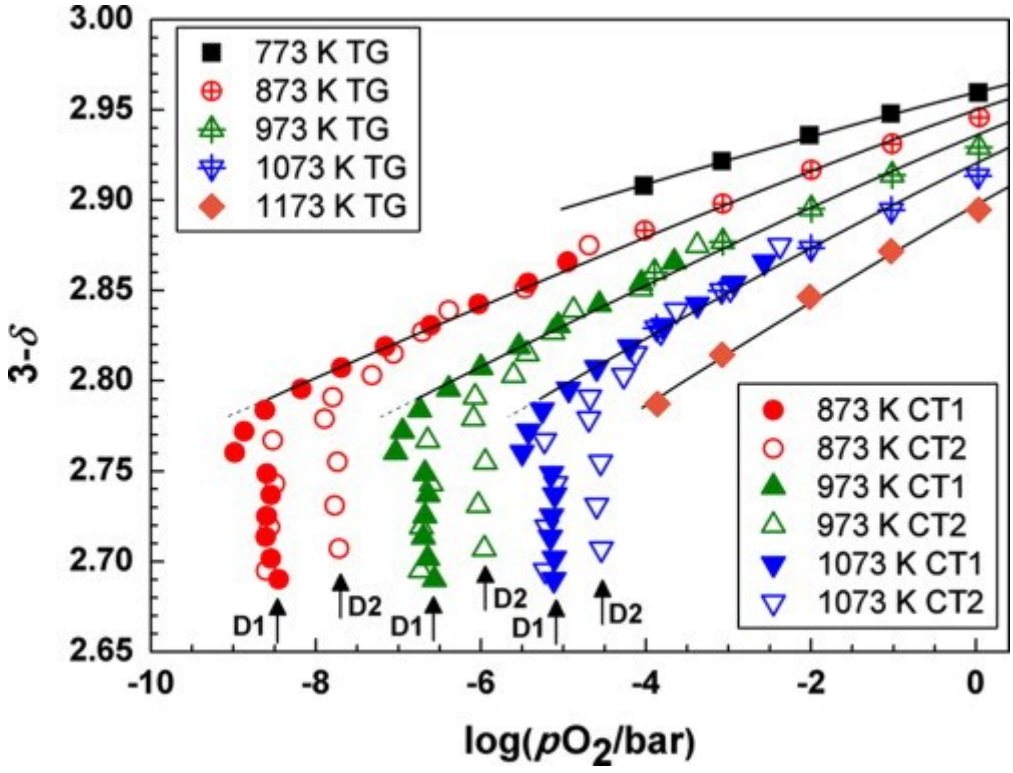

Figure 2.8: $La_{0.6}Sr_{0.4}CoO_{3-\delta}$ δ-pO_2 plot for temperatures 873 K - 1073 K from Kuhn et al (2013). The material starts to decompose at a much higher pO_2 than acceptable for the CLWGS process. In the figure "TG" refers to experimental data obtained through TGA analysis, and "CT1" or "CT2" refer to coulometric titration measurements taken via simple reduction or via a ''two-step-forward one-step-back'' reduction/oxidation procedure respectively. Decomposition pO_2 is indicated by D1 and D2. The solid lines indicate fits to the TGA data from CT1, and the dashed lines are used to indicate represent a non-equilibrium region at which the sample exhibits a super-reduced state.

2.2.5 Strontium doped lanthanum chromite perovskite

Strontium doped lanthanum chromite perovskites ($La_{1-x}Sr_xCrO_{3-\delta}$) have application as electrode materials for magnetohydrodynamic power generation (Meadowcroft, 2002) and high temperature SOFC separators (Mori et al, 2001). This class of material has good thermal shock resistance and chemical stability at high temperatures (Gupta & Mahapatra, 2015). However an investigation by Mizusaki et al (1984) into the oxygen non-stoichiometry for these materials (Fig. 2.9) indicates that higher temperatures in comparison to i.e. $La_{1-x}Sr_xFeO_{3-\delta}$ type materials may be required in order to fully utilise

the oxygen capacity of the material, which is not preferable if higher energy costs can be avoided.

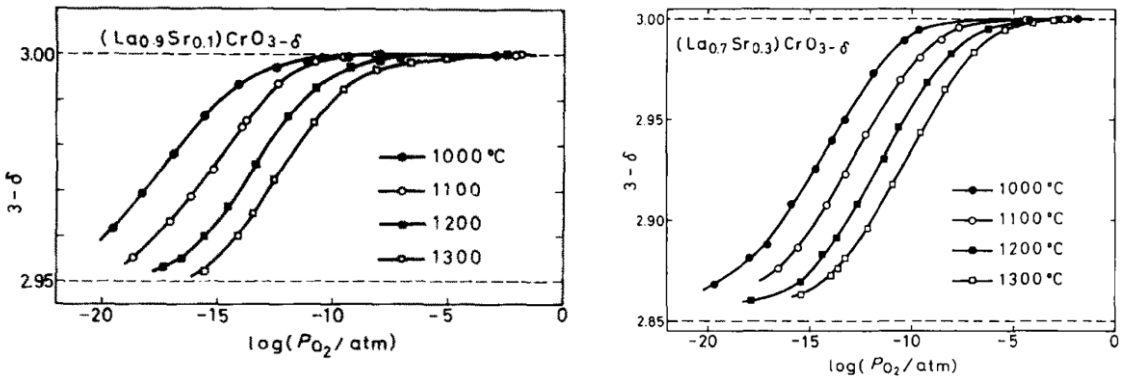

Figure 2.9: $La_{0.9}Sr_{0.1}CrO_{3-\delta}$ and $La_{0.7}Sr_{0.3}CrO_{3-\delta}$ δ-pO_2 plot for temperatures 1273 - 1573 K. Higher temperatures may be required in order to fully utilise the oxygen capacity of the material which is not preferable if higher energy costs can be avoided (Mizusaki et al, 1984).

2.2.6 Using multiple metal cations doped on the B-site of the perovskite

Another advantage of the perovskite structure is its ability to be able to dope multiple cations onto the A or B sites of the material and allowing for desirable properties which each cation might exhibit individually to be combined in a single material.

One class of materials of interest is $La_{1-x}Sr_xFe_{1-y}Mn_yO_{3-\delta}$ which can combine the higher oxygen capacity possible with Mn and the stability of Fe. Markov et al (2015) investigated the material $La_{0.5}Sr_{0.5}Fe_{0.67}Mn_{0.33}O_{3-\delta}$, a strontium doped lanthanum ferrite manganite with B site iron and manganese doping of 67% and 33%, and found that the oxygen content and ion conductivity of the material at particular pO_2s increased with increasing manganese doping. It is therefore suggested that a $La_{0.6}Sr_{0.4}Fe_{0.67}Mn_{0.33}O_{3-\delta}$ material, could benefit from the stability of the $La_{0.6}Sr_{0.4}FeO_{3-\delta}$ material and also have a larger oxygen capacity provided by the Mn cations. An investigation by Luciani et al (2018) on $La_{0.6}Sr_{0.4}Fe_{1-y}Mn_yO_{3-\delta}$ type materials found that increasing the Mn content on the B-site increased the reactivity towards steam, allowing hydrogen production at lower temperatures (Fig. 2.10). Increasing the Fe content on the other hand also gave higher volumes of hydrogen production according to this study but restricted to higher temperatures. The results in Fig. 2.10 are from two runs where the samples are pre-reduced with hydrogen and oxidised with steam at 1273 K holding for two minutes.

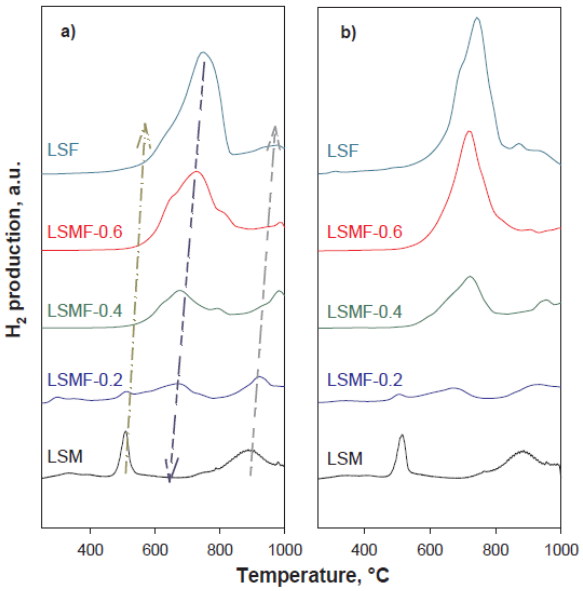

Figure 2.10: Hydrogen production profiles from two water splitting tests from Luciani et al 2018 (a being the first and b being the second). LSF, LSMF-0.6, LSMF-0.4, LSMF-0.2 and LSM refer to $La_{0.6}Sr_{0.4}FeO_{3-\delta}$, $La_{0.6}Sr_{0.4}Fe_{0.6}Mn_{0.4}O_{3-\delta}$, $La_{0.6}Sr_{0.4}Fe_{0.4}Mn_{0.6}O_{3-\delta}$, $La_{0.6}Sr_{0.4}Fe_{0.2}Mn_{0.8}O_{3-\delta}$ and $La_{0.6}Sr_{0.4}MnO_{3-\delta}$ respectively. Two peaks at 500 °C and 900 °C can be see for LSM. On the other hand, the oxidation of LSF occurs in the temperature range 600 °C to 800 °C with the maximum at 750 °C. A higher Fe content results in an increase in H_2 production while increasing the Mn content allows for the use of lower oxidation temperatures.

Doping cobalt onto the B-site has been considered as a compromise between stability and higher oxygen conductivity under operating conditions. Kuhn et al (2012) studied the oxygen non-stoichiometry of $La_{1-x}Sr_xFe_{1-y}Co_yO_{3-\delta}$ materials with Co and Fe doping on the B-site. It was found that the presence of Fe on the B-site in addition to Co only very slightly allowed the material to reach lower pO_2s before showing signs of decomposition, with the materials with y= 0.6 and 0.8 performing the best at 1073 K showing signs of decomposition at $\sim 10^{-15}$. Five TPR and TPO cycles using CO and H_2O feeds at 1123 K were carried out by Murugan (2011) using $La_{0.6}Sr_{0.4}Fe_{0.8}Co_{0.2}O_{3-\delta}$ who found that the material gave lower hydrogen production than LSF731 and observed the formation of a secondary phase of La_2CoO_4 after the experiment which indicates material instability. In the same work, a B-site Ni containing perovskite with the formula $La_{0.7}Sr_{0.3}Fe_{0.9}Ni_{0.1}O_{3-\delta}$ was also synthesised, though this material did not show any improvement over LSF731 in terms of material stability, hydrogen production and product quality.

2.2.7 Ceria-zirconia oxides

As a non-perovskite alternative, ceria-zirconia oxides also demonstrate non-stoichiometry. Kuhn et al (2013) studied the oxygen non-stoichiometry of ceria-zirconia ($Ce_{1-x}Zr_xO_{2-\delta}$) oxides and found that with higher zirconia content the ease with which the material could be reduced greatly increased, reflected by a > 40% decrease in reduction enthalpy. The material changes from a cubic phase at values of $x \leq 0.2$ to a tetragonal phase at $x > 0.2$ when calcination is carried out at higher temperatures. The pO_2 range of the material in reduced and oxidised states also seems to be promising for use in the CLWGS process as seen in Fig. 2.11 where it extends to low values of log pO_2 that are applicable.

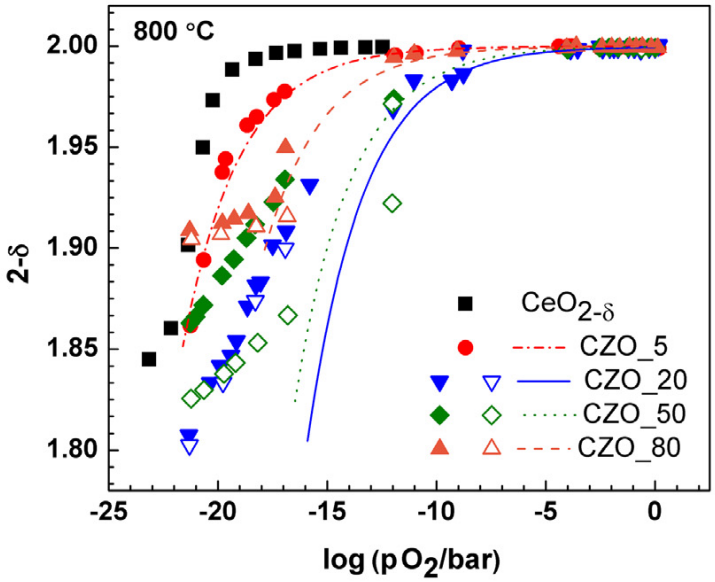

Figure 2.11: Oxygen non-stoichiometry vs. pO_2 for $Ce_{1-x}Zr_xO_{2-\delta}$ at 1073 K from Kuhn et al (2013). CZO_5, CZO_20, CZO_50 and CZO_80 and refer to $Ce_{0.95}Zr_{0.05}O_{2-\delta}$, $Ce_{0.8}Zr_{0.2}O_{2-\delta}$, $Ce_{0.5}Zr_{0.5}O_{2-\delta}$ and $Ce_{0.2}Zr_{0.8}O_{2-\delta}$ respectively. The lines correspond to a model-based fit described in the paper. The open symbols for CZO_20, CZO_50 and CZO_80 indicate a second reduction measurement following reoxidation of the original sample. The authors suggest that CZO_20 is insensitive to redox cycling at the investigated temperatures owing to the repeatability of measurements (shown in the figure).

2.3 Thermodynamic advantage of non-stoichiometric materials for CLWGS

In sections 2.1 and 2.2 the OCMs were classified based on their thermodynamic behaviour in the pO_2 range for the WGS reaction as either exhibiting discrete phase changes where oxygen is exchanged at fixed chemical potentials, or as being non-

stoichiometric where oxygen is exchanged at an essentially infinite number of chemical potentials.

The selection of a good OCM for the CLWGS process is also dependant on the thermodynamics of the material: specifically, the relationship between the pO_2 of the gas phase and the oxygen non-stoichiometry δ of the solid phase. Since the conversion at any given point in time while the reaction is happening is defined by the pO_2 at which the phase change is at, it is important for the material to be able to access a high oxygen capacity at the right pO_2 values to achieve a good water to hydrogen conversion.

2.3.1 Conventional reactor system with mixed feeds

Metcalfe et al (2019) demonstrated that a packed bed CLWGS reactor utilising an appropriate non-stoichiometric OCM can be designed which is unconstrained by the limitations of the overall chemical equilibrium and can produce essentially pure separate H_2 and CO_2 product streams.

For a conventional reactor system operating using mixed feeds of H_2O and CO, the equilibrium constant for the water-gas shift reaction is given as follows:

$$K_{WGS} = \frac{\left(\frac{p_{CO_2}}{p_{CO}}\right)}{\left(\frac{p_{H_2O}}{p_{H_2}}\right)} \qquad \text{Eq. 2.25}$$

In this equation K_{WGS} represents the equilibrium constant for WGS and the outlet gas partial pressures for CO_2, CO, H_2O and H_2 are represented with p. This equation is applicable when the WGS reaction has proceeded to completion and equilibrium has been achieved between the forward and reverse reactions.

The equilibrium constant for WGS at 1093 K tends to unity (Callaghan 2006, Wenzel et al 2016). Therefore for a feed of 1:1 H_2O and CO, a maximum possible conversion of only 50% would be possible, with the ratio of components in the outlet stream being 1:1:1:1 H_2O, H_2, CO_2 and CO. For a conventional mixed feed reactor, any improvement on this conversion would require altering the flowrates of reactants, temperature changes, or the use of expensive additional separation stages. Since the WGS reaction is equimolar, the conversion could not be improved by changing the pressure either.

2.3.2 OCMs with single phase change

For the case of unmixed feeds being fed to a chemical looping reactor in counter-current operation, the full potential of the use of non-stoichiometric OCMs can be unlocked. Cases can now be considered in order to explore the consequences of the relationship between pO_2 and δ when designing OCMs depending on the number of phase changes that the OCM would be expected to undergo during cycling.

The case given in Fig. 2.12 represents the most basic relationship scenario, with an OCM that has only a single phase change.

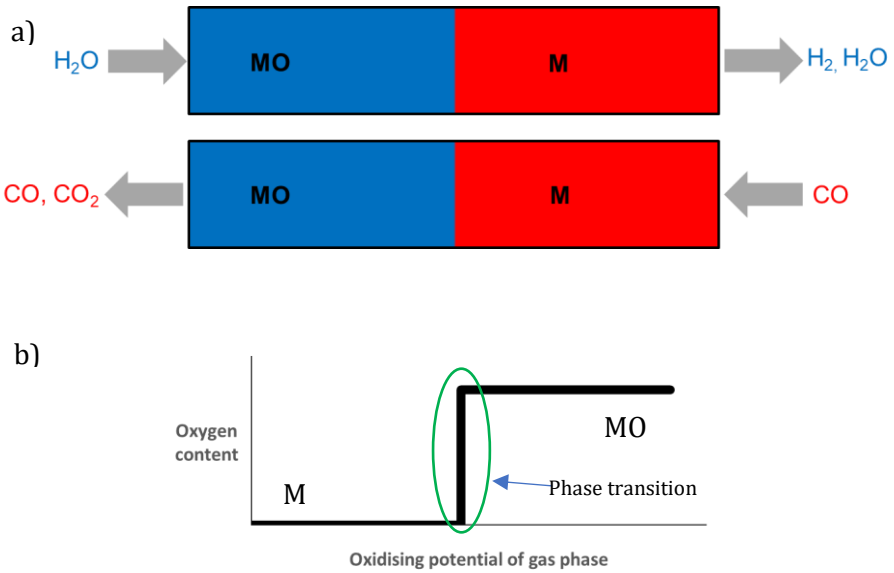

Figure 2.12: a) The reactants and products for a CLWGS system making use of an OCM with only a single phase change. Equivalent to a metal/metal-oxide (M/MO) type system. b) Plot of the oxygen content vs gas phase oxidising potential for a single phase change material.

In this case the material can exist in only one of two phases, which is common with metal/metal-oxide (M/MO) systems as described by the reactions below:

$$H_2O + M \leftrightarrow MO + H_2 \qquad \text{Oxidation half cycle (Eq. 2.26)}$$

$$MO + CO \leftrightarrow M + CO_2 \qquad \text{Reduction half cycle (Eq. 2.27)}$$

In their work Metcalfe et al (2019) explain how for a M/MO type system the composition of the gas at the phase transition will determine the composition of the gas that leaves the reactor and hence the conversion of H_2O to H_2 - essentially the ratio of H_2O:H_2 is in

equilibrium with the phase transition. This ratio remains constant for any given temperature due to the fact that thermodynamic activities associated with pure stoichiometric solids are unity. If both of the outlet gases (H_2O/H_2 and CO_2/CO) are in equilibrium with the phase transition, then they will also be in equilibrium with each other.

At 1093 K the value of the equilibrium constant for WGS is unity (Callaghan 2006, Wenzel et al 2016), so $K_{ox}K_{red} = 1$, where K_{ox} and K_{red} are equilibrium constants for oxidation and reduction half cycles. This is shown in Fig. 2.13.

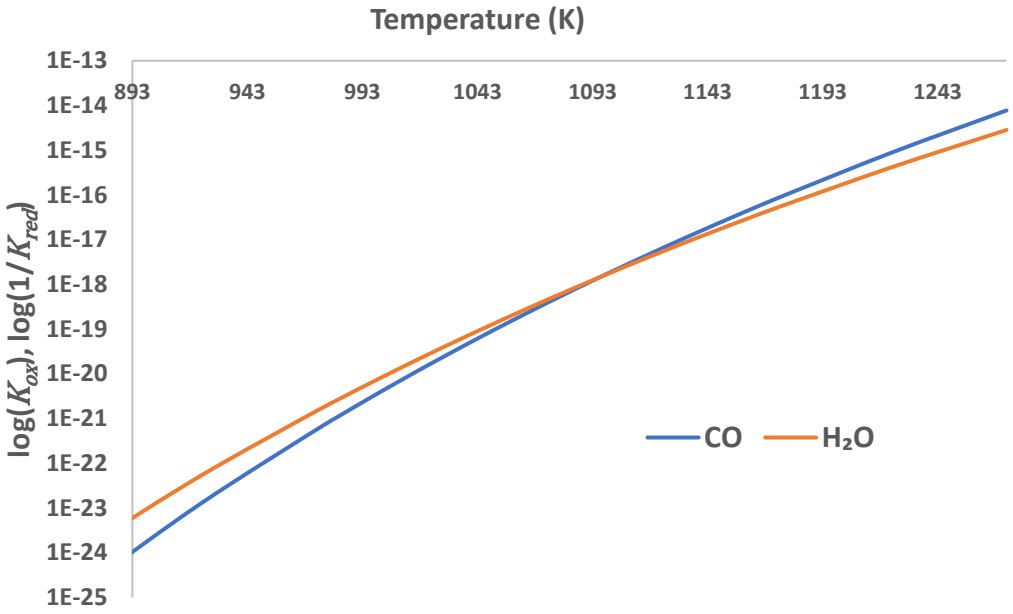

Figure 2.13: Equilibrium constants for water splitting reaction and carbon monoxide oxidation reactions. The product of the equilibrium constants for both half reactions is equal to unity at roughly 1093 K.

If we assume that we are at 1093 K and product gases have negligible quantities of product components, we can see that if we were to achieve a high conversion of H_2O to H_2 we would be penalised with having to make do with a low conversion of CO to CO_2. The only way to achieve equal conversions would be to properly satisfy the oxygen balance by increasing the amount of CO by an appropriate multiple which in practise would increase the costs of operating the CLWGS reactor. Also most of the gas would be passing through unreacted. A system with a single phase change OCM will therefore be highly dependant on the oxidising potential of the gas phase.

2.3.3 OCMs with multiple phase changes

Another possible case is when the OCM exhibits multiple phase transitions. For this sort of system the outlet composition of the gas stream will have the potential to be in equilibrium with the pO_2 of more than one phase transition at which oxygen exchange between the solid phase and the gas phase can occur. For example this is the case with $M/MO/MO_2$ oxide systems such as that shown in Fig. 2.14.

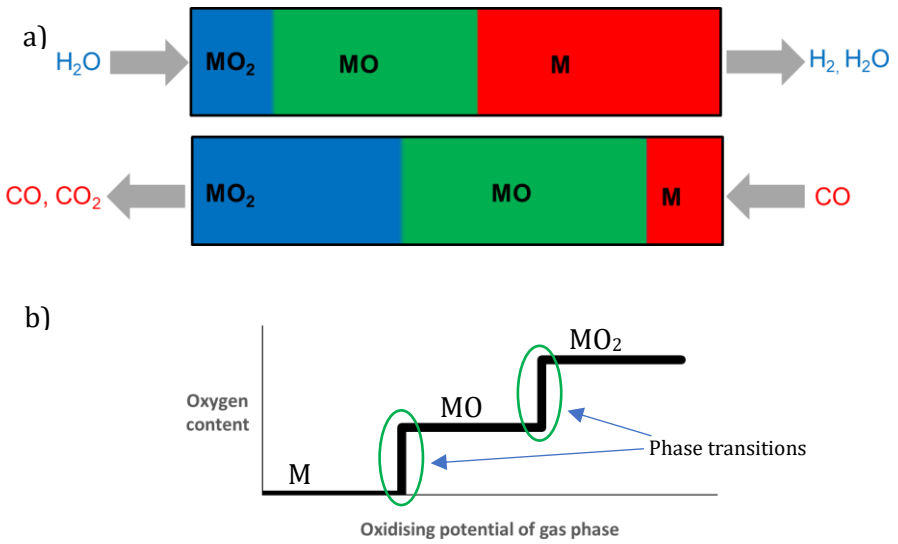

Figure 2.14: a) The reactants and products for a CLWGS system making use of an OCM with two phase changes. Equivalent to a $M/MO/MO_2$ type system. b) Plot of the oxygen content vs. gas phase oxidising potential for material with two phase changes.

In the example, the OCM remains in the most oxidised MO_2 phase near to the H_2O inlet, while at the CO inlet the OCM remains in the metallic phase. When flowing the gas streams through the bed, the H_2O oxidising agent enters the reactor from the left-hand side and is reduced by passing through the MO and M zones and exits the reactor in equilibrium with the most reducing M zone. Likewise the CO reducing agent enters the reactor from the right hand-side and is oxidised by passing through the MO and MO_2 zones exiting the reactor in equilibrium with the most oxidising MO_2 zone.

Metcalfe et al (2019) explained that since the gases are flown counter-currently through the bed such that the H_2 stream exits at the inlet of the CO stream and vice versa, the ratio of partial pressures of H_2O:H_2 at the outlet would be equal to the ratio of partial pressures of CO_2:CO at the inlet. The reverse will also be true, where the ratio of partial

pressures of H_2O:H_2 at the inlet would be equal to the ratio of partial pressures of CO_2:CO at the outlet.

This means that for a phase transition for some ratio of H_2O:H_2, the conversion of H_2O to H_2 would be equal to the conversion of CO to CO_2, and for the same feed duration equal amounts of oxygen would be exchanged with the OCM for both half cycles.

A practical example of such an OCM is with iron oxide which exhibits the phase transitions Fe/FeO/Fe_3O_4. In this case the conversion of H_2O to H_2 can be maximised by utilising the reducing phase transition at the Fe/FeO transition, and the conversion of CO_2 to CO can be maximised by utilising the phase transition at the FeO/Fe_3O_4 transition.

It becomes clear that for the highest conversions to be achieved the oxidising potential of the oxidising agent or the reducing agent should not pass that of the corresponding phase transition. This is especially important since in industrial processes it would be expected that the gas streams would not be pure H_2O or CO streams, but contain quantities of H_2 or CO_2 as well. A change in the purity of the inlet stream past the phase transitions at the reactor inlets would decrease the possible conversions and/or result in the system potentially reverting to one with only a single phase transition. The system would also be susceptible to thermal effects since pO_2 is a function of temperature.

2.3.4 OCMs exhibiting non-stoichiometry of oxygen content

The case given in Fig. 2.15 represents the opposite to the single phase transition case. The constant gradient means the OCM essentially can be thought of as having an infinite number of such phase changes with small variations in the oxidation state; the material is 'non-stoichiometric'. As long as the pO_2 of the inlet gas stream remains in the range where oxygen transfer occurs between the solid phase and the gas phase, then it will always be in equilibrium with the current oxygen chemical potential. This sort of system would also have flexibility to variations in the pO_2 of the phase changes from temperature changes and inlet feed compositions.

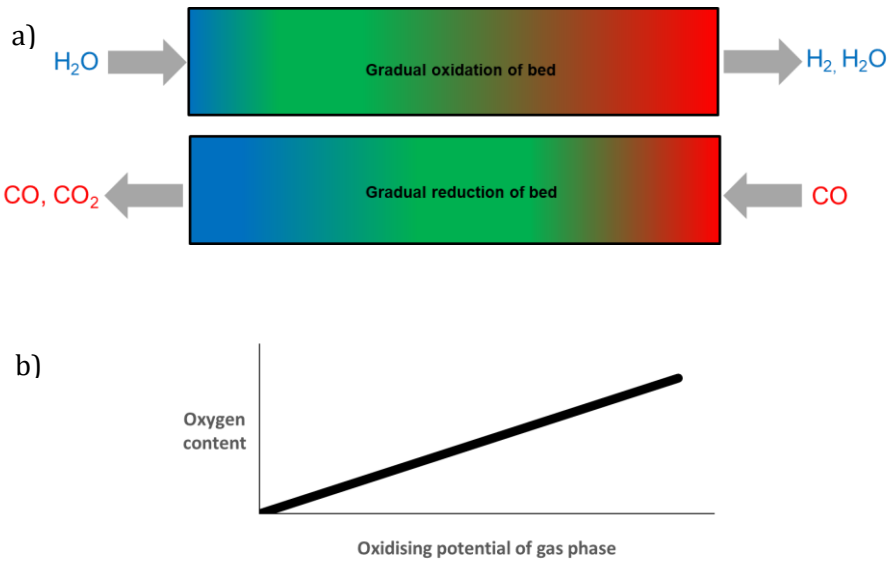

Figure 2.15: a) The reactants and products for a CLWGS system making use of an OCM with effectively infinite phase changes. Equivalent to a non-stoichiometric material system. b) Plot of the oxygen content vs gas phase oxidising potential for material that can accommodate a continuously variable amount of oxygen as a function of the gas phase oxidising potential.

A suitable non-stoichiometric system (such as those with perovskite-oxides) would utilise an OCM that does not undergo phase changes and so can donate or receive oxygen at any oxygen chemical potential. The outlet composition will be in equilibrium with any oxidising potential since the OCM could accommodate a continuously variable amount of oxygen: the oxygen content of the OCM is always changing. This means that as long as there is a spatial gradient in the reactor, it is possible to achieve both a good H_2O conversion and a good CO conversion. A packed bed in counter-current operation is required in order to maintain this gradient. In this mode, the oxidising water vapour stream leaves the reactor from the most reduced end, and the reducing carbon monoxide stream leaves the reactor from the most oxidised end, which allows for the conversions possible to be maximised (Metcalfe et al, 2019).

2.4 Summary

This chapter provided a review of the various OCMs studied in the literature, and based on the thermodynamic advantages outlined in section 2.3 this work will focus on the use

of materials from the non-stoichiometric family of materials for use as OCMs in CLWGS. In addition, the thermodynamic advantages of using non-stoichiometric materials can only be realised by using a packed bed reactor since the oxidation profile would be lost if a fluidised bed or circulating reactor configuration were to be used.

Iron containing perovskites of the form $ABO_{3-\delta}$ have been suggested as promising alternative materials (Murugan et al, 2011). These materials can avoid any significant phase changes from occurring during oxidation and reduction reactions due to the ease with which their oxygen storage capacity may be manipulated: by forming oxygen vacancies through incorporating various cations of different valance states within their structure. Previous work has demonstrated how a fixed-bed chemical looping reactor, with the non-stoichiometric perovskite $La_{0.6}Sr_{0.4}FeO_{3-\delta}$ as the OCM, was able to overcome the chemical equilibrium constraints associated with the water-gas shift reaction (Metcalfe et al, 2019). A discussion on the case for a hypothetical benchmark which arises from the thermodynamics of the WGS reaction is given and proposed in the next chapter, and a reactor model is used as a tool to verify its theoretical basis.

Chapter 3: The optimal non-stoichiometric oxygen-carrier material thermodynamics for the chemical looping water-gas shift process

The performance of a thermodynamically limited non-stoichiometric OCM for the CLWGS process can be predicted by focusing on the effect on conversion of the relationship between the chemical potential of the OCM and the oxygen partial pressure of the gas phase which it is in equilibrium with. In this chapter the optimal scenario for the thermodynamics for the non-stoichiometric OCM is proposed, and the δ-pO_2 data for some of the non-stoichiometric OCMs covered in chapter 2 are compared against the optimal scenario. Further experiments in chapter 4 cover the preliminary screening of several non-stoichiometric OCMs to verify these predictions.

An equilibrium reactor model is used to verify the validity of the proposed optimal thermodynamic behaviour. The effect on conversions and outlet gas concentrations is investigated using the model by varying the gradient and midpoint of the δ-pO_2 plot relative to the proposed optimal scenario.

3.1 Optimal thermodynamic behaviour of an OCM for CLWGS

The manner in which the oxygen stoichiometry of the non-stoichiometric OCM changes under different oxygen partial pressure atmospheres (pO_2s) will affect the amount of oxygen available to be taken up from or released to passing gas streams. An ideal material would exhibit a large change in oxygen content in the active range of the pO_2 regime relevant to the water-gas shift (WGS) reaction equilibria where most of the change in conversion occurs. This pO_2 range may be determined from the behaviour of the gas phase equilibrium relationships during oxidation and reduction stages ($H_2O \rightleftharpoons H_2 + ½\ O_2$ and $CO + ½\ O_2 \rightleftharpoons CO_2$) which are given in Eq. 3.1 and Eq. 3.2, and the following analysis in this section will explain how the pO_2 range may be quantified.

$$y_{H_2O} = \frac{y_{H_2} {p_{O_2}}^{½}}{K_{ox}} \qquad \text{Eq. 3.1}$$

$$y_{CO} = \frac{y_{CO_2}}{K_{red} {p_{O_2}}^{½}} \qquad \text{Eq. 3.2}$$

In Eq. 3.1 and Eq. 3.2 K_{ox} and K_{red} are the equilibrium constants for the oxidation and reduction stage reactions. It should be noted that the chemical potentials of the oxidation and reduction stage gas streams are being defined using redox couples of H_2O/H_2 and CO/CO_2. The oxygen partial pressure of the gas streams may be found by calculating the oxygen partial pressure that is in equilibrium with the H_2O/H_2 couple during the oxidation half cycle, and the CO/CO_2 couple during the reduction half cycle.

The overall conversion of H_2O for a CLWGS reactor system is given by the outlet stream during the oxidation half cycle and is given by the following equation:

$$X_{H_2O} = \frac{(y_{H_2})_{outlet}}{(y_{H_2})_{outlet} + (y_{H_2O})_{outlet}} \qquad \text{Eq. 3.3}$$

Likewise the overall conversion for CO is given by:

$$X_{CO} = \frac{(y_{CO_2})_{outlet}}{(y_{CO_2})_{outlet} + (y_{CO})_{outlet}} \qquad \text{Eq. 3.4}$$

Assuming that no carbon deposition occurs in the reactor, and that there are no leaks, and there is no axial dispersion, the total hydrogen and carbon in the gas phase ($y_{H_{constant}}$ and $y_{C_{constant}}$) will be conserved according to the following equations:

$$y_{H_2} + y_{H_2O} = y_{H_{constant}} \qquad \text{Eq. 3.5}$$

$$y_{CO} + y_{CO_2} = y_{C_{constant}} \qquad \text{Eq. 3.6}$$

For a CLWGS system, the maximum conversions are achieved by flowing the reducing agent and the oxidising agent through the oxidising end and reducing end respectively. At equilibrium, and symmetric operation (equal flowrates and half cycle durations) the following equations apply:

$$\frac{(y_{CO_2})_{outlet}}{(y_{CO})_{outlet}} = \frac{(y_{H_2O})_{outlet}}{(y_{H_2})_{outlet}} = \frac{X_{CO}}{1 - X_{CO}} = \frac{1 - X_{H_2O}}{X_{H_2O}} \qquad \text{Eq. 3.7}$$

These equations can be substituted into Eq. 3.1 and Eq. 3.2 to generate Eq. 8 and Eq.9.

$$p_{O_2} = {K_{ox}}^2 \left(\frac{1-X_{H_2O}}{X_{H_2O}}\right)^2 \quad \text{Eq. 3.8}$$

$$p_{O_2} = \left(\frac{1}{K_{red}}\right)^2 \left(\frac{X_{CO}}{1-X_{CO}}\right)^2 \quad \text{Eq. 3.9}$$

Using Eq. 3.8 and Eq. 3.9, a plot of the change in the conversions of H_2O to H_2 and CO to CO_2 with log pO_2 is given in Fig. 3.1 for temperatures of 893 K, 1093 K and 1293 K. It can be seen that at low pO_2s the conversion of H_2O to H_2 is the most favourable, while at higher pO_2s the conversion of CO to CO_2 is more favourable. This analysis assumes that owing to the reaction stoichiometry of the WGS reaction, the moles of CO_2 produced is equal to the moles of CO consumed, while the moles of H_2 produced is equal to the mols of H_2O consumed. In addition the kinetics of the gas-solid reactions are assumed to be very fast, and that they are instead controlled by the thermodynamic parameters.

In Fig. 3.1, the intercept (log pO_2) at which X_{H_2O} is equal to X_{CO} affects the proportion of the usable oxygen capacity of a non-stoichiometric OCM. This is because the range of pO_2s where oxygen transfer can occur between the solid phase and the gas phase is defined by the δ-pO_2 relationship of the non-stoichiometric OCM. If a non-stoichiometric OCM has a δ-pO_2 relationship that exhibits most of its change in δ at a pO_2 range in Fig. 3.1 corresponding to a high value of X_{H_2O} (and corresponding low value of X_{CO}) or vice versa, then the actual conversion to both H_2 and CO_2 will be low. This is because the oxidation profile across the bed is preserved from the end of one half cycle to the start of the next, such that during steady state each oxidation/reduction half cycle will have equal amounts of oxygen being exchanged between the solid phase and the gas phase.

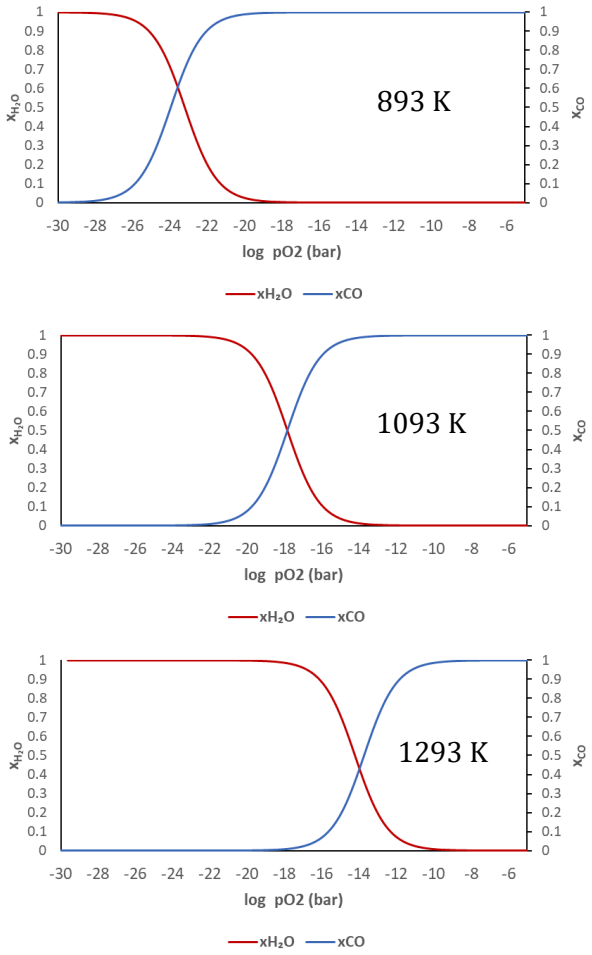

Figure 3.1: Plots of the conversions of water vapour to hydrogen and carbon monoxide to carbon dioxide as a function of the common logarithm of pO_2. The effect of changing temperatures at 893 K, 1093 K and 1293 K on the conversions is shown.

It is postulated that an optimal δ-pO_2 curve for a non-stoichiometric OCM for CLWGS would have a gradient that matches as closely as possible the gradient of the equilibrium plot in Fig. 3.1 around the $X_{H_2O} = X_{CO}$ intercept in order to ensure that the oxygen capacity is distributed optimally per step change in log pO_2 and to maintain equally high conversions to both products. Section 3.4 will focus on utilising a mathematical reactor model in order to verify the validity of this hypothesis for the optimal δ-pO_2 curve.

Decreasing the temperature improves the value of conversion at $X_{H_2O} = X_{CO}$, from ~0.4 at 1293 K to ~0.6 at 893 K, though in real non-stoichiometric OCMs this may be complicated by the prevalence of increased kinetic limitations at lower temperatures. The equilibrium constant for WGS approaches unity at 1093 K and at this temperature $X_{H_2O} = X_{CO} = 0.5$, which is at a log pO_2 -17.8 bar and a 1:1 ratio of H_2O:H_2 or CO:CO_2. It is

important to use inlet gas pO_2s that capture most of the range of applicable pO_2s for the change in δ. For a typical operating CLWGS system at 1093 K the pO_2 of the inlet gas during reduction is roughly $\sim 10^{-23}$ bar and $\sim 10^{-7}$ bar during oxidation[190].

For a non-stoichiometric OCM, in order to achieve stable high conversions of both reactants, it is necessary to ensure that the influence of both oxidation and reduction half cycles is equal. This is not so important if the base usable oxygen capacity of the non-stoichiometric OCM is very large anyway, however since this section aims to optimise the thermodynamics of the non-stoichiometric OCM we assume from now on that a temperature of 1093 K is being used so as to simplify the analysis.

The relations given in Fig. 3.1 only represent the limits of the gas phase thermodynamics. In reality, the δ-pO_2 relationship of a non-stoichiometric OCM may not necessarily show a gradient in the active pO_2 range dictated by the gas phase thermodynamics, meaning that even though it is thermodynamically favourable in the gas phase, conversion to H_2 or CO_2 will not occur. In addition this analysis is only truly applicable to pure non-stoichiometric OCMs; a phase changing OCM with two or more phase changes at the correct chemical potentials could in theory also achieve high conversions.

In order for the solid phase δ-pO_2 curves to closely approximate the shapes of the equilibrium conversion curves, a logistic function can be used as described in Eq. 3.10 which allows for easy manipulation of the shape of the δ-pO_2 curve,

$$\delta\left(p_{O_2}\right) = \frac{\delta_{\max}}{1+e^{-k_{\text{grad}}\left(\log_{10} p_{O_2} - \log_{10} p_{O_2 \text{mid}}\right)}} \qquad \text{Eq. 3.10}$$

where the parameter $\delta_{\max}$ is the maximum degree of non-stoichiometry of the OCM, $\log_{10} p_{O_2 \text{mid}}$ is the pO_2 value of the midpoint of the sigmoid (for the optimal scenario at 1093 K this is the intercept where the conversion of H_2O to H_2 and CO to CO_2 are equal) and k_{grad} is the steepness.

The derivative of Eq. 3.10 with respect to pO_2, is given as follows:

$$\frac{d\delta(p_{O_2})}{dp_{O_2}} = \frac{\delta_{\max} k_{grad} e^{k_{grad}\left(log_{10}\, p_{O_2} - log_{10}\, p_{O_2 mid}\right)}}{p_{O_2}\, ln\, 10\left(e^{k_{grad}\left(log_{10}\, p_{O_2} - log_{10}\, p_{O_2 mid}\right)} + 1\right)^2} \qquad \text{Eq. 3.11}$$

For the optimal δ-pO_2 plot at 1093 K shown in Fig. 3.2, the value of k_{grad} was determined by minimising the difference between the pO_2 values determined via the WGS reaction equilibria and from Eq. 3.10 such that the values of $\log_{10} p_{O_2}$ were identical to 4 decimal places for each datapoint, using 544 datapoints in total. The resulting optimal shape for the δ-pO_2 plot at 1093 K has k_{grad} and $\log_{10} p_{O_2 mid}$ values of -1.15 and -17.8 bar respectively at δ_{max} value of 0.15.

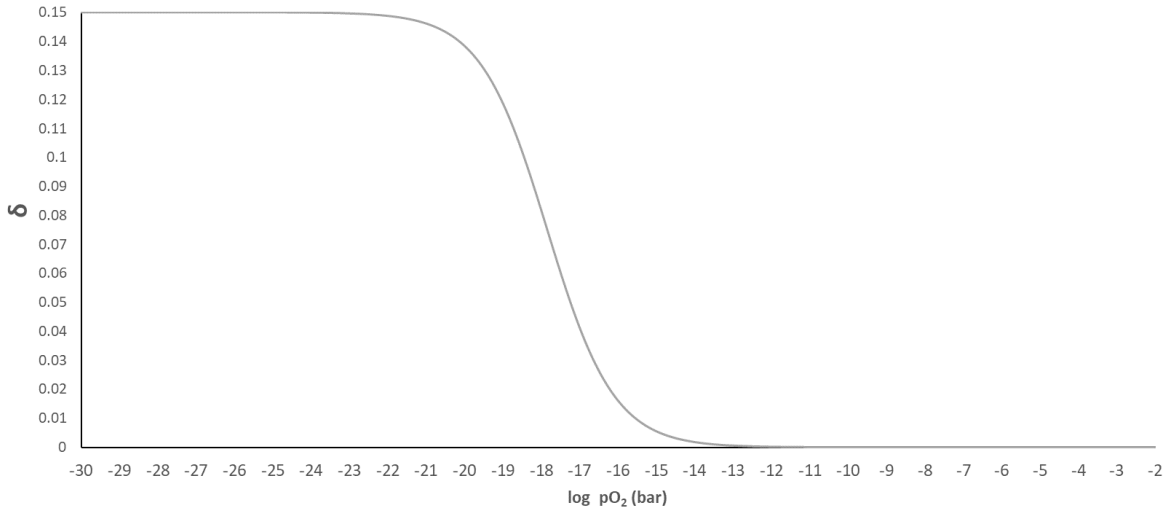

Figure 3.2: The optimal shape of the δ-pO_2 curve at 1093 K. The optimal fitted values of k_{grad} and $log_{10}\, p_{O_2 mid}$ are -1.15 and -17.8 bar respectively.

3.2 Comparing optimal scenario to non-stoichiometric OCMs from literature

The δ-pO_2 plots from literature for the non-stoichiometric OCMs LSF641 (Kuhn et al, 2011), LSM821 (Mizusaki et al, 2000), and CZ82 (Kuhn et al, 2013) were given in chapter 2. This section will attempt to carry out an initial screening of these non-stoichiometric OCMs by comparing their thermodynamic behaviour with that of the optimal non-stoichiometric OCM scenario presented in section 3.1.

At pO_2s where the gradient $\frac{d\delta}{d\, log\, p_{O_2}}$ is close to zero, the non-stoichiometric OCM will be unable to exchange oxygen with a passing gas phase stream and hence conversions of

reactants will be adversely affected. For a stoichiometric metal oxide type material, the value of $\frac{d\delta}{d \log p_{O_2}}$ would be zero at all partial pressure values other than at the point(s) at which the phase transition(s) occur.

The gradient $\frac{\partial \delta}{\partial \log p_{O_2}}$ for each material was determined by fitting a 6th order polynomial curve to the shape of the corresponding δ-pO_2 plots and differentiating with respect to log pO_2. These polynomials are valid for the range of pO_2s from 10^{-8} to 10^{-22} bar and are given in table 3.1. A total of 118, 23 and 13 fitting points were used for LSF641, LSM821 and CZ82 respectively. The fit for LSF641 was derived from the defect model given by Eq. 2.22 hence the larger number of points. To avoid large swings between points, oscillations were minimised by ensuring that the nodes were more densely distributed near the edges of the interval. In addition a logistic function based on Eq. 3.10 was also fitted for comparison, shown in table 3.1, and shows a good match to the polynomial fit.

Table 3.1: Polynomial and logistic function fits for δ-pO_2 relationship for LSF641, LSM821 and CZ82. A high number of significant figures are used in Eq. 3.12, 3.14 and 3.16 due to the sensitivity of the fits. Due to reported decomposition, for LSF641 the fit is valid for the range of pO_2s from 10^{-8} to 10^{-25} bar, for LSM821 the fit is valid for the range of pO_2s from 10^{-8} to 10^{-18} bar and for CZ82 the fit is valid for the range of pO_2s from 10^{-8} to 10^{-21} bar.

Non-stoichiometric OCM	**Polynomial Fit**	**Logistic Function Fit**
LSF641 Polynomial fit reference: Kuhn et al (2011)	$\delta = -0.000000115478689112838(\log_{10} p_{O_2})^6 - 0.000010577325473520 8(\log_{10} p_{O_2})^5 - 0.000386047952422136(\log_{10} p_{O_2})^4 - 0.0072656712546822(\log_{10} p_{O_2})^3 - 0.074840606635054 8(\log_{10} p_{O_2})^2 - 0.402478599222931 \log_{10} p_{O_2} - 0.690102230163141$ Eq. 3.12	$\delta = \frac{0.250}{1 + e^{0.52(\log_{10} p_{O_2} + 23.03}} + 0.197$ Eq. 3.13
LSM821 Polynomial fit reference: Mizusaki et al (2000)	$\delta = 0.000002192374916657 43(\log_{10} p_{O_2})^6 + 0.000022382219107564 1(\log_{10} p_{O_2})^5 + 0.000896543770560584(\log_{10} p_{O_2})^4 + 0.017868484892857 4(\log_{10} p_{O_2})^3 + 0.187895216085516(\log_{10} p_{O_2})^2 + 0.995516349190254 \log_{10} p_{O_2} + 2.0896242606451$ Eq. 3.14	$\delta = \frac{0.230}{1 + e^{0.99(\log_{10} p_{O_2} + 17.84}}$ Eq. 3.15
CZ82 Polynomial fit reference: Kuhn et al (2013)	$\delta = 0.000000042947454 4746955(\log_{10} p_{O_2})^6 + 0.000003593062603 58324(\log_{10} p_{O_2})^5 + 0.000113910394859752(\log_{10} p_{O_2})^4 + 0.001663408436689 56(\log_{10} p_{O_2})^3 + 0.011417415517989 3(\log_{10} p_{O_2})^2 + 0.028489042248150 3 \log_{10} p_{O_2} + 0.000047636237256 1212$ Eq. 3.16	$\delta = \frac{0.642}{1 + e^{0.25(\log_{10} p_{O_2} + 24.18}}$ Eq. 3.17

Each OCM has a total usable capacity. This refers to the total change in δ that can occur within the CLWGS pO_2 operating range without suffering from decomposition and phase

segregation of the OCM at extreme reducing oxygen partial pressures. For example, while LSF641 has a total oxygen stoichiometry of 3 – δ = 3 given in the formula $La_{0.6}Sr_{0.4}FeO_{3-\delta}$, the actual usable capacity is to about a δ of 0.25 before decomposition occurs in the plot given in Fig. 2.6. In addition, for LSF641 while most of the change in δ per step in log pO_2 occurs in the higher pO_2 range, this is more limited by a plateau in the lower log pO_2 range meaning that during cycling most of the capacity for $0 < \delta < 0.25$ will be unused unless enough moles of a feed with a high oxidising potential are flown during the oxidation half cycle to overcome the plateau and reach log pO_2s with a greater change in δ.

For the case of this analysis, the total usable capacity for each OCM has been defined as according to the active range of pO_2 where the reaction can occur. This is used to scale the y-axis of the thermodynamic conversion vs. log pO_2 plot to match that of the OCM limits. A normalised δ-p_{O_2} plot for each OCM is given in Fig. 3.3. The normalised degree of non-stoichiometry, δ_n, can be calculated via Eq. 3.18. δ_{min} in Eq. 3.18 refers to the minimum degree of non-stoichiometry.

$$\delta_n = \frac{\delta - \delta_{min}}{\delta_{max} - \delta_{min}} \qquad \text{Eq. 3.18}$$

It should be noted that since δ_n is a normalised degree of non-stoichiometry, this method does not take into account the size of the total usable oxygen capacity of an OCM, but the optimal way in which this can be used up per step change in log pO_2. A higher total usable capacity will be better regardless as less mass of OCM will have to be used to in a reactor for the same moles of oxygen.

Comparisons are made at 1093 K, so the intercept of the equilibrium conversions vs log pO_2 plot for reduction and oxidation half cycles shown in Fig. 3.1 is at 50% conversion at a log pO_2 of ~17.8 bar. The plot for each material and comparison with the optimal thermodynamics are given in Fig. 3.3 and 3.4.

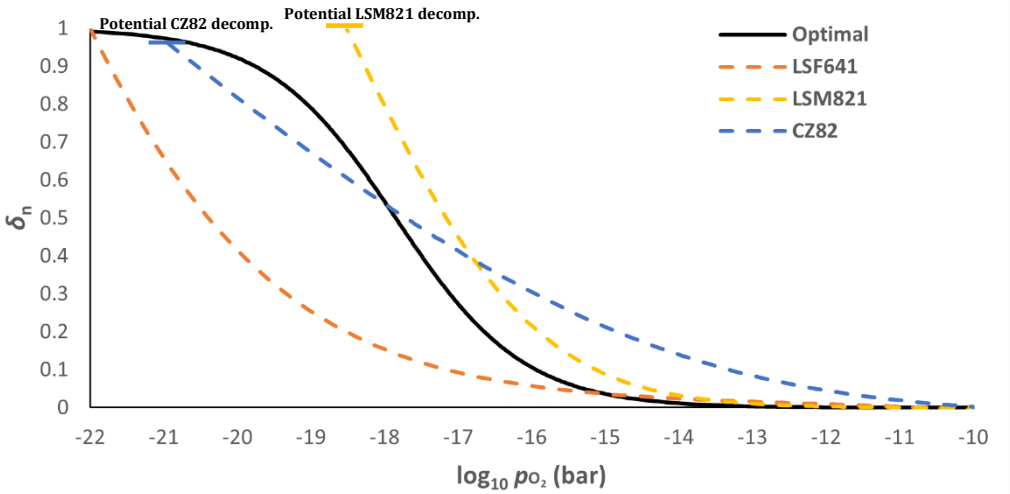

Figure 3.3: δ_n vs. log pO_2 profiles for LSF641, LSM821 and CZ82 using Eq. 3.18 and the fits in table 3.1. The optimal profile is also given as a comparative benchmark. The data is valid for a temperature of 1093 K.

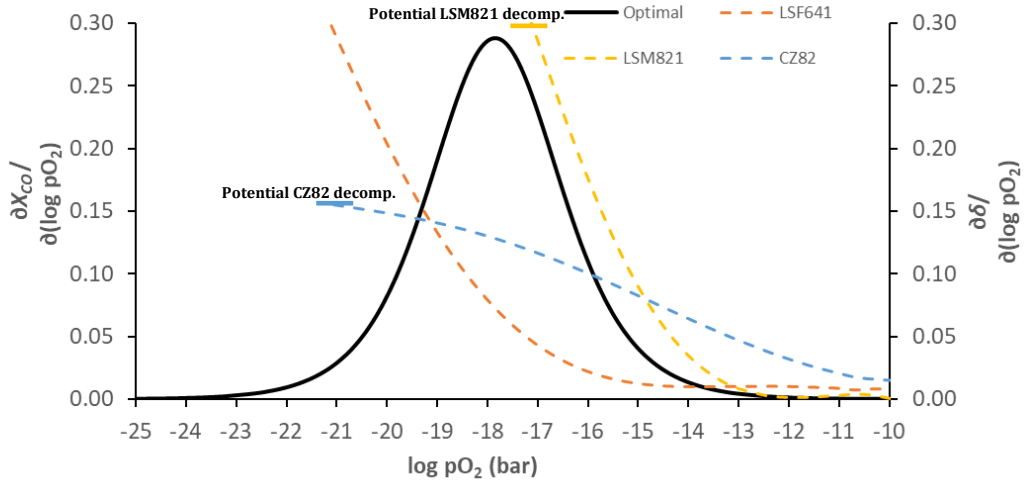

Figure 3.4: Comparison of oxygen capacity distribution for LSF641, LSM821 and CZ82 for CLWGS, based on Eq. 3.18 and fits in table 3.1.

While LSM821 seems to make best use of its oxygen capacity, it is prone to decomposition at pO_2s < 10^{-18} bar at which there is no accurate data on the relationship between δ and log pO_2. On the other hand LSF641 is stable down to lower log pO_2s, but has a much lower usable oxygen capacity, especially at pO_2s < 10^{-18} bar owing to the

plateau at δ=x/2=0.2. In chapter 2 it was seen that this plateau is not present for the strontium doped lanthanum chromite perovskite oxides either, suggesting that these could be promising OCMs with more usable oxygen capacity albeit with the difficulties of operating at a higher temperature. It is also proposed that a hybrid $La_{0.6}Sr_{0.4}Fe_{1-y}Mn_yO_{3-\delta}$ type material could benefit from the stability of LSF641 at more reducing atmospheres and could also allow for more usable oxygen capacity to be available under operating conditions. A look at the oxygen capacities for such materials at 1093 K are given in the preliminary capacity screening experiment in chapter 4 section 4.4.2. CZ82 shows better use of its oxygen capacity than LSF641, however a lack of data at $pO_2s < 10^{-21}$ bar means that further investigation will be necessary to determine if this is significant enough to effect cycling performance due to potential decomposition.

3.3 Derivation of thermodynamically limited reactor model for CLWGS

A CLWGS reactor model is required that can be used to verify the hypothesis for optimal non-stoichiometric OCM behaviour outlined in 3.1. Dynamic mathematical models may be developed to gain a better understanding of the axial concentration profiles inside the chemical-looping reactor, which is normally difficult to determine experimentally and limited to inlet/outlet information. This will help in the process of designing and optimising chemical looping systems for applications on an industrial scale, as well as investigating the performance of various OCMs in the conceptual stage.

Garcia-Labiano et al (2005) developed a changing grain size particle model to simulate the performance of OCMs under non-isothermal conditions, though this was limited to low reactant concentrations. Noorman et al (2011) developed a particle model which described the oxidation and reduction rates of the particle at higher concentrations and more realistic process conditions, and combined this with a packed-bed reactor model to produce a rigorous simulation of a CLC system. Diglio et al (2015) and Spallina et al (2017) both developed one-dimensional models for a packed-bed reactor using experimental kinetic data for a Ni based OCM in CLR with methane as the reducing agent. Zhou et al (2015) and Diglio et al (2016) have also gone on to produce simple hydrodynamic simulations for fluidised bed reactor systems with Ni based OCM, and

have highlighted the importance of the effect of operating conditions and OCM choice on process feasibility and hydrogen selectivity.

The aforementioned studies make use of OCMs of which experimental and literature data is more readily available. However there is a lack of information regarding the kinetics of non-stoichiometric perovskite-type materials in chemical looping processes. This section describes the use of a thermodynamic model based on the δ-pO_2 thermodynamics of the OCM to produce an isothermal model that simulates a laboratory scale CLWGS packed bed reactor.

An approach to model a CLWGS system with a non-stoichiometric OCM was first described by de Leeuwe et al (2021), which supports the assumptions in the model used in this thesis. A pseudo-homogeneous one-dimensional model was used for the simulation, which does not consider differences in temperature and concentration between the OCM and the gas phase (as an ideal gas), and does not account for transport restrictions. de Leeuwe et al (2021) found that the effects of axial dispersion and radial gradients could be ignored as they provided minimal improvement to results and did not justify the increase in computation time required. It is assumed that there is an even distribution of the heat generated from the reactions over the unit volume. The kinetics of the gas-solid reactions are assumed to be very fast, and that they are instead controlled by the thermodynamic parameters, hence assuming that there exists an equilibrium between the OCM and the bulk fluid. It was also taken that the flowrate of the inlet gas is always constant and flown in opposite directions depending on the stage of the current half cycle (oxidation or reduction). Carbon formation reactions (e.g. reverse Boudouard reaction) were ignored to simplify the model.

A simple material balance (essentially input plus generation equals output plus accumulation) is developed by performing elemental analyses over an increment *dx* along the bed for water, carbon monoxide, free oxygen, hydrogen and carbon and are given in equations 3.19 – 3.24.

$\dot{N}\frac{\partial y_{H_2O}}{\partial x} = r_{H_2O} - \frac{\partial y_{H_2O}}{\partial t}\varepsilon\,\rho_g$	Water balance	Eq. 3.19
$\dot{N}\frac{\partial y_{CO}}{\partial x} = r_{co} - \frac{\partial y_{CO}}{\partial t}\varepsilon\,\rho_g$	Carbon monoxide balance	Eq. 3.20
$\frac{\partial \delta}{\partial t}(1-\varepsilon)\ \rho_s = -r_{H_2O}$	Oxygen balance (oxidation)	Eq. 3.21
$\frac{\partial \delta}{\partial t}(1-\varepsilon)\ \rho_s = r_{CO}$	Oxygen balance (reduction)	Eq. 3.22
$y_{H_2} + y_{H_2O} = y_{H_{constant}}$	Hydrogen balance	Eq. 3.23
$y_{CO} + y_{CO_2} = y_{C_{constant}}$	Carbon balance	Eq. 3.24

$\dot{N}$ is the molar flowrate of the gas stream in mol/s. ρ_g represents the molar density of the gases in mol/m^3. ε is the voidage of the bed. The rate of reaction of CO and H_2O, r_{CO} and r_{H_2O} (mol/m^{3}s), are given in terms of the rate of change of $\frac{\partial \delta}{\partial t}$, which represents the rate of change of the degree of non-stoichiometry δ with time. The term $\frac{\partial \delta}{\partial t}$ is equal to the rate of transfer of oxygen between solid and gas phases. The oxygen content of a non-stoichiometric OCM decreases as δ increases and vice versa, meaning that $\frac{\partial \delta}{\partial t}$ is negative during the oxidation stage and positive during the reduction stage hence the negative sign for Eq. 3.21. Eq. 3.23 and 3.24 are equal to the total mole fractions of reactants ($y_{H_{constant}}$ and $y_{C_{constant}}$) assuming that there is no carbon deposition, and for the purposes of this work both are set for 5% reactant feeds for better comparison to the experimental results in later chapters.

Using the chain rule, the term $\frac{\partial \delta}{\partial t}$ can be related to other terms assuming the process is limited by thermodynamics:

Oxidation $$\frac{\partial \delta}{\partial t} = \frac{d\delta}{dp_{O_2}} \frac{dp_{O_2}}{dy_{H_2O}} \frac{\partial y_{H_2O}}{\partial t} \quad \text{Eq. 3.25}$$

Reduction $$\frac{\partial \delta}{\partial t} = \frac{d\delta}{dp_{O_2}} \frac{dp_{O_2}}{dy_{CO}} \frac{\partial y_{CO}}{\partial t} \quad \text{Eq. 3.26}$$

In order to determine $\frac{\partial \delta}{\partial p_{O_2}}$, it is necessary to be able to relate the degree of non-stoichiometry δ to key process parameters such as oxygen partial pressure. For LSF641, Eq. 2.22 described by Kuhn et al (2011) and covered in chapter 2 can be used to determine this relationship, and the polynomial fit previously given in Eq. 3.12 used to calculate the values of $\frac{\partial \delta}{\partial p_{O_2}}$ at different pO_2 values. For other OCMs with different properties, their respective δ-pO_2 relationships must be determined and used.

The terms $\frac{\partial p_{O_2}}{\partial y_{H_2O}}$ and $\frac{\partial p_{O_2}}{\partial y_{CO}}$ may be related to fundamental equilibrium analytical expressions for the gas phase equilibrium reactions during oxidation and reduction stages ($H_2O \rightleftharpoons H_2 + ½\ O_2$ and $CO + ½\ O_2 \rightleftharpoons CO_2$) as follows:

Oxidation stage $$K_{ox} = \frac{y_{H_2} {p_{O_2}}^{0.5}}{y_{H_2O}} \quad \text{Eq. 3.27}$$

$$\frac{\partial pO_2}{\partial y_{H_2O}} = -2{K_{ox}}^2 y_{H_{constant}} \frac{y_{H_2O}}{{y_{H_2}}^3} \quad \text{Eq. 3.28}$$

Reduction stage $$K_{red} = \frac{y_{CO_2}}{y_{CO} {p_{O_2}}^{0.5}} \quad \text{Eq. 3.29}$$

$$\frac{\partial pO_2}{\partial y_{CO}} = -2\left(\frac{1}{K_{red}}\right)^2 y_{C_{constant}} \frac{y_{CO_2}}{{y_{CO}}^3} \quad \text{Eq. 3.30}$$

Eq. 3.19 and Eq. 3.20 may be converted to a system of ODEs by assuming a finite difference thus discretising the equation along the length of the reactor. The ode45 solver in MATLAB was used to compute solutions for this work.

$$\frac{\partial y_{jg}}{\partial x} \approx \frac{y_i - y_{i-1}}{\Delta x} \qquad \text{Eq. 3.31}$$

In Eq. 3.31, *i* represents incremental position along the bed and *j* represents species CO and H_2O depending on whether the oxidation or reduction stage is being carried out. The material balance equations may be solved sequentially through each element with increment 1 defined at the CO inlet and the final increment defined at the H_2O inlet. A total of 100 increments were used. In order to verify that artificial diffusion related to the convection term was not occurring a numerical experiment was carried out using double and half the number of increments and it was seen that the solutions were independent of grid spacing, meaning that the use of the upwind scheme was sufficient.

It should be noted that an analytical solution for Eq. 3.19-3.20 exists in the field of chromatography column modelling as a first order advection equation using a linear advection isotherm and can be approximated by a Gaussian function (Guiochon et al, 2006). The ideal continuous δ-p_{O_2} relationship for non-stoichiometric OCMs is analogous to concepts of the boundary profile in the ideal model of chromatography. In chromatography, sharpening effects from various physical processes can lead to a deviation from the ideal model causing the input concentration-time profile to change as it migrates through the column.

3.4 Verifying hypothesis for the optimal thermodynamic behaviour for a non-stoichiometric OCM using a model of a packed-bed reactor carrying out CLWGS

The reactor model given in section 3.3 can be used to verify the case for an optimal shape to the δ-pO_2 curve for a non-stoichiometric OCM. In section 3.1 it was proposed that an optimal δ-pO_2 relationship at 1093 K would have a gradient centred around a log pO_2 corresponding to 1:1 H_2O to H_2 or CO_2 to CO. Moving the region where δ shows changes to a higher or a lower log pO_2 would compromise the conversions that could be achieved. In order to optimally distribute oxygen capacity per step change in log pO_2, an ideal non-stoichiometric OCM is expected to match as closely as possible the gradient of the active range in Fig. 3.1 around the turning point at 1:1 ratio of reactants to products. The reactor model can investigate the effect on conversion and product quality of using

different shapes to the δ-log pO_2 curve by altering the gradient of the curve, or translating the curve to higher or lower log pO_2 values along the x-axis by using the logistic relationship given in Eq. 3.10.

By taking the ratio of usable solid phase oxygen capacity to gas phase oxygen capacity per half cycle, a dimensionless number, λ_O, can be defined in order to help with analysis:

$$\lambda_O = \frac{(\delta_{red} - \delta_{ox}) N_{OCM}}{\dot{N}_{O_2} t} \qquad \text{Eq. 3.32}$$

In Eq. 3.32, the degrees of non-stoichiometry of the OCM during steady cycling at the end of the reduction and oxidation half cycles are given by δ_{red} and δ_{ox} respectively. The molar flow rate of oxygen at the inlet is given by $\dot{N}_{O_2}$ and t represents the duration of a half cycle. The total moles of OCM (N_{OCM}) is determined by the following formula:

$$N_{OCM} = \rho_s \pi r^2 L (1 - \epsilon)(1 - \varepsilon) \qquad \text{Eq. 3.33}$$

In Eq. 3.33 r represents the radius of the bed, ρ_s is the molar density of the solid phase, L represents the length of the bed, and ϵ and ε are used to indicate the porosity and voidage of the bed respectively.

The limiting reactant is the gas phase when the value of λ_O is greater than 1. In this scenario the conversions of CO and H_2O will largely be limited by the chemical equilibrium. On the other hand, the limiting reactant is the solid phase when the value of λ_O is less than 1 and gas conversion will then be restricted by the solid phase oxygen capacity.

For this model, the only parameters changed were those relating to the δ-pO_2 relationship. Due to the material balance the conversions are only dependant on the values of $\log_{10} p_{O_2 mid}$, k_{grad} and λ_O. In Eq. 3.32 any combination of $\delta_{red} - \delta_{ox}$, $\dot{N}_{O_2}$, t and N_{OCM} can be used to generate a value of λ_O without altering the resulting conversions. Therefore the values for flowrate, temperature, pressure, redox reaction durations and OCM mass were not changed between cases. These values were kept constant and are as follows in table 3.2.

Table 3.2: Model parameters that were set constant for each case.

Set parameter	Value
Bed length (cm)	8
Bed diameter (mm)	4
OCM mass (g)	1.03
Inlet gas stream flowrate (ml min^{-1})	50
Temperature (K)	1093
Pressure (bar)	1
Reaction durations (s)	60

Due to the absence of H_2 or CO_2 in the inlet streams, their pO_2s are not well defined. In order to avoid this problem, the notional pO_2 used in the boundary conditions were chosen to be the equilibrium pO_2 of water dissociation and CO disproportionation at the reactor temperature (1093 K) and are shown in table 3.3. For the initial condition, the pO_2 values across the packed bed at the start of one half cycle (e.g. reduction) were set to be the same as those from the end of the previous half cycle (oxidation), in order to ensure that the gas would be in equilibrium with the solid phase at the start of the half cycle. Due to the fact that the system is operated at very low pO_2 values this approximation does not appreciably change the oxygen balance of the system.

Table 3.3: Mole fractions of components in the reactant feeds used in the simulation. The oxidation and reduction inlet streams correspond to a log pO_2 of -7.2 bar and -22.4 bar respectively at 1093 K.

Component in feed	Mole fraction
CO	4.97×10^{-2}
CO_2	2.57×10^{-4}
H_2O	5.00×10^{-2}
H_2	2.42×10^{-7}

3.4.1 Optimal δ-pO_2 curve scenario at 1093 K

For the optimal scenario given in Fig. 3.2, the effect on outlet gas concentration of some different values of λ_O are given in Fig. 3.5. The value of λ_O was changed by varying the

value of δ_{max} of the δ-pO2 logistic equation appropriately. The corresponding values of conversion are given in Fig. 3.6, and these are taken during steady cycling when the difference between the values of X_{CO} and X_{H_2O} was < 0.01.

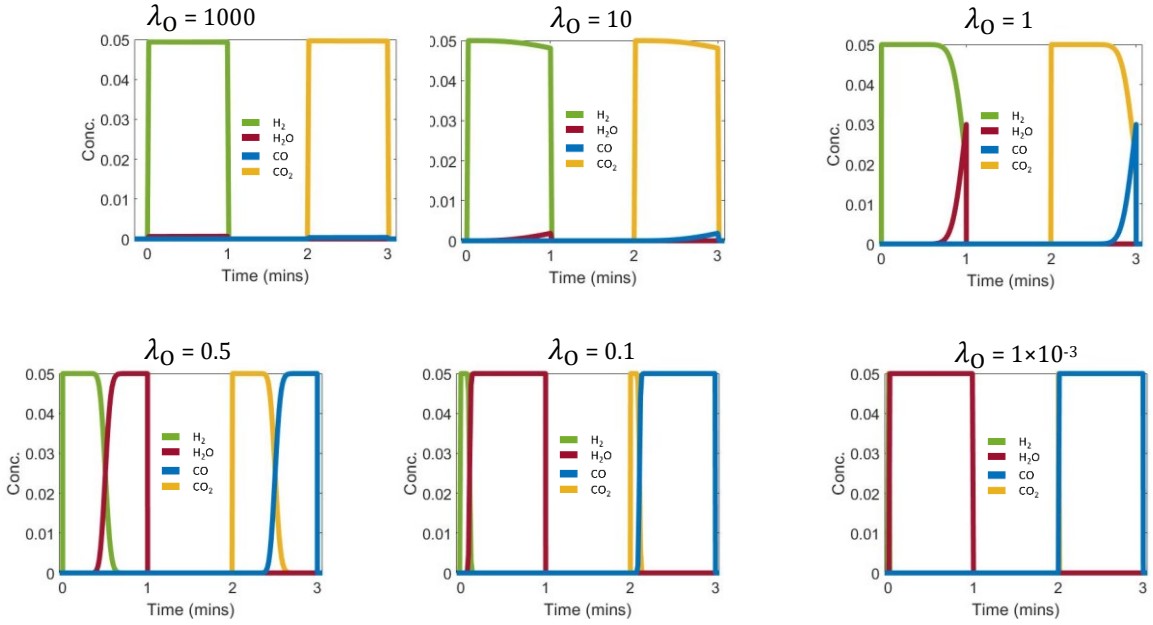

Figure 3.5: Outlet concentration profiles determined from the simulation using different values for λ_O of the δ-pO2 plot at 1093 K. The values of k_{grad} and $log_{10}\, p_{O_2 mid}$ are kept constant at -1.15 and -17.8 bar respectively. The profiles are taken during steady cycling when the difference between X_{CO} and X_{H_2O} is < 0.01.

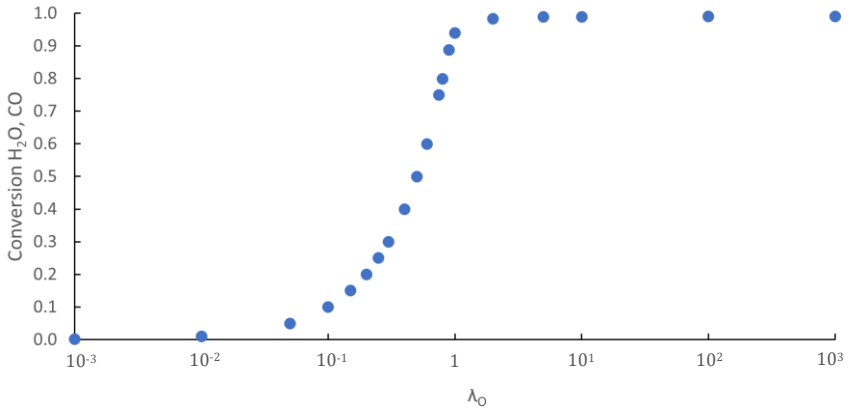

Figure 3.6: Conversions determined from the simulation using different values for λ_O for the δ-pO2 plot at 1093 K. The values of k_{grad} and $log_{10}\, p_{O_2 mid}$ are kept constant at -1.15 and -17.8 bar respectively. The values of conversion that are shown are those during steady cycling when the difference between X_{CO} and X_{H_2O} is < 0.01.

It can be seen in Fig. 3.6 that λ_O is asymptotic towards a X_{CO} and X_{H_2O} value of 1. This is to be expected because of the use of a continuous relationship δ-pO_2 function (associated with non-stoichiometric OCMs), and therefore the conversion when λ_O = 1 is not 100% but is instead limited to ~94%. The conversion increases by roughly ~0.4% when the value of λ_O is increased from 2 to 10. In addition the conversion increases by about ~4.5% when increasing λ_O from 1 to 2. Essentially this means that there is not much to be gained from increasing the value of λ_O much past >2 since there is no substantial improvement in the product purity.

As expected, lower values of λ_O result in less usable oxygen capacity and gives a decrease in conversions and product quality. For λ_O < 0.5 significant quantities of unreacted feed gas are seen in the outlet concentration profiles in Fig. 3.5. It should be noted that this theoretical scenario is not limited by the thermodynamics - it would still be possible to achieve high conversions because the gradient of the curve k_{grad} and $\log_{10} p_{O_2 mid}$ are not changed, they are still set to the optimal value. However, the value of λ_O would need to be increased appropriately by a suitable increase in for example the mass of OCM (which in turn may be more expensive industrially).

Increasing λ_O will increase the time taken for stable conversions to be achieved if the same feed duration as lower capacity OCMs is used. In the simulation, scenarios with higher values of λ_O took more cycles to reach steady cycling (the longest at λ_O = 1000 took > 20,000 cycles). However since it would be expected that the feed duration and flowrate would be appropriately increased in order to fully take advantage of higher capacity OCMs this would not pose a disadvantage for industrial scale applications. Since this analysis aims to compare the different cases under the same process conditions however (given before in table 3.2), the same feed durations had to be used hence the longer time to reach steady cycling.

3.4.2 Translation of δ-pO₂ curve to higher or lower log pO₂s at 1093 K

The midpoint of the sigmoid will affect how much of the oxygen capacity can be accessed by the passing gas phase streams, and this section will explore the different scenarios for different values of $\log_{10} p_{O_2 mid}$. Fig. 3.7 shows how the logistic plot is shifted when using different values of $\log_{10} p_{O_2 mid}$. As mentioned before all other model parameters other than those relating to the δ-pO_2 relationship, specifically the midpoint, were kept the same as shown before in table 3.2. The value of k_{grad} is also kept constant, at the optimal fitted value of -1.15.

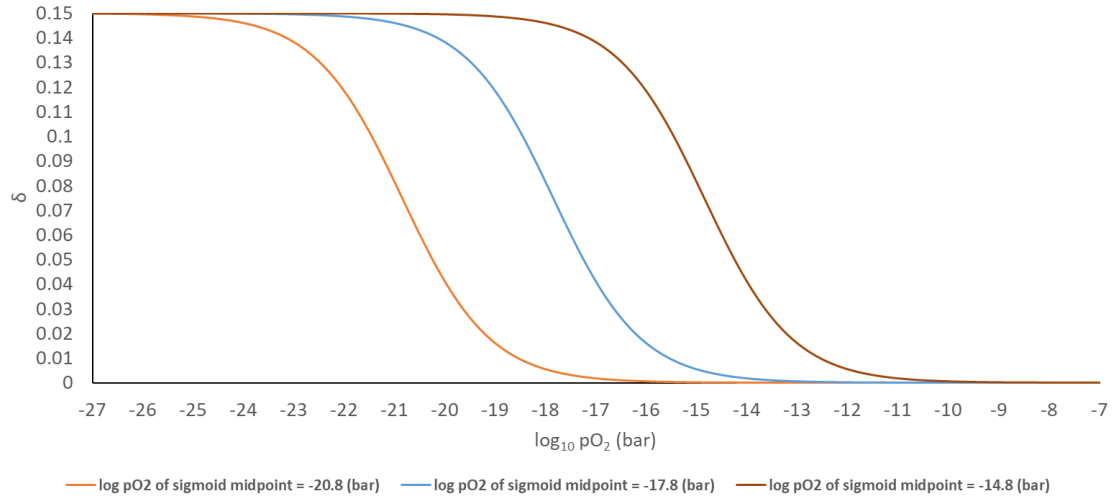

Figure 3.7: Example showing how the logistic plot is shifted to higher or lower values of oxygen partial pressure depending on the value of $log_{10}\, p_{O_2 mid}$. For this work, simulations were carried out for $log_{10}\, p_{O_2 mid}$ values of -17.8 ± 9 bar.

Fig. 3.8 shows the outlet concentrations achieved for λ_O value of 1, and Fig. 3.9 shows the conversions possible at the different values of $\log_{10} p_{O_2 mid}$ for a range of λ_O values.

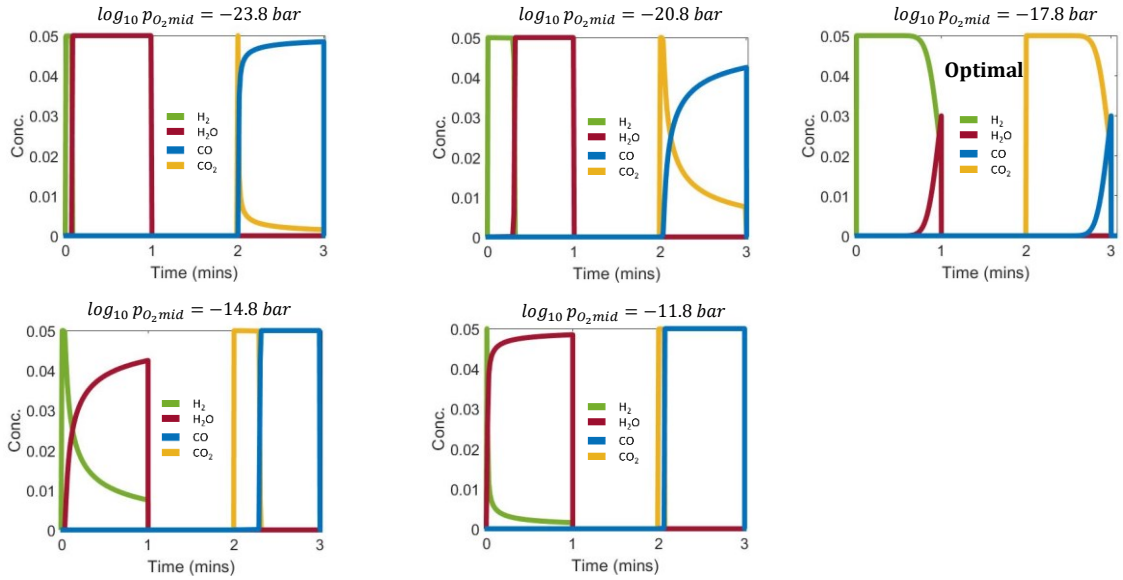

Figure 3.8: Outlet concentration profiles determined from the simulation at λ_O value of 1 using different values for the midpoint of the sigmoid. The value of k_{grad} is kept constant at -1.15. The optimal value of $log_{10}\, p_{O_2 mid}$ is at -17.8 bar. The profiles are taken during steady cycling when the difference between X_{CO} and X_{H_2O} is < 0.01.

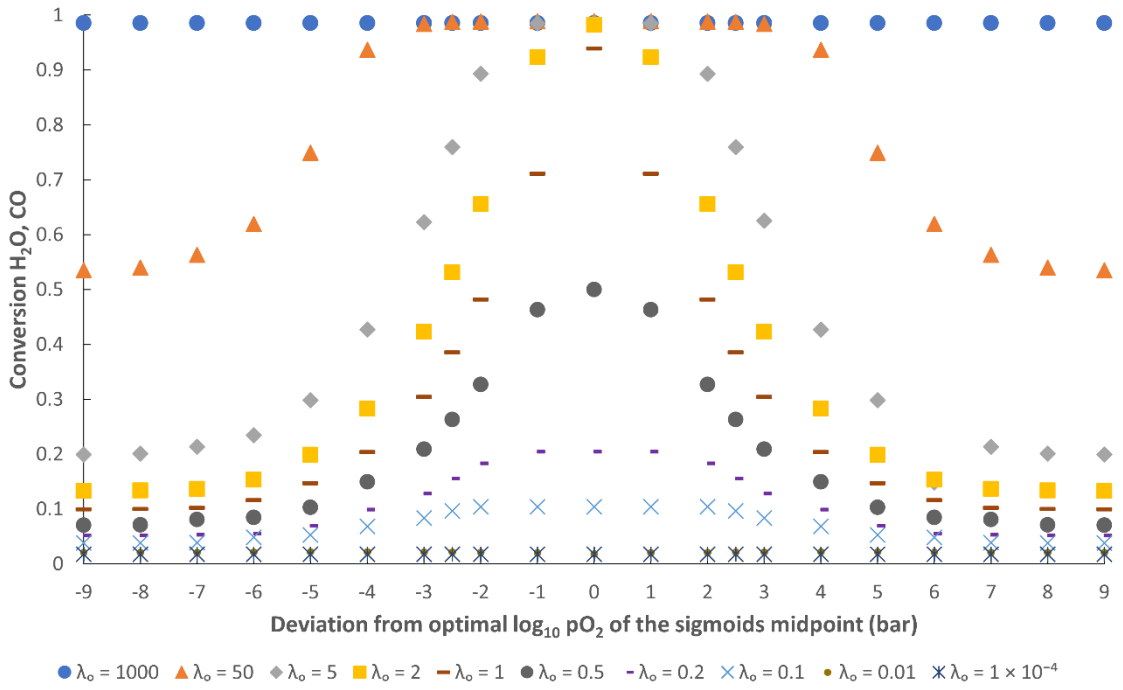

Figure 3.9: Conversions determined from the simulation using different values for the midpoint of the sigmoid at various values of λ_O. The value of k_{grad} is kept constant at -1.15. The optimal value of $log_{10}\, p_{O_2 mid}$ is at -17.8 bar. The values of conversion that are shown are those during steady cycling when the difference between X_{CO} and X_{H_2O} is < 0.01.

From Fig. 3.8 and 3.9 it can be seen that the highest conversion and best product quality may be achieved when the value of $\log_{10} p_{O_2 mid}$ is at the intercept from the X_{CO} and X_{H_2O} curves in Fig. 3.1 which is at a log pO_2 of -17.8 bar. At a λ_O value of 1, it is not possible to achieve a conversion that is an improvement over ~94% using any other $\log_{10} p_{O_2 mid}$ value. This agrees with the proposed theory for an optimal δ-pO_2 curve for non-stoichiometric OCMs described in section 3.1 – this theory stated that for an ideal non-stoichiometric OCM the curves of the gas phase thermodynamics and the solid phase δ-pO_2 relationship must match as closely as possible.

For simulations with the higher λ_O value of 50, the decrease in conversions in deviations from the optimal $\log_{10} p_{O_2 mid}$ of -17.8 bar is not significant until around -21.8 bar and -13.8 bar. Even though the available oxygen capacity is not being optimally distributed, there is still enough usable oxygen capacity to be able to achieve similar conversions to the best scenario. This means that for scenarios with higher λ_O values, it is possible to still achieve very high conversions when at large deviations from the 1:1 reactant to product ratio point. Lower values of λ_O on the other hand show a more significant decrease in conversions at log pO_2s closer to -17.8 bar.

In Fig. 3.8 and Fig. 3.9 at $\log_{10} p_{O_2 mid}$ values that deviate further away from the optimal $\log_{10} p_{O_2 mid}$ of -17.8 bar, the available oxygen capacity for exchange in the active region has been sufficiently diminished so as to significantly lower the conversions possible. For $\log_{10} p_{O_2 mid}$ = -26.8 bar, due to the shift in the δ-pO_2 curve there is more change in δ in the lower log pO_2 region where the oxidation half reaction is thermodynamically more favourable than the reduction half reaction. This would give initial favourable conversions to H_2, however it is held back by the lower extent of reaction of the CO oxidation stage in that range, meaning that the bed will be less reduced at the start of subsequent oxidation cycles thereby resulting in a gradual decrease in hydrogen production. Therefore, the conversion to products is limited by the less favourable half cycle, and both eventually converge at a lower conversion. Likewise, at the $\log_{10} p_{O_2 mid}$ of -8.8 bar, there is more change in δ in the higher log pO_2 region where the reduction half reaction is thermodynamically more favourable than the oxidation half reaction. While this gives initial favourable conversions to CO_2, it results in the system being held

back by the lower extent of reaction of the H_2O splitting stage in that range, meaning that the bed will be less oxidised at the start of subsequent reduction cycles thereby resulting in a gradual decrease in CO_2 production. The conversion to products is limited by the less favourable half cycle, which is how X_{H_2O} and X_{CO} both converge to a lower value.

The conversions achieved using δ-pO_2 curves with $\log_{10} p_{O_2 mid}$ values which are equidistant in positive or negative differences from -17.8 bar (the optimal midpoint) are equal, because the same proportion of the δ-pO_2 curve is available for oxygen exchange due to using fixed gas phase oxidising potentials, and also because the gas phase X_{H_2O} and X_{CO} curves (seen in Fig. 3.1) are symmetrical around the conversion intercept. This also results in the outlet concentration profiles at equidistant midpoints from log pO_2 - 17.8 bar being mirrored versions of each other. For example, in Fig. 3.8 for the case of the δ-pO_2 curve with $\log_{10} p_{O_2 mid}$ value of -20.8 bar, complete breakthrough of unreacted H_2O occurs from ~20 s into the oxidation half cycle, whereas only a gradual increase in unreacted CO occurs and a more limited CO breakthrough by the end of the reduction half cycle. This is because the oxidation half reaction is thermodynamically more favourable at lower log pO_2 values. Therefore the rate of conversion to H_2 is greater which results in the earlier more complete breakthrough of H_2O since the reduction half cycle is unable to sufficiently regenerate the OCM as there is less usable oxygen capacity based on the shift in the δ-pO_2 plot. The reverse of this phenomenon is true in the higher range of log pO_2 values. For this reason, the shape of the concentration profile for $\log_{10} p_{O_2 mid}$ = -20.8 bar is mirrored in the equidistant δ-pO_2 curve with $\log_{10} p_{O_2 mid}$ value of -14.8 bar, with only a gradual increase in unreacted H_2O occurring and a limited breakthrough in the oxidation half cycle, while a complete breakthrough of unreacted CO occurs at ~ 20 s into the reduction half cycle.

In the optimal scenario in Fig. 3.8, with $\log_{10} p_{O_2 mid}$ = -17.8 bar, the extent of reaction of both oxidation and reduction half reactions are balanced and distributed evenly around the 1:1 reactant to product ratio point, and so the shape of the concentration profiles of both half cycles are identical. Since the bed can be oxidised or reduced to the same

extent at the end of each half cycle there is no disadvantage to being able to achieve the highest conversions.

3.4.3 Increasing or decreasing steepness of δ-pO_2 curve at 1093 K

The gradient of the ideal non-stoichiometric OCM δ-pO_2 plot (given before in Fig. 3.2) represents the ideal distribution of oxygen capacity per step change in log pO_2 for the region where the gradient occurs in the WGS equilibria plots in Fig. 3.1, and was fitted as k_{grad} = -1.15 for the logistic plots. All other model parameters were kept the same as before. The value of $\log_{10} p_{O_2 mid}$ was set to -17.8 bar. At lower values of k_{grad}, the δ-pO_2 relationship eventually tends to become a horizontal line, while at higher values of k_{grad} the relationship approaches that of a single phase changing OCM.

The effect on outlet concentrations and conversions from the simulation for different multiples of k_{grad} are given in Fig. 3.10 and 3.11. The results are taken from the point in the simulation where enough cycles have passed for steady cycling to be achieved which is defined as when the difference between X_{CO} and X_{H_2O} is < 0.01.

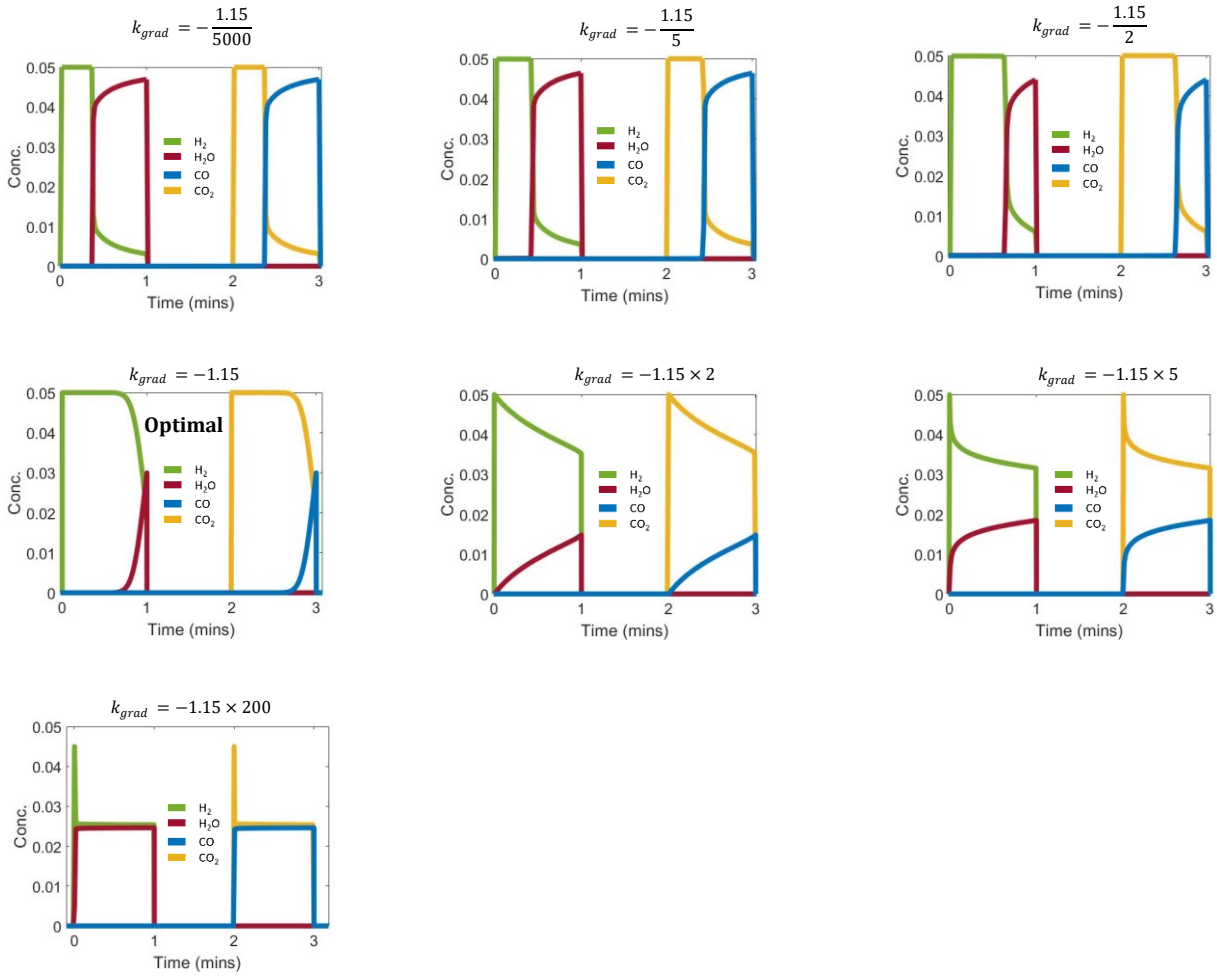

Figure 3.10: Outlet concentration profiles determined from the simulation using different values for the value of k_{grad}. The optimal value of k_{grad} is at -1.15. The value of $log_{10}\, p_{O_2 mid}$ is set constant to the optimal fitted value of -17.8 bar in each case. The profiles are taken during steady cycling when the difference between X_{CO} and X_{H_2O} is < 0.01.

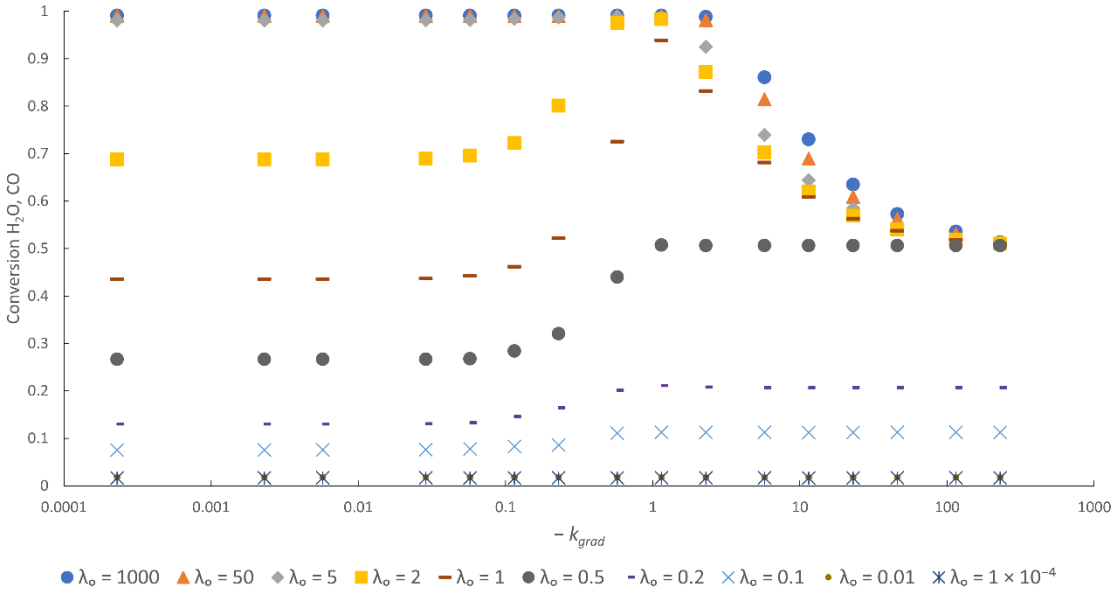

Figure 3.11: Conversions determined from the simulation using different values for gradient of the δ-pO₂ curve k_{grad}. The optimal value of k_{grad} is at -1.15. The value of $log_{10}\, p_{O_2 mid}$ is set constant to the optimal fitted value of -17.8 bar in each case. The values of conversion that are shown are those during steady cycling when the difference between X_{CO} and X_{H_2O} is < 0.01.

From Fig. 3.10 and Fig 3.11 it can be seen that the conversions and product quality decrease as the value of k_{grad} decreases or increases in varying multiples from the optimal value at k_{grad} = - 1.15. As was seen in section 3.4.2 with the investigations at different $\log_{10} p_{O_2 mid}$ values, in Fig. 3.11 it can be seen that there is a leeway to have a less optimal value of k_{grad} while still achieving high conversions when the gas phase is the limiting reactant.

A broader δ-pO_2 curve (using lower values of k_{grad}) results in a wider range of pO_2s at which oxygen exchange can occur which means that the usable oxygen capacity of the OCM is distributed more sparsely in the range of pO_2s given by the shape of the equilibrium conversion curves given before in Fig. 3.1. At the lower values of k_{grad} the δ-pO_2 curve still encompasses the full range of the applicable pO_2s for the change in δ. Despite a poorer pO_2 distribution, a very large λ_O value (achieved through either a very low oxygen flowrate, a very large δ_{max} value, a significant increase in the moles of OCM, or very short half cycle durations) results in a convergence to only a marginally lower value of conversion. Due to the material balance this can also still be a very high

conversion seen especially at the largest λ_O values at 5, 50 or 1000. At low values of k_{grad} (such as at k_{grad} = -1.15/5000) Fig. 3.10 shows that pure production of H_2 or CO_2 is possible for a portion of the half cycle before complete breakthrough of almost pure reactant gas. This is because at low k_{grad} values and scenarios where the solid phase is the limiting reactant, the size of the change in δ in the pO_2 range for CLWGS is decreasing, hence the OCM will be exhausted sooner and more of the inlet gas will pass through the reactor unreacted earlier on in the half cycle.

Conversely a steeper δ-pO_2 curve (using higher values of k_{grad}) results in the range of pO_2s where oxygen exchange occurs with the gas phase stream being concentrated in a more limited range of pO_2s. This range is less than the range given by the shape of the equilibrium conversion curves given before in Fig. 3.1, resulting in less oxygen capacity being available at oxidising potentials in the thermodynamically active range for WGS. This causes the outlet conversion profiles to feature worse product quality as shown in Fig. 3.10, and gives lower conversions. At higher values of k_{grad}, complete breakthrough of the reactant gasses never occurs, but the total concentration of product gas decreases and there is significant unreacted gas present throughout the entire half cycle. The δ-pO_2 plot approaches that of an OCM with a single phase transition at a log pO_2 of -17.8 bar at very high values of k_{grad}. This means that the conversion for simulations where the gas phase is the limiting reactant (λ_O>1) tends towards that which is associated with a 1:1 ratio of reactants to products, which is 50%. This results in the outlet conversion profiles being close to 50% reactant and 50% product in the profile for k_{grad} = -1.15 × 200 following the initial spike.

The ideal scenario is that where the value of k_{grad} is equal to -1.15, which matches exactly the gradient of the corresponding gas phase thermodynamics X_{CO} and X_{H_2O} vs. log pO_2 plot from Fig. 3.1, and at a λ_O value of 1 it is not possible to achieve a conversion that is an improvement over ~94% using any other value of k_{grad}, hence successfully verifying the theory postulated earlier that the solid phase gradients should match the gas phase gradients as closely as possible.

3.5 Summary

This chapter showed how the performance of OCMs in the CLWGS process can be explained by focusing on the effect on conversion of the relationship between the oxygen non-stoichiometry of the OCM δ and the pO_2 of the gas phase. The case for a hypothetical non-stoichiometric OCM which arises from the thermodynamics of the water-gas shift reaction was proposed and verified by use of a reactor model. This theory can be applied as a theoretical optimum and as a benchmark to aid in predicting the conversion performance of new non-stoichiometric OCMs, provided that they have sufficiently fast kinetics with the reactant streams to make the process thermodynamically limited.

The work detailed in this chapter is limited to a model and its underlying assumptions applied to a purely hypothetical OCM δ-pO_2 relationship. In order to verify this theory empirically, the behaviour of a real OCM must be investigated experimentally with knowledge of its δ-pO_2 relationship. In this respect, the next chapter (chapter 4) will provide information into various experimental methods that make such an investigation possible and that are used in this thesis. Some interesting OCMs that were identified in section 3.2 by making use of the benchmark, including CZ82 and a potential $La_{0.6}Sr_{0.4}Fe_{1-y}Mn_yO_{3-\delta}$ type material, will be screened for their usable oxygen capacity in chapter 4. It was noted that strontium doped lanthanum chromite perovskite oxides also lacked the limiting plateau that was present for LSF641, but data was only available from the literature review in chapter 2 at higher temperatures. A combined $La_{0.6}Sr_{0.4}Fe_{1-y}Cr_yO_{3-\delta}$ type material will therefore also be investigated for oxygen capacity at 1093 K in chapter 4.

Chapter 5 will then give information regarding a more detailed investigation into the δ-pO_2 thermodynamics of LSFM6473, a potential OCM selected in this work, while chapter 6 will carry out an investigation into the thermochemical expansivities of this material in an in-situ packed bed reactor. Finally chapter 7 provides details of rigorous reactor experiments carried out to verify the performance capabilities of selected OCMs.

Chapter 4: Experimental set-up

This chapter provides the details of the various laboratory equipment used to carry out the investigations in this thesis.

A description of the TGA set-up is provided in this chapter. Based on the OCM literature review in chapter 2 and the discussion of optimal material thermodynamics in chapter 3, materials of the types $La_{1-x}Sr_xFe_{1-y}B_yO_{3-\delta}$ (where B may be Mn or Cr) and $Ce_{1-x}Zr_xO_{2-\delta}$ were selected as interesting materials to further investigate their oxygen capacity in the active pO_2 range relating to CLWGS through preliminary TGA experiments. These OCMs were then narrowed down further to select materials to use to operate in the packed bed integral reactor. LSF641 was used as a reference material. Details on the material synthesis method are also given.

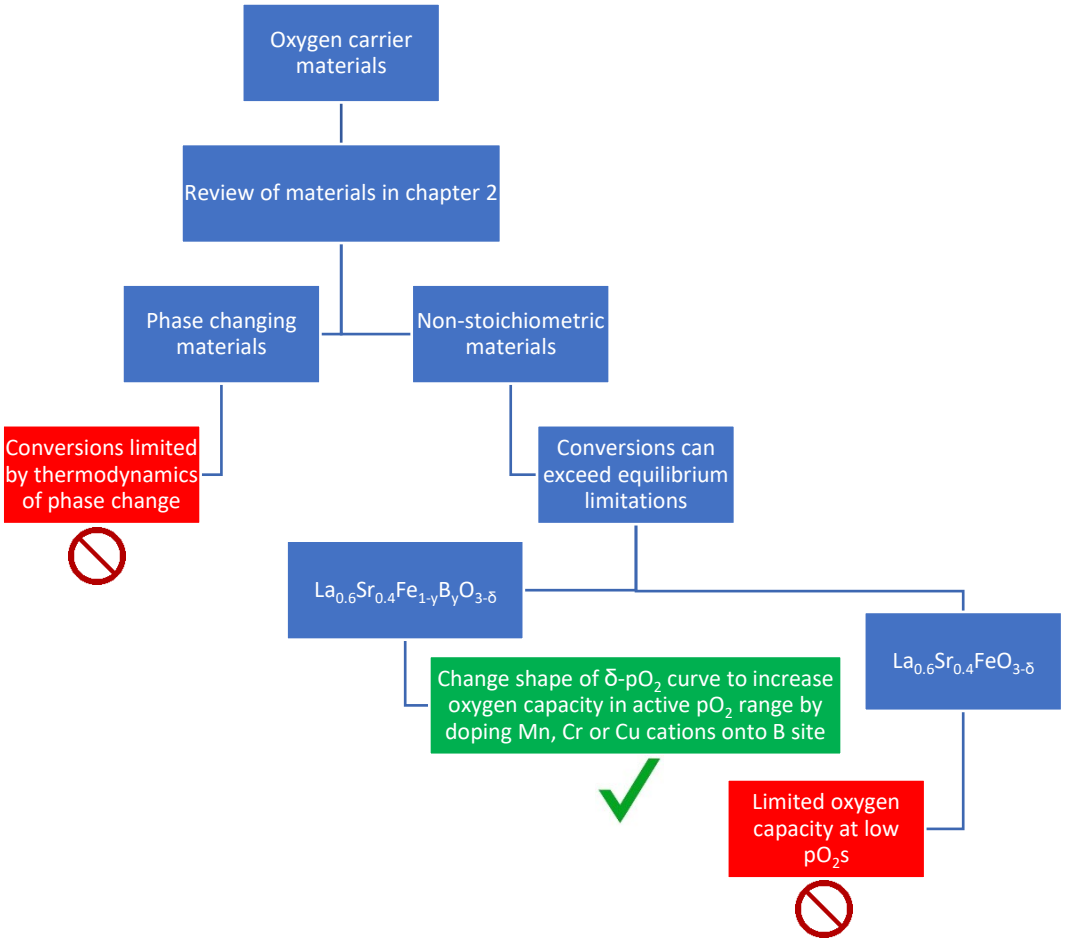

Figure 4.1: Methodology for selecting OCMs for screening, summarising thesis so far.

Information is also provided on the operation of a packed bed integral reactor with which CLWGS experiments were carried out on selected OCMs, as well as the use of in-situ x-ray diffraction carried out at the ID22 facility at the ESRF to probe the internals of a CLWGS reactor with a $La_{1-x}Sr_xFe_{1-y}Mn_yO_{3-\delta}$ type material.

This chapter also provides information on the use of iodometric titrations and XANES analysis to determine the valance state of Fe and Mn cations on the B-site of $La_{1-x}Sr_xFe_{1-y}Mn_yO_{3-\delta}$ type materials.

4.1 Synthesis of materials

4.1.1 Perovskite oxide materials

The perovskite powders for this study were synthesised via the sol-gel Pechini process (Triyono et al, 2018). Depending on the material being synthesised, the correct mass of lanthanum (III) nitrate hexahydrate ($La(NO_3)_3 \cdot 6H_2O$), strontium nitrate ($Sr(NO_3)_2$) and either manganese (III) nitrate tetrahydrate ($Mn(NO_3)_3 \cdot 4H_2O$), iron(III) nitrate nonahydrate ($Fe(NO_3)_3.9H_2O$), chromium (III) nitrate nonahydrate ($Cr(NO_3)_3 \cdot 9H_2O$), citric acid and ethylene glycol were mixed and dissolved in deionised water in the molar ratios required to produce 20 g of perovskite shown in table 4.1. The citric acid was added to the solution in a molar ratio of 1:1 between the citric acid and the metal ions. After the citric acid was fully dissolved, ethylene glycol was added into the solution at a molar ratio 1:1.2 between the citric acid and the ethylene glycol. The mixture was left to dry for 24 hours in an oven at 348 K. Afterwards the dried material was transferred to an alumina crucible for calcination at 1473 K for 10 hours in a box furnace. The resulting powder product was sieved to 80-160 μm particle size. This size was chosen as smaller sizes can result in problems with larger pressure drops across the lab-scale reactor bed, as predicted by the Kozeny-Carman equation.

Table 4.1: Quantities of raw materials required to produce 20 g of perovskite. All raw materials were supplied by Sigma-Aldrich.

	$La_{0.6}Sr_{0.4}Fe_{0.67}Mn_{0.33}O_3$	**$La_{0.6}Sr_{0.4}Fe_{0.67}Cr_{0.33}O_3$**
$Fe(NO_3)_3{\cdot}9H_2O$ (g) (>98%)	24.7666	24.8766
$Mn(NO_3)_2.6H_2O$ (g) (>99%)	7.6163	-
$Cr(NO_3)_3{\cdot}9H_2O$ (g) (>99%)	-	12.1952
$Sr(NO_3)_2$ (g) (99%)	7.7057	7.7399
$La(NO_3)_3{\cdot}6H2O$ (g) (99.9%)	23.4366	23.5406
Citric Acid (g) (99.5%)	34.9767	35.1319
Ethylene Glycol (g) (>99.8%)	13.4516	13.5113

For the case of $La_{0.6}Sr_{0.4}Fe_{1-y}Mn_yO_{3-\delta}$, doping ratios with y = 0, 0.1, 0.33, 0.5, 0.67 and 1 were also synthesised, with quantities of relevant reagents in table 4.1 adjusted accordingly.

The phase composition of the samples were analysed by X-ray powder diffraction (XRD) (Panalytical X'Pert Pro) with a CuKα anode (40 kV, 40 mA) with angular range 15° < 2θ < 90° and step size 0.0167°. This is a technique which allows for the detection of crystalline phases. The reflection of incident x-rays off of the atoms in a crystalline solid results in the formation of secondary waves from which the constructive interference may be determined by Bragg's Law. Since the angle and intensity of the transmitted rays are unique to a specific structure, the peaks from an XRD diffractogram may be compared to a database in order to verify the crystal structure of the material.

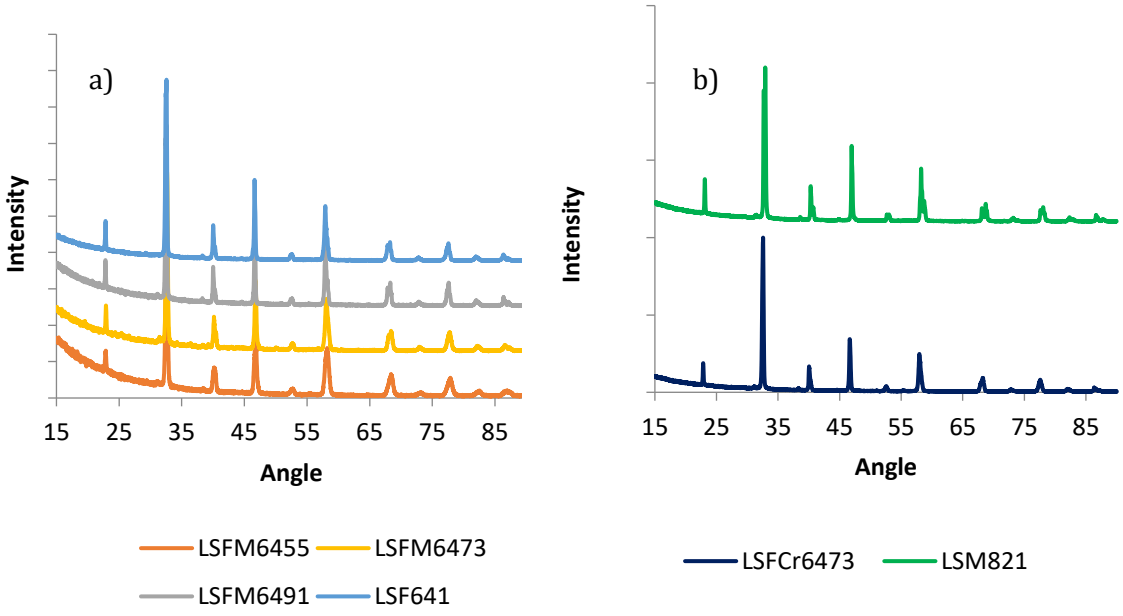

Figure 4.2: a) XRD diffractograms of $La_{0.6}Sr_{0.4}Fe_{1-y}Mn_yO_{3-\delta}$ type materials synthesised in this work at room temperature in air for values of y = 0, 0.1, 0.33, 0.5. Showing patterns for the fully oxidised as-synthesised material. b) XRD diffractograms for $La_{0.6}Sr_{0.4}Fe_{0.67}Cr_{0.33}O_{3-\delta}$ and $La_{0.8}Sr_{0.2}MnO_{3-\delta}$ materials synthesised in this work. Showing patterns for the fully oxidised as-synthesised material.

Scans were taken of the perovskite oxide materials in the fully oxidised as-synthesised state at room temperature in air shown in Fig. 4.2, in order to confirm if they were as single-phase. Unfortunately $La_{0.6}Sr_{0.4}Fe_{1-y}Mn_yO_{3-\delta}$ samples with y = 0.67 and y = 1 could not be synthesised as a single phase perovskite and therefore were omitted from further investigation. For samples with only Mn doping on the B-site, LSM821 was used as this material could be synthesised as single phase.

A Rietveld refinement for LSFM6473 from synchrotron data was carried out detailed in chapter 6, and the values of the cell parameters a_{hex} and c_{hex} were determined to be 5.52 Å and 13.43 Å respectively.

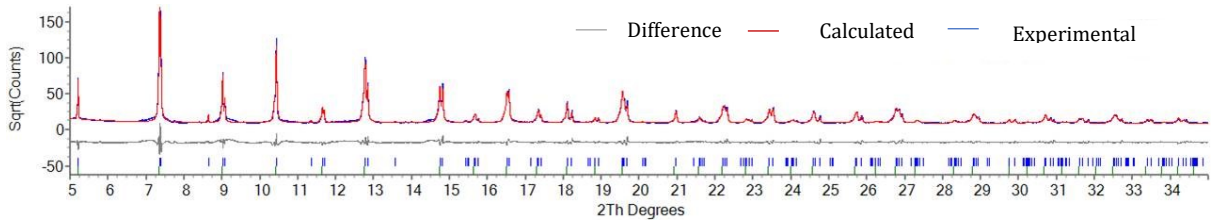

Figure 4.3: Rietveld refinement carried out for the as-synthesised fresh LSFM6473 sample from synchrotron data. The difference in between the expected peak shapes and the X-ray diffraction scan is shown. The values of the cell parameters a_{hex} and c_{hex} were found to be 5.52 Å and 13.43 Å respectively.

4.1.2 Ceria-zirconia oxide materials

The ceria-zirconia oxide powders for this study were also synthesised by the sol-gel Pechini method and followed the similar procedure as shown by Kaspar et al (2003). Stoichiometric amounts of $Ce(NO_3)_3{\cdot}6H_2O$ and $Zr(NO_3)_3{\cdot}xH2O$ (x~6) were dissolved in deionised water, followed by the addition of citric acid and ethylene glycol in the same ratios as described in section 4.1.1. The mixture was left to dry at 348 K for 24 hours before being transferred to an alumina crucible for calcination at 973 K and 1123 K respectively for $Ce_{0.5}Zr_{0.5}O_{2-\delta}$ and $Ce_{0.8}Zr_{0.2}O_{2-\delta}$ for 10 hours. The lower calcination temperature was chosen for $Ce_{0.5}Zr_{0.5}O_{2-\delta}$ as higher temperatures are known to result in the formation of secondary phases for materials with increased Zr doping (2007). The resulting powder was sieved to particle size of 80-160 µm.

Table 4.2: Quantities of raw material required to produce 20 g of ceria-zirconia oxide. All raw materials were supplied by Sigma-Aldrich.

	$Ce_{0.5}Zr_{0.5}O_2$	$Ce_{0.8}Zr_{0.2}O_2$
$Ce(NO_3)_3{\cdot}6H2O$ (g) (>99%)	29.7020	43.2294
$Zr(NO_3)_3{\cdot}xH2O$ (g) (>99%)	15.8169	5.7551
Citric Acid (g) (99.5%)	26.2834	23.9086
Ethylene Glycol (g) (>99.8%)	10.1083	9.1949

Like with the perovskite materials, the phase composition of the ceria-zirconia oxide samples in the fully oxidised as-synthesised state were analysed by XRD (Fig. 4.4), in order to confirm if they were single-phase.

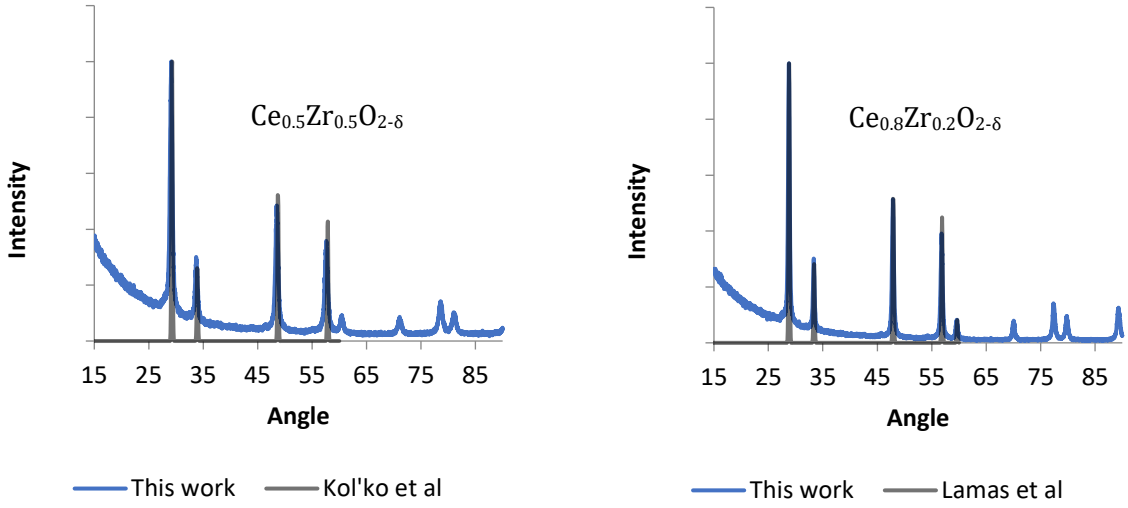

Figure 4.4: XRD diffractograms for $Ce_{0.5}Zr_{0.5}O_{2-\delta}$ and $Ce_{0.8}Zr_{0.2}O_{2-\delta}$. Showing patterns for the fully oxidised as-synthesised material. Data from this work is compared with diffraction data from Kol'ko et al (2007) and Lamas et al (2005) for $Ce_{0.5}Zr_{0.5}O_{2-\delta}$ and $Ce_{0.8}Zr_{0.2}O_{2-\delta}$ respectively.

The peaks of the powders are fairly broad which indicates the presence of a small crystallite size and is in agreement with that which is expected from the sol-gel Pechini method (Quinelato et al, 2000). The synthesised ceria-zirconia oxides are confirmed to be structurally identical to that when compared to the XRD diffractograms from Kol'ko et al (2007) and Lamas et al (2005) for $Ce_{0.5}Zr_{0.5}O_{2-\delta}$ and $Ce_{0.8}Zr_{0.2}O_{2-\delta}$ respectively. Both materials appear to be single phase cubic/ Fm-3 m.

4.2 Packed bed integral reactor

4.2.1 System operation

The packed-bed integral reactor set-up (IGI systems) consisted of flow system, reactor furnace, reactor bed, permeation oven and a gas analyser (QGA single-quadrupole soft-ionization mass spectrometer supplied by Hiden Analytical). The furnace (IGI systems) was oriented vertically and operated at a set-point of 1093 K. The relevant part of the flow system consisted of 7 computer-controlled mass flow controllers (Brooks Instrument, SLA5850) for the gasses inputted to the system and 5 valves as depicted in the diagram in Fig. 4.5 with all the flows set to 50 ml/min at standard temperature and pressure. The direction of flow was controlled by switching the positions of the valves from A to B.

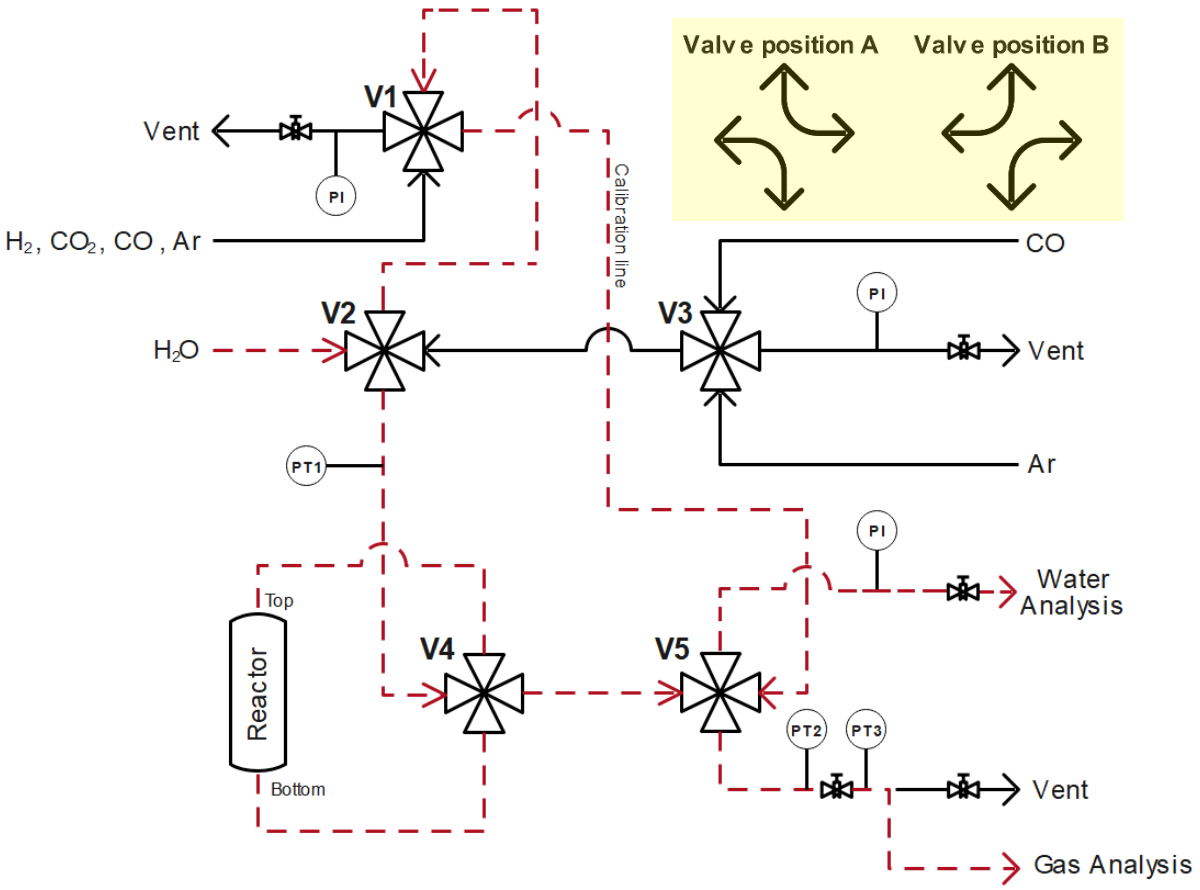

Figure 4.5: General flow system outline, arrows indicate flow directions for the two different valve positions, A and B. The broken red lines represent lines where heated lines are wrapped. Locations of pressure indicators (PI), pressure transducers (PT1-PT3) and valves (V1-V5) are shown. When flowing reactor outlet gases to the mass spectrometer for analysis, valve V5 is always kept in position A. Valve V5 is switched to position B during calibration stages, where it is not desired to analyse the reactor outlet.

During cycling, water vapour was generated by flowing argon to a permeation oven (set at 392 K). A chilled mirror hygrometer (Alpha Moisture System) was used to measure the dew-point of the water vapour stream, with an uncertainty of ± 0.2 K, and confirm it was at 306.1 K, which corresponds to 5% water vapour concentration. Water vapour was flown to the hygrometer by setting valves V1, V2 and V5 to positions A, B and A respectively. To avoid condensation, the lines where water vapour was flown were wrapped with heated lines (shown by the broken red lines in Fig. 4.5) and set to 333 K controlled with a temperature control box, and the QGA also had a heated silica capillary inlet line in order to ensure accurate readings and prevent blockages or damage to the internals from condensation. This was important as condensation can lead to unstable

water vapour measurements from the mass spectrometer and incorrect recording of the reactor conversions.

5± 0.25 vol. % compositions of components (H_2, CO, CO_2) and 5%± 0.06 vol. % H_2O were used, and 99.999 vol. % zero grade argon was used for purging the reactor and mass spectrometer (the H_2, CO, CO_2 gases were supplied by BOC). For some additional experiments looking at the behaviour of OCMs with the use of different oxidising and reducing agents, the CO feed to the reactor was replaced with a 5%± 0.25 vol. % CH_4 in Ar feed, while in another case the water vapour feed to the reactor was replaced with 5%± 0.25 vol. % CO_2 in Ar feed.

Each CLWGS cycle during the experiment involved the six steps outlined below and shown in Fig. 4.6.

1) Argon was flown to purge the reactor for 2 minutes, entering from the top of the reactor. V2, V3 and V4 were set to positions B, A and B respectively.
2) Water vapour was delivered to the reactor for 1-5 minutes depending on the experiment, entering from the top of the reactor. V2 and V4 were set to positions A and B respectively.
3) Step 1 was repeated
4) Flow direction was switched to flow argon from the opposite end of the reactor bed for 2 minutes. This was done by switching V4 to position A.
5) CO was delivered to the reactor for 1-5 minutes depending on the experiment. V2, V3 and V4 were set to positions B, B and A respectively.
6) Step 4 was repeated

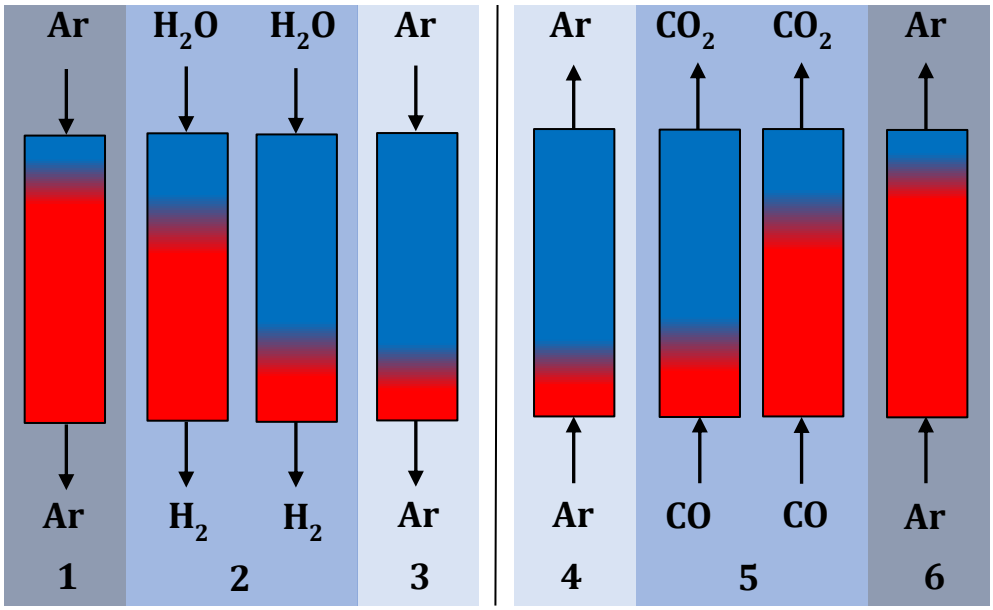

Figure 4.6: Visual representation of the six CLWGS cycle steps used in the experiments. Using oxidising and reducing streams of 5 vol. % H_2O in Ar balance and 5 vol. % CO in Ar balance. Direction of flow is switched depending on which half cycle is being carried out. Refer to the six points above the figure for descriptions of the system valve configurations for each stage.

In addition, after every 15 cycles calibration gases (for CO, CO_2, H_2O and H_2) were flown through to the gas analyser via valve V5. One gas was flown for 30 minutes after every 15 cycles, meaning that all the calibration gases were flown after every 60 cycles. During calibration, the reactor is kept at temperature and purged with argon.

The mass flow controllers (one MFC for each of the 7 potential inlet gasses) were connected to a computer system that enabled direct programmable control of the flowrate setpoint on different system lines to the reactor and/or to the gas analysis system via a user interface. In order to prevent leaks that could occur through the MFC (when the line from the gas cylinder to the MFC was still pressurised) a solenoid valve was attached to the outlet of each MFC that would automatically close when the MFC flowrate setpoint was set to zero. For safety purposes, the solenoid valves were also designed to close in the event of an interlock shutdown or when a relay module became disconnected for > 5 minutes.

One of the biggest difficulties of using a packed bed reactor is the prevention of pressure imbalances across the system between the gas inlets and the reactor. In order to equalise the pressure along each line, needle valves were incorporated to critical parts

of the system near the end of gas venting lines and before the gas analyser. Three pressure transducers (Omega, PG309-100GV) shown in Fig. 4.5 as PT1, PT2 and PT3 were also incorporated into the system to determine the pressure drop across the reactor bed and calculate the molar flowrate ratios. An oxygen balance was carried out between half cycles according to Eq. 4.1 by applying Eq. 4.4.

$$n_{rat} = \left(\frac{P2_{ox}^2 - P3_{ox}^2}{P2_{red}^2 - P3_{red}^2}\right)^{0.5} \qquad \text{Eq. 4.1}$$

where n_{rat} is the ratio of the molar flowrates for oxidation and reduction half cycles, *P2* and *P3* are the pressure measurements recorded by PT2 and PT3 on either side of the needle valve as shown in Fig. 4.5, and the subscripts *ox* and *red* indicate measurements taken during either oxidation or reduction half cycles respectively.

The presence of leaks can result in gasses not being flown to the gas analyser, or in extreme circumstances the introduction of air into the system which could then oxidise the OCM and render the experiment unreliable resulting in an incorrect oxygen balance. Leaks during the flowing of carbon monoxide, which is a highly toxic gas, also presented a safety issue. In order to ensure that the measurements from the gas analysis were accurate, checks were carried out prior to each experiment to minimise the leak rate for the system. This involved flowing argon to pressurise each line in the system individually to 2 bara before stopping flow and isolating the line using manual shut-off valves. A pressure drop rate of <0.1 bar/hour in the currently tested line was taken as the acceptable standard as this was the limit of detection afforded by the pressure indicators. Larger more obvious leaks could be easily detected using Snoop Liquid Leak Detector fluid (Swagelok). The QGA could also be used to detect the presence of a leak based on the cracking pattern of ambient air, see section 4.2.2 regarding gas analysis.

The reactor beds were prepared by loading a measured amount of the desired OCM into a quartz tube with internal diameter 4 mm and wall thickness 2 mm. Quartz wool plugs were then used to hold the material in place at both ends and glass rods were inserted on either side to prevent it from shifting during cycling. Two elbow pieces were glued to the top and bottom ends of the quartz tube using commercial high-temperature resistant adhesive to connect to the flow system.

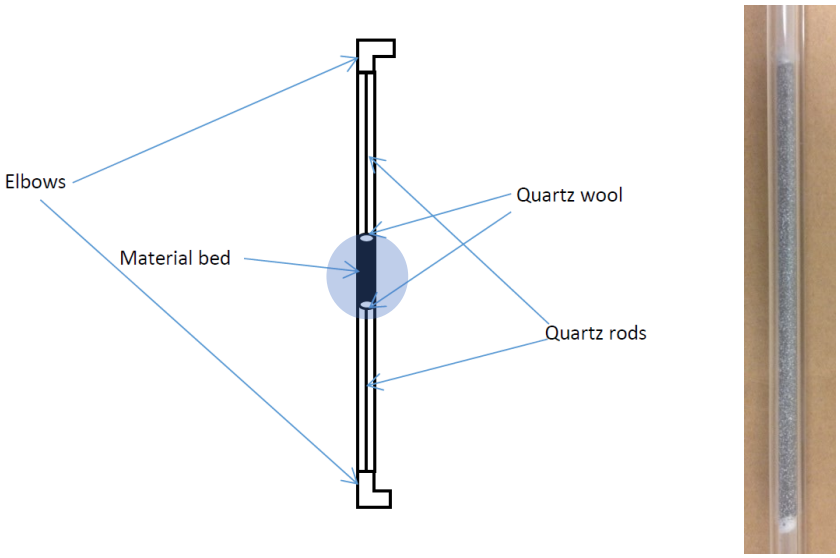

Figure 4.7: (Left) Labelled diagram showing a completed reactor bed. (Right) Close-up photograph of the material bed section of the reactor, highlighted by the blue circle in the left diagram.

4.2.2 Gas analysis

Data collection for gas analysis was carried out by use of the QGA. This system used a twin oxide coated iridium filament as this enabled residual gas analysis to be carried out at lower temperatures (~1900 K) than with other available filaments such as tungsten or rhenium which require temperatures of ~2400 K and ~2300 K respectively (Hiden Analytical, 2016). The reaction of tungsten filament with oxygen can also produce carbon dioxide and carbon monoxide by-products which is undesirable since this work requires these gasses to be carefully monitored. The use of lanthanum hexaboride filaments on the other hand require operating temperatures of ~1300 K and according to the manufacturer are too brittle and not robust enough for the purposes of residual gas analysis; the decreased lifetime would be undesirable (Hiden Analytical, 2016).

The QGA mass spectrometer allows for detection down to 5×10^{-14} Torr/ppb levels with an inlet flowrate of 20ml/min at standard temperature and pressure and acquisition rate of 8 measurements per second. Any additional gas was sent towards a vent via a tee-piece to avoid damaging the filaments. In Fig. 4.8 during operation, analysis gas first enters the machine through the capillary line by the operation of the bypass scroll pump. The gas exits the capillary at low pressure and with a high velocity, before passing through an orifice which results in a further reduction in pressure to ~ 3 mbar. The gas is then passed through into an ultrahigh vacuum (UHV) mass spectrometer chamber from which it is evacuated via a turbomolecular drag pump operating at 60 L/s (Edwards Vacuum).

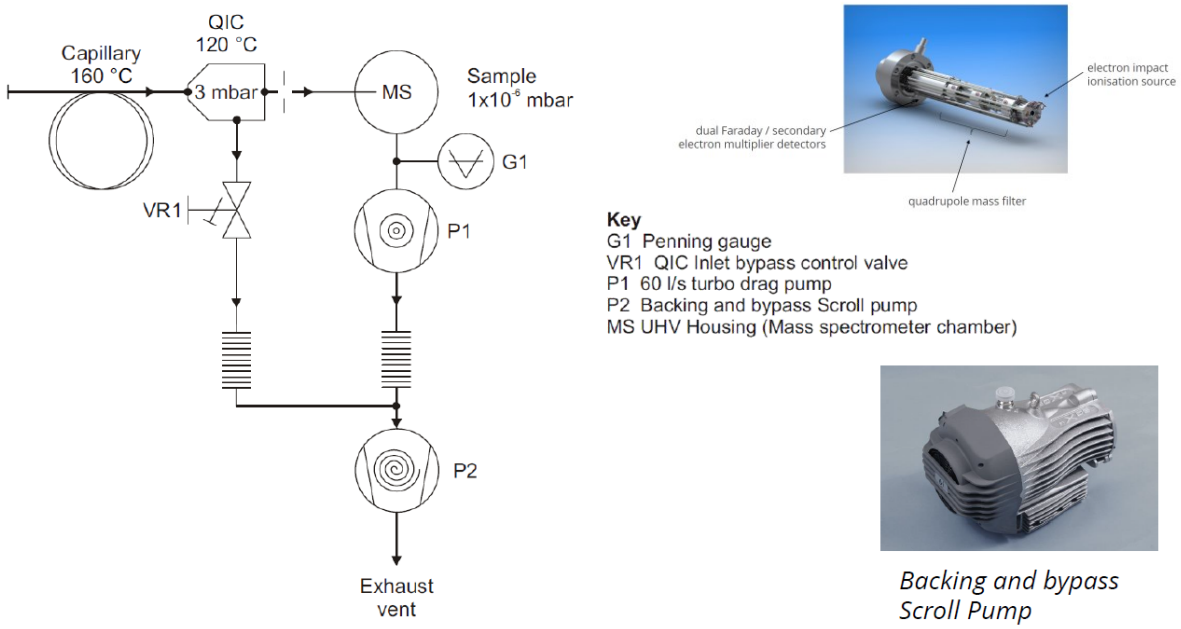

Figure 4.8: Schematic of the QGA vacuum system from the manufacturer (Hiden Analytical, 2016).

The mass filter (which in this case is an electron-impact ion source mounted onto a Quadrupole) consists of 2 pairs of parallel, equidistant metal rods (circular or hyperbolic) and is housed inside the UHV chamber, allowing for neutral particles from the sampling line to be ionised. The two pairs of metal rods must have equal but opposite potentials (one pair is positively charged while the other is negatively charged). Ions entering the quadrupole field undergo deflection due to differences in potential, and the extent of this deflection is related to the mass-to-charge ratio of the specie. An internal over pressure detector allows for system protection and can react to

any unexpected rise in pressure, while the Penning Gauge acts as an external pressure sensor in case the filament is switched on under high pressure conditions (Tyrer-Tomkinson, MASsoft Professional Version 7 Training Manual).

The choice of detector for this system was a Secondary Electron Multiplier (SEM), which produces an ion current that is measured by a sensitive amplifier and allows for the high acquisition rate for these experiments. A positive voltage is applied to the electrons that results in an increase in the sensitivity and lowers the partial pressure that can be measured. The maximum pressure of SEM systems are typically limited to 10^{-5} to 10^{-6} Torr in order to avoid dynode pyrolysis from water vapour. While parameters such as dwell time and settle time can be modified to increase the acquisition rate, a degree of care is also required as this can result in a decrease in the signal to noise ratio and hence effect the accuracy of the data.

Cracking patterns may arise during ionisation when high energy electrons also result in fragmentation of the molecular ions. Cracking patterns are a function of the electron energy and therefore may be characteristic of a species under standard conditions. The example in Fig. 4.9 shows the cracking pattern taken from the gas analyser during the sampling of ambient air with the heating function of the inlet capillary line enabled. Ar was used as the balance gas for each gas mixture in this work in order to avoid confusing mass 28 for N_2 or CO.

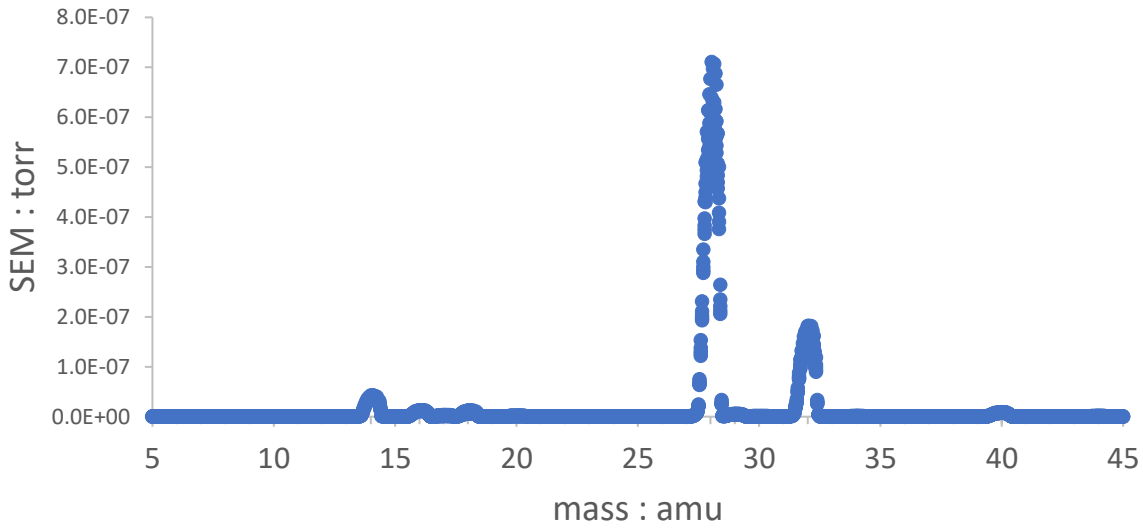

Figure 4.9: Cracking pattern taken from gas analyser during sampling of ambient air and with heating on capillary line enabled. The peak at mass 28 corresponds to CO or N_2, while the peaks at mass 18 and 32 correspond to the species H_2O and O_2. A 4:1 ratio of the peaks at mass 28 to mass 32 indicates the presence of a leak.

In Fig. 4.9, the major peak at mass 28 corresponds to CO or N_2, while the other peaks such as those at mass 18 and 32 correspond to the other species H_2O and O_2. The ratio of the peaks at mass 28 and mass 32 can be used as an indicator of the presence of a leak if this ratio is 4:1 and no other gas with this ratio is currently flowing. In some cases, such as when there is a blockage in the flow system, the flowrate can drop to below the draw rate for the gas analyser thereby resulting in air being pulled into the system from the vent line and causing a false positive leak detection.

During experiments, calibration gases (for CO, CO_2, H_2O and H_2) were periodically flown to the gas analyser sequentially after every 15 cycles. These calibrations were important in order to account for the drift in mole fractions over time due to the differing sensitivity of each gas with the filament. Prior to the start of cycling, calibrations were also performed with all calibration gases, as well as with only pure Ar flown as a zero gas. This was done to determine the calibration factors at regular periods, the splitting factors for CO_2 contribution to the CO signal and H_2O contribution to H_2 signal, and background current. The true current was determined by subtracting the data for when only pure Ar was fed. The splitting factors for CO_2 contribution to the CO signal and H_2O

contribution to H_2 signal were determined for each experiment (typical values around 0.11 and 0.01 respectively) and applied as in the following equations:

$$I_{CO} = I_{COCO_2} - SF_{COCO_2} I_{CO_2} \qquad \text{Eq. 4.2}$$

$$I_{H_2} = I_{H_2H_2O} - SF_{H_2H_2O} I_{H_2O} \qquad \text{Eq. 4.3}$$

where I_{CO} and I_{H_2} are the corrected currents for CO and H_2, I_{COCO_2} and $I_{H_2H_2O}$ are the currents for mass 28 including splitting of CO_2 molecules and mass 2 including splitting of H_2O molecules, SF_{COCO_2} and $SF_{H_2H_2O}$ are the splitting factors for each case, and I_{CO_2} and I_{H_2O} are the currents for mass 44 and mass 18 respectively.

By using the calibration factors taken at various times throughout an experiment a linear plot could be derived and applied to each measurement. Mole fractions for all 5 species (CO, CO_2, H_2O, H_2, Ar) were determined by dividing the ratio of the current of that specie to its calibration factor with the sum of ratios for each current of each specie with their corresponding calibration factors as shown in Eq. 4.4.

$$y_n = \frac{\frac{I_n}{CF_n}}{\sum_{n=1}^{n} \frac{I_n}{CF_n}} \qquad \text{Eq. 4.4}$$

Where y_n is the mole fraction of component n, I_n is the corrected current for component n, and CF_n is the calibration factor for component n.

The molar flowrate could then be determined via Eq. 4.5.

$$\dot{N} = \frac{y_n F}{60 \times 22400} \qquad \text{Eq. 4.5}$$

where $\dot{N}$ is the molar flow rate (mol/s), y_n is the mole fraction of component n, and F is the volumetric flowrate (ml/min) at 298 K and 1 bar. According to the ideal gas law, the molar volume of a gas at standard temperature and pressure is 22.4 L/mol.

By integrating over full cycles the time-averaged conversions for CO and H_2O were then calculated as follows:

$$\overline{x}_{CO} = \frac{\int_{cycle} (y_{CO_2})_{outlet} \dot{N}\, dt}{\int_{cycle} (y_{CO})_{outlet} \dot{N}\, dt + \int_{cycle} (y_{CO_2})_{outlet} \dot{N}\, dt} \qquad \text{Eq. 4.6}$$

$$\overline{x}_{H_2O} = \frac{\int_{cycle} (y_{H_2})_{outlet} \dot{N}\, dt}{\int_{cycle} (y_{H_2O})_{outlet} \dot{N}\, dt + \int_{cycle} (y_{H_2})_{outlet} \dot{N}\, dt} \qquad \text{Eq. 4.7}$$

4.3 In-situ X-ray diffraction

The advantage of being able to carry out in-situ XRD analysis (instead of ex-situ as detailed in section 4.1) is that it allows for the changes in crystal structure of the material to be determined at the conditions of the reaction rather than ambient conditions. This can allow for an understanding of the relevant kinetics to be determined as well as seeing changes in structure as functions of position in the bed and time. The most challenging aspect of this analysis is the appropriate and practical design of a system with the appropriate geometry to maintain such reaction conditions and allow for incident x-rays to access the bed.

For this purpose, a vertically oriented reactor furnace (IGI systems) with an isothermal zone of 20 cm at 1273 K was used with the same reactor system as that explained in section 4.2. Thin slits on the front and back of the furnace enabled incident x-rays to access the reactor bed, and the furnace which was held up by a motor crane could be raised and lowered in order to scan different points along the bed. Fig. 4.10 shows a photograph of the system in ID22.

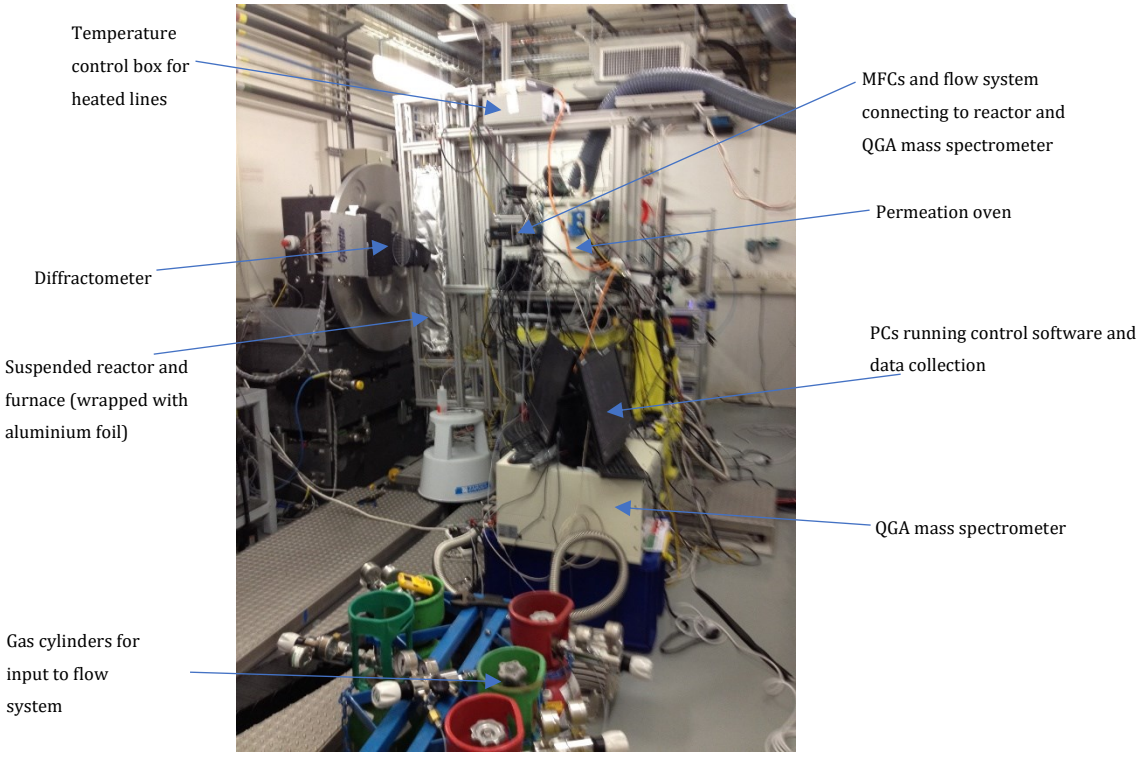

Figure 4.10: Photograph of packed bed integral reactor system set-up inside the hutch at ID22. The rotational stage holding the detectors and filtering crystals can be seen next to the suspended reactor furnace. The furnace was covered in a thin aluminium foil layer in order to reduce heat losses due to radiation, of which the power of the synchrotron generated radiation was sufficient to pass through and no contribution to the diffraction pattern could be detected.

The in-situ XRD experiments were carried out at the European Synchrotron Radiation Facility at the testing bay ID22 on the material LSFM6473. This facility has an 844 m circumference electron particle accelerator that functions at an energy of 6 GeV, and the x-rays produced at the ID22 in-vacuum undulator source have energies ranging from 6 to 80 keV. This allows for operation at high energies to overcome the large sample size (4mm diameter) and get close to the La K edge of 39 keV to minimise absorption. The high fluxes of x-rays also make it possible to accurately determine the peak structure at a rapid rate during redox cycling. The precision of the analytical crystals on the ID22 detector gives the sharp peaks that make it possible to resolve the small lattice parameter changes associated with small variations in the degree of non-stoichiometry when the OCM is not going through a phase change.

The diffractometer used for the experiment consisted of 9 Si (111) crystals and 9 $LaBr_3$ scintillator detectors mounted onto a rotating stage capable of recording peaks in the range of 0-25° (see Fig. 4.11). A fan geometry allowed for a large quantity of angles to be recorded while corresponding to minimal movements of the stage, shown in Fig. 4.11c. For ex-situ measurements a sample (capillary) is positioned onto the diffractometer axis in Fig. 4.11a, and the beam follows the green route. The red routes correspond to the corrected 2θ angles from the analyser crystal.. During operation the bank of 9 detectors is scanned vertically in order to measure the diffracted intensity in terms of 2θ, and the instrumental contribution to FWHM of the diffraction peaks is ~0.003° 2 theta (with a Si (111) reflection at 31 keV) shown in Fig. 4.11b.

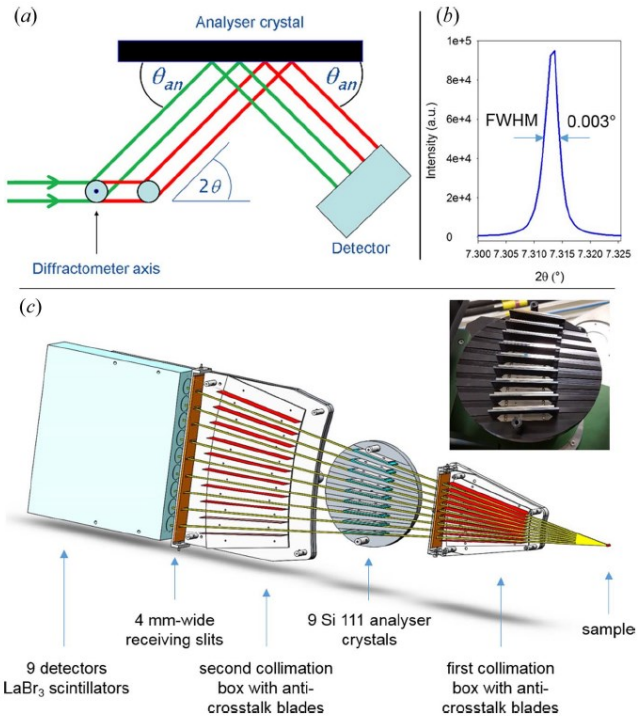

Figure 4.11: Schematics of the diffractometer at ID22 taken from Dejoi et al (2018). The diffractometer used for the experiment consisted of 9 Si (111) crystals and 9 $LaBr_3$ scintillator detectors mounted onto a rotating stage capable of recording peaks in the range of 0-25°. A fan geometry allowed for a large quantity of angles to be recorded while corresponding to minimal movements of the stage, shown in Fig. 4.11c. For ex-situ measurements a sample (capillary) is positioned onto the diffractometer axis in Fig. 4.11a, and the beam follows the green route. The red routes correspond to the corrected 2 theta angles from the analyser crystal. During operation the bank of 9 detectors is scanned vertically in order to measure the diffracted intensity in terms of 2ϑ, and the instrumental contribution to FWHM of the diffraction peaks is ~0.003° 2ϑ (with a Si (111) reflection at 31 keV) shown in Fig. 4.11b. The inset photograph in Fig. 4.11c shows the nine Si (111) analyser crystals.

The beamline was calibrated for 35 keV operation with a spot size of approximately 1 mm × 1 mm. For cycling experiments the optimal scan range of 2.2 degrees was determined and scan speed determined to use was 10 degrees/minute in two theta. A reactor bed with an inner diameter of 4 mm was used of bed length 10 cm and LSFM6473 sample mass 2.2 g (0.01 mols). In order to quantify the temperature changes occurring during the chemical reactions in situ, Y_2O_3 was also added to the OCM bed in a ratio of 1:5 by mass. The diffraction peaks of Y_2O_3 do not overlap with LSFM6473 and is inert at reaction conditions (Swamy et al, 1999). The expansivity of Y_2O_3 can be used to determine the sample temperature and is described in more detail in chapter 6.

Data was analysed via Rietveld refinement using least squares between theoretical and measured diffraction patterns on TOPAS software (Coelho, 2020). This allowed for a theoretical pattern to be built by varying the lattice cell parameter and stresses to minimise the least squares difference from the recorded pattern. A measurement of error is also given which allows to see the presence of other phases.

4.4 Thermogravimetric analysis

4.4.1 Equipment

A thermogravimetric analysis (TGA) unit (Rubotherm GmbH) was used to carry out investigations into the oxygen content of OCMs at different pO_2 values. These pO_2 values were generated by using a variety of buffer gases of CO_2/CO (supplied by Air Products). Fig. 4.12 shows the CO_2/CO buffer gas ratios that are required to generate a range of log pO_2s at the temperatures of 993 K, 1043 K, 1093 K, 1143 K and 1193 K. To generate additional pO_2 data points the buffer gases 1:5 CO_2/CO and 20:1 CO_2/CO were blended using different flowrates.

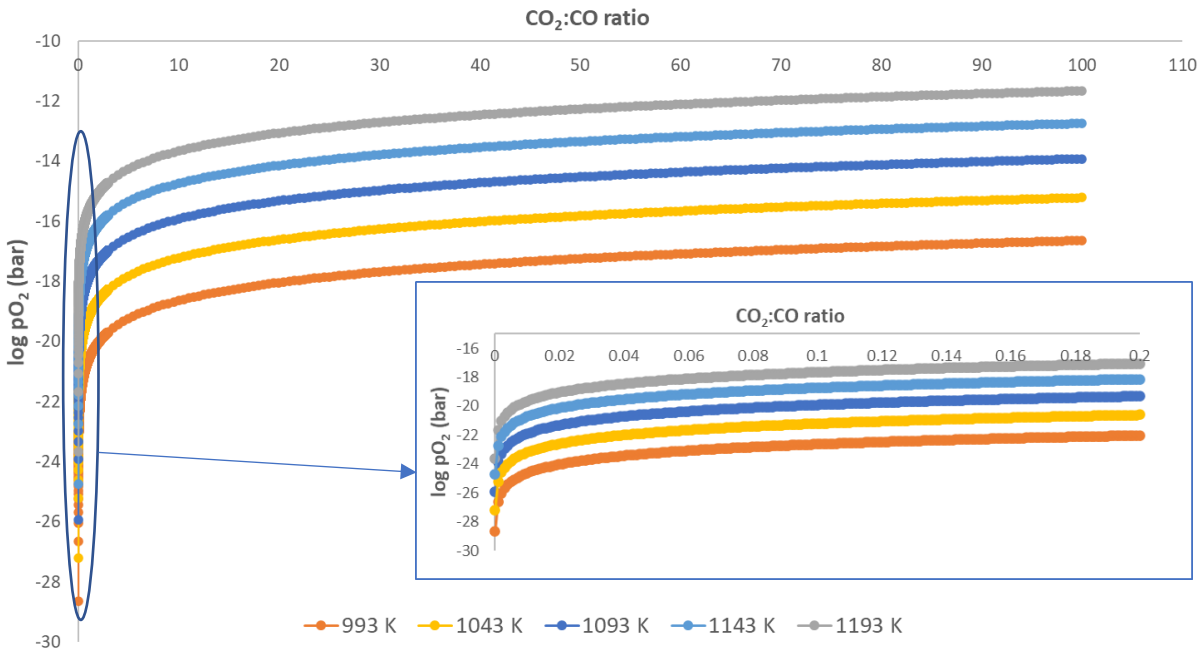

Figure 4.12: CO_2/CO ratios and corresponding log pO_2 values for temperatures of 993 – 1193 K. In practise it becomes harder to achieve CO_2/CO ratios higher than 100 at the measurement temperatures.

In practise it is difficult to accurately achieve CO_2/CO ratios of > 100, however for the purpose of this study the range of pO2s of interest are < 10^{-15} bar, making the TGA method sufficient. 0.1% O_2 in Ar and 5% O_2 in Ar gas compositions were used to generate datapoints for log pO_2s at -2.989 bar and -0.699 bar.

The TGA apparatus consisted of a balance with a sensitivity of 0.1 µg and furnace operated via a computer program. The balance was isolated from the effects of heat, and the sample crucible was attached to the end of a hang-down wire at a reproducible position.

For the TGA analysis the effect of the gas buoyancy on the sample weight was very small in comparison with the changes associated with the variation in sample oxygen content, however this was nonetheless accounted for in the analysis based on blank measurements with an empty alumina crucible carried out before the actual experiment. The alumina crucible used was suspended from the magnetic balance with a platinum hook, which is reliable for temperatures for up to 1293 K (Ebnesajjad, 2011).

The following equation was used to determine the oxygen non-stoichiometry change ($\Delta\delta$) of the reduced sample from the fresh sample based on the mass change observed on the TGA:

$$\Delta\delta = \frac{molecular\ mass\ of\ sample \times change\ in\ mass\ of\ sample}{molar\ mass\ of\ oxygen \times sample\ mass\ at\ reference\ pO_2} \qquad \text{Eq. 4.8}$$

4.4.2 Preliminary experiments to screen oxygen capacity in OCMs for integral reactor experiments

Preliminary experiments were carried out to determine the change in oxygen content of selected OCMs from chapter 3 in the pO_2 range of roughly between 10^{-15} bar and 10^{-21} bar. By cycling selected materials between oxidising and reducing buffer gases in the range of thermodynamically active pO_2s it is possible to estimate the usable oxygen capacity for the material. The usable oxygen capacity is a more accurate indication of the true oxygen capacity of the material as any capacity outside of the active pO_2 region will not serve to increase conversions. The materials which show greater changes in oxygen content in this region should specifically perform better in the CLWGS process with the possibility for longer feed durations before having to switch half cycles.

For the preliminary experiments, about 0.0009 mols of sample for each OCM was heated to 1093 K under 20% O_2 in Ar prior to the start of cycling. Each buffer gas (1:20 CO_2 to CO and 20:1 CO_2 to CO, both in Ar balance) was flown for 2 hours at a flowrate of 8.8 x 10^{-3} mol/min before switching to the oxidising or reducing gas to ensure that a stable equilibrium between the solid and the gas was reached. At the temperature of operation (1093 K) the log pO_2s of the buffer gasses 1:20 and 20: 1 CO_2 to CO correspond to -15.32 bar and -20.52 bar respectively. This process was repeated for 10 redox cycles. The change in oxygen content for each OCM recorded by the TGA between the pO_2s for the buffer gases was calculated via Eq. 4.8 and is shown plotted per cycle in Fig. 4.13.

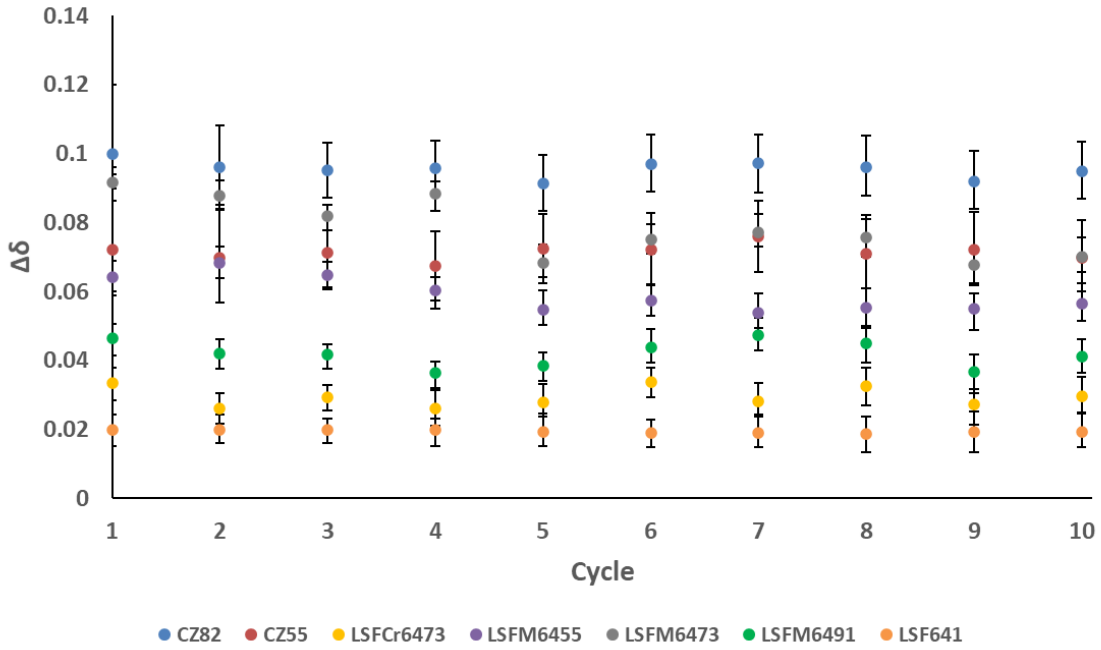

Figure 4.13: Change in δ value per redox cycle for selected OCMs from preliminary TGA investigation.

The large errors in the data in Fig. 4.13 is due to the experiment being limited by using a small amount of sample in each case, as well as the propagation of errors from the noise in the measurement of mass from the TGA between two reference pO_2s instead of from the oxygen non-stoichiometry of the fresh material (assuming δ=0). However, as a preliminary method to screen materials it provides a general picture of which OCMs would tend to have higher oxygen capacity in the pO_2 range of interest and therefore would be more interesting to analyse in more detail for the purpose of this thesis.

The oxygen content change for the OCM LSF641 is around 0.02, so it can be seen that only a fraction of the total oxygen capacity of the material is actually being used in this case. Doping 2/3 of Cr onto the B-site was found to increase the average oxygen change slightly to about 0.03. The selected Mn quantities that were doped also appear to give a further increase, with 1/10 Mn and 1/2 Mn on the B-site giving yet higher oxygen content changes. The ceria zirconia oxide material with doping ratio Ce/Zr = 0.5 is higher yet, followed by the perovskite oxide with Mn B-site doping ratio 2/3 and finally with the ceria zirconia oxide material with Ce/Zr = 0.2. The highest capacity material CZ82 has ~5 times more capacity than LSF641 in the active range of pO_2s.

The discrepancy between LSFM6473 and LSFM6455 with LSFM6473 having more oxygen content change than LSFM6455 despite having less Mn doping on the B-site, may be due to either the large errors in this experiment, or due to subtle changes to the δ-pO_2 curve resulting from the addition of Mn. This may suggest that there is an optimal doping ratio of Mn on the B-site which modifies the δ-pO_2 curve in such a way as to allow for greater oxygen exchange potential in the selected pO_2 range. Doping Cr on the other hand does not appear to have noticeably improved the oxygen exchange potential, possibility due to the lower temperature of operation at 1093 K.

The materials CZ82 and LSFM6473 which have the highest capacities from among the perovskite oxide and ceria zirconia oxide type materials respectively are the best candidates and will make good comparison with LSF641. Later on in chapter 7 these materials are tested in a working reactor carrying out the CLWGS process to produce hydrogen and to see what benefits to conversions and product quality can be gained over LSF641.

4.5 Iodometric titration

Since thermo-gravimetric analysis is only capable of giving relative values of the oxygen content, iodometric titrations were carried out to confirm the absolute value of the oxygen content of OCMs of interest in the as-synthesised form, as well as in reduced states. An illustration of this process is given in Fig. 4.14.

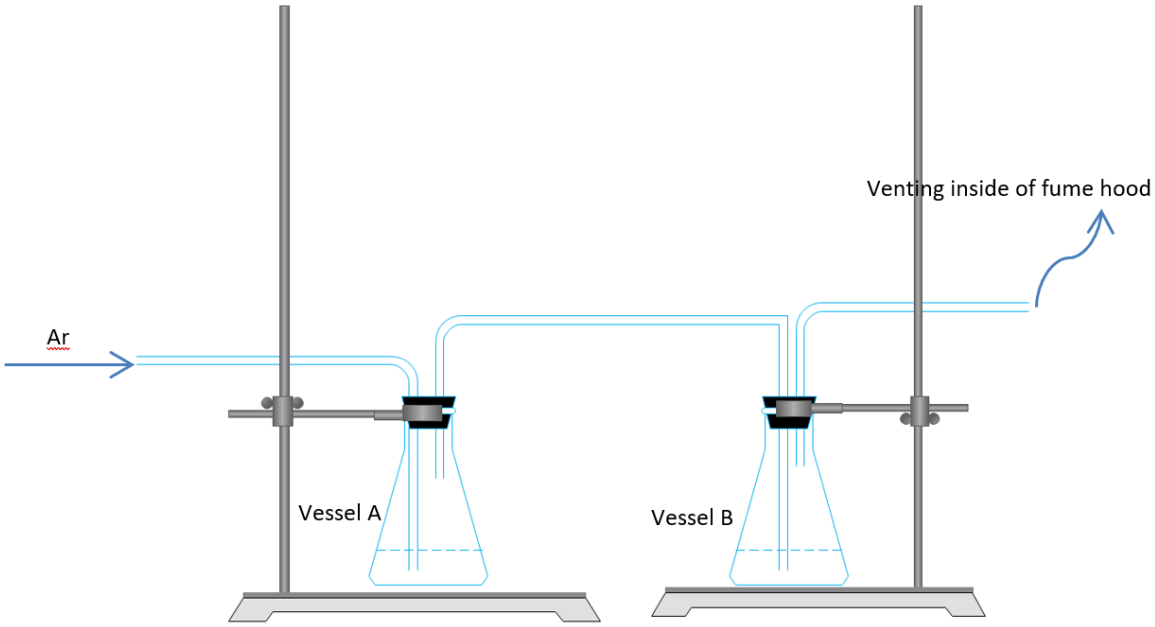

Figure 4.14: Diagram of the set-up for iodometric titration experiments, indicating how the vessels are connected under the argon blanket.

Samples of up to 60 mg were dissolved in vessel A, containing 6M HCl under a continuously flowing argon blanket and facilitated by gradual heating. The argon blanket was used to generate an inert atmosphere to prevent the reaction between KI and oxygen in the air, as well as to ensure Cl_2 was flushed into vessel B.

Once the sample in vessel A had fully dissolved an excess of KI was added to the vessel resulting in the reduction of iron cations to the 2+ state and the formation of I_2. A titration was then carried out using 0.02M sodium thiosulphate. The sodium thiosulphate was standardised using a solution of 0.02M KIO_3 with starch indicator as according to the following equation:

$$6S_2O_3^{2-} + IO_3^- + 6H^+ \rightarrow 3S_4O_6^{2-} + I^- + 3H_2O \qquad \text{Eq. 4.9}$$

While the sample was dissolving in the first vessel, the evolved chlorine gas was captured in a secondary vessel downstream (vessel B) containing KI solution which was also subsequently titrated.

The reactions with iodine are given in the following equations:

$$B^{Z+} + (Z-2)I^- \leftrightarrow B^{2+} + 0.5(Z-2)I_2 \qquad \text{Eq. 4.10}$$

$$I_2 + 2S_2O_3^{2-} \leftrightarrow 2I^- + S_4O_6^{2-} \qquad \text{Eq. 4.11}$$

In the equations, the symbol B represents the B-site ion, while Z represents the average valence state of the B-site ions. Chlorine, which is flown into the secondary vessel is reduced to the -1 state via the following reaction:

$$Cl_2 + 2I^- \leftrightarrow I_2 + 2Cl^- \qquad \text{Eq. 4.12}$$

The reaction was heated to around 353 K since the dissolution of Cl_2 in H_2O is close to zero at this temperature.

An expression for Z can be derived from the iodine reaction equations through stoichiometry:

$$\frac{n_{Na_2S_2O_3}}{Z-2} = \frac{mass_{sample}}{Mr_{sample}} \qquad \text{Eq. 4.13}$$

where $n_{Na_2S_2O_3}$ is the moles of sodium thiosulphate required to complete the titration, $mass_{sample}$ is the mass of the OCM dissolved in vessel A, and Mr_{sample} is the molecular weight of the OCM and is a function of the sample non-stoichiometry. As an example for $La_{1-x}Sr_xFe_{1-y}Mn_yO_{3-\delta}$ type materials, Mr_{sample} is given by:

$$Mr_{sample} = (1-x)Ar_{La} + xAr_{Sr} + (1-y)Ar_{Fe} + yAr_{Mn} + (3-\delta)Ar_O \qquad \text{Eq. 4.14}$$

where Ar_{La}, Ar_{Sr}, Ar_{Fe}, Ar_{Mn} and Ar_O are the atomic masses of La, Sr, Fe, Mn and O respectively.

An expression for the oxygen non-stoichiometry of $La_{1-x}Sr_xFe_{1-y}Mn_yO_{3-\delta}$ can be derived by carrying out a simple charge balance. Assuming +3 valence state for La, +2 for Sr and -2 for O we can write:

$$3(1-x) + 2x + Z(1-y) + Zy = 2(3-\delta) \qquad \text{Eq. 4.15}$$

This simplifies to:

$$\delta = \frac{3+x-Z}{2} \qquad \text{Eq. 4.16}$$

This equation for δ is also valid for $La_{1-x}Sr_xBO_{3-\delta}$ type materials with only a single cation on the B-site, since the parameter *y* cancels out.

By combining the previous equations, a single formula for the oxygen content of $La_{1-x}Sr_xFe_{1-y}Mn_yO_{3-\delta}$ type materials can be derived as a function of the moles of sodium thiosulphate used in titration and the sample mass.

$$\delta = \frac{n_{Na_2S_2O_3}((1-x)Ar_{La}+xAr_{Sr}+(1-y)Ar_{Fe}+yAr_{Mn}+3Ar_O)-mass_{Sample}(1+x)}{Ar_O n_{Na_2S_2O_3}-2mass_{Sample}} \qquad \text{Eq. 4.17}$$

4.6 XANES analysis

In order to investigate the valence state of B-site cations for perovskite oxides of the type $La_{1-x}Sr_xFe_{1-y}Mn_yO_{3-\delta}$ and understand the contributions of Fe and Mn ions towards changes in the δ-pO_2 thermodynamics, X-ray absorption near edge structure (XANES) spectroscopy was carried out at the Diamond Light Source on the B18 beamline to support observations from iodometric titrations.

XANES is underpinned by the fundamental phenomenon of an x-ray photon being absorbed by an electron in a tightly bound quantum core level. An electronic core level may participate in the absorption if the binding energy of the core level is less than the incident x-ray energy, in which case the electron is removed from its quantum level. Energy in excess of the electronic binding energy passes to a photo-electron which is ejected from the atom.

Beer's Law can be used to determine the probability that the incident x-rays can be absorbed:

$$I = I_o e^{-\mu t} \qquad \text{Eq. 4.18}$$

where *I* is the intensity of the transmitted beam, I_0 is the intensity of the incident x-ray on the sample and *t* is the thickness of the sample. Fig. 4.15 shows a visualisation of this concept:

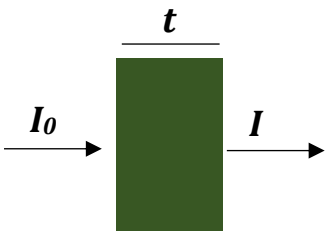

Figure 4.15: An incident monochromatic x-ray beam with an intensity of I_0 passes through a sample with specific thickness t and the resulting transmitted beam has an intensity of I. The x-ray intensity is proportional to the number of x-ray photons.

The absorption coefficient is a smooth function of energy, and depends on the sample density ρ, atomic number Z, atomic mass Ar, and x-ray energy E and is given roughly as in Eq. 4.19.

$$\mu \approx \frac{\rho Z^4}{ArE^3} \qquad \text{Eq. 4.19}$$

Either transmission or fluorescence geometries can be used for XAFS measurements. For transmission the absorption coefficient is given in Eq. 4.20, while for fluorescence the absorption coefficient is given in simplified form in Eq. 4.21.

$$\mu(E) = log\left(\frac{I_0}{I}\right) \qquad \text{Eq. 4.20}$$

$$\mu(E) \propto \frac{I_f}{I_0} \qquad \text{Eq. 4.21}$$

A fast-scanning double crystal Si (111) monochromator was used to obtain measurements at the Fe K-edge at 7.112 keV and the Mn K-edge at 6.539 keV. Fe scans were taken in transmission mode using ion chamber detectors and Mn scan were taken using fluorescence mode using a 9 element Ge solid state detector system respectively. While transmission mode can provide the best signal-to-noise ratio and is representative of the bulk, fluorescence was used for the Mn scans due to the samples being more dilute. Total electron yield count was not used as none of the K-edges were at energies of < 3 keV.

Sample masses of 6.3 mg were used for scanning of the Fe K-edge, while masses of 5.2 mg were used for scanning of the Mn K-edge. Samples were diluted with cellulose and

pressed to pellets of diameter 13 mm in order to optimise the effective edge-step. The focus at the sample was 200 × 250 μm (H × V) FWHM. The data was normalised using Athena software.

4.7 Summary

This chapter provided a description of the various equipment and analytical methods that were used to carry out the investigations in this thesis, including details on the operation of a packed-bed integral reactor for lab scale CLWGS experiments, an iodometric titration setup to determine the oxidation state of OCMs, XANES analysis and TGA analysis. From the preliminary experiments carried out from TGA analysis the OCMs with the most oxygen capacity in the pO_2 range from around pO_2 10^{-15} bar to 10^{-21} bar were identified. Of these screened materials, LSFM6473 from among the perovskite oxides and CZ82 from among the ceria zirconia oxides were selected for further analysis.

Chapter 5: Investigation of the oxygen non-stoichiometry of $La_{0.6}Sr_{0.4}Fe_{0.67}Mn_{0.33}O_{3-\delta}$

The strontium doped lanthanum ferrite LSF641 has been found not to undergo phase segregation while undergoing extensive CLWGS cycling (Metcalfe et al 2019, de Leeuwe 2019), which indicates the material to have longer lifetime during operation and potentially lower costs of material replacement in an industrial plant. In addition the fast reaction kinetics of the gas-solid reactions means the process can be controlled by the thermodynamic parameters (Mizusaki et al 1985, ten Elshof et al 1997, Teraoka et al 2006, Søgaard et al 2007) . The relationship between the solid phase oxygen non-stoichiometry and gas phase oxygen partial pressure of LSF641 has been extensively investigated by Kuhn et al (2011) who showed the occurrence of a plateau at pO_2s $\approx 10^{-15}$ bar. This plateau (discussed in chapters 2 and 3) hinders the extent to which it is possible to access the oxygen exchange capacity of the OCM with changing pO_2s of the gas phase during this plateau.

By contrast, the oxygen non-stoichiometry of the strontium doped lanthanum manganates $La_{1-x}Sr_xMnO_{3-\delta}$ investigated by Mizusaki et al (2000) found that the aforementioned plateau seen in LSF641 was not present for these materials thereby making it easier to access more of the oxygen capacity of the material. Despite this it was also found that the $La_{1-x}Sr_xMnO_{3-\delta}$ group of materials was prone to phase segregation at higher pO_2s than that of LSF641. If the material were to change to the brownmillerite phase due to decomposition during extensive cycling this would limit the lifetime of the material and increase the costs of material replacement.

Markov et al (2015) investigated the material $La_{0.5}Sr_{0.5}Fe_{0.67}Mn_{0.33}O_{3-\delta}$, a strontium doped lanthanum ferrite manganite with B site iron and manganese doping of 67% and 33%, and found that substitution of Mn onto the B-site resulted in the elimination of the plateau and an increase in ion conductivity of the material at $pO_2 > 10^{-13}$. This was explained by the tendencies of the Fe3+ and Mn3+ cations to tetrahedral and fivefold oxygen coordination respectively. A separate investigation by Luciani et al (2018) on $La_{0.6}Sr_{0.4}Fe_{1-y}Mn_yO_{3-\delta}$ type materials found that increasing the Mn content on the B-site

increased the reactivity towards steam, allowing hydrogen production at lower temperatures.

It is therefore proposed that a $La_{0.6}Sr_{0.4}Fe_{1-y}Mn_yO_{3-\delta}$ material, as a hybrid, could benefit from the well-established stability of the $La_{0.6}Sr_{0.4}FeO_{3-\delta}$ material during extensive redox cycling, and could also enable more of the oxygen capacity of the material to be available in operating conditions. A high oxygen capacity, high stability OCM is desired in order to achieve high conversions, longer cyclic feed durations and a long usable lifetime. The preliminary investigation in chapter 4 studied various doping ratios on the B-site of the perovskite, and of the ratios investigated the doping ratio of 2/3 Fe and 1/3 Mn resulted in an OCM with the largest oxygen capacity under operating range log pO_2s among the perovskite oxides investigated. This chapter aims to take a closer look at the thermodynamic properties of the material $La_{0.6}Sr_{0.4}Fe_{0.67}Mn_{0.33}O_{3-\delta}$ (LSFM6473), which was selected in chapter 4 as one of the materials with higher oxygen capacity in the pO_2 range relevant to the WGS reaction thermodynamic equilibria.

5.1 Determining non-stoichiometry of LSFM6473 via TGA

The δ-pO_2 relationship of LSFM6473 was built up by taking the values of δ at the corresponding pO_2s for each temperature with the CO_2/CO buffer gases. For each experiment about 0.5 g of 80-160 µm LSFM6473 powder was placed into an alumina crucible and suspended from the TGA magnetic balance. This was then subjected to the experiment program, where the material was first treated with a stream of 8.8×10^{-3} mol/min 20±0.025 mol% oxygen in Ar and heated at a rate of 20 K/min to the temperature of interest. After this the material was reduced with the most reducing buffer gas before oxidising with the second most reducing gas (or blend of buffer gases), working back up to 20% O_2. Each gas was held for long enough to reach equilibrium between the sample and gas atmosphere, which in this case was assumed to be when the mass change was less than 5×10^{-5} g/min. Between each buffer gas stage, Ar was flown through in order to flush the system. By connecting a mass spectrometer to the outlet gas stream, it was confirmed that there were no carbon compounds being formed during the oxidation due to carbon deposition during reduction.

The resulting oxygen non-stoichiometry of LSFM6473 is shown as a function of the oxygen partial pressure and temperatures from 993 K to 1193 K in Fig. 5.1. At the highest log pO_2 point (log pO_2 = -0.699 bar) the change in mass recorded by the instrument was less than the measurement error thus indicating almost full oxidation of the sample. With decreasing pO_2 and increasing temperature, δ increases, as expected from the reduction reaction in Eq. 5.1.

$$2B_B^{\bullet} + O_O^x \rightleftharpoons 1/2O_2 + 2B_B^x + V_O^{\bullet\bullet} \qquad \text{Eq. 5.1}$$

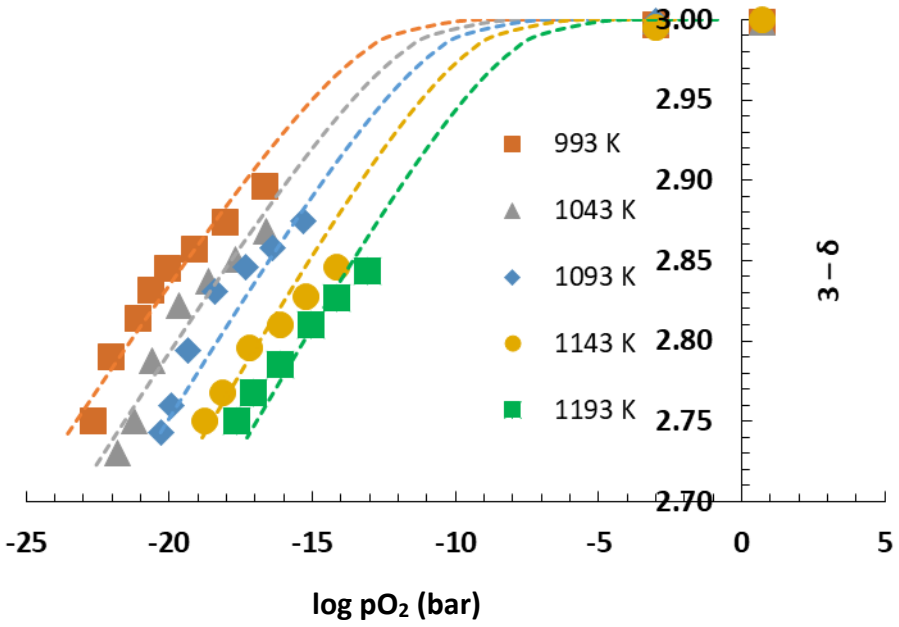

Figure 5.1: Oxygen non-stoichiometry (3-δ) versus log pO_2 for $La_{0.6}Sr_{0.4}Fe_{0.67}Mn_{0.33}O_{3-\delta}$ at temperatures 993 K, 1043 K, 1093 K, 1143 K and 1193 K. The error in each measurement is less than the size of the marker. Due to it being difficult to generate CO_2:CO ratios of > 100 at the measurement temperatures, measurements at higher pO_2s could not be made. The dotted lines indicate model fits using partial molar quantities derived from the TGA data to provide insight into the region which could not be measured experimentally.

Compared with when there is no Mn doping on the B-site in the case of LSF641, the plateau present at δ=0.2 (seen previously in Fig. 2.6) has been eliminated, while the isotherms have been shifted to a higher pO_2. This suggests increased reducibility accompanied with increased possibility of decomposition occurring at higher pO_2s. In order to verify this, XRD powder diffraction analysis was carried out on a sample reduced using 1:20 CO2/CO buffer gas at 1093 K. The XRD diffractogram data in Fig. 5.2

does not show any noticeable sign of phase segregation of the reduced sample, indicating that this increased possibility of reduction is likely not significant. Further analysis is required at lower pO_2s to determine the exact limit of decomposition.

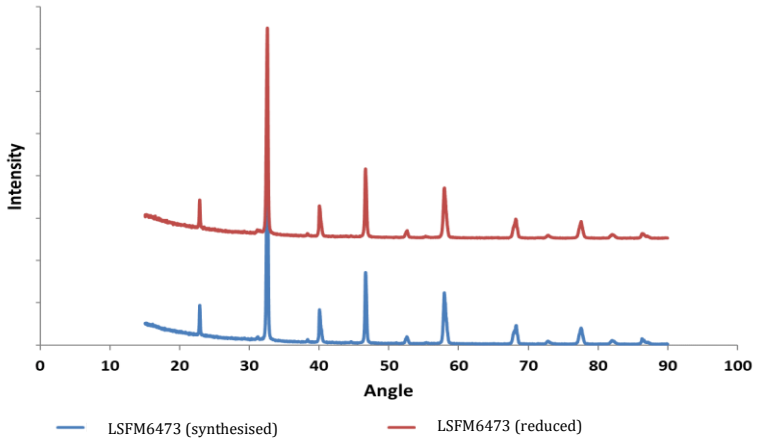

Figure 5.2: XRD diffractograms of LSFM6473 showing patterns for the fully oxidised as-synthesised material and following reduction using a 1:20 CO_2/CO buffer gas at 1093 K.

A model which considers delocalized electrons and randomly distributed oxygen vacancies was developed by Mizusaki et al (1991), and can be used to fit the data and provide insight into the δ-pO_2 behaviour at the chemical potentials which could not be measured via TGA. It is assumed that the configurational contributions due to electronic states are negligible and irrespective of the total number of conduction electrons a constant electron activity or constant Fermi level is assumed. Only the ionic chemical potential and ionic concentration are affected by changes in oxygen chemical potential, which reflects the oxygen vacancy concentration.

From the δ-pO_2 plot in Fig. 5.1, the oxygen chemical potential at a certain pO_2 in equilibrium with the gas (μ_O – equilibrium in 1 atm O_2) can be calculated by:

$$\mu_O - \mu_O^0 = \frac{RT}{2} \ln pO_2 \qquad \text{Eq. 5.2}$$

μ_O is also related to $\mu_O = h_O - Ts_O$ (the partial molar reduction enthalpy and entropy). The following equations for $h_O - h_O^0$ and $s_O - s_O^0$ can then be obtained using the Gibbs-Helmholtz relation:

$$h_O - h_O^0 = \frac{R}{2}\frac{\partial \ln pO_2}{\partial \frac{1}{T}} \qquad \text{Eq. 5.3}$$

$$s_O - s_O^0 = -\frac{1}{2}\frac{\partial RT \ln pO_2}{\partial T} \qquad \text{Eq. 5.4}$$

The δ-pO_2 data in Fig. 5.1 can therefore be interpolated to obtain plots of $\frac{R}{2}\ln pO_2$ vs 1/T and $\frac{RT}{2}\ln pO_2$ vs T. To account for deviations from the ideal solution the parameter *a* can be introduced for partial molar enthalpy. This accounts for the additional changes in enthalpy from interactions between lattice ions and defects.

$$h_O - h_O^0 = \Delta h_O^0 - a\delta \qquad \text{Eq. 5.5}$$

The constant *a* was first introduced by Mizusaki et al (1984) and provides a convenient method to represent the interactions among lattice ions and defects.

The partial molar entropy can be approximated by taking into account the configurational entropy changes of the oxygen lattice sites as follows:

$$s_O - s_O^0 = \Delta s_O^0 + R \ln \frac{\delta}{3-\delta} \qquad \text{Eq. 5.6}$$

The relationship between oxygen potential and defect concentration can therefore be expressed by combining the previous equations as follows:

$$\frac{RT}{2}\ln pO_2 = \Delta h_O^0 - a\delta - T\left(\Delta s_O^0 + R \ln \frac{\delta}{3-\delta}\right) = \Delta G_O^0 - a\delta - RT \ln \frac{\delta}{3-\delta} \qquad \text{Eq. 5.7}$$

The dotted lines in Fig. 5.1 indicate a model fit using the above formula. The fitting parameters are given in table 5.1. The purpose of using the model is to provide insight into the pO_2 range which the TGA instrument did not measure.

Table 5.1: Fitting parameters ΔG^0 and a for model. Δh^0 and Δs^0 are determined from the slope and intercept of the linear plot of ΔG^0 versus T.

T (K)	ΔG_0^0 (kJ mol^{-1})	a (kJ mol^{-1})	Δh_0^0 (kJ mol^{-1})	Δs_0^0 (J mol^{-1}K^{-1})
993	-160.32	322.31	-281.15	120.50
1043	-155.11	324.52		
1093	-151.28	321.42		
1143	-145.46	320.38		
1193	-135.02	329.96		

In summary, a much higher proportion of the active log pO_2 region is being utilised by LSFM6473 and the gradient takes a near constant value, whereas for LSF641 this tended towards zero in the active range with increasing log pO_2. The gradient tends to be greater for the case of LSFM6473 in the active log pO_2 range than for LSF641, except for a very short range of pO_2s $\sim 10^{-21}$ bar where they are roughly equal. Towards pO_2 values of 10^{-15} bar, the gradient for LSF641 becomes closer to zero than for LSFM6473. This suggests that most of the oxygen exchange capacity benefits from Mn doping in comparison to no Mn doping is being seen in the higher pO_2 range of the active region for WGS, rather than the lower part of the range where LSF641 already showed some capacity. Based on the analysis compared to the benchmark it should therefore be possible to carry out cycling at longer feed durations before having to switch half cycles with the use of LSFM6473 as compared to LSF641.

5.2 Valance state of B-site Fe and Mn cations of LSFM6473

While it has been shown so far that doping a modest amount of manganese onto the B-site of $La_{0.6}Sr_{0.4}FeO_{3-\delta}$ can result in an increase in the oxygen capacity of the material giving improved performance, a more detailed investigation into the oxidation states of Fe and Mn cations during redox reaction is required to better understand the nature of this increase in oxygen capacity. For this purpose iodometric titration experiments were

carried out, as well as XANES analysis at the Diamond Light Source on the B18 beamline to support the observations from the iodometric titrations.

5.2.1 Analysis via iodometric titration

The usable oxygen content for LSFM6473 was previously investigated in chapter 4 by carrying out 10 consecutive cycles alternating between buffer gases of 1:20 CO_2/CO and 20: 1 CO_2/CO at 1093 K, however with these investigations the oxygen content only needed to be determined in reference to two known oxygen partial pressures given by the buffer gasses.

In order to confirm that the absolute oxygen content of a fresh as-synthesised sample of LSFM6473 was $\delta = 0$, the δ determined via TGA (assuming that $\delta = 0$ for the fresh sample) was compared with the value of the δ found via iodometric titration. A 503 mg sample of $La_{0.5}Sr_{0.5}Fe_{0.67}Mn_{0.33}O_{3-\delta}$ was reduced under a 1:5 CO2/CO buffer gas at 993 K and the corresponding mass change recorded by the TGA was noted.

The mass change was 7.470 µg, and assuming that $\delta = 0$ for the fresh sample, gives a δ change of 0.206. The same reduced sample was then used for further analysis via iodometric titration, where δ was determined to be 0.212±0.02. This agrees closely with the value determined via TGA, and allows us to make the assumption that $\delta = 0$ for the fresh material. This is in agreement with other works that have studied LSF641 (Kuhn et al, 2011) and LSM641 (Mizusaki et al, 1991) which also found $\delta = 0$ for these materials in the fully oxidised as-synthesised state.

Further experiments were carried out to investigate the valence state of the B-site of the perovskite for instances with and without Mn doping. Samples of LSFM6473, LSM821 and LSF641 were reduced to achieve stable δ values of roughly ~0.2 and 0.1. The δ of the reduced samples was confirmed via both TGA and iodometric titrations with both in good agreement with each other in table 5.2.

Table 5.2: δ values and corresponding B-site valences samples in a reduced state, for the materials LSFM6473, LSF641 and LSM821.

Compound	**Average B-site valence (TGA)**	**δ (TGA)**	**Average B-site valence (iodometric titration)**	**δ (iodometric titration)**	**Colour change in second flask**
$La_{0.6}Sr_{0.4}Fe_{0.67}Mn_{0.33}O_{2.8}$	+2.978	0.206 (reduced material)	+2.976	0.212±0.024 (reduced material)	Yes
$La_{0.6}Sr_{0.4}FeO_{2.8}$	+3.052	0.174 (reduced material)	+3.048	0.176±0.012 (reduced material)	No
$La_{0.8}Sr_{0.2}MnO_{2.9}$	+3.004	0.098 (reduced material)	+3.012	0.094±0.030 (reduced material)	Yes

The occurrence of a colour change in the second flask during titration could be considered as a sign of the presence of 4+ ions on the B-site of the reduced samples, specifically Mn4+. Results in table 5.2 indicates that 4+ ions are present only in the manganese doped samples. The reaction of Mn ions with Cl^- during sample dissolution leads to the formation of chlorine gas, which is flushed into the second flask, and is exacerbated by the presence of Mn4+ ions according to the following equations:

$$Mn^{3+} + Cl^- \rightarrow Mn^{2+} + 0.5Cl_2 \qquad \text{Eq. 5.8}$$

$$Mn^{4+} + 2Cl^- \rightarrow Mn^{2+} + Cl_2 \qquad \text{Eq. 5.9}$$

While the values in table 5.2 only give the combined Fe and Mn changes in the valence state, XANES analysis was able to further isolate the extent to which Fe or Mn plays in the change in valence state of the B-site following reduction.

5.2.2 XANES analysis of B-site valence states

A XANES investigation was carried out in order to probe the K-edge shifts for Fe and Mn and see how the change in their oxidation states affect δ between $La_{0.6}Sr_{0.4}FeO_{3-\delta}$ and $La_{0.6}Sr_{0.4}Fe_{0.67}Mn_{0.33}O_{3-\delta}$ as well as the material $La_{0.8}Sr_{0.2}MnO_{3-\delta}$ which contains only Mn on the B-site, in the fully oxidised state and in a reduced state (synthesised using a collection of buffer gases at various pO_2s). XANES spectra are given in Fig. 5.3, which includes the metal oxides as references.

For LSFM6473 and LSM821, the Mn K-edge shift is from a mainly 4+ state to a mainly 3+ state, while for LSFM6473 and LSF641 the Fe K-edge shift mainly occurs in the 3+ and 2+ states with likely very little Fe4+ actually present. Generally, one can infer that at relatively high pressures, pO_2 > 3 bar, Mn cations in the perovskite structure maintain a 4+ oxidation degree. Once the pressure starts to decrease below 10^{-3} bar this results in a partial reduction of Mn4+ to Mn3+ cations. For LSFM6473, the further reduction of Fe3+ can only occur once all Fe4+ and Mn4+ cations are exhausted, and it is likely that the additional presence of the Mn4+ cations which must be reduced (and have a much larger Mn K-edge shift than for Fe) is resulting in the disappearance of the isotherm plateau in Fig. 5.1.

$$2Mn^{4+} + O^{2-} \rightleftharpoons 1/2O_2 + 2Mn^{3+} + V_O$$

However the improved oxygen capacity of LSFM6473 is not necessarily derived from the presence of the Mn 4+ ions (Gokon et al (2019) found that the oxygen storage capacity of the related material $La_{0.5}Sr_{0.5}FeO_{3-\delta}$ was 6 times greater than that of the related material $La_{0.5}Sr_{0.5}MnO_{3-\delta}$ from the fully oxidised as synthesised state), but rather from the shift this causes in the δ-pO_2 curve in the very specific pO_2 range which sees the greatest conversions for the WGS reaction.

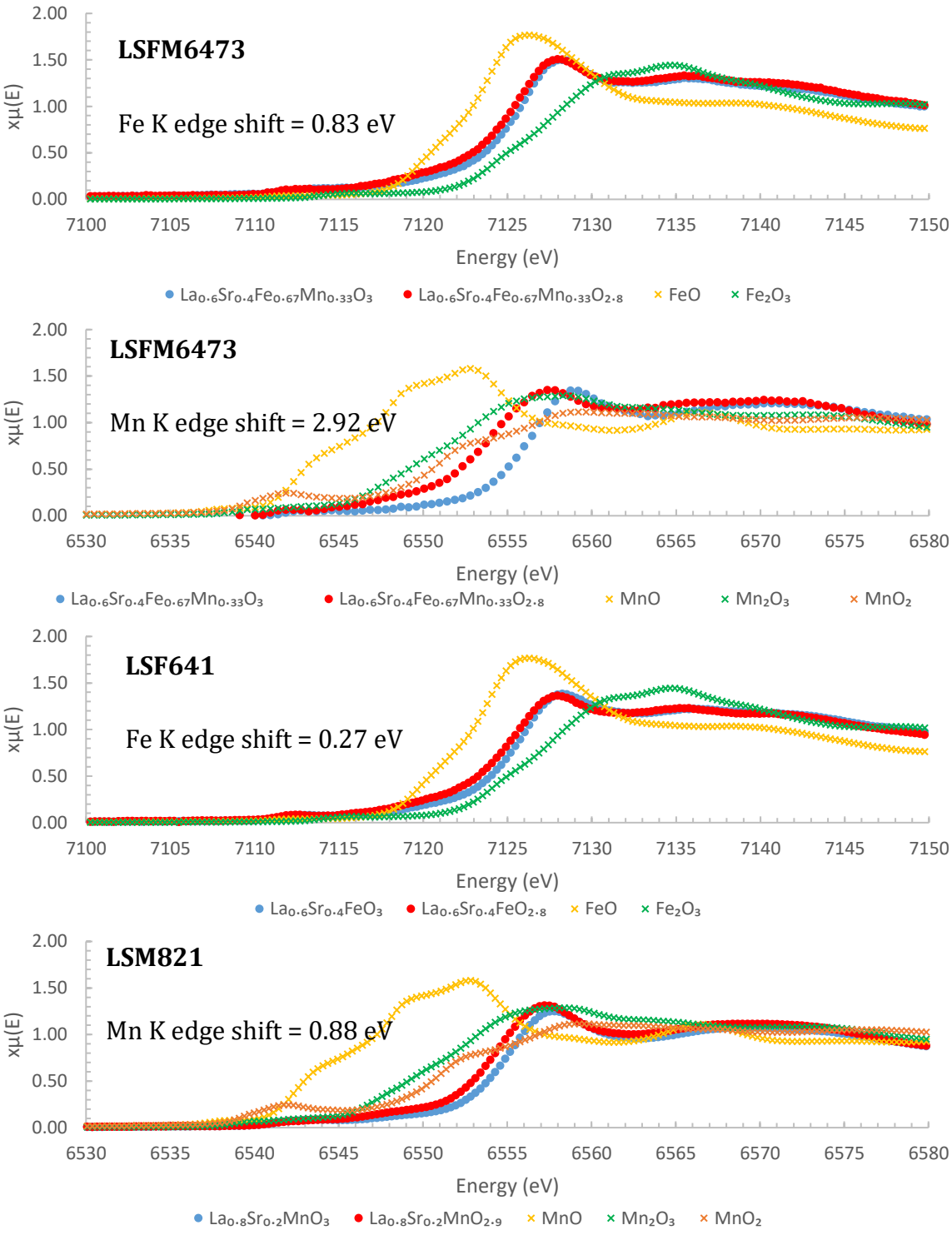

Figure 5.3: Normalised XANES spectra for $La_{0.6}Sr_{0.4}Fe_{0.67}Mn_{0.33}O_3$, $La_{0.6}Sr_{0.4}Fe_{0.67}Mn_{0.33}O_{2.8}$, $La_{0.6}Sr_{0.4}FeO_3$, $La_{0.6}Sr_{0.4}FeO_{2.8}$, $La_{0.8}Sr_{0.2}MnO_3$ and $La_{0.8}Sr_{0.2}MnO_{2.9}$. K edge shift values determined by finding the difference in E0 between the stoichiometric and reduced samples.

5.3 Summary

This chapter has shown that doping 1/3 proportion of Mn onto the B-site of the perovskite LSF641 altered the shape of the δ-pO_2 curve in such a way so as to eliminate the plateau present for LSF641 which limited the oxygen exchange potential of that OCM. This change in the δ-pO_2 relationship comes from the presence of Mn 4+ ions in the reduced δ≈0.2 of LSFM6473. Although increased Mn4+ presence does not necessarily translate to greater oxygen capacity for the OCMs for CLWGS, but rather a subtle shift in the δ-pO_2 curve combined with the elimination of the plateau which allows it to better match the shape of the ideal benchmark curve identified in chapter 3.

Chapter 6: In-situ XRD study of a packed bed reactor of LSFM6473 undergoing CLWGS

It has been shown that LSFM6473 has a larger usable oxygen transfer capacity for the CLWGS process than previously investigated LSF641, and should therefore be possible to achieve conversions to CO_2 and H_2 both in excess of 50%, and be cycled for longer feed durations before switching half cycles. The structural properties of the material under operating conditions using in-situ XRD are investigated in this chapter to better understand the chemical and physical characteristics of the crystal phases. For industrial applications knowledge of the stability of the material during extensive operation is important, as potential phase segregation can lead to decreased performance during the lifetime of the material. Morphological evolution of the OCM during the oxidation and reduction reactions in the cyclic looping process can affect the available surface area during reaction due to ionic diffusion in the solid phase with molar volume changes (Cheng et al, 2018), resulting in gradual deactivation of the OCM.

Ex-situ room temperature XRD diffractograms of samples that were reduced using buffer gasses did not show signs of phase segregation for LSFM6473 in chapter 5. However in ex-situ XRD the sample is measured at ambient conditions and as such this does not offer definitive proof of whether any phase changes were occurring during cycling at the operating temperature of interest and then being reversed either during oxidation or due to the additional structural changes of the material from the thermal effects of cooling the material down to room temperature following cycling. It is for this reason that in-situ XRD analysis is necessary as it allows for sample measurements to be carried out in the environment of interest.

Specifically, the use of in-situ analysis has the benefit of allowing us to determine the lattice parameter of the OCM and the chemical potential at different positions and times along the reactor bed under operating conditions, and by deriving the thermal and chemical and thermal expansivities we can use fundamental equations relating to the structure of the material to calculate how the oxygen non-stoichiometry of the OCM is changing during cycling. This allows for a better assessment of the internals of the fixed bed reactor carrying out cyclic looping, as well as allowing for another tool of verifying

the benefits of the higher usable oxygen capacity of LSFM6473 in comparison to the LSF641 benchmark. This will also be useful for potential future reactor size design by knowing how the materials volume expands during reduction and oxidation.

It should be noted that this in-situ analysis was only possible using the synchrotron facility in ID22 at the ESRF due to the requirement for high fluxes of x-rays to be able to measure the changes to the crystal structure during reaction while still achieving data of high enough precision to resolve the small changes in lattice parameter.

6.1 Lattice cell parameter and material stability

6.1.1 Material characterisation

The crystal structure of LSFM6473 was investigated in order to determine whether the material behaved as a single-phase perovskite under operating conditions. The lattice parameter of the fresh material was determined from capillary experiments at room temperature via Rietveld refinement. This could be indexed on the basis of a hexagonal regime (R-3c) with a_{hex} equal to 5.52330 Å and c_{hex} equal to 13.42606 Å. Here a_{hex} and c_{hex} refer to the perpendicular directions in the unit cell of the hexagonal unit cell. This is in agreement with the findings of Kammer et al (2005) and Markov et al (2015) who studied the structure of similar Mn doped $La_{0.5}Sr_{0.5}Fe_{0.67}Mn_{0.33}O_3$ and $La_{0.6}Sr_{0.4}Fe_{1-y}Mn_yO_3$ materials respectively and found them to best fit the hexagonal regime at room temperature.

At operating temperature of 1093 K the material was better fit using a cubic (Pm-3m) rather than a rhombohedral structure, with a_{cub} equal to 3.93675 Å and c_{cub} equal to 3.93245 Å. Note that for cubic systems a_{cub} and c_{cub} should essentially be equal. The hexagonal unit cell can be converted into a cubic unit cell and vice versa by use of the following two equations based on the shape of the crystal structure:

$$a_{cub} = \frac{a_{hex}}{\sqrt{2}} \qquad \text{Eq. 6.1}$$

$$c_{cub} = \frac{c_{hex}}{2\sqrt{3}} \qquad \text{Eq. 6.2}$$

Where *a* and *c* are perpendicular directions in the unit cell of either the cubic or hexagonal unit cells depending on the subscript. Applying these relations allows for a good way to directly compare the values obtained based on a rhombohedral or cubic fitting parameter. The angle theta of the hexagonal cell was calculated from Eq. 6.3 and as shown in Fig. 6.1 was found to be closer to 60° at operating temperatures which corresponds to a cubic cell for operating temperature.

$$\theta = cos^{-1}\frac{2c_{hex}^2 - 3a_{hex}^2}{2c_{hex}^2 + 6a_{hex}^2} \qquad \text{Eq. 6.3}$$

Further investigations revealed the extent of the change in lattice parameter under difference gas atmospheres. Fig. 6.2 shows the change in the unit cell parameter under operating conditions with different buffer gas atmospheres. In order to carry out the initial activation of the bed (to enable steady cycling to be reached faster in later experiments) a 1:5 CO_2/CO buffer gas was fed to the bed and here the cubic unit cell parameter shows an increase from 3.920 ± 0.0020 Å to 3.950 ± 0.0001 Å. For the values of δ which LSFM6473 goes through during cycling, the oxidation or reduction of the material only changes the amount of oxygen vacancies in the lattice and the oxidation number of the B-site ions while the oxidation number of the oxygen cations or A-site ions remain constant. As the material is reduced or oxidised, the coordination and oxidation number of the B-site ions change and this affects the size of the B-site ions and hence the size of the unit cell of the perovskite structure. As the number of oxygen vacancies increase the lattice parameter therefore increases.

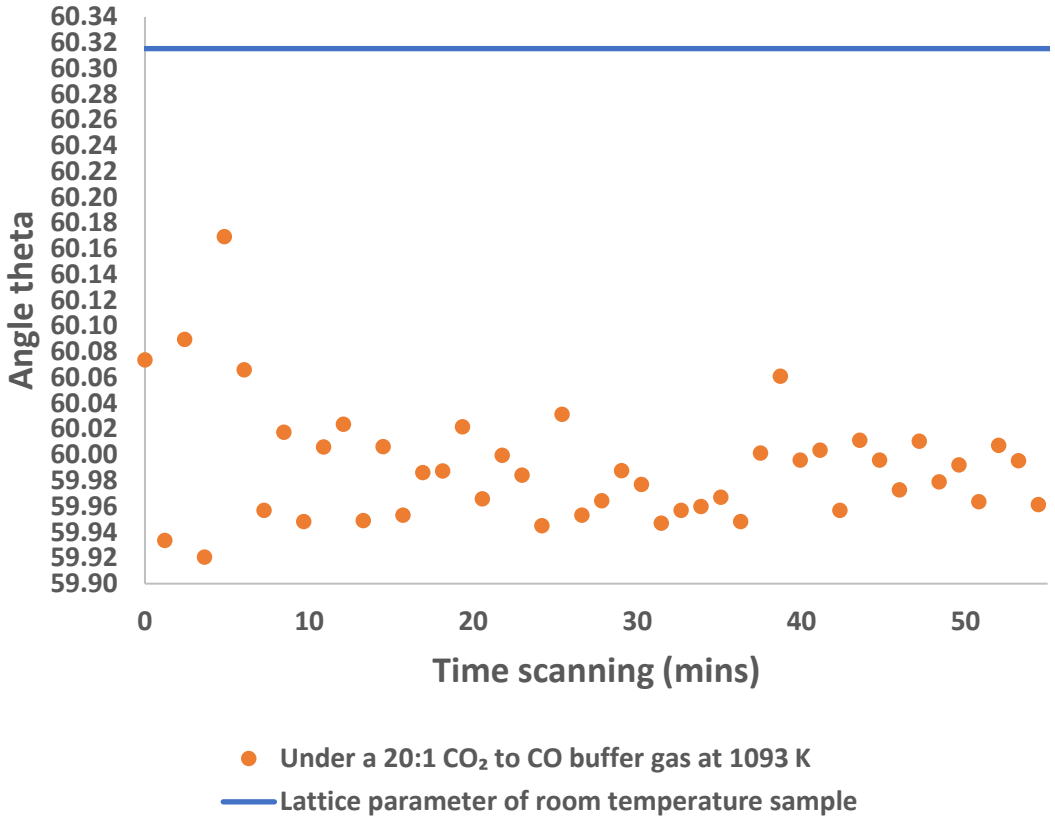

Figure 6.1: Comparison of angle theta for LSFM6473 at room temperature and at 1093 K under a 20:1 CO_2/CO buffer gas. All gases were fed at a nominal molar flowrate of 3.4 × 10^{-5} mol s^{-1}.

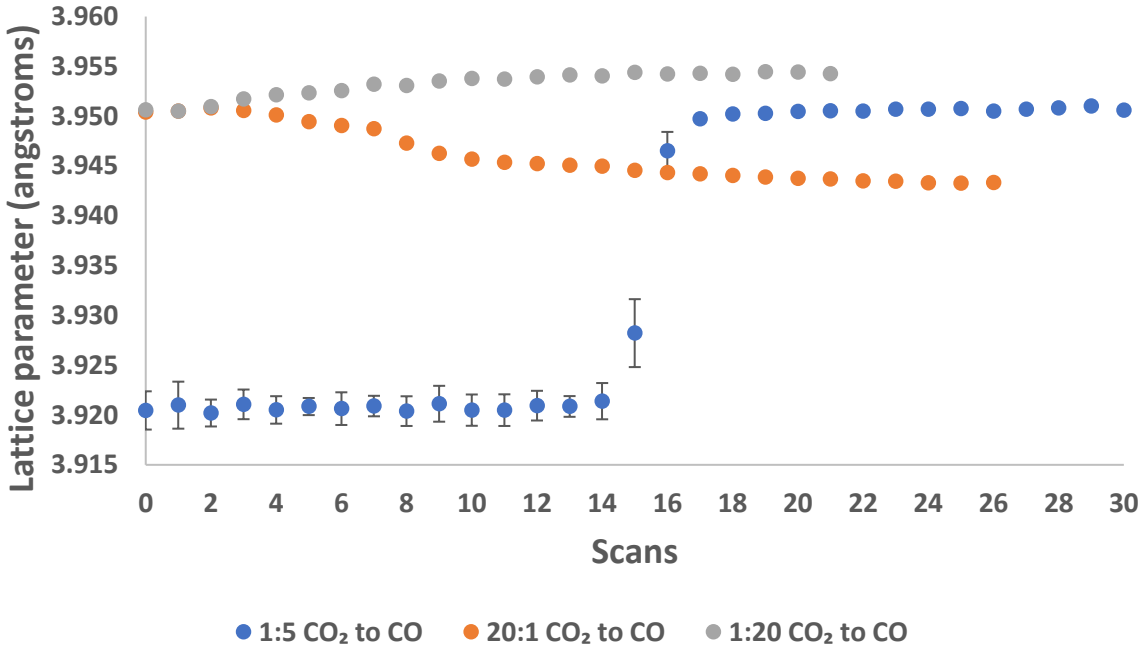

Figure 6.2: Behaviour of the lattice parameter at a point 19.95 mm above the CO inlet when coming into equilibrium with 3 different buffer gas atmospheres: 1:5 CO_2/CO, 20: 1 CO_2/CO and 1:20 CO_2/CO. All gases were fed at a nominal molar flowrate of 3.4 × 10^{-5} mol s^{-1}.

The size of the increase in the lattice parameter is directly related to the power of the reducing agent. In the case of Fig. 6.2, the strongest reducing buffer 1:20 CO_2/CO shows the material reaching the largest lattice parameter values, since large changes in the oxygen non-stoichiometry are often accompanied with respectively large dimensional changes of the lattice.

6.1.2 Determination of temperature during operation

An understanding of the temperature gradient along the chemical looping packed bed reactor is important since the thermodynamic calculations involving LSFM6473 require knowledge of the true temperature of the reactor bed during experiments in order to properly account for the dependence of δ on temperature, and since temperature change during reaction would affect the isothermal operation of the bed.

In the description of the experimental set-up in chapter 4 it was explained how Y_2O_3 would be inert under the pO_2 range relevant and not take part in reactions with the carbon based gases involved in the reaction (Swamy et al, 1999). A method of Rietveld refinement was used to determine the temperature gradient that resulted from heat convection vertically of the reactor from measurements of unit cell parameter based on the empirical data from Swamy et al (1999) and Taylor et al (1984) by use of Eq. 6.4:

$$T = \frac{-B+\left(B^2-4\times A\left(C-a_{Y_2O_3}\right)\right)^{0.5}}{2A} \qquad \text{Eq. 6.4}$$

where T is the sample temperature, $a_{Y_2O_3}$ is the measured unit cell parameter, A = 1.29340×10^{-8} Å/K², B = 6.46011×10^{-5} Å/K, C = 10.58733218 Å.

TOPAS v7 software was used to carry out the Rietveld refinement. The sample peak shape contributions were described by convolving terms describing isotropic size and strain broadening onto an instrumental peak shape determined empirically from a Si standard. The wavelength of x-ray used for the XRD measurements was 0.3544767 A from the Si calibration. The site occupancies of La, Sr, Fe and Mn were kept constant at 0.6, 0.4, 0.67 and 0.33 respectively. This was then used to refine unit cell parameters, oxygen site occupancy, atomic displacement parameters (anisotropic for oxygen) and sample contributions to the peak shape were refined.

All experiments were carried out on a single bed of length 10.0 cm, diameter 4 mm and mass 2.68 g (this includes +20% Y_2O_3 based on 2.23 g LSFM6473). The vertical bed was split into 15 points each 6.65 mm apart for analysis, point 1 being at the bottom (reduced end) and point 15 being at the top (oxidised end). 3 different buffer gases were used, cycling was carried out using 5% H_2O and 5% CO feeds (60 cycles), and in separate experiments between 20:1 CO_2 to CO and 1:20 CO_2 to CO feeds (20 cycles). Fig. 6.3 shows the temperature change during cycling between 5% H_2O and 5% CO, as well as between the buffer gases 20:1 CO_2 to CO and 1:20 CO_2 to CO, and when there is no reaction after having reached steady state. Fig. 6.4 shows the temperature variation at single points in the bed during cycling with 5% H_2O and 5% CO feeds.

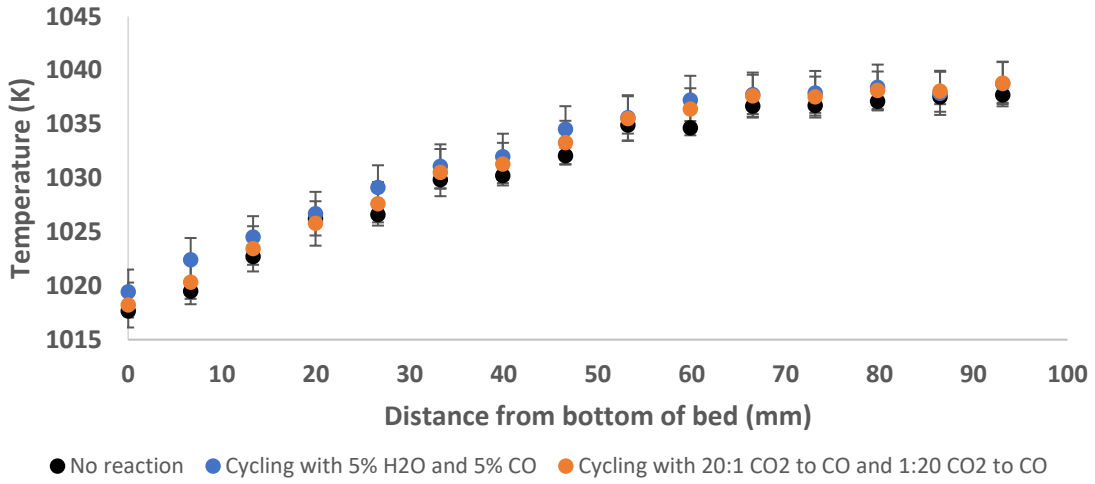

Figure 6.3: Average temperature at each point in the LSFM6473 bed during cycling with 5% gases in WGS, during cycling with buffer gases 20:1 CO_2 to CO and 1:20 CO_2 to CO, and during no reaction in equilibrium with a 1:5 CO_2 to CO buffer gas. 2.23 g of active LSFM6473 was used with gas molar flowrate of 3.4 × 10^{-5} mol s^{-1}. The error bars are ± 1 one standard deviation.

While the furnace was set to operate at 1093 K, the temperature of the solid material as determined by the Y_2O_3 measurements appears to be in the range 1018 to 1039 K instead. A thermocouple measurement of the furnace was taken as roughly 1086 K. This discrepancy may be due to a temperature gradient between the furnace and the reactor bed and may account for the lower actual temperature of the solid material, as well as insufficient external insulation.

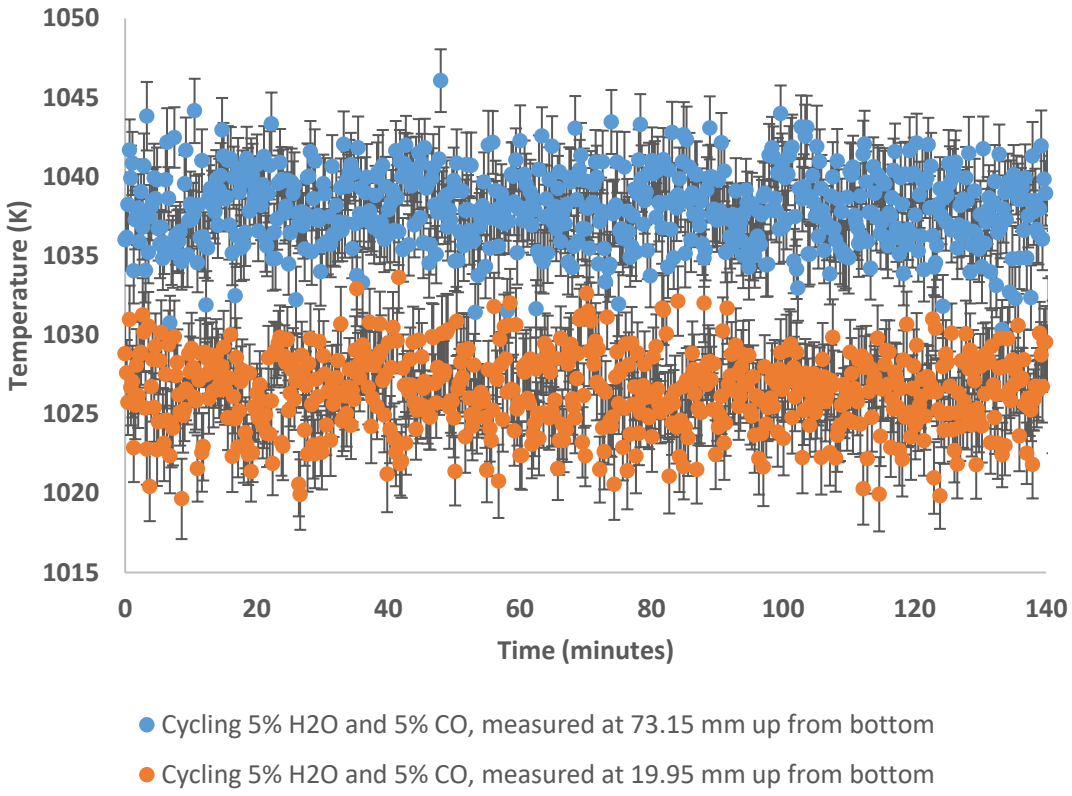

Figure 6.4: Temperatures determined at two points 19.95 mm and 73.15 mm up from the CO inlet of the bed. The measurements are during water-gas shift cycling with 5% H_2O and 5% CO feed gases for 15 cycles. There do not appear to be any visible trends to the data. The data is consistent with Fig. 6.3 with higher temperatures near the top of the reactor bed. The error bars are ± 1 one standard deviation.

In Fig. 6.3 the temperature profiles during cycling with 5% gases or the buffer gases are compared to the profile with no reaction. The data shows no significant increase in temperature at the H_2O inlet after accounting for heat rise from the conditions when there is no reaction, and no decrease in temperature at the CO inlet. It should be noted that the uncertainty of the measurements is greater than any rise or increase in temperature between reaction and no reaction scenarios.

While Fig. 6.3 shows that there is a change in temperature between the oxidising and reducing ends of the reactor of 19.3 K due to heat rise, Fig. 6.4 shows that the temperature at a single point does not undergo any noticeable change over the course of a cycle and there does not appear to be any sort of trend in the temperature at a single point. In Fig. 6.4 owing to the nature of the Rietveld refinement which converges the fit to a local minimum, the presented uncertainty of the data is actually an underestimate of

the true uncertainty in the raw data as the scatter of the data for both positions appear to be greater than the uncertainty from the Rietveld refinement.

6.1.3 Material stability during redox cycling with buffer gases

The same LSFM6473 bed described in section 6.1.2 was cycled between buffer gases 20:1 CO_2 to CO and 1:20 CO_2 to CO for 20 cycles. This allowed for the lattice parameter to be tracked as a function of position across the bed, and to see how the material changed when using CO_2 as the oxidising agent as well as to give controlled inlet conditions for comparison to bed simulations of oxygen non-stoichiometry as well as to see if during cycling under known oxygen partial pressure conditions it remained as a single-phase perovskite. The outlet mole fractions are shown in Fig. 6.5 and the conversions per cycle can be seen in Fig. 6.6. The beam is initially positioned at the top of the bed at the H_2O inlet, and the reactor bed is then moved down by 6.65 mm increments via a motor platform after each cycle to allow for scans to be taken at 15 points along the length of the bed.

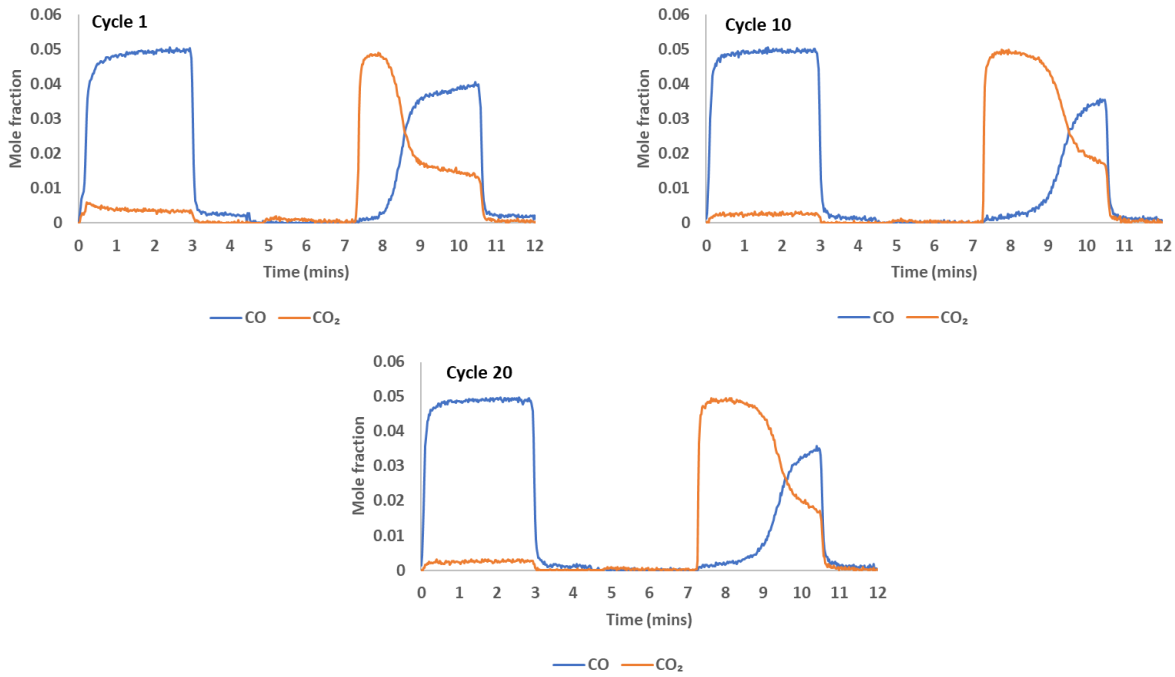

Figure 6.5: Outlet gas compositions for cycles 1, 10 and 20 using 1:20 CO_2 to CO and 20:1 CO_2 to CO buffer gases. Reactor set-point was 1093 K with 2.23 g of active LSFM6473 material with nominal molar flowrate of 3.4 × 10^{-5} mol s^{-1}. Uncertainty in the measurements was ± 100 µmol based on the mass spectrometer data.

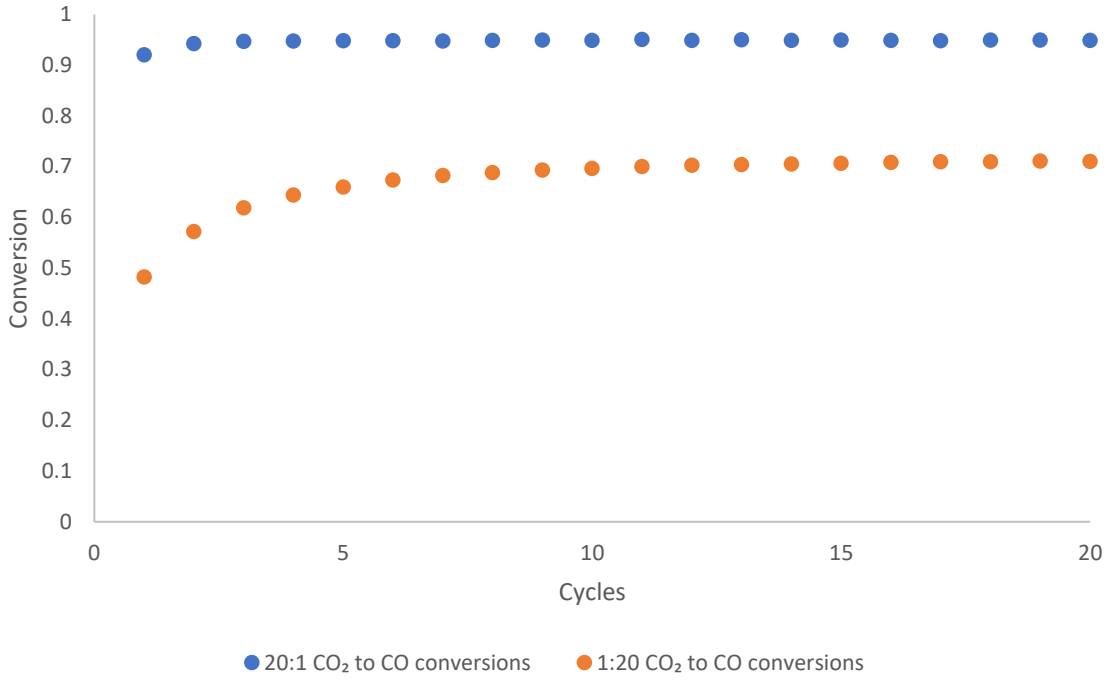

Figure 6.6: Conversion per cycle using counter-current buffer gas feeds of 20:1 CO_2 to CO (the oxidising agent in blue) and 1:20 CO_2 to CO (the reducing agent in orange) buffer gases. 2.23 g of active LSFM6473 material was used along with gas nominal molar flowrate of 3.4 × 10^{-5} mol s^{-1} at 1093 K.

Prior to cycling, the bed had been reduced with a buffer gas of 1:20 CO_2 to CO, hence the initial cycles with 20:1 CO_2 to CO show much higher conversions than the first few cycles for the previous half cycle duration or temperature optimisation experiments and reach steady state much faster. The conversions during later cycles however are lower than those achieved using 5% gases due to the lower quality of the buffer gas feeds. The 1:20 ratios (or vice versa) of the oxidising and reducing feeds are able to exchange 0.05 moles of oxygen in either case since they consist of 5% CO_2 and 0.25% CO, or 0.25% CO_2 and 5% CO respectively, but the presence of CO_2 or CO in the feeds lowers the conversions.

Despite this however the conversions achieved with the reducing buffer gas feed are still much lower than that achieved with the oxidising buffer gas feed (roughly 70% compared to 90%). This should not be the case since as previously stated the gas feeds are symmetrical. In addition, the concentration profiles in Fig. 6.5 show almost full conversion of the oxidising buffer gas feed but a significant breakthrough of CO in the reducing buffer gas feed. The extent of this breakthrough decreases with progressive

cycles but is still significant. The oxygen balance is found not to close in between oxidation and reduction half cycles giving a discrepancy of 24% at most.

Instead, further analysis reveals that since the entire bed had come into equilibrium with the 1:20 buffer gas of CO_2 to CO prior to the experiment, which comes to a fairly reducing pO_2 of -20.5 log pO_2 at 1093 K (or -21.8 log pO_2 at 1043 K), the short feed durations combined with the weaker oxidising agent (20:1 CO_2 to CO comes to -15.3 log pO_2 at 1093 K or -16.6 log pO_2 at 1043 K) meant that the bed appears not to have reached steady state during the 20 cycles that were carried out. A linear relation was fitted to the conversion data in Fig. 6.6 for cycles 12 to 20 and found that the gradient for the reducing feed conversions was roughly 40 times larger than that for the oxidising feed conversions. The presence of the large CO breakthroughs in Fig. 6.5 is because the material is still in a greatly reduced state at the start of the reduction half cycle meaning that there is less oxygen available for the gas feed to remove from the solid.

Analysis of the lattice parameter profile across the bed as shown in Fig. 6.7 confirms the assumption that the bed had not reached steady state. This figure corresponds to cycles 5-20. Each “U” shaped trough on the graph corresponds to 1 whole cycle, with the lattice parameter decreasing during oxidation half cycle and increasing during reduction half cycle to complete the shape. The changes in lattice parameter per cycle between adjacent positions are not consistent between any point on the bed, even in the centre which shows a gradual increasing trend. Also the changes in lattice parameter per half cycle are largest at the oxidising inlet and progressively become smaller going towards the CO inlet. This suggests that there is a greater oxygen non-stoichiometry change of the material at the oxidising inlet, because the bed is seeing more of the oxidising buffer gas which can donate more oxygen to the material than would be possible if it were in equilibrium with the reducing feed. The uncertainty associated with the lattice parameter is smaller than the marker for most of the bed length, although there is a larger uncertainty associated with the measurements at the reducing end of the bed. It can be seen in Fig. 6.7 that the uncertainty at the extreme reducing end is larger than the average lattice parameter change in the entire half cycle. This means that the in-situ XRD technique used was not able to determine accurately the changes in lattice parameter

corresponding to the smallest changes in oxygen non-stoichiometry at the reducing end, since the solid would see very little oxygen removal having previously come into equilibrium with the 1:20 CO_2 to CO gas. It is expected that the use of 5% gases in a bed that has achieved stable cycling will have more success and the larger changes in δ at the reducing end might reduce the uncertainty of the measurements.

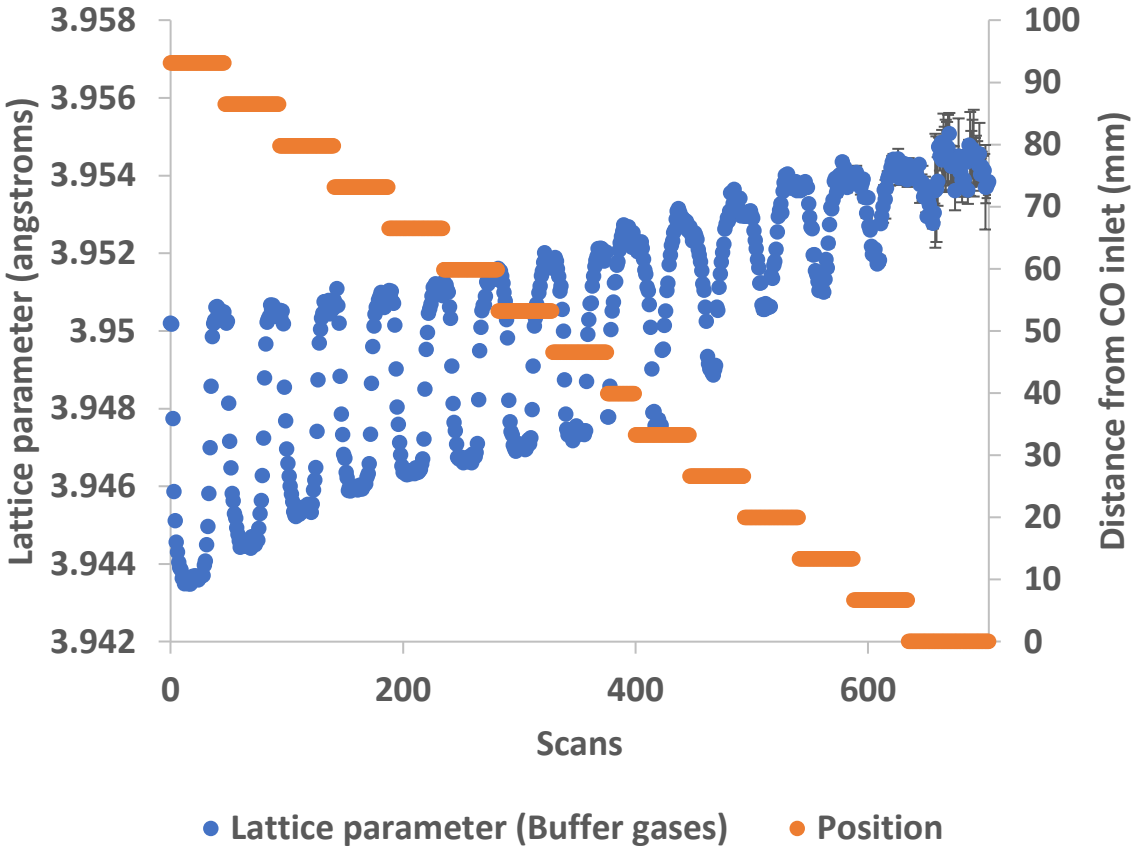

Figure 6.7: Lattice parameter changes for 15 cycles at each point in the LSFM6473 bed during buffer gas cycling. Errors for most points are smaller than the size of the marker, except for points at the reducing inlet. The data for the 9th oxidation half cycle is omitted due to an experimental error causing this data to be lost.

Despite the uncertainty at the reducing end, the lattice parameter at other positions appears to start and end at the same range of values between the cycles, suggesting reproducible outlet conversions and hence stability of the material. The results in this section highlight the importance of the starting point of the bed when cycling between buffer gasses: since the bed had previously come into equilibrium with a 1:20 buffer gas

of CO_2 to CO, the bed was not able to reach steady state due to using a weakly oxidising buffer gas (20:1 CO_2 to CO) as the oxidising agent.

6.1.4 Material stability during redox cycling with WGS gases

In the previous section it was shown that an in-situ XRD analysis of the reactor bed was able to track the changes of the lattice parameter of LSFM6473 with relative accuracy and was able to determine to what extent each section of the bed was being utilised based on the size of the lattice parameter change over a half cycle. The uncertainty present in the data as well as the scatter at the reduced end of the bed was too large to accurately determine the lattice parameter changes near the CO inlet, due to the small changes in the δ state occurring. In this section 60 cycles are carried out switching between 5% feeds and a much larger change in the δ state of the solid is expected.

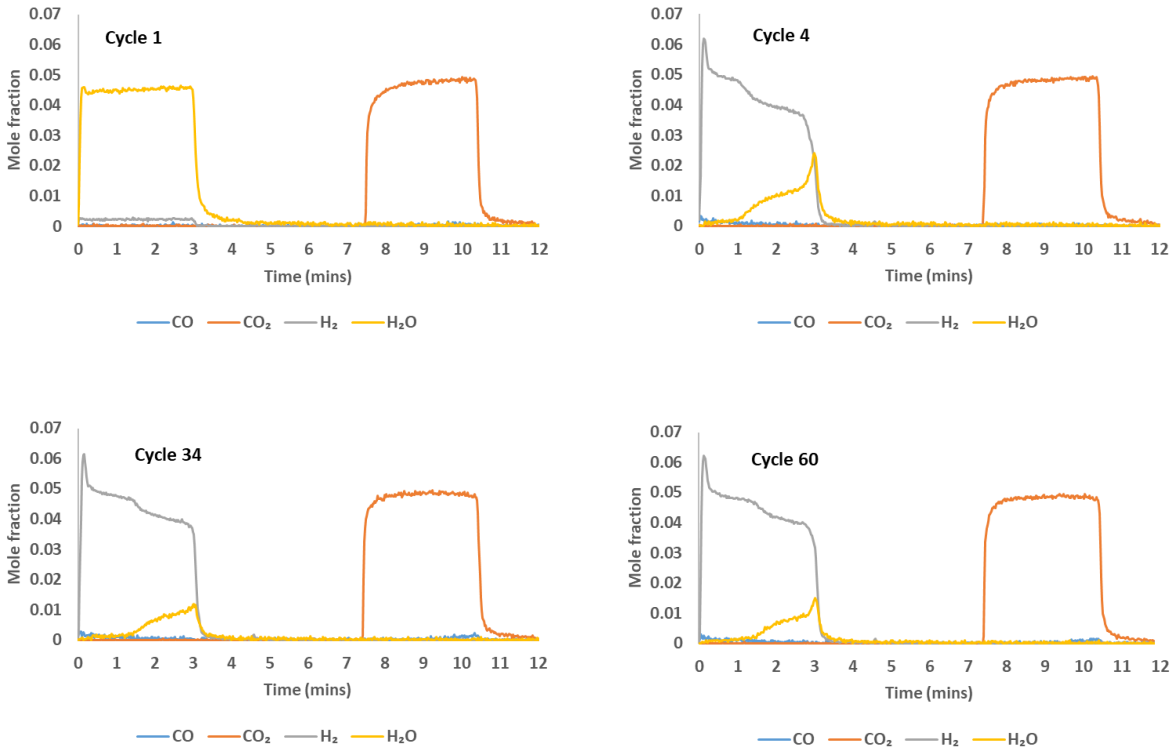

Figure 6.8: Outlet gas compositions for cycles 1, 4, 34 and 60 using 5% H_2O and 5% CO gases. Reactor set-point was 1093 K with 2.23 g of active LSFM6473 material with nominal molar flowrate of 3.4 × 10^{-5} mol s^{-1}. Uncertainty in the measurements was ± 100 µmol based on the mass spectrometer data.

The concentration profile of the outlet gas in Fig. 6.8 follows the same pattern as seen before in previous experiments. The concentration of H_2 initially exceeds 5% at the start of the profile and then drops 4% as the H_2O concentration starts to increase towards the

latter part of the cycle. The first cycle shows almost pure H_2O coming through the reactor due to the bed being only partially in a reduced state from the pre-treatment - a 20:1 CO_2 to CO buffer gas comes to about -15.3 log pO_2 at 1093 K corresponding to a lower conversion based on the thermodynamics of the active region of change in H_2O conversion discussed in chapter 3. The H_2O concentration curve is overcome by the H_2 curve in latter cycles, with the increase in H_2 concentration occurring later in the half cycle.

The conversions over the course of the 60 cycles are shown in Fig. 6.9. The bed was pre-treated with a 20:1 CO_2 to CO buffer gas feed prior to the experiment to reach steady cycling quicker. For 3 minute feed durations the bed is able to reach steady cycling after roughly 15 cycles. This is faster than would have been possible going from a completely fresh material - indeed section 7.2.2 later in the thesis shows that a similar bed with LSFM6473 takes 15 cycles to reach steady state from a fresh material but has to use the longer feed duration of 5 minutes in order to do so. The conversions per cycle start from a near zero value for the case of H_2O and almost 100% for CO before reaching steady state at 87% and 97% respectively.

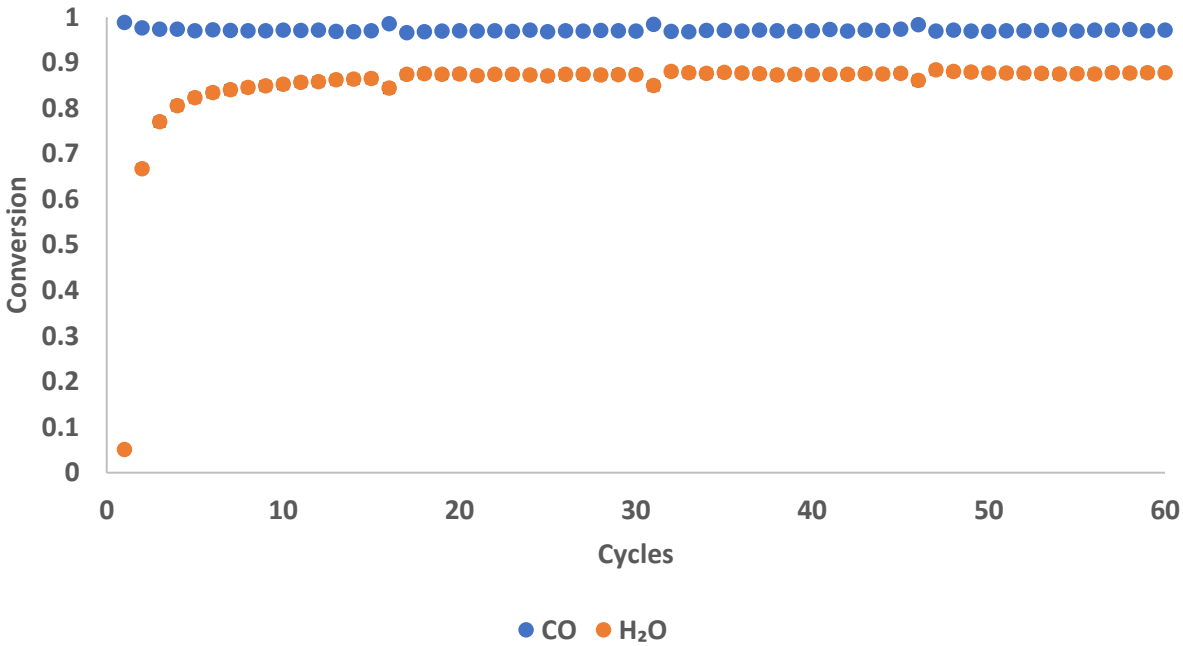

Figure 6.9: Conversion per cycle for 5% H_2O and 5% CO WGS cycling gases. 2.23 g of active LSFM6473 was cycled between counter-current feeds of 5% H_2O and 5% CO in argon for 60 cycles at a temperature of 1093 K with gas nominal molar flowrate of 3.4 × 10^{-5} mol s^{-1}.

The lattice parameter profile across the bed shown in Fig. 6.10a was determined via the same procedure as described in section 6.1.3. The beam is initially positioned at the bottom of the bed at the H_2O inlet, and the reactor bed is then moved up by 6.65 mm increments. Lattice parameter values determined from the scans taken of the final 15 cycles are shown, when steady cycling is occurring. The results show that the lattice parameter is far more stable in the central section of the bed as compared to the buffer gas experiment, and changes between more consistent values (for roughly 33.25 mm and 59.85 mm above the CO inlet between 3.950 Å and 3.946 Å).

In Fig. 6.10a the changes in lattice parameter over a cycle are larger at the ends of the bed and smaller in the central section because the ends of the bed come into contact with the reactant gases at more oxidising or reducing potentials, suggesting that the WGS bed is undergoing steady cycling and the material is stable. The changes in lattice parameter are largest and occur more rapidly at the reducing end of the bed. The larger change in lattice parameter may be due to the larger change in δ value per step change in log pO_2 for LSFM6473 as shown before in Fig. 5.1. Interestingly the lattice parameter at the start of the first cycle is at a value of 3.95438 Å and does not return to this value after the reduction half cycle, instead jumping to a value of 3.95886 Å. This is unlike another the cycles where the lattice parameter starts and ends at similar values over the course of the cycle. One possible explanation is that the bed, which is most reduced at the CO inlet, is being slightly reduced by the argon purge gas that is flown through the reactor during the calibration stage carried out after every 15 cycles.

The size of the uncertainty at the reduced end is smaller than what was seen in the buffer gas experiments, with almost all being smaller than the size of the marker. As the δ state changes for this experiment were larger than that for the buffer gas experiment, the in-situ XRD technique was able to accurately track the changes in lattice parameter as shown by Fig. 6.10b, with almost no noise and uncertainty smaller than the markers.

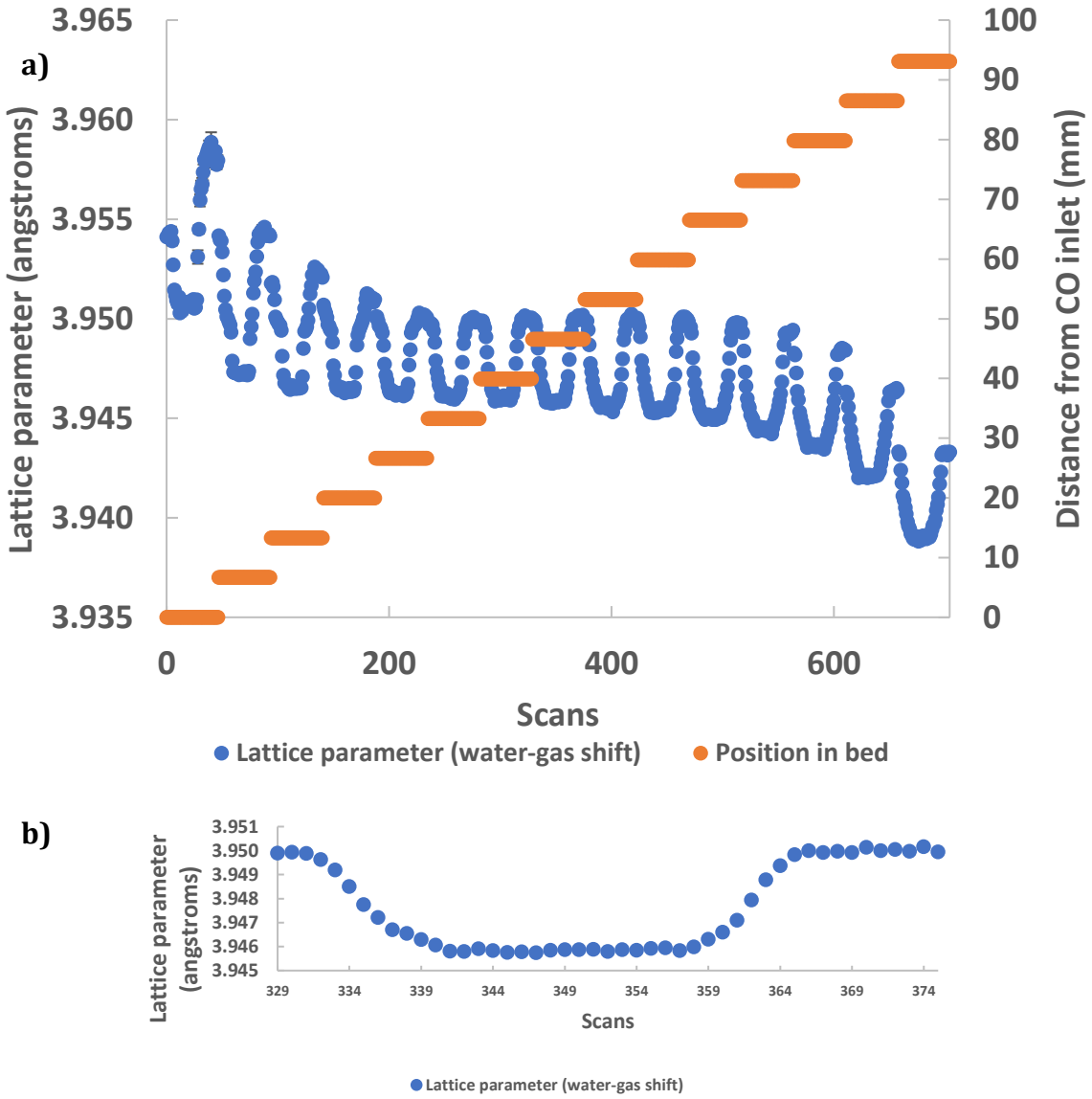

Figure 6.10: a) Lattice parameter changes for 15 cycles at each point in the LSFM6473 bed during water-gas shift cycling. The data corresponds to cycles 31-45 in figure 19. Errors for most points are smaller than the size of the marker. b) Change in lattice parameter over the course of the 8th cycle at a point 46.55 mm above the CO inlet.

6.2 Thermal and chemical expansivities to determine LSFM6473 in-operando oxygen non-stoichiometry

6.2.1 Thermal and chemical expansivities

An understanding of the thermochemical expansivities of suitable OCMs is important in the design of CLWGS systems. It is known that changing chemical conditions can alter the ionic and electronic conductivity along with the elastic modulus of OCMs, and stresses caused by thermal effects can potentially lower the mechanical integrity of the

OCM (Bishop et al 2014, Fertman et al 2015). Knowledge of thermochemical expansivities also enables the lattice cell parameters of the perovskite to be linked to the oxygen non-stoichiometry, which is useful for predicting the performance of reactor beds under operating conditions.

The scans taken at each point along the bed were used to find the cubic cell parameters, and the corresponding internal temperature was found via Rietveld refinement for each gas atmosphere. In order to calculate the chemical expansivity the unit cell parameter values at the closest possible temperatures for each buffer gas were used. Based on the buffer gas in use and the temperature the pO_2 could then be determined, and then the oxygen non-stoichiometry could be found by using the δ-pO_2 relationship determined in chapter 5. This procedure was repeated for other temperatures as well and then these values are plotted in the graph shown in Fig. 6.11.

The gradient of the line corresponds to the chemical expansivity. The relationship is non-linear, with the increase in lattice parameter becoming less with increasing δ. For $0.13<\delta<0.21$ the extracted chemical expansivity is found to be 0.1055 Å, and for $0.21<\delta<0.31$ the chemical expansivity is 0.0339 Å. It is largely independent of temperature as can be seen in the graph, although the temperature range is limited.

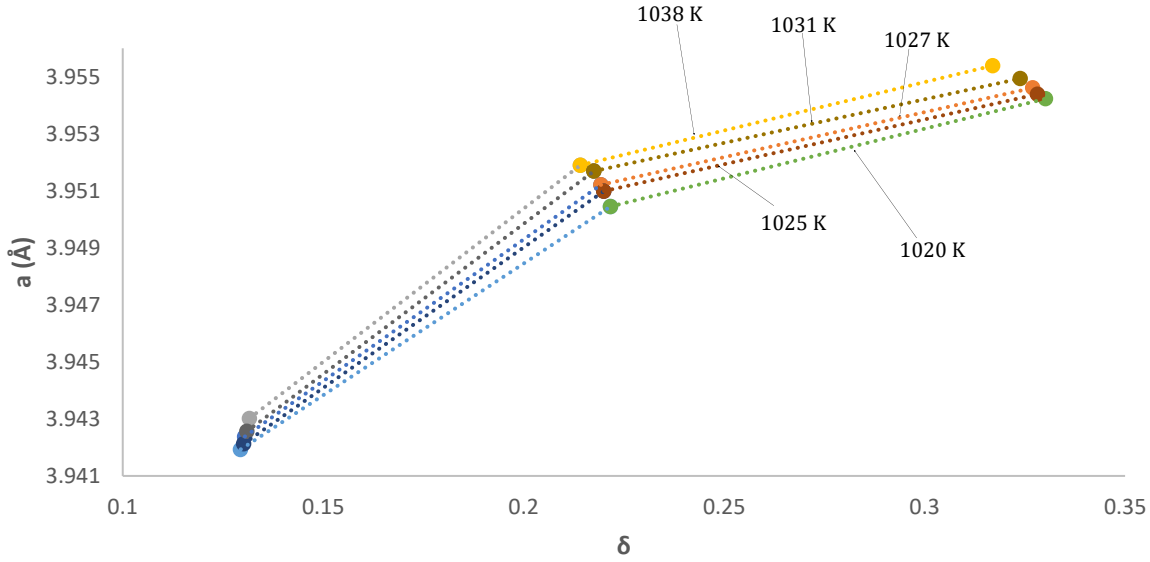

Figure 6.11: Lattice parameter versus δ (calculated from the TGA work in chapter 5). 3 different buffer gases were used to get the pO_2 for each point. Temperatures found from internal measurement technique with Y_2O_3 were used in calculations.

The temperature versus lattice parameter data was then plotted for each buffer gas in Fig. 6.12. This temperature difference is from the gradient across the bed, not from different furnace set-point.

Thermal expansivity values are 8.48 x 10^{-5} (± 8.30 x 10^{-6}) Å/C, 6.52 x 10^{-5} (± 6.32 x 10^{-6}) Å/C and 6.34 x 10^{-5} (± 2.71 x 10^{-5}) Å/C for 1:5, 20:1 and 1:20 respectively. The gradients are similar for 1:20 CO_2 to CO and 20:1 CO_2 to CO buffer gases, but different with 1:5 CO_2 to CO.

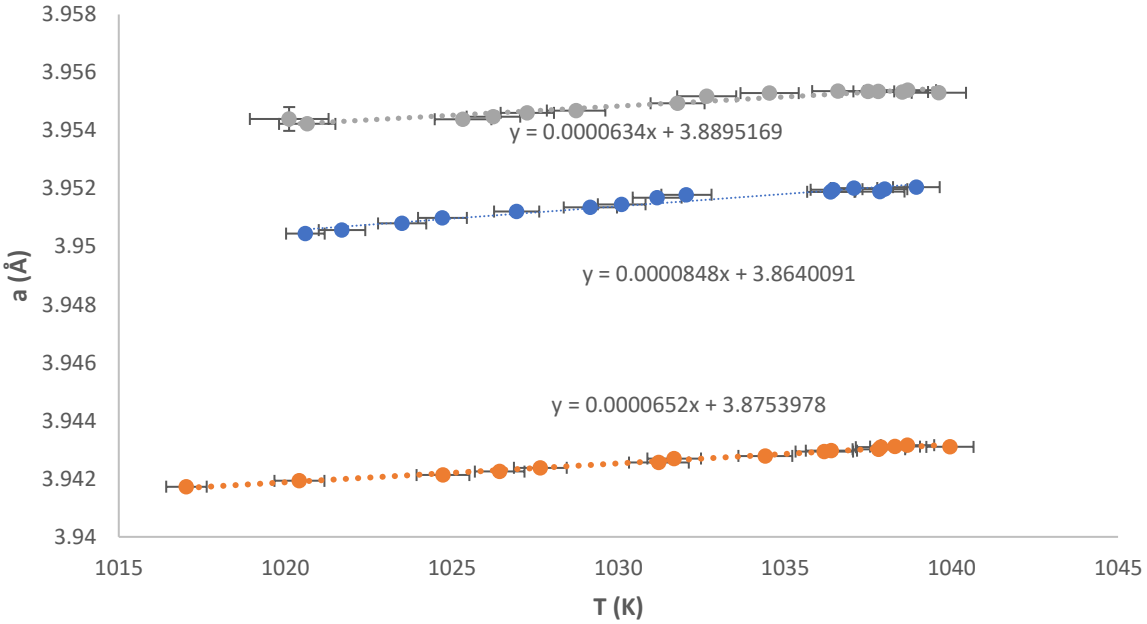

Figure 6.12: Lattice parameter as a function of temperature determined from Y_2O_3 measurement technique. The gradient is determined by taking a measurement at 15 separate equidistant points moving up the bed.

The thermal expansivity values extracted from Fig. 6.12 have not taken into account the difference in δ between the data points. In order to account for this, a more robust procedure for estimating the thermal expansivity involves a multivariate least squares regression procedure across the whole dataset. This was a least squares procedure that aimed to minimise the following equation:

$$w_i = a_i - \hat{a}_i \qquad \text{Eq. 6.5}$$

where the residual for the *i*th data point w_i is defined as the difference between the observed response value a_i and the fitted response value $\hat{a}_i$, and is identified as the error associated with the data.

As this was a 3 variable regression process, the following model formula was used to fit with the data which relates the unit cell parameter to the oxygen non-stoichiometry:

$$f(\delta, T) = a = \frac{\partial a}{\partial \delta}\left(\delta - \delta_{ref}\right) + \frac{\partial a}{\partial T}\left(T - T_{ref}\right) + a_{ref} \qquad \text{Eq. 6.6}$$

Where δ is the oxygen non-stoichiometry, a is the lattice cell parameter, $\frac{\partial a}{\partial T}$ is the thermal expansivity, T is temperature, a_{ref} is the reference lattice cell parameter at a known temperature (T_{ref}) and pO_2 which in this case is chosen to be 1017 K and 20:1 CO2 to CO, $\frac{\partial a}{\partial \delta}$ is the chemical expansivity and δ_{ref} is δ at a temperature of 1017 K and pO_2 of 20:1 CO2 to CO found from the TGA work. From the fits using the values of thermal and chemical expansivity are given in table 6.1 for the 3 buffer gases.

Table 6.1: Chemical and thermal expansivities of LSFM6473 under various buffer gasses at 1093 K.

Buffer gas at 1093 K	**Chemical expansivity (Å)**	**Thermal expansivity (Å/K)**
1:5 CO_2/CO	0.04788	9.422 x 10^{-5} (± 9.26x 10^{-6})
1:20 CO_2/CO	0.00218	6.327 x 10^{-5} (± 6.44 x 10^{-6})
20:1 CO_2/CO	0.1262	6.118 x 10^{-5} (± 6.13 x 10^{-6})

The values of thermal expansivity extracted via the multivariate least square regression for buffer gasses 1:20 and 20: 1 CO_2/CO are in good agreement with their equivalent values from Fig. 6.12, suggesting that the influence of δ between data points was not as significant in this specific case. The chemical expansivity can be seen to be non-linear in the range of potential δ values, as was the case seen in Fig. 6.11.

6.2.2 In operando oxygen non-stoichiometry

The thermochemical expansivities determined for LSFM6473 can also be used to determine the oxygen non-stoichiometry of the OCM in an integral packed bed reactor operating at 1093 K.

In addition the reactor model introduced in chapter 3 may make use of the δ-pO_2 thermodynamics of LSFM6473 discussed in chapter 5 in order to predict the oxygen non-stoichiometry at any point in the bed and compare with the values predicted by the

XRD data. For the WGS experiments from section 6.1.4 the oxidation profile at the end of the oxidation half cycle and at the end of the reduction half cycle can be seen in Fig. 6.13 compared with the values determined from either XRD or the model.

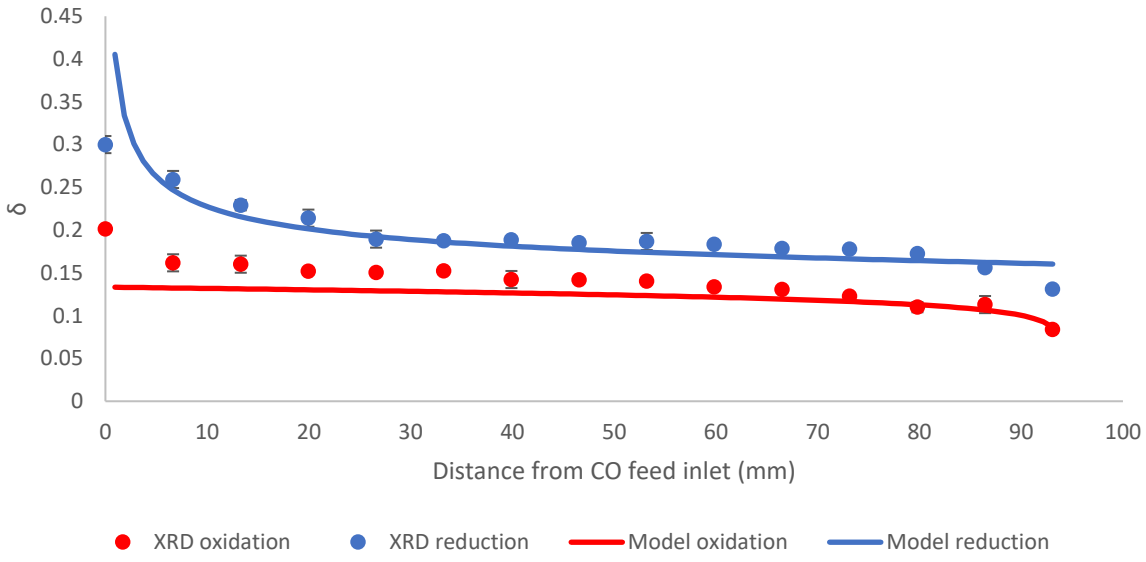

Figure 6.13: Oxidation profile across the LSFM6473 reactor bed during CLWGS cycling, A comparison is given of predicted δ values from XRD and by use of the reactor model introduced in chapter 3. 2.23 g of active LSFM6473 was cycled between counter-current feeds of 5% H_2O and 5% CO in argon for 60 cycles at a temperature of 1093 K with gas nominal molar flowrate of 3.4 × 10^{-5} mol s^{-1}. The bed length is 100 mm, with 4 mm diameter.

In Fig. 6.13, δ is the most sensitive to changes at the inlet/outlet ends, as that part of the bed has the most contact with reactant gas in its initial more reducing or oxidising state. In the figure water vapour is flown across the bed from the right-hand side resulting in a decrease in δ especially at the end of the bed, while carbon monoxide is flown in from the left-hand side resulting in an increase in δ near the CO inlet. At the end of each half cycle the direction of flow is switched and so for consequent cycles the oxidation front is pushed back and forth through the bed. At stable cycling the bed moves between consistent profiles of the oxidation front through the bed.

The comparison in Fig. 6.13 shows how the XRD results agree with moderate success to the values predicted by the model. However there are issues with the XRD data being unable to predict the extent of reduction at the ends of the bed, and the centre of the bed which appears to have stable δ values appears to have a slight gradient in the XRD data.

The large gradient shown by the model at the reducing end is concerning because if a phase change were to occur the available oxygen capacity of the OCM could either be decreased or the OCM could no longer behave as a non-stoichiometric perovskite hence resulting in a drop in product quality. However in this case there does not seem to be any such drop in product quality, and the system can consistently switch between the two half cycles achieving stable conversions as shown earlier in Fig. 6.8 and Fig. 6.9.

Fig. 6.14 shows a profile of the change in oxygen non-stoichiometry over the course of the 8th CLWGS cycle at a single point 46.55 mm above the CO inlet. Values of δ determined via XRD technique are compared against the model.

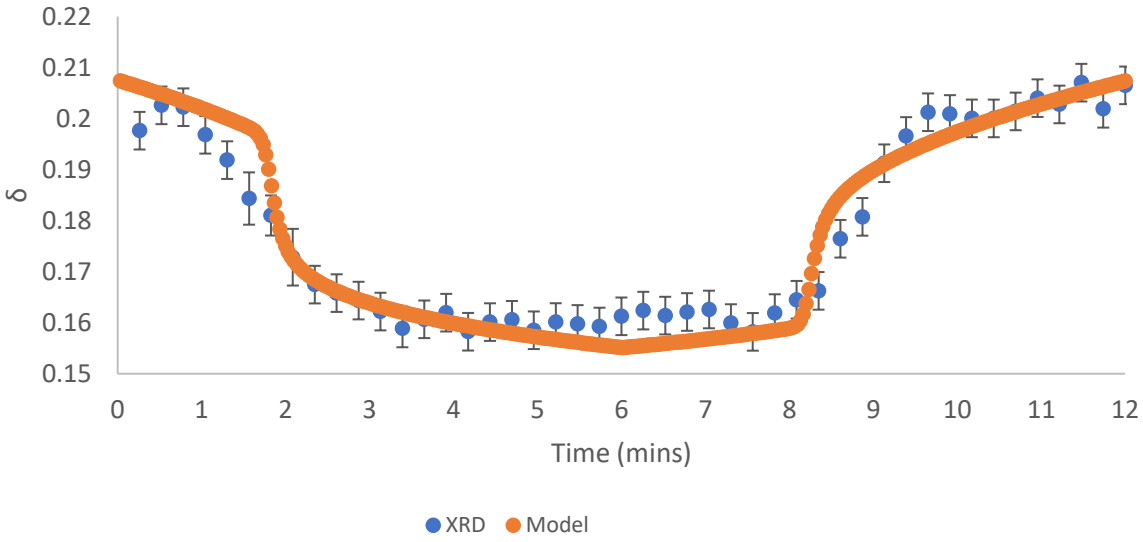

Figure 6.14: Blue points represent the oxygen non-stoichiometry during the 8th WGS cycle of a single point 46.55 mm above the CO inlet of the reactor bed when flowing counter-current streams of 5% H_2O and 5% CO at 1093 K. The bed length is 100 mm, with 4 mm diameter and material mass 2.23 g. The orange line represents the oxygen non-stoichiometry with time predicted by the simulation.

The shape of the curve for the change in δ with time in Fig. 6.14 does not appear to be symmetrical but tends to return to the same point after each whole cycle. The size and timing of the change in δ appears to match well with that of the simulation. The noise as well as the uncertainty which is present in the data however is problematic. In section 6.1 it was seen how larger dimensional changes in the crystal resulted in a more accurate reading.

Chapter 7 investigates more closely the effect of altering process parameters such as flowrate and temperature on the concentration profiles, and the simulation is expanded to incorporate these different parameters.

6.3 Summary

For the case of LSFM6473, in-situ XRD was carried out to gain an understanding of the internals of the reactor system and the material stability during cycling. The lattice parameter of the material was tracked as a function of position along the bed. For the case of cycling between 20:1 CO_2 to CO and 1:20 CO_2 to CO buffer gases it was not possible to accurately determine the changes in lattice parameter corresponding to the smallest changes in δ at the reducing end where the uncertainty was larger than the average lattice parameter change in the entire half cycle . This was also not helped by the fact that the solid had previously come into equilibrium with a 1:20 CO_2 to CO gas and so would see very little oxygen removal and take a long time to reach steady cycling. However when cycling the material between feeds of 5% H_2O and 5% CO, the bed was able to reach steady state more quickly and the lattice parameters could be more accurately tracked in the extreme reducing end.

Thermal and chemical expansivities were determined for LSFM6473 and used to predict the internal variations in oxygen non-stoichiometry along the bed. Due to the small change in cell parameter, the cycling experiment using buffer gases of 20:1 and 1:20 CO_2/CO could not accurately determine changes in cell parameter at the reducing end, while when undergoing WGS the larger change in oxygen content enabled better comparison with the simulation.

Chapter 7: Chemical looping water-gas shift cycling with $La_{0.6}Sr_{0.4}Fe_{0.67}Mn_{0.33}O_{3-\delta}$ and $Ce_{0.8}Zr_{0.2}O_{2-\delta}$ in a packed bed reactor

TGA studies in chapter 5 showed that doping a modest amount of manganese onto the B-site of LSF641 changed the shape of the δ-pO_2 curve and eliminated the presence of the plateau in the central pO_2 range. As a result, LSFM6473 was found to exhibit higher oxygen capacity than previously investigated materials for CLWGS, suggesting it will be possible to increase the duration of half-cycle feeds in a CLWGS reactor and still achieve high conversions. CZ82 was also suggested in chapter 2 as a high oxygen capacity OCM potentially with a similar δ-pO_2 curve shape to that of LSFM6473. Both LSFM6473 and CZ82 should also be able to overcome the theoretical maximum limit for conversion of both reactants when compared to a conventional WGS reactor.

For this chapter experiments are carried out using CZ82 and LSFM6473 with unmixed feeds of CO and H_2O and it is expected that both reactants will be able to achieve conversions in excess of 50% and thereby overcome the equilibrium limitations of mixed reactants. In addition this chapter will serve to verify experimentally the proposed theory in chapter 3 for an optimal δ-pO_2 relationship for a non-stoichiometric OCM.

The purpose of this chapter is to study the performance of CZ82 and LSFM6473 in a working fixed bed integral reactor and look at the conversions possible at different feed durations and temperatures, and prove that an understanding of the thermodynamics of such materials is sufficient to model and predict their performance in a working reactor.

7.1 Benchmark data with LSF641

When considering the effect of processing conditions like feed durations on conversions and product quality it is helpful to have a benchmark material to which comparisons can be made. LSF641 was chosen as the material of choice for this purpose due to the existing literature on this material.

For the experiment a bed of 0.01 mols LSF641 (2.21 g measured) was cycled with 1 and 2 minute feed durations of 5% H_2O and 5% CO, and the bed length was measured as 17.5

cm. Outlet concentration profiles at the different feed lengths, and conversions per cycle are given in Fig. 7.1 and 7.2.

The mean residence time for the LSF641 bed is calculated to be 44 ms. In the later sections of this chapter separate experiments are also carried out using 0.01 mols of LSFM6473 and CZ82 as the OCMs, respectively giving mean residence times of 22 ms and 29 ms at most. This indicates that the reactor geometry and gas flowrate is not expected to hinder the shape of the concentration profiles. For the case of LSF641, the slight tail seen at the ends of the profiles in Fig. 7.1, more so for water vapour, is more likely due to pressure imbalance in the system and potential cold spots in the pipework. The WGS reaction is known to exhibit fast kinetics (Metcalfe et al 2019, de Leeuwe et al 2021), and comparisons between model and experimental results later on in section 7.7.1 also add credence to the assumption of assuming a system limited only by the thermodynamics.

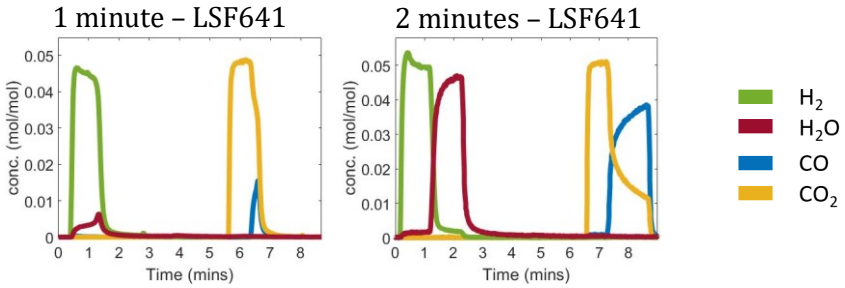

Figure 7.1: Outlet H_2/H_2O and CO_2/CO mole fractions during cycling at steady state with 2.21 g (0.01 mols) LSF641. The effect on the outlet compositions are shown for half cycle durations of 2 and 1 minutes, during the cycles 30, 60 and 90 respectively. Cycling between 5% H_2O and 5% CO gases at 1093 K at nominal molar flowrate of 3.4×10^{-5} mol s^{-1}. The error in the readings is ± 100 µmols based on the calibrations from the mass spectrometer.

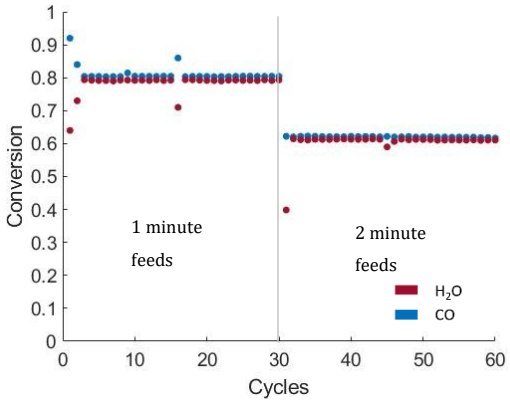

Figure 7.2: H_2O and CO conversion per cycle for each feed duration for LSF641. 2.21 g of LSF641 was cycled between counter-current feeds of 5% H_2O and 5% CO in argon. Conversions with feed durations of 2 and 1 minutes are shown.

In the concentration profiles in Fig. 7.1 it is seen that unreacted water vapour passes through the reactor at an earlier point in the 1 minute half cycle in comparison to the longer 2 minutes. However the rate of hydrogen and carbon dioxide production for the 1 minute half cycles is higher than that for 2 minutes. This suggests that using feed durations much further than 2 minutes would risk wiping out the profile across the bed and result in unreacted 5% gases of CO and H_2O flowing through the bed. It is expected that the use of OCMs with higher capacity in the active pO_2 range should be able to undergo cycling at longer feed durations while still maintaining a high hydrogen production rate, and the breakthrough of unreacted gas should occur later in the half cycle.

As the bed had already been activated prior to the experiment the conversions in Fig. 7.2 quickly reach a stable value of ~80% at the start of 1 minute feed duration cycling. The material shows a good responsivity to changes in feed duration, reaching steady cycling in no more than a single cycle after switching to 2 minute feed durations, with the conversions dropping to ~61%. This is an expected behaviour as the operating range of partial pressures is not significantly affected by changes to feed duration, meaning that a bed already at steady cycling will quickly reach equilibrium with a new feed duration. These conversions are clearly in excess of 50%, and thus have overcome the equilibrium limitations of mixed reactants that was covered in chapter 2. A mass balance was also

carried out showing that carbon formation did not occur within measurement uncertainty.

7.2 Performance using different half cycle durations

7.2.1 Cycling with CZ82 at different half cycle durations

When optimising the operation of a packed bed CLWGS reactor one of the key parameters to consider is the feed duration. It is expected that shorter feed durations would result in an increase in the conversion since there is a smaller change in oxygen content of the material, and the use of higher capacity OCMs should allow for longer feed durations to be used than with LSF641 and still achieve high conversions. This hypothesis is tested by cycling 0.01 mols of 80-160 µm CZ82 (1.62 g measured) using feed durations of 5, 4, 3, 2 and 1 minutes of 5% H_2O and 5% CO. The bed length was measured as 11.7 cm. 45 cycles were carried out at each feed duration in order to reach steady state at 1093 K. Fig. 7.3 and Fig. 7.4 show the effect of feed duration on the outlet gas composition during the 45th cycle of each feed duration with CZ82.

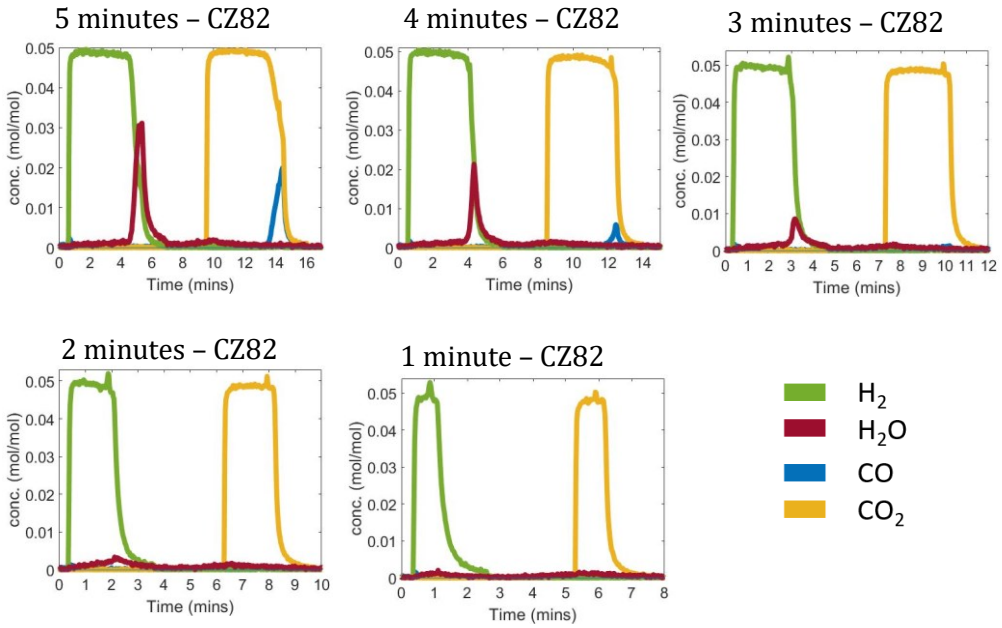

Figure 7.3: Outlet H_2/H_2O and CO_2/CO mole fractions during cycling at steady state with 1.62 g (0.01 mols) CZ82. The effect on the outlet compositions are shown for half cycle durations of 5, 4, 3, 2 and 1 minutes, during the 45th cycle for each duration. Cycling between 5% H_2O and 5% CO gases at 1093 K at nominal molar flowrate of 3.4 × 10^{-5} mol s^{-1}. The error in the readings is ± 100 µmols based on the calibrations from the mass spectrometer.

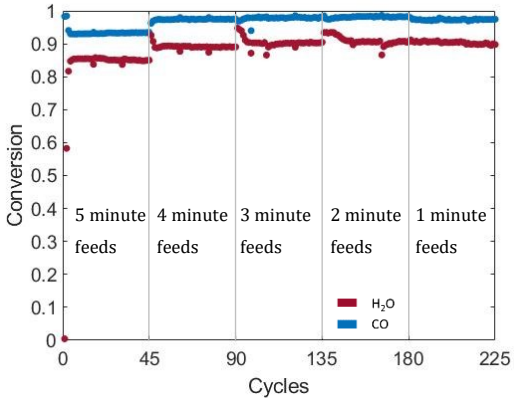

Figure 7.4: H_2O and CO conversion per cycle for each feed duration for CZ82. 1.62 g of CZ82 was cycled between counter-current feeds of 5% H_2O and 5% CO in argon. Conversions with feed durations of 5, 4, 3, 2 and 1 minutes are shown.

In Fig. 7.3 it can be seen that for CZ82 the shorter feed duration cycles can give almost pure H_2 (in the case of 1 minute) and CO_2 (in the case of 1, 2 and 3 minutes). However changing the feed duration is more complicated that simply extending or shortening the length of the concentration profile. Longer feed durations have the effect of lowering the product quality, with H_2O breakthrough occurring in the case of 4 and 5 minute feed durations. This behaviour means that an appropriate feed length would have to be chosen in order to satisfy a certain target product quality: for example if a feed length of 4 minutes were to be chosen Fig. 7.3 shows that this would result in a mixed product of CO_2 with a small amount of CO meaning that an additional separation stage would be required before the CO_2 could be used.

Fig. 7.4 shows the H_2O and CO conversions for each cycle with CZ82. During the initial 5 minute feed duration cycles, Fig. 7.4 shows the reactor is able to quickly reach steady state after only 4 cycles and maintains a steady degree of conversion. The H_2O conversion jumps from a near-zero value during cycle 1 up to a value of 85% at cycle 4. The CO conversion on the other hand starts from a value of almost 100% conversion before dropping to a steady cycling value of 93%. This is because the OCM is initially in a fresh unreacted state having been synthesised in air, meaning that it will start from a fully oxidised state without oxygen vacancies. This results in the H_2O in cycle 1 passing through the reactor unreacted and the almost complete conversion of CO during the first reduction step. The subsequent oxidation half cycles cannot return the system to the

initial fully oxidised state where it had been in equilibrium with air, and the following oxidation and reduction half cycles result in more of the bed being utilised and eventually a shift of the chemical potential gradient to a stable state between the two feed inlets.

This reason for the difference in product quality between oxidation and reduction half cycles, as well as conversions, is due to a discrepancy in H_2O flowrate (determined via pressure transducer logging data as ~10% higher than the setpoint of 50 ml/min), causing the bed to become oxidised more than it is reduced per cycle. The concentration of CO in the outlet streams would be expected to be higher for a system with equal flowrates of oxidising and reducing inlet streams at 50 ml/min. An oxygen balance accounting for this flowrate difference was found to close to within 2.6% average across the 45 cycles as shown in table 7.1, with oxygen exchange of 421 μmol and 433 μmol average during oxidation and reduction.

Table 7.1: Oxygen balance for each feed duration for CZ82, accounting for 10% water vapour flowrate discrepancy. The averages for each feed duration are given. The moles of oxygen uptake during oxidation and removal during reduction are in good agreement for each feed duration and lie within the uncertainties. In order to avoid skewing the data, the average for the initial 5 minute feed duration cycles has been taken from cycles 4 to 45 due to the activation of the bed, and averages for the other feed durations are also taken at steady state.

Feed duration (mins)	Cycles	Moles oxygen uptake during oxidation	Moles oxygen removed during reduction
5	4 to 45	4.34×10^{-4} ($\pm 7.66 \times 10^{-6}$)	4.33×10^{-4} ($\pm 5.68 \times 10^{-6}$)
4	48 to 90	3.68×10^{-4} ($\pm 6.25 \times 10^{-6}$)	3.62×10^{-4} ($\pm 4.96 \times 10^{-6}$)
3	96 to 135	2.79×10^{-4} ($\pm 4.86 \times 10^{-6}$)	2.74×10^{-4} ($\pm 3.96 \times 10^{-6}$)
2	146 to 180	1.87×10^{-4} ($\pm 3.47 \times 10^{-6}$)	1.84×10^{-4} ($\pm 2.74 \times 10^{-6}$)
1	181 to 225	9.33×10^{-5} ($\pm 2.14 \times 10^{-6}$)	9.19×10^{-5} ($\pm 1.54 \times 10^{-6}$)

Fig. 7.1 showed the concentration profile for a 1 minute feed duration oxidation half cycle for LSF641. A comparison between CZ82 and LSF641 at 1 minute feed durations shows that the H_2O breakthrough for LSF641 occurs far sooner, and H_2O fraction rises to about 0.006 before the valve switch. This means that the capacity of the bed in the case

of LSF641 is less, and the position along the bed which corresponds to the product gas composition is closer to the corresponding outlet since the oxidation or reduction fronts move further through the bed. During steady cycling the opposite end of the bed to the feed is not affected, and the full capacity of the material is not being used in either case of CZ82 or LSF641 at 1 minute feed durations. For the full capacity to be used the reactant would have to be flown long enough for complete breakthrough to occur and for the oxidation profile to be wiped out (%5 H_2O or 5% CO to be seen in the outlet), though this would compromise steady cycling conversions. The greater the oxygen capacity of the OCM, the longer it takes for this to happen.

Fig. 7.3 shows an unexpected small peak occurs towards the end of the concentration profiles of H_2 and CO_2. It is likely that this spike is occurring as a result of the valve switch to the argon purge and the pressure drops between the various gas paths and the reactor bed not being balanced. The value of the system pressure measured by the pressure transducer located at the H_2O inlet to the reactor bed was found to change by about 0.13 bar when switching between argon and H_2O before stabilising. The size of this spike in the profile is negligible for LSF641 since the system had been disassembled and then reassembled between these experiments, which would cause changes to the size of the pressure drops.

It can be seen that the outlet concentration profiles for H_2 /H_2O and CO_2 /CO in Fig. 7.3 for the same feed durations are not equivalent with each other, with H_2O showing an increase at an earlier position in the profile for 3, 4 and 5 minutes than CO, which does not show increases until 4 and 5 minutes. This difference is likely due to the use of a higher H_2O flowrate, meaning that more water molecules are present entering and leaving the reactor in the same length of time and thus more oxygen vacancies are taken up and the capacity of the material is exhausted sooner than it would be with a lower CO flowrate. Another possible reason, though unlikely to play a major effect, is the thermodynamics of the material, specifically the shape of the δ-pO_2 curve for CZ82 (shown in chapter 2). The gradient of the curve is asymptotic towards $\delta = 0$, meaning that the change in δ is smaller per step change of pO_2 in the higher log pO_2 range than in the lower log pO_2 range. Therefore, since there is less capacity at the H_2O inlet this

would mean that during the reduction half cycle the breakthrough of the CO curve should occur sooner than the H_2O curve does. This does not happen in the case of the experimental data in Fig. 7.3 suggesting that this has a negligible effect for the case of CZ82 (also due to the lack of a plateau in the middle of the pO_2 range as in LSF641), and is overwritten by the H_2O flowrate discrepancy.

Following the experiment it was noticed that the CZ82 powder had undergone a colour change from yellow to black, where the fresh sample prior to the experiment has been yellow. Colouration in zirconia compounds have been widely reported in literature under different heating treatments. Zhu et al (1992) investigated the colour changes associated with 12 mol% ceria-doped zirconia noting a black colour after subjecting the material to a 1 hour reduction in H_2+Ar at 1803 K. They attributed this colouration to the reduction of ceria (4+ to 3+) due to the colour centers related to Ce(III). Since the last half cycle was a reduction half cycle at the end of the experiment it follows that a change in the colour of the reduced end of the bed would occur.

The values of conversion in Fig. 7.4 are relatively constant for the duration of the 5 minute feed cycles. Following regular calibrations each 15 cycles where the bed is flushed with argon, the bed can rapidly return to its steady cycling state after only 1 cycle. The use of a longer half cycle duration to begin with before switching to consecutively shorter durations practically allows for the initial activation of the bed and steady state to be reached far sooner than possible with shorter feed durations.

During steady cycling for the 5 minute feed duration cycles, the oxidation half cycle achieves almost 100% conversion of H_2O to H_2 until after the fourth minute which sees a H_2O breakthrough and conversion dropping to about 40% at the end of the half cycle. The reduction half cycle is similar although the CO curve does not completely breakthrough the CO_2 curve at the end of the half cycle. While the presence of H_2O in the H_2 product could be overcome with a downstream evaporation stage, the separation of CO from the CO_2 is a more costly operation to perform, meaning that 5 minutes feed duration is not an ideal setting for this parameter.

After switching to the 4 minute feed duration cycles, the system was able to return to steady state after only 2 cycles demonstrating excellent responsiveness to a change in operating conditions. The log pO_2 (bar) consistently ranges between -21.5 to -17 during steady state cycling for each feed duration and this allows for the bed to quickly reach a steady conversion after changing the feed duration. The decrease in feed duration caused a higher conversion of H_2O and CO to be achieved at 89% and 97% respectively. Oxygen balance across the 45 cycles closed to within 2.5%. There is a lower concentration of H_2O and CO in their respective outlets, but the 0.006 mole fraction of CO in the outlet means the CO_2 would still require processing before use.

The increase in conversion with decreasing feed duration becomes less significant from 3 minutes and shorter since less of the bed is being used. Conversions of H_2O and CO increase to 90% and 98% respectively, only a 1% increase in comparison to the 4 minute feed duration cycles. This trend continues for 2 minutes and 1 minute feed durations which have similar conversions to the 3 minute cycles and any conversion increase is < 1%. For these cycle durations the CO concentration in the outlet CO_2 is also mostly negligible, no more than roughly 0.1% at the end of the reduction half cycle. Since the conversion increase is also negligible with shorter feed durations, 3 minutes seems to be the optimal feed duration to use for CZ82 cycling since it would be far more practical to eliminate having to potentially use a CO/CO_2 separation step as with longer feed durations, and this feed duration will be used for further experiments detailed in this thesis. The oxygen balance averaged across each 45 cycle feed duration for 3 to and 1 minutes all close to within < 3.5%. Carbon and hydrogen balances over all feed durations closed to < 5% suggesting no noticeable presence of carbon deposition and presence of leaks.

7.2.2 Cycling with LSFM6473 at different half cycle durations

As with CZ82, LSFM6473 was also investigated using the same reactor program as in section 7.2.1, with 0.01 mols of 80-160 μm material (2.21 g measured) being used at 1093 K with bed length 8.7 cm. Cycles with feed durations of 5, 4, 3, 2 and 1 minutes of 5% H_2O and 5% CO were carried out. Reactant gas flowrates of 50 ml/min were used. 45 cycles were done at each feed duration in order to reach steady state. Fig. 7.5 and Fig.

7.6 show the effect of feed duration on the outlet gas composition during the 45th cycle of each feed duration with LSFM6473.

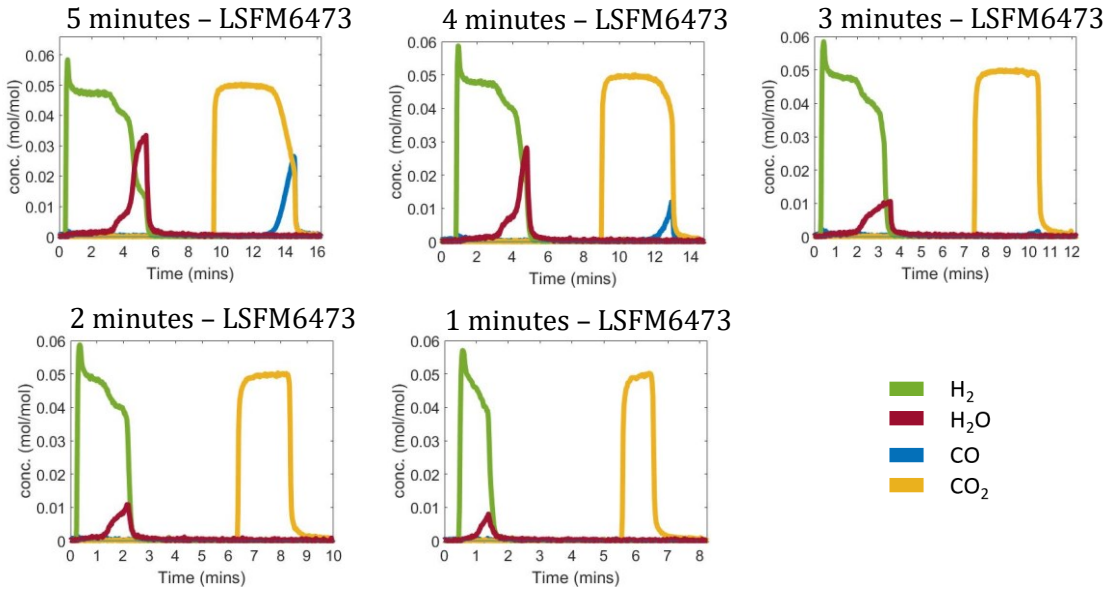

Figure 7.5: Outlet H_2/H_2O and CO_2/CO mole fractions during cycling at steady state with LSFM6473. The effect on the outlet compositions are shown for half cycle durations of 5, 4, 3, 2 and 1 minutes, during the 45th cycle for each duration. 2.21 g of LSFM6473 was used with 5% H_2O and 5% CO gases at 1093 K at nominal molar flowrate of 3.4 × 10^{-5} mol s^{-1}. Uncertainty in the measurements was ± 100 µmol based on the mass spectrometer data.

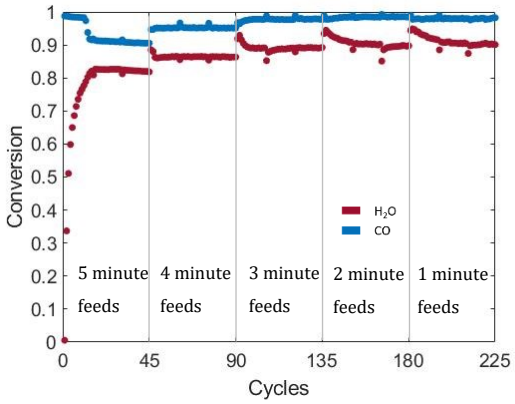

Figure 7.6: H_2O and CO conversion per cycle for each feed duration for LSFM6473. 2.21 g of LSFM6473 was cycled between counter-current feeds of 5% H_2O and 5% CO in argon at 1093 K at nominal molar flowrate of 3.4 × 10^{-5} mol s^{-1}. The conversions achieved with feed durations of 5, 4, 3, 2 and 1 minutes are shown.

In comparison with CZ82, of note is the difference in product quality in the oxidation half cycle, where in the case of each feed duration there is a fraction of H_2O in the outlet. This is still significant even at shorter feed durations with roughly 8 times greater mole fraction of H_2O in the outlet at 1 minute feed durations when compared with CZ82. The product quality of the reduction half cycle on the other hand is mostly similar to that seen with CZ82, with negligible CO seen in the outlet (there is a very slight peak at < 0.1% at the end of the half cycle) until after 3 minute feed durations, although the concentration of CO in the outlet after 3 minutes is seen to be greater than with CZ82. Overall the presence of H_2O in the outlet product stream, while undesirable, requires a much less complicated separation process that with CO from CO_2, making the product quality of the reduction half cycle the bottleneck as was the case with CZ82.

As with the CZ82 half cycle duration experiment in section 7.2.1, there was also a discrepancy in the flowrate of water vapour (~10% higher than the setpoint of 50 ml/min). While this is generally undesirable, it does allow for a valid comparison to be made with the CZ82 system in analysis, as the flowrate discrepancy in both experiments was found to be the same. Table 7.2 shows the oxygen balance at the different feed durations after having accounted for the discrepancy in flowrates. The values are in good agreement except during the initial 5 minute cycles. This is due to the activation of the bed which is starting from the freshly synthesised material. A further 45 cycles carried out after the 1 minute feed durations shows good agreement with only a roughly 0.99% difference between oxidation and reduction. This discrepancy was not observed in the data for CZ82 due to the faster responsiveness of that system at the start of cycling.

Table 7.2: Oxygen balance for each feed duration for LSFM6473, accounting for 10% water vapour flowrate discrepancy. The averages for each feed duration are given. The moles of oxygen uptake during oxidation and removal during reduction are in good agreement for each feed duration and lie within the uncertainties. In order to avoid skewing the results due to the initial activation of the bed, the average for the first set of 5 minute feed duration cycles is taken from cycles 16 to 45 where steady cycling has been reached.

Feed duration (mins)	Cycles	Moles oxygen uptake during oxidation	Moles oxygen removed during reduction
5	16 to 45	4.32×10^{-4} ($\pm 6.90 \times 10^{-6}$)	4.29×10^{-4} ($\pm 5.55 \times 10^{-6}$)
4	49 to 90	3.64×10^{-4} ($\pm 5.71 \times 10^{-6}$)	3.59×10^{-4} ($\pm 4.82 \times 10^{-6}$)
3	100 to 135	2.81×10^{-4} ($\pm 4.45 \times 10^{-6}$)	2.78×10^{-4} ($\pm 3.81 \times 10^{-6}$)
2	151 to 180	1.90×10^{-4} ($\pm 3.18 \times 10^{-6}$)	1.87×10^{-4} ($\pm 2.65 \times 10^{-6}$)
1	196 to 225	9.53×10^{-5} ($\pm 1.70 \times 10^{-6}$)	9.39×10^{-5} ($\pm 1.45 \times 10^{-6}$)

It should be noted that the material is in an as-synthesised state at the start of the experiment with δ close to 0. As was encountered in the case of CZ82, at the start of the experiment the conversions for H_2O start from a value close to zero and gradually increase while the CO conversion start from almost 100% and drops to a steady cycling value. The reasons for this are the same as explained for CZ82 in section 7.2.1.

Fig. 7.6 shows the conversions of H_2O and CO per cycle. In comparison with CZ82, Fig. 7.6 shows that LSFM6473 gives only marginally lower conversions at longer feed durations (e.g. 85% H_2O conversion at 4 minutes as opposed to ~90% in CZ82). This is in line with the TGA buffer gas experiments from chapter 4 which showed that the δ change for CZ82 was roughly 36% greater than for LSFM6473 when cycling between pO_2s of 10^{-20} bar to 10^{-15} bar. Differences in conversion become more noticeable with increasing feed length as more of the capacity is used up and the reactant gas concentration curves breaks through the product gas curves.

LSFM6473 requires a longer response time to reach steady state than was seen with CZ82, taking 15 cycles before reaching its initial steady state during 5 minute feed duration cycling as opposed to just 4 cycles with CZ82. After the initial activation of the material the number of cycles taken for the conversions to stabilise increases with shorter feed durations, taking only 2 cycles to stabilise with 4 minute feed durations

while taking roughly 7 cycles to stabilise with 3 minute feed durations. This is an expected behaviour since with increasing feed durations the oxidation front can be moved further into the bed, and more of the bed is being utilised hence it takes less time to reach steady cycling.

As with the cycle duration experiment for CZ82 in section 7.2.1, there was a roughly 10% greater flowrate of water vapour than the setpoint of 50/min, meaning that if the flowrates of CO and H_2O were equal, then the CO concentration should be higher than it is in the outlet concentration profiles in Fig. 7.5. In order to verify this assumption, the experiment was repeated using the same LSFM6473 reactor with the error in flowrate corrected. The pressure balance in the system was also adjusted by use of needle valves on the lines to prevent the occurrence of pressure drops when switching valves and avoid the initial surge in H_2 concentration. The same process conditions as before were used except the flowrates for both CO and H_2O were set to 55 ml/min.

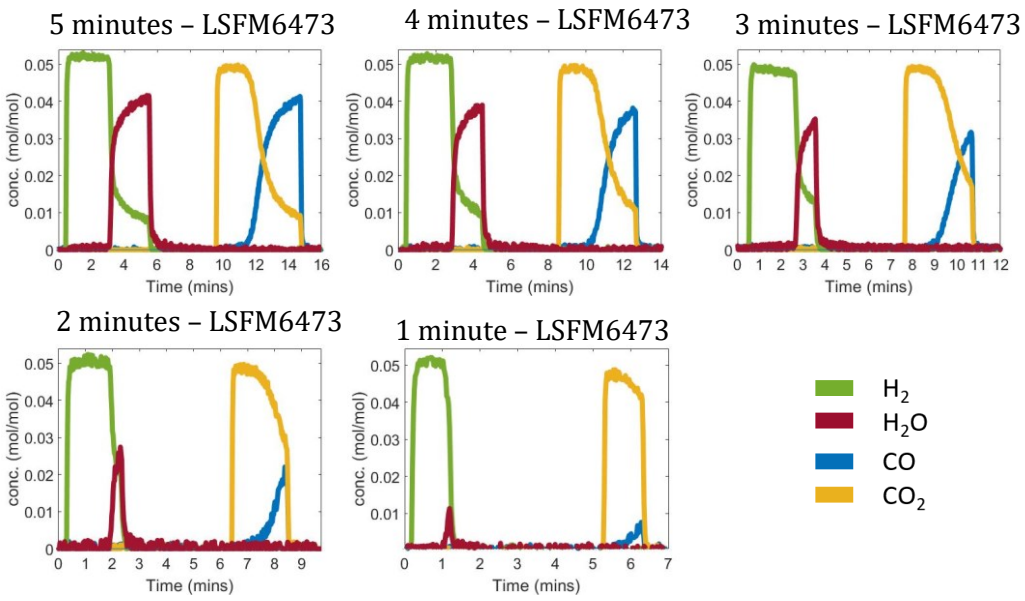

Figure 7.7: Outlet H_2/H_2O and CO_2/CO mole fractions during cycling at steady state with LSFM6473. A repeat experiment for the results from Fig. 7.7, but with equal feed flowrates of 55 ml/min. Outlet gas compositions are shown for half cycle durations of 5, 4, 3, 2 and 1 minutes during steady cycling. 2.21 g of LSFM6473 was used with 5% H_2O and 5% CO gases at 1093 K at nominal molar flowrate of 3.4 × 10^{-5} mol s^{-1}. Uncertainty in the measurements was ± 100 µmol based on the mass spectrometer data.

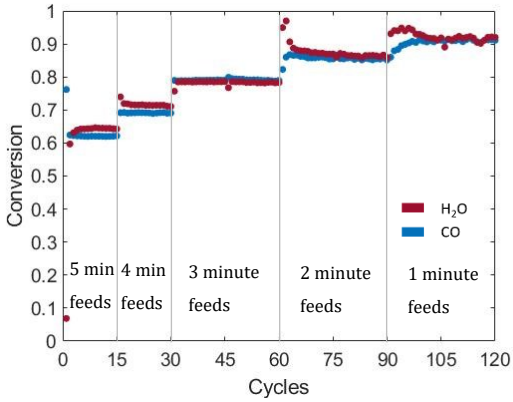

Figure 7.8: H_2O and CO conversion per cycle for each feed duration for LSFM6473. Repeat of experiment in Fig. 7.7, but with equal feed flowrates of 55 ml/min. 2.21 g of LSFM6473 was cycled between counter-current feeds of 5% H_2O and 5% CO in argon at 1093 K at nominal molar flowrate of 3.4 × 10^{-5} mol s^{-1}. The conversions achieved with feed durations of 5, 4, 3, 2 and 1 minutes are shown.

The flowrates were confirmed to be equal via a flowmeter, and the needle valves in the system were better adjusted to minimise the effect of the pressure drop at valve switch, hence there is no rise in H_2 concentration past 5% at the start of the cycles. Both concentrations of H_2O and CO in the outlet in Fig. 7.7 have increased due to the fact that more gaseous compounds are being fed into the reactor at the higher flowrate. This also allows for the features of the reactant gas breakthrough to be seen more clearly. At shorter feed durations the concentration of water vapour starts to increase at a point in time that is proportionally later in the half cycle in comparison with longer feed durations. For example, the water vapour increase first occurs after ~2.8 minutes for the case of 5 minutes feed duration, 2.5 minutes for the case of 4 minutes feed duration and after ~ 2 minutes duration for 3 minutes feed duration. In other words this means that at 5 minutes feed duration, pure hydrogen can be produced for roughly 56% of the total half cycle time, whereas for the case of the shorter 3 minute feed durations, pure hydrogen can be produced for roughly 67% of the total feed duration. The feed durations can therefore be optimised depending on whether the purity of the product or the total production of hydrogen is more important.

The use of higher flowrates results in a decrease in the conversions in Fig. 7.8 compared to Fig. 7.6 which used a lower CO flowrate. As the bed had been previously used in experiments initial stable cycling at 5 minute feed durations is reached in only roughly 2 cycles. Conversions generally appear to take longer to reach a stable value at shorter feed durations as less of the bed is utilised during cycling. At all 5 feed durations, the

equilibrium limitations of the conventional WGS reactor has been overcome, and high purity high conversion hydrogen production is possible. There were no carbon species visible in the oxidation half cycles for lower CO flowrates which suggests that an industrial scale plant could eliminate the need for a PSA separation stage (the separation of water vapour via evaporation is much more straightforward) if unequal flowrates were used.

Overall when making a direct comparison with CZ82 the results suggest that for the case of unequal flowrates the optimal feed duration to use for LSFM6473 is 3 minutes, which is the same as was seen for CZ82. In the case of both materials the use of feed durations longer than 3 minutes is potentially undesirable due to the significant presence of CO in the reduction half cycle outlet stream. For unequal flowrates, the main distinguishing factor is the product quality of the oxidation half cycle since the differences in conversions at shorter feed durations are only < 1%. For the case with equal flowrates with LSFM6473, the optimal feed duration is better suited to 2 minutes, as the concentration of CO does not completely exceed the CO_2 concentration at this duration. Both CZ82 and LSFM6473 were shown to have a higher oxygen capacity than LSF641 in chapter 4, and the integral reactor cycling results at different feed durations in this chapter supports this observation. Both materials are able to be cycled at longer feed durations than LSF641, with the potential for H_2 production with minimal H_2O in the outlet, or CO_2 production with minimal CO in the outlet, neither of which was possible with LSF641.

The results also suggest that there exists a degree of flexibility with regards to product quality, where it may be possible to use unequal flowrates in order to achieve pure CO_2 or pure H_2 production and stable cycling. This could be desirable when operating at an industrial scale, where the flowrates could be adjusted to meet the requirements for different applications, depending on whether the purity of H_2 needs to be maximised or the conversion of H_2O needs to be maximised.

7.3 Performance using different operating temperatures

7.3.1 Cycling with CZ82 at different temperatures

For the case of the CLWGS packed-bed reactor described in this work the choice of the system temperature has an effect on the conversions and product quality that can be achieved, since the CO equilibrium constant degrades with increasing temperature. The experiments performed in this thesis are isothermal experiments, with the aim of keeping the temperature along the length of the reactor bed constant.

Previous experiments which investigated the half cycle feed duration in sections 7.2.1 and 7.2.2 used a temperature of 1093 K. This was because a mixed WGS reactor system operated at 1093 K would in theory be able to achieve maximum conversions for both reactants of 50% (Metcalfe et al, 2019), as the equilibrium constant for WGS at this temperature is unity, making this a good temperature for the purpose of comparison. Therefore, in order to determine the optimal temperature at which to operate the reactor in terms of conversion and outlet gas concentration, the investigations in this section range around a temperature of 1093 K.

0.01 mols (1.62 g measured) of 80-160 μm CZ82 in a packed bed reactor of length 11.7 cm was cycled 30 times at a temperature of 1093 K followed by 30 cycles each at temperatures of 1043 K, 993 K and 943 K respectively. Fig. 7.9 and Fig. 7.10 show the outlet concentration profiles and the conversions per cycle during the experiment.

In Fig. 7.9 a large tail can be seen on both the oxidation and reduction half cycles. CO is seen at the start of the profile during oxidation, and H_2O is seen at the start of the profile during reduction. While the presence of CO at the start of the oxidation half cycles may suggest that surface carbon deposition is occurring which is getting flushed out, the presence of H_2O at the beginning of the reduction half cycles as well cannot be explained by carbon deposition. Another observation is that the concentration of H_2O and CO appears to increase when the direction of the purge is being switched, which may be explained by some of the gasses getting stuck in the system somewhere and being removed later. Pressure spikes were observed on the mass spectrometer at the end of half cycles when the valves are switched, which implies that the different lines have significant pressure differences.

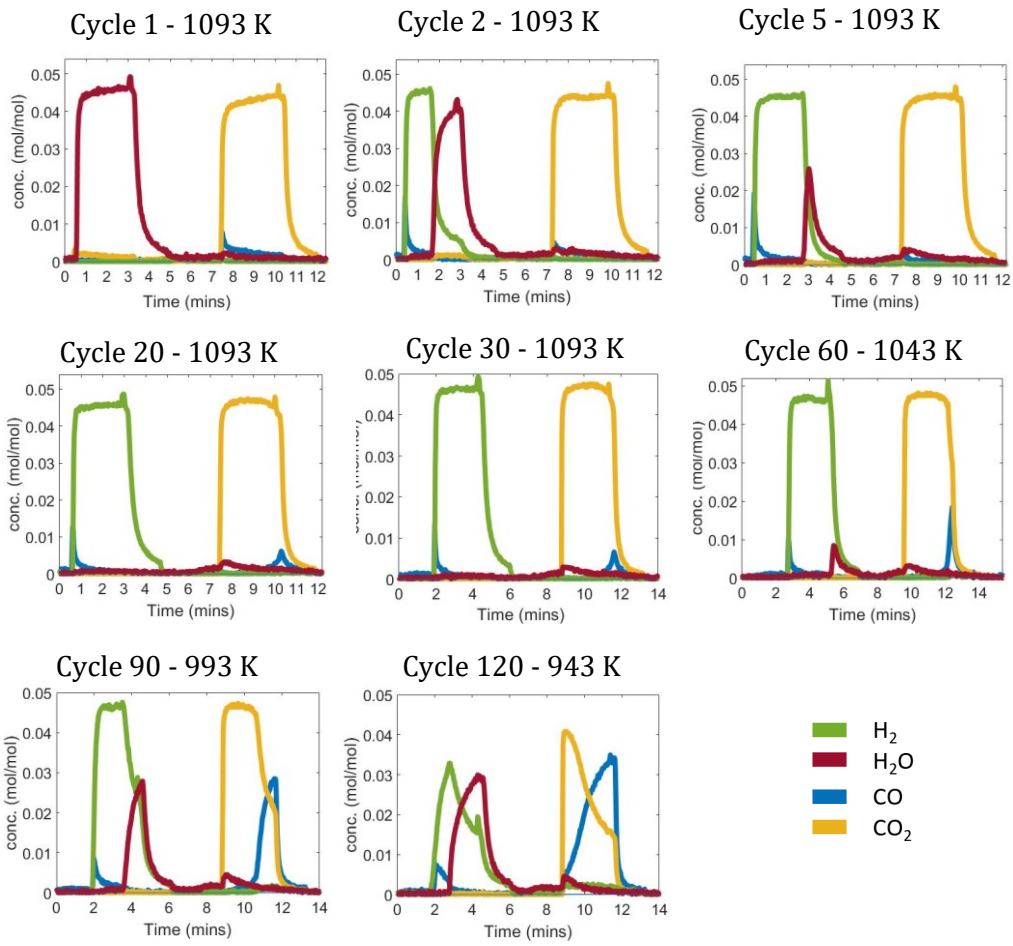

Figure 7.9: Outlet mole fractions from the temperature stability experiments. Both oxidation and reduction half cycles are shown at 1093 K, 1043 K, 993 K and 943 K respectively. 1.62 g of CZ82 was used with 5% H_2O and 5% CO gases at nominal molar flowrate of 3.4 × 10^{-5} mol s^{-1}. Uncertainty in the measurements was ± 100 µmol based on the mass spectrometer data.

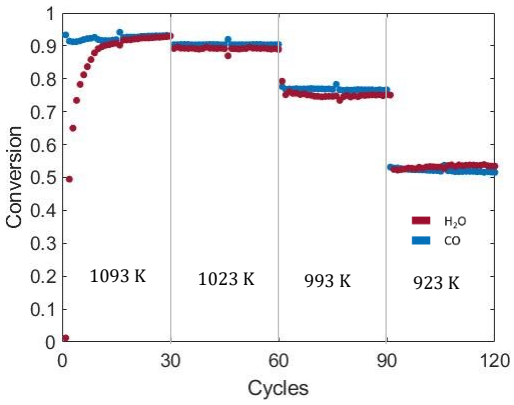

Figure 7.10: H_2O and CO conversion per cycle for each temperature for CZ82. 4 different temperatures were investigated (1093 K, 1023 K, 993 K and 923 K), of which 30 cycles were carried out at each. 1.62 g of CZ82 was used with 5% H_2O and 5% CO gases at nominal molar flowrate. of 3.4 × 10^{-5} mol s^{-1}.

In order to verify whether the presence of CO at the start of the oxidation profiles is due to surface carbon deposition, a sample of the bed from the reduced CO inlet end was taken for a temperature programmed oxidation experiment. The sample was oxidised using a 20% O_2 in He gas and a mass spectrometer was used to measure any evolved CO and CO_2. No signs of evolution of carbon gasification compounds could be seen. Considering the presence of H_2O at the start of the reduction half cycle and purge direction valve switch, it is therefore more likely that the extra H_2O and CO is due to a significant pressure imbalance in the system.

In Fig. 7.9, with higher temperatures the rate of the increase in water concentration appears to greatly decrease. This effect appears to completely dominate the oxidation half cycles and results in the production of almost pure hydrogen at 1093 K. The effect on the concentration of outlet carbon monoxide appears to be very similar. Higher temperatures result in a significant reduction in the rate of the carbon monoxide increase as well as the initial increase to occur at a time later into the half cycle.

In Fig. 7.10 the conversions for both half cycles at all temperatures investigated are more than 50% (though 993K falls close to the limit), which demonstrates that the unmixed reactor system can achieve conversions greater than that of a conventional mixed feed system. Fig. 7.10 shows that the bed requires roughly 14 cycles to start to reach steady state at 1093 K. This behaviour supports the earlier observation made in section 7.2.1 that longer feed durations initially allow for a completely fresh bed to reach stable cycling sooner. The use of higher temperatures appears to be more favourable in terms of both product purity and conversion. An oxygen balance on the system was found to close to roughly 2% during steady cycling.

7.3.2 Cycling with LSFM6473 at different temperatures

0.01 mols (2.21 g measured) of 80-160 μm LSFM6473 in a packed bed reactor of length 8.8 cm was cycled 45 times at a temperature of 993 K followed by 45 cycles each at temperatures of 1043 K, 1093 K, 1143 K and 943 K respectively. The greater number of cycles at the initial temperature of 993 K was to ensure that the fresh material was sufficiently activated and as such to get reliable values of the conversion at this temperature.

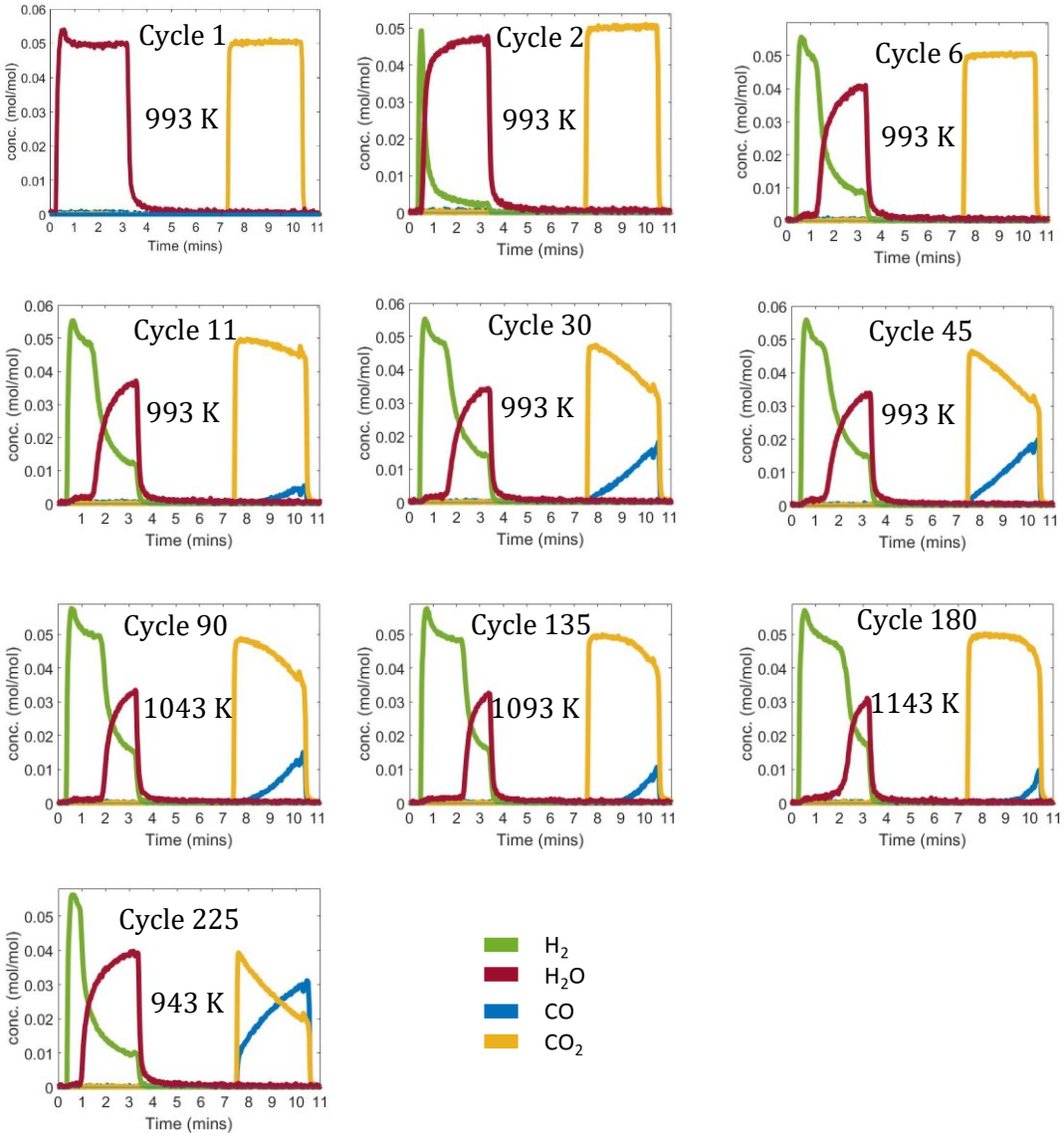

Figure 7.11: Outlet mole fractions from the temperature stability experiments. Both oxidation and reduction half cycles are shown at 993 K, 1043 K, 1093 K, 1143 K and 943 K respectively. 2.21 g of LSFM6473 was used with 5% H_2O and 5% CO gases at nominal molar flowrate of 3.4 × 10^{-5} mol s^{-1}. Uncertainty in the measurements was ± 100 µmol based on the mass spectrometer data.

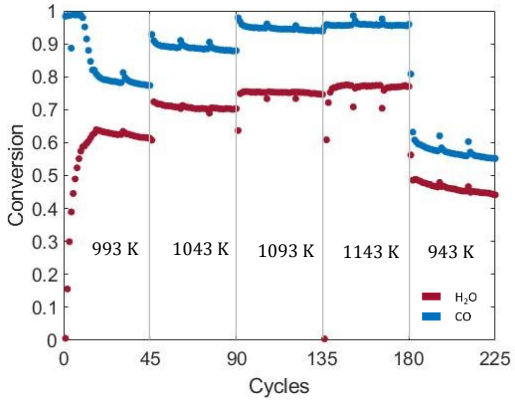

Figure 7.12: H_2O and CO conversion per cycle for each temperature for LSFM6473. 5 different temperatures were investigated, of which 45 cycles were carried out at each.

The H_2 concentration initially exceeds 5% at the start of the profile in Fig. 7.11 before falling to a plateau which becomes more prominent as the feed duration increases before starting to fall as the bed reaches capacity or the flow of H_2O is stopped. This is unexpected and does not match up with the behaviour seen in CZ82 and LSF641, since the mole fraction of H_2O fed to the reactor is 5% and should not be possible to exceed. The hydrogen balance closes to within 4% so it is possible that this is either due to some sort of instrumental error - one possibility is that the line to the permeation tube was at a higher pressure than the other lines, causing some of the H_2O to condense and thus resulting in a surge of extra H_2O when the direction of the valves are switched during cycling. Another possibility is that the H_2O is getting adsorbed onto the OCM and is desorbing at the end of the cycle causing an initial surge in the profile.

With increasing temperature, the increase in concentration of CO in the outlet stream occurs later on into the half cycle, while for the temperature range 1043 – 1143 K, higher temperatures appear to result in a very slight gradual increase in the concentration of water vapour earlier on in the half cycle, whereas this increase occurs more sharply at lower temperatures. It is likely that with the use of shorter feed durations this effect would have been even more noticeable. In chapter 2 it was shown how the equilibrium constant for the WGS reaction tended to unity at ~1093 K. At temperatures higher than 1093 K, the log of the equilibrium constant for the carbon monoxide oxidation half reaction exceeds that of water splitting, which may explain the reason for the earlier increase in water vapour concentration. Likewise at temperature

lower than 1093 K, the log of the equilibrium constant for the water splitting half reaction exceeds that of carbon monoxide oxidation which may explain the higher concentrations of CO in the outlet stream earlier in the half cycle. At 993 K it is likely a decrease in the equilibrium constants of both half reactions results in a significant decrease in the activity of the material.

In practise this means that the length of time where pure H_2 may be produced will decrease with increasing temperature, and this could not be overcome by decreasing the feed duration since sections 7.2.1 and 7.2.2 have shown that this does not equate to simply truncating the length of the concentration profile. In addition, section 7.2.2 also showed that even at the shortest feed durations when using LSFM6473 the H_2O peak could not be eliminated.

The concentration of CO in the outlet profile shows a decrease with rising temperature, with negligible amounts present at 1093 K. At none of the investigated temperatures does breakthrough of the CO curve occur. These results suggest that operation at higher temperatures would be beneficial for the reduction half cycle with higher conversions and CO_2 purity, however the earlier rise in H_2O concentrations would also lower the purity of the H_2 product, resulting in a trade-off having to be made. Since the separation of water vapour from the hydrogen is more straightforward, it may be that higher temperatures are preferable for better product quality and conversions. The greatest improvement in product quality appears to be in the jump from 993 K to 1043 K.

After accounting for flowrate discrepancy (H_2O flowrate ~120%) the oxygen balance closes well, with the largest discrepancy being no more than 2.86% in the case of 1093 K. In addition to the oxygen balance, the carbon balance for all temperatures was found to close to within 6.2%

Fig. 7.12 shows the H_2O and CO conversion per cycle for the LSFM6473 temperature experiments. As the material was initially in a completely oxidised state following synthesis, the conversions of CO and H_2O are very different, with ~99% conversion of CO for the first 8 cycles and a gradual rise in conversion of H_2O starting from close to zero in the first cycle. As the bed starts to reach an equilibrium between oxidising and

reducing fronts, the conversions of both reactants gradually reach a steady cycling value of 92% and 85% respectively for H_2O and CO after ~23 cycles.

Conversions show the largest increase going up from the lowest temperatures, with only marginal gains when going from 1093 K to 1143 K. No matter what the temperature chosen, conversions were found to always exceed 50%, which is the theoretical thermodynamic limit of a mixed conventional WGS reactor[56] explained in chapter 2.

7.4 Substitution of water vapour by carbon dioxide as the oxidising agent

For the CLWGS process, hydrogen is produced from the water splitting half reaction with water vapour. Liu et al (2012) has previously validated the substitution of steam by carbon dioxide by reproducing conversions with both gases in a fluidised bed at 1123 K. The Gibbs free energy and equilibrium constants for Eq. 7.1 and Eq. 7.2 with iron oxide as the OCM are similar (Dueso et al, 2015).

	$\Delta G_{1123\ K}$ (kJ/mol)	
$3Fe + 4H_2O \rightarrow Fe_3O_4 + 4H_2$	-12.234	Eq. 7.1
$3Fe + 4CO_2 \rightarrow Fe_3O_4 + 4CO$	-16.391	Eq. 7.2

In order to revisit the validity of this assumption, a bed of LSFM6473 that was previously used for half cycle duration optimisation experiments in section 7.2.2 was used for further cycling experiments at 1093 K using feed durations of 3 minutes. 30 cycles were carried out using carbon dioxide as the oxidising agent followed by 30 cycles using water vapour. The resulting concentration profiles at steady cycling are given in Fig. 7.13 and a comparison of the conversions using the two oxidising agents is given in Fig. 7.14.

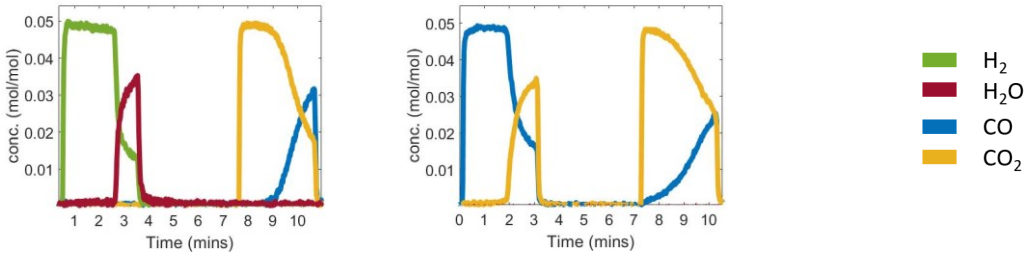

Figure 7.13: Outlet mole fractions from CO_2 substitution experiments, using 2.21 g of LSFM6473. For the first 30 cycles 5% H_2O and 5% CO gases at flowrates of 55 ml/min were used. For cycles 31-60 5% CO_2 and 5% CO gases at flowrates of 50 ml/min (nominal molar flowrate 3.4 × 10^{-5} mol s^{-1}) were used. The profiles in both plots are taken during steady cycling. Uncertainty in the measurements was ± 100 µmol based on the mass spectrometer data.

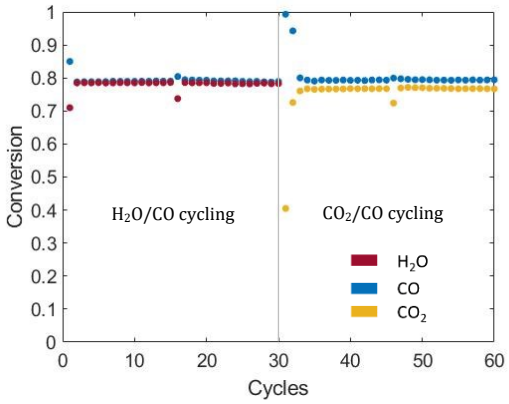

Figure 7.14: H_2O/CO conversion per cycle for first 30 cycles, and CO_2/CO conversion per cycle for latter 30 cycles. Using 2.21 g of LSFM6473. For the first 30 cycles 5% H_2O and 5% CO gases at flowrates of 55 ml/min were used. For cycles 31-60 5% CO_2 and 5% CO gases at flowrates of 50 ml/min (nominal molar flowrate 3.4 × 10^{-5} mol s^{-1}) were used.

In the experiments the flowrate of H_2O and CO during the first 30 cycles were measured as 55 ml/min both, while the flowrates of CO_2 and CO during the latter 30 cycles were measured as 50 ml/min. In Fig. 7.13 is can be seen that the concentration profile and hence the product quality is affected by this difference in flowrates. For the oxidation half cycle, the breakthrough of CO_2 occurs earlier than the corresponding breakthrough of H_2O by roughly 30 seconds. For the reduction half the maximum concentration of unreacted CO that passes through the reactor is higher for the H_2O system than for the system with CO_2 substitution. However the proportion of unreacted CO passing through the reactor starts to increase at an earlier time in the half cycle for the CO_2 substituted system. In general the discrepancy in the flowrates has a larger effect on the shapes of

the concentration profiles than the use of different oxidising agents, for which any difference is difficult to discern.

The overall conversions between the H_2O and the CO_2 systems given in Fig. 7.14 are still comparable as long as the flowrates (and half cycle durations) for both oxidising and reducing agents are the same. This successfully validates assumption that a H_2O operating system could be substituted with CO_2.

In practise this means that most of the operational issues associated with the use of water vapour, such as cold spots and susceptibility to pressure imbalances, can be avoided with the use of a carbon dioxide substituted system while still providing information on the operation of a CLWGS system equivalent with the use of water vapour. This is most useful for specific situations where the generation of a reliable stream of water vapour is tricky, or in smaller laboratory-scale investigations.

7.5 Comparison with traditional metal oxide oxygen-carrier material

In order to compare the performance of the non-stoichiometric OCMs identified in this work to more traditional OCMs with a limited number of phase changes, iron oxide was selected as the material of choice. Iron oxide acts as a conventional OCM and undergoes the phase changes $Fe/FeO/Fe_3O_4$, meaning it can only donate or receive oxygen at fixed oxygen chemical potentials. This therefore means that the conversion of the reactants are limited to the oxygen potential of the phase change.

Iron oxide is a cheaper and more readily available OCM in comparison, and benefits from high oxygen capacity, but is limited with a maximum H_2O conversion of ~67% conversion from the Fe/FeO phase change, and a maximum CO conversion of ~67% limited by the FeO/Fe_3O_4 phase change (refer to the Baur-Glaessner phase diagram shown previously in chapter 2 in Fig. 2.1)

Commercially available iron oxide (Fe_2O_3, Sigma-Aldrich) was used for this study and was prepared for the experiments by crushing and sieving iron oxide chunks to form particles of size 80-160 μm. A bed of iron oxide was prepared with 0.01 mols of sample (1.60 g) and bed length 14.2 cm for comparative purposes. 120 cycles were carried out

at 1093 K using feed durations of 1 minute and concentration profiles and conversions are shown in Fig. 7.15 and Fig. 7.16.

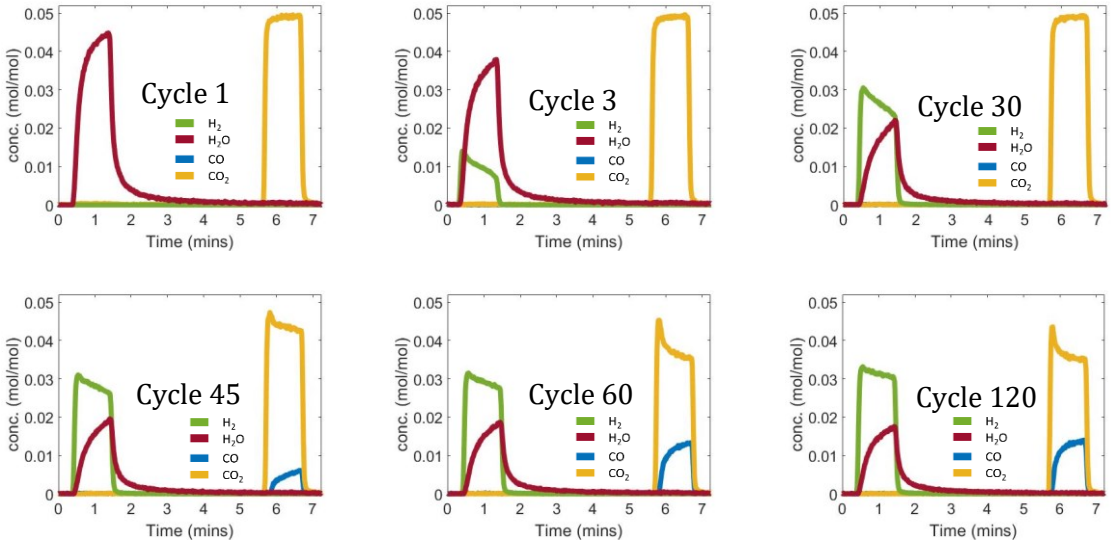

Figure 7.15: Outlet mole fractions from iron oxide cycling experiments, using 1.60 g of Fe_2O_3. 5% H_2O and 5% CO gases at flowrates of 50 ml/min were used. Uncertainty in the measurements was ± 100 µmol based on the mass spectrometer data.

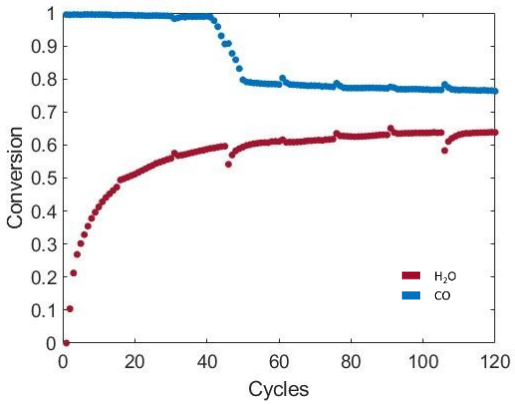

Figure 7.16: H_2O/CO conversion per cycle for 120 cycles. 1.60 g of iron oxide was cycled between counter-current feeds of 5% H_2O and 5% CO in argon using flowrates of 50 ml/min.

In the concentration profiles in Fig. 7.15 no H_2 can be seen in the first cycle since the bed is initially in a completely oxidised state as Fe_2O_3. In the subsequent cycles the material is reduced by CO and therefore the conversion of H_2O shown in Fig. 7.16 gradually starts to increase until steady H_2 production is achieved. The slight spikes in the values of conversion after every 15 cycles are due to gas calibrations where the bed is being

purged with pure argon. After accounting for flowrate discrepancy (H_2O flowrate ~110% that of CO) the oxygen balance closes to ~1.3%.

A very high conversion of CO is seen initially in Fig. 7.16 (around 99%) until about cycle 41, where there is a sharp drop to about 79% at cycle 50. This suggests that there is a physical change occurring in the OCM at this point; it is likely that this is because H_2O is not a strong enough oxidising agent to oxidise the material back to Fe_2O_3 during the oxidation half cycles, and it is instead oxidised to Fe_3O_4 hence limiting the usable oxygen capacity. The conversions over the 120 cycles show that more CO_2 is being produced than which is possible theoretically for the Fe_2O_3/Fe_3O_4 phase transition alone. Assuming that the 1.60 g of iron oxide undergoing reaction over the 120 cycles is being reduced first to Fe_3O_4 and then to FeO, a mass balance shows that ~67% of the Fe_3O_4 formed is being reduced to FeO. The water conversion in Fig. 7.16 appears promising at about 63% during steady cycling, close to the thermodynamic limit defined by the Baur Glaessner diagram, and shows no signs of decreasing during the course of the 120 cycles. Conversions do not seem to be fully stabilised after 120 cycles and further cycling would be worthwhile to validate the phase change behaviour.

Metal oxides can generally only exist in a limited number of oxidation states (albeit wüstite can have iron deficient composition with the iron/oxygen ratio in the range 0.83-0.95, the material is still overall limited by the phase changes at Fe/FeO and FeO/Fe_3O_4) as opposed to the non-stoichiometric materials investigated in this work which exhibit a continuous profile of oxidation stages. Overall, despite the larger oxygen capacity of iron oxide, thermodynamic limitations associated with the fixed chemical potentials at these limited phase changes result in lower conversions in comparison to LSF641, LSFM6473 and CZ82 at the same feed length of 1 minute.

To investigate the stability of the material and discern phase changes, ex-situ XRD scans were taken of the material post-cycling by taking samples of the material from 5 points roughly along the bed. These were one from the H_2O inlet, three points in the middle and one point at the CO inlet end of the bed. The last half cycle at the end of the experiment was a reduction half cycle.

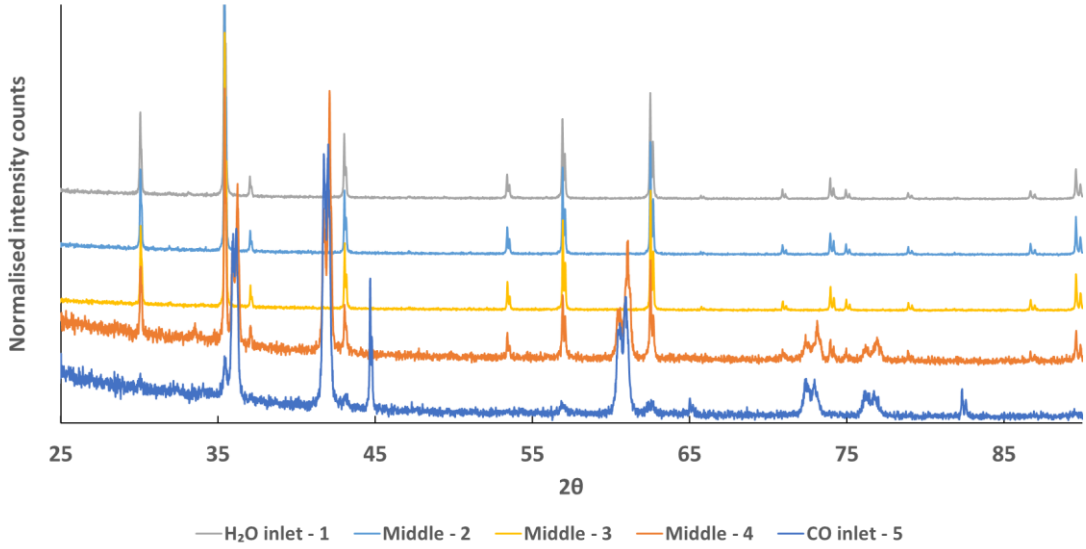

Figure 7.17: XRD diffractograms taken at five points along the iron oxide bed post experiment. Scans are taken from position 1-5, with 1 being at the H_2O inlet and 5 being at the CO inlet.

While positions 1-3 remain fairly consistent with no new peaks that can be seen, Fig. 7.17 shows significant changes in the diffractograms of positions 4 and 5 with the addition of multiple new peaks. Phase identification was carried out showing that these correspond to mostly magnetite at the top end (positions 1-3), with no wüstite or metallic iron phases. However position 4 corresponded to roughly 33.5% magnetite and 65.5 % wüstite phases, and position 5 corresponded to roughly 7.9% magnetite, 86.2% wüstite and 5.9% metallic iron phases.

It is possible that carrying out further cycles could eventually lead to increase in iron phase, significant carbon formation and iron carbide, which could lead to pressure drop problems across the bed. These phase changes suggest that iron oxide has a shorter lifetime span in comparison to LSF641, LSFM6473 or CZ82.

7.6 Long-term cycling performance with LSFM6473

Lower levels of product output will eventually occur as a result of OCM deactivation due to a multitude of different reasons. Due to the higher cost and involved material synthesis times with LSFM6473 in comparison to traditional materials like iron oxide it is not desirable to have to regularly replace this material, and so it is important to investigate the long term cycling performance of this material.

The non-stoichiometry behaviour of LSFM6473 investigated in Fig. 5.1 in chapter 5 raised the question of whether there can be seen any phase segregation of the material as the log pO_2s investigated at 1093 K were not below 10^{-21} bar (the expected gas atmosphere conditions in the bed during reduction are normally $pO_2 \approx 10^{-22}$ bar).

A bed of 0.01 mols LSFM6473 (2.21 g) measuring 8.3 cm in length was cycling with counter current streams of 5% H_2O and 5% CO at 1093 K using feed durations of 3 minutes. This bed had previously been activated during a limited number of trial cycles, hence the activation time for the bed is far faster than seen with LSFM6473 before in the temperature optimisation experiment in section 7.3.2. Concentration profiles and conversions are given in Fig. 7.18 and Fig. 7.19.

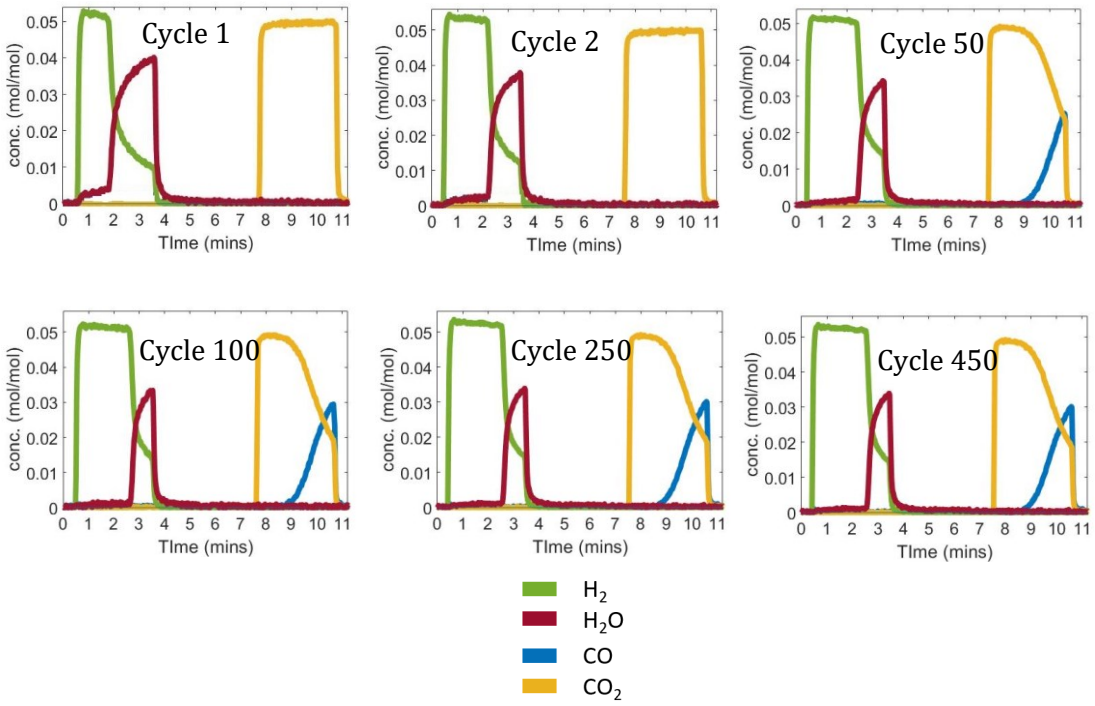

Figure 7.18: Outlet mole fractions from the long-term cycling experiment with LSFM6473. Both oxidation and reduction half cycles are shown. 2.21 g of LSFM6473 was used with 5% H_2O and 5% CO gases at nominal molar flowrate of 3.4×10^{-5} mol s^{-1}. Feed duration of 3 minutes was used. Uncertainty in the measurements was ± 100 µmol based on the mass spectrometer data.

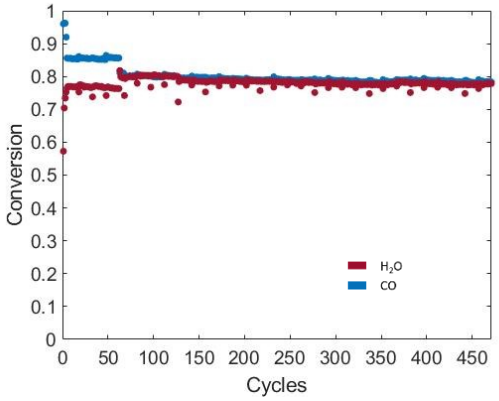

Figure 7.19: H_2O and CO conversion per cycle from long-term cycling experiment with LSFM6473. 2.21 g of LSFM6473 was cycled between counter-current feeds of 5% H_2O and 5% CO in argon at 1093 K at nominal molar flowrate of 3.4 × 10^{-5} mol s^{-1}. Feed duration of 3 minutes was used.

After the first ~60 cycles it was noticed that there was a discrepancy in the flowrates of the reactant gases, with the flowrate of water vapour ~10% greater than that of CO. To account for this difference and to ensure that the conversions closed, the flowrate of CO was increased by 10% to 55 ml/min in order to match the water vapour flowrate.

As the bed had already been used for some trial cycling prior to the experiment, the system quickly reaches steady cycling within ~5 cycles, developing an oxygen chemical potential gradient as a function of the length of the bed. The gas conversions once stabilised do not appear to show any obvious signs of change. An absolute deviation of 1.9% was noted once the bed had reached stable conversions, and the standard error of a linear regression carried out was less than the gradient, thereby indicating good material stability.

Fig. 7.18 shows how the outlet gas concentrations change for the selected cycles. As the OCM is in a more oxidised state at the start of the cycle, pure CO_2 may be seen at the first few cycles with the water vapour feed unable to fully re-oxidise the bed. An oxidation front moves through the bed over the first few cycles until reaching a stable point along the bed for which consistent cycles may be carried out.

In addition there are no signs of carbon deposition on the samples, with carbon balances based on the total amount of carbon entering and leaving the reactor closing well. No carbon species could be seen in the oxidation half cycles. Additional temperature

programmed oxidation tests carried out on solid samples from the bed also showed no signs of gaseous carbon evolution. This is a promising result indicating the material is a good OCM candidate and could offer a long usable lifetime without deactivation.

An XRD diffractogram in Fig. 7.20 from a sample taken from the reduced end of the bed, which is subject to the lowest pO_2s, show no signs of additional peaks. There is a slight peak shift to lower 2 theta angles which is an expected result as from previous chapters, due to the formation of oxygen vacancies.

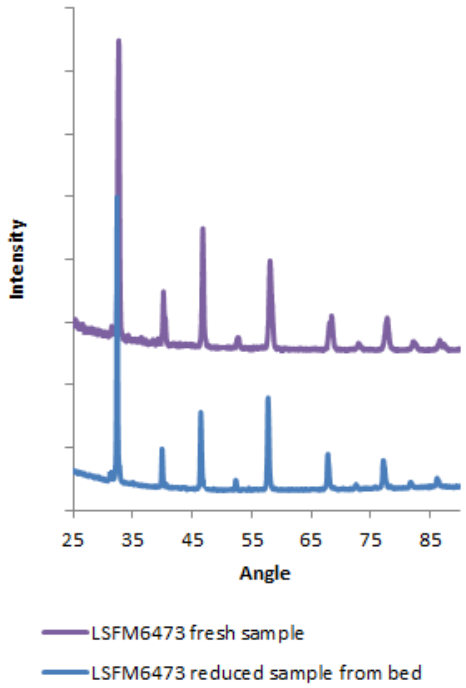

Figure 7.20: XRD powder diffractograms of fresh LSFM6473 powder compared to reduced sample taken from bed after the long-term cycling experiment.

SEM images of LSFM6473 comparing it in the fresh unreacted state with the state after carrying out > 450 cycles are shown in Fig. 7.21 below, to see if any visual difference could be noticed. The image on the left was taken of the fresh sample, and the image on the right was taken from the reduced end of the bed after cycling. No obvious change in morphology and structure can be seen from the images. This may be due to the OCM not undergoing phase changes and only seeing some small changes in the cell size which would result in minimal stress on the material, as well as possibly being due to the geometry of the packed bed minimising the effect of attrition.

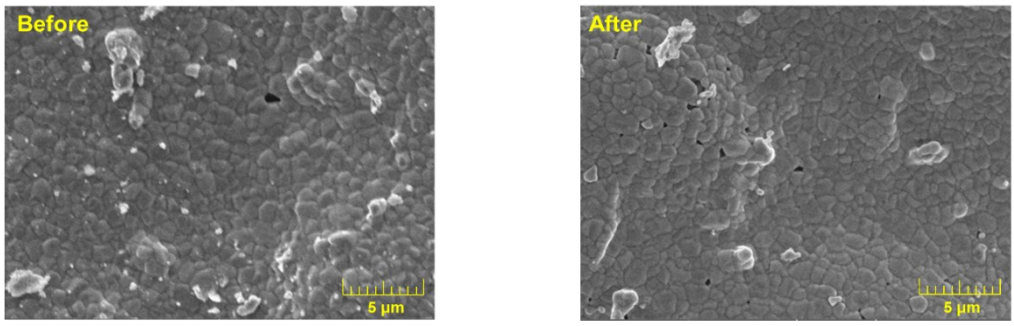

Figure 7.21: SEM micrographs of LSFM6473 before (fresh sample) and after cycling. No macro structural changes appear to be visible.

7.7 Simulation of CLWGS reactor using thermodynamically limited model

The reactor model (outlined earlier in the thesis in chapter 3) can provide additional information of the changes in δ of the OCM along the bed with time, where such information is often difficult to obtain experimentally. Apart from process conditions, the only required inputs for this model to simulate the bed is the δ-pO_2 thermodynamics of the OCM. A model which only requires knowledge of the δ-pO_2 thermodynamics is a useful tool to test the performance of OCMs without having to carry out lengthy laboratory experiments and will ultimately speed up applications to future testing with new OCMs and to large scale production. A 6^{th} order polynomial function was used to fit the δ-pO_2 data for LSFM6473, which was determined from the TGA experiments detailed in chapter 5, and for CZ82, which was taken from Kuhn et al (2013). The experimental results are used to validate the results of the model and see to what accuracy it allows for simulating different feed durations, temperatures, and inlet feed pO_2s.

7.7.1 Effect of half cycle duration for LSFM6473 and CZ82

To determine the effect of different half cycle durations a packed bed reactor of 1.62 g CZ82 and length 11.7 cm, and a packed bed reactor with 2.21 g LSFM6473 and length 8.7 cm was simulated. Both utilised a reactor internal diameter of 4 mm and set flowrates to match the experiments described in section 7.2. The simulation uses 5% streams of reactant gas at the inlets for both half cycles as the boundary conditions. For the initial pO_2 of the gas stream fed to the reactor, the proportion of H_2 and CO_2 in the inlet streams was determined based on the water dissociation and Boudouard reactions (equilibrium constants at 1093 K for these reactions were determined via publicly available data from

NIST). For each half cycle thereafter, the δ profile of the bed at the start of the half cycle was defined to be the same as that from the end of the previous half cycle, in order to ensure that the gas would be in equilibrium with the solid phase at the start of the half cycle.

The outlet concentration profiles predicted by the model during steady cycling for 1, 3 and 5 minute feed durations for CZ82 and LSFM6473 are shown in Fig. 7.22. These are compared against their respective experimental values with the aim of validating the model results and demonstrating that the δ-pO_2 relationships are sufficient to simulate the bed. This analysis focuses on the outlet gas compositions calculated at the ends of the reactor bed and the profiles during steady state. An inert purge of argon has been added in for the model data to separate the oxidation and reduction feeds and to synchronise with the experimental data. The flowrates have been adjusted to account for flowrate discrepancy discovered in the experimental sections.

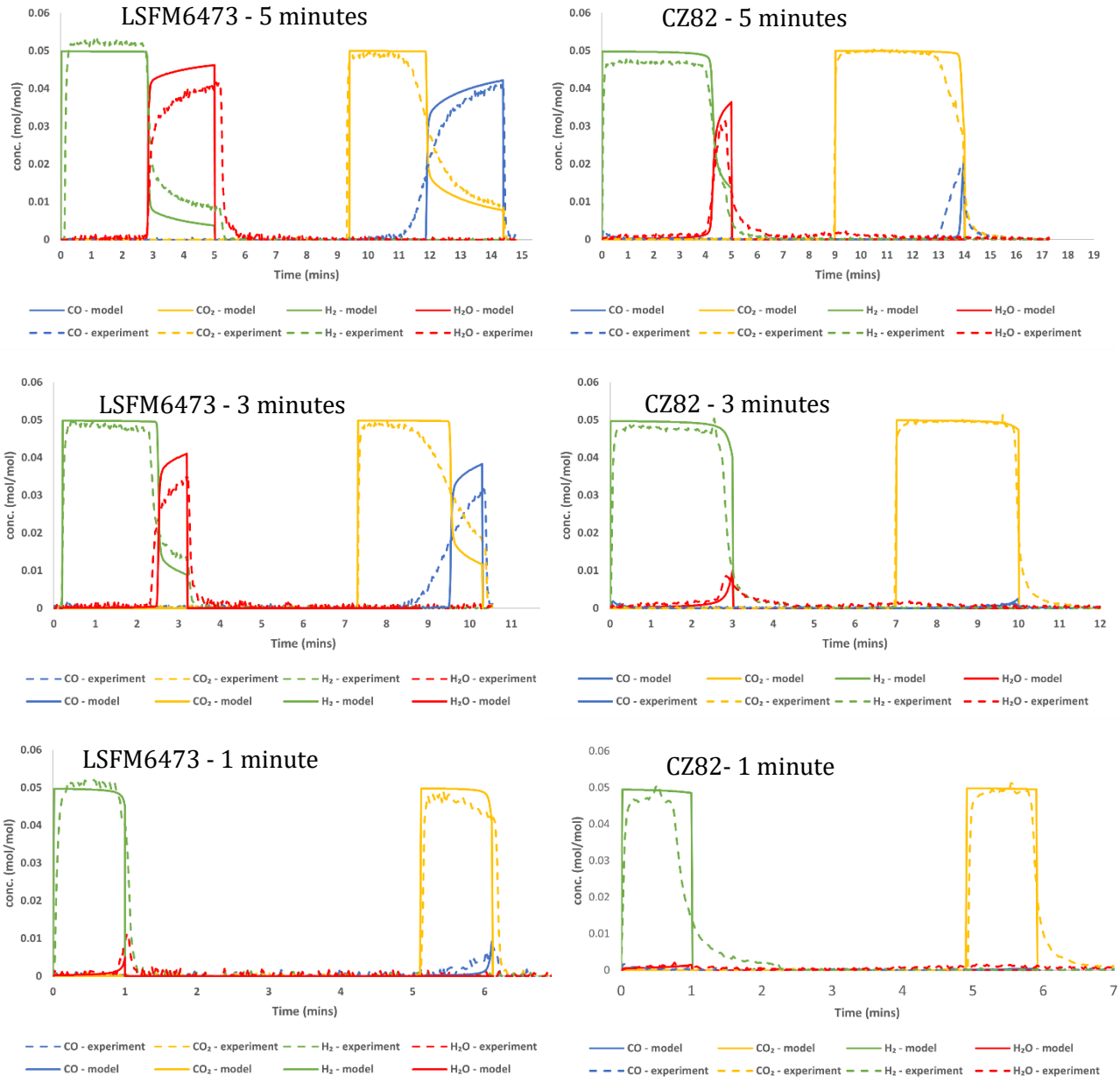

Figure 7.22: Outlet gas compositions with respect to time from simulations with LSFM6473 and CZ82. Half cycle durations for 1, 3 and 5 minutes are shown and compared against the previously determined experimental results. Inlet feeds of 5% H_2O and 5% CO are used with flowrates of 55 ml/min both for the case of LSFM6473, and 55 ml/min and 50 ml/min for the case of CZ82. The mass of LSFM6473 simulated is 2.2 g and the mass of CZ82 simulated is 1.6 g.

Overall the simulation appears to show a moderate level of success in predicting the experimental results, although it generally does not perform as well in predicting the reduction half cycle curves as it does the oxidation. For the reduction half cycles the

model initially underpredicts the experimental data before over-predicting the breakthrough towards the end of the half cycle. This is likely due to complex behaviours going on between the gas phase and the solid phase which the model does not consider.

The model does not predict the initial slope and the tail present in the experimental data, instead giving a sharp rise or a sharp drop at the end of both oxidation and reduction half cycles. The flow of the gas through the pipework and the reactor, problems with pressure imbalances, and interactions between the CO and H_2O with the solid phase likely results in some residual gases left behind which takes a while to clear and which the model does not consider.

The shape of the oxidation profiles for LSFM6473 generally follows the experimental data more closely. Despite overpredicting the amount of unreacted gas in the outlet, the H_2O profile tends to match the shapes of the experimental curves well, especially in regards to the downwards slope of the experimental data at the end of the oxidation half cycle. The model is able to successfully predict the time in the half cycle at which the H_2O breakthrough occurs as well as the duration of the breakthrough. The kinetics were not included in the simulation because of the fast kinetics of these materials, and the simulation results suggest this to be a reasonable assumption since the only major differences are the rise and falls of the curves at the start and end, as well as the more complicated shape of the CO_2 profile.

The CZ82 simulations show similar behaviour as for LSFM6473, with a slightly better prediction of the oxidation half cycle in comparison to reduction. In the case of 5 minutes feed duration, the simulation initially underpredicts the concentration of CO in the reduction half cycle, before overpredicting it towards the end. Again, differences in the shapes of oxidation and reduction half cycles are likely due to complex interactions between the gasses and the solid. For the case of the oxidation half cycle, adsorption may likely play some role, and this ultimately results in the actual rate of the increase or decrease of H_2O being slower than the idealised case presented by the simulation.

The rectangular product gas profile shapes for the case of 1 minute feed durations simulation with CZ82 indicates that the full capacity of the OCM has not been fully

utilised. The presence of the tail in the experimental data suggests the presence of residual gases in the system which takes time to flush out.

To further check the validity of the model results an oxygen balance was carried out to determine the moles of oxygen entering and leaving during oxidation and reduction half cycles respectively. For 1 minute feed durations the model gives 9.27×10^{-5} moles and 9.34×10^{-5} moles of oxygen exchanged for LSFM6473 and CZ82 respectively, and both fall within the uncertainties of the experimental values. At longer feed durations however there is a larger discrepancy. At 5 minute feed durations the model gives 3.93×10^{-4} moles and 3.85×10^{-4} moles of oxygen exchanged for LSFM6473 and CZ82 respectively, and both fall outside the uncertainties for the experimental values of the oxidation half cycle (or reduction half cycle) of 4.32×10^{-4} ($\pm 6.90 \times 10^{-6}$) moles and 4.34×10^{-4} ($\pm 7.66 \times 10^{-6}$) moles. While this is still a reasonable agreement, this behaviour suggests that the accuracy of the model decreases with longer feed durations.

Experimental results in Fig. 7.4 and Fig. 7.6 had shown that for the same feed duration CZ82 was able to reach steady cycling in fewer cycles than LSFM6473, and the conversions predicted by the model in Fig. 7.23 agree with this observation, with LSFM6473 reaching steady state after roughly 12 cycles and CZ82 reaching steady state after roughly 3 cycles. The reason for CZ82 to reach stable cycling faster than LSFM6473 is likely due to the gradient of the transition in their respective δ-pO_2 relationships. This gradient is steeper in the case of CZ82 than LSFM6473, meaning more of the available oxygen capacity is being utilised at values of pO_2 that equate to a higher conversion of reactant to products. The transition falls closer to the 1:1 H_2:H_2O/CO:CO_2 log pO_2 of -17.8 bar in the case of CZ82. The conversions predicted for both materials during steady cycling (~90%) are ~5% higher than the actual experimental values. This can be seen as a reasonable discrepancy as the simulation presents the case for an ideal scenario

without accounting for the limitations of a real system as previously described in this section.

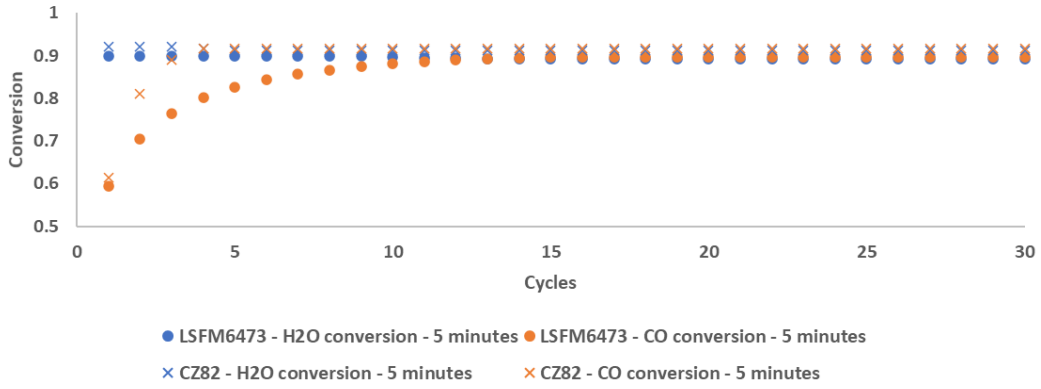

Figure 7.23: Conversions per cycle for LSFM6473 and CZ82 with 5 minute feed durations determined by the simulation using conditions matching that of experiment in section 7.2. Inlet feeds of 5% H_2O and 5% CO are used with flowrates of 55 ml/min both for the case of LSFM6473, and 55 ml/min and 50 ml/min for the case of CZ82. The mass of LSFM6473 simulated is 2.2 g and the mass of CZ82 simulated is 1.6 g.

7.7.2 Effect of flowrate for LSFM6473

In the experimental section various problems with flowrate discrepancies between the water vapour and carbon monoxide streams were described. By adjusting these flowrates to match it was possible to ensure the oxygen balance per cycle closed and achieve matching conversions to products. On the other hand, significant differences in the product quality were observed from the use of unequal flowrates.

While consistent and equal flowrates are generally easier to manage on an industrial scale, in certain instances fine-tuning the flowrates of reactant gases to the reactor in order to achieve a certain purity of hydrogen or carbon dioxide may be desirable. This section aims to explore the sensitivity of the reactor system to changes in flowrates between half cycles by comparing experimental data to the simulation.

In section 7.2.2 it was seen that increasing the flowrate while keeping the same cycle duration resulted in an increase in the amount of unreacted gases passing through the reactor. The onset of the H_2O or CO breakthrough occurs earlier on in their respective half cycles because the OCM capacity tends to be exhausted sooner since more moles of

oxygen are being exchanged in the same duration, and the maximum concentration of the reactant gas profile in the outlet stream will increase.

Of interest is the investigation of the relationship between flowrate and feed duration. Specifically it is hypothesised that the shape of the outlet concentration profile would be the same as for a longer feed duration if a faster flowrate was used at shorter feed durations, since the total moles of oxygen being exchanged would still be the same. Fig. 7.24 considers the case where LSFM6473 is cycled for 3 minutes with H_2O at 55 ml/min, and 1 minute with CO at 165 ml/min, and the simulation results are compared with experimental data. The experimental data was acquired using the same reactor bed as from section 7.2.2.

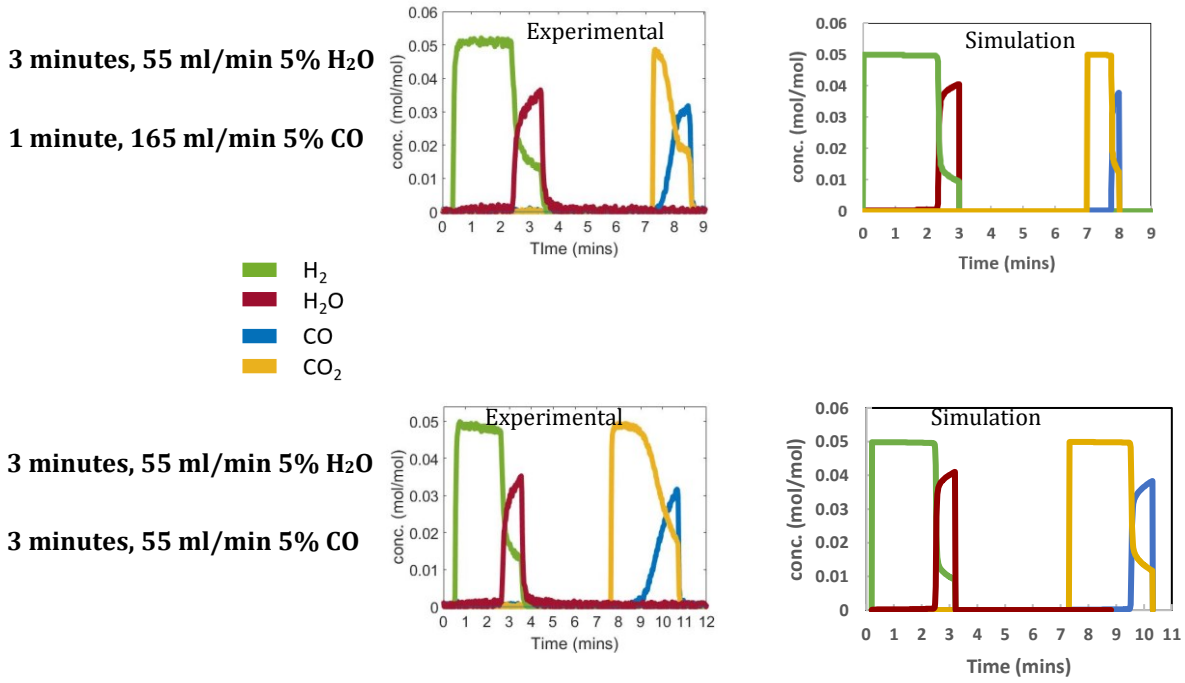

Figure 7.24: Comparison using experimental bed from section 7.2.2 with simulation, where 0.01 mol LSFM6473 is cycled for 3 minutes with 5% H_2O at 55 ml/min, and 1 minute with 5% CO at 165 ml/min. This is compared against the case where LSFM6473 is cycled for 3 minutes in both half cycles with equal feeds of 55 ml/min. Since the total oxygen exchange is still the same, the shape of the outlet concentration profiles are similar.

From Fig. 7.24 it can be seen that the shape of the oxidation half cycle matches better with the experimental results than the reduction half cycle. As seen before, the experimental data shows an earlier increase in CO concentration which is not taken into

account by the model. Both profiles match well with each other when comparing the case of 3 minutes 55ml/min flowrate with 1 minute 165 ml/min flowrate, with the shape of the reduction profile during the shorter 1 minute feed duration approaching a truncated version of the longer 3 minute profile. The profiles show slight differences in terms of the point in the half cycle at which CO breakthrough starts to occur and these differences are most likely due to slight discrepancies in the flowrate of the CO stream at the higher flowrate.

Further simulations were carried out to determine the effect of small discrepancies between oxidation and reduction half cycle flowrates on the product quality. Clearly the effect of flowrate discrepancy on the outlet product quality is significant. The flowrate of either CO or H_2O is increased while the other is kept constant and the effect on product quality is noted. In Fig. 7.25, for 3 minute feed durations with LSFM6473, an increase of 15 ml/min in the CO flowrate increases the quantity of unreacted CO gas in the outlet stream by 42 %, while the quantity of H_2O increases by 36 % when the flowrate of H_2O is increased by the same amount. The different effect on each half cycle is related to the δ-pO_2 thermodynamics, and the position of the gradient transition slope around -17.8 log pO_2 at 1093K. Careful control of the oxidation/reduction half cycle flowrates can therefore be considered for the operation of a larger scale rig on desired product quality.

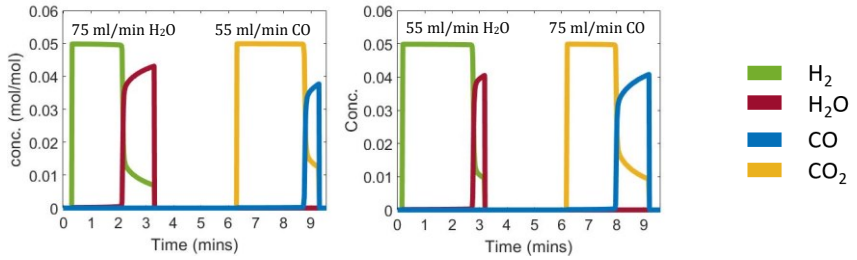

Figure 7.25: Effect of flowrate discrepancy on outlet concentration profiles under equal feed durations. Simulation of a 0.01 mol LSFM6473 bed of length 8.7 cm at 1093 K with ± 15 ml/min changes to oxidising or reducing feed flowrates.

7.7.3 Effect of temperature for LSFM6473

To further verify the model and investigate the effect of different temperatures on product quality the model can be utilised. The δ-pO_2 isotherms determined at various

temperatures in chapter 5 are used. The simulation uses the same length of bed and mass of OCM as the experimental data in section 7.3, and the additional 20% water vapour flowrate that was seen for the experimental data was also replicated in the model. Results are given in Fig. 7.26 showing a comparison between experimental and model results.

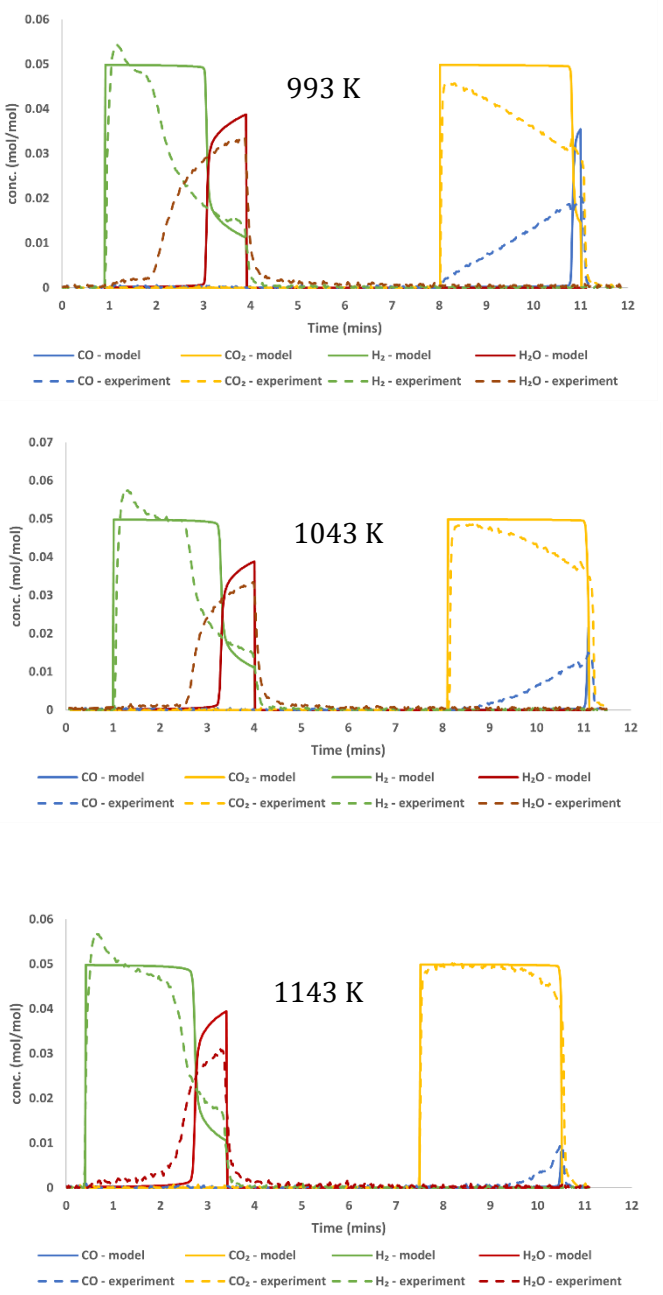

Figure 7.26: Outlet gas compositions with respect to time from temperature simulations with LSFM6473. Temperature of 993 K, 1043 K and 1143 K are shown and compared against the previously determined experimental results. Inlet feeds of 5% H_2O and 5% CO are used with flowrates of 60 ml/min for H_2O and 50 ml/min for CO. The mass of LSFM6473 simulated is 2.2 g.

In Fig. 7.26 at each temperature the model fails to predict the gradual rise in the CO concentration from the start of the reduction half cycle that is seen in the experimental data. This may also be due to the presence of the pressure imbalance in the experimental data – the half cycle duration optimisation experiments where the pressure spike was eliminated did not see the occurrence of CO straight away – which is difficult to replicate in the model. It is also likely that imprecision in the selection of the temperature may contribute to the inaccuracy of the outlet profiles – the results suggest that the temperature of the δ-pO_2 isotherm used for the model in each case is slightly lower than the actual experimental temperature due to the higher maximum of the unreacted gas concentration peaks. Despite this, the model still overpredicts the true conversions for each case, due to the later breakthrough of unreacted gas in the half cycles.

7.8 Summary

This chapter has investigated the performance of the two high oxygen capacity OCMs CZ82 and LSFM6473 in a packed bed integral reactor carrying out the CLWGS process. In chapter 3 these materials, among several others, had been identified as capable of achieving high conversions at longer feed durations based on the shape of their δ-pO_2 curves in comparison to LSF641, as well as the TGA screening investigation in chapter 4.

Cycling results found that both materials were able to achieve high conversions in excess of the 50% theoretical maximum for a conventional mixed WGS reactor for which the principle was shown by Metcalfe et al (2019) where the material LSF641 was investigated, as well as in excess of the traditional phase changing OCM iron oxide. In addition both materials were also able to achieve high conversions at longer feed durations than LSF641, validating the assumptions made regarding selection criteria for OCMs with good δ-pO_2 relationships in chapter 3.

For both materials it was found that the effect of increasing the half cycle duration was not equivalent to extending the length of the profile from a shorter feed duration. Instead longer feed durations resulted in a lowering of the product quality. Higher temperatures were found to lead to a marginal decrease in the product quality, accompanied by an increase in conversion

Overall, while the experimental results were held back by operational difficulties in maintaining equal flowrates of oxidising and reducing agents, this allowed for a look at the effect of changes to flowrate and the sensitivity of the reactor system to unexpected deviations from intended flow. In the case of CZ82, the use of 1 minute feed durations while using 10% higher flowrate of water vapour than carbon monoxide resulted in the production of nearly pure H_2 and CO_2. This is a promising result since in the case of any other investigated material including LSFM6473 (or LSF641) a small but noticeable concentration of H_2O was always present even at the shorter feed lengths.

Finally a simulation of the reactor was carried out and showed that the concentration profiles possible with such materials can be reasonably predicted using a thermodynamically-limited pseudo homogeneous 1D reactor model with the only required input being the δ-pO_2 thermodynamics of the OCM. However complications arising from the interactions of H_2O with the solid phase and pressure imbalances in the experimental data, as well as further interactions of the gas phase CO meant that the shape of the reduction half cycles were in general less accurate than the oxidation half cycles, and the conversions that resulted were an overprediction in comparison to the experimental values. The poor prediction of the reduction half cycle may also be due to the inaccuracy of the δ-pO_2 isotherm from chapter 5 which was limited in the range of oxygen partial pressures studied.

Chapter 8: Conclusion

8.1 Summary of thesis

The principle goal of this PhD thesis was to develop a methodology to identify non-stoichiometric OCMs with suitable thermodynamic properties for the CLWGS process, prioritising high oxygen capacity and stability in order to achieve high conversions using repeatable cycles and long feed durations. The CLWGS process is capable of overcoming the thermodynamic limitations associated with conventional mixed-feed WGS reactor systems, and suitable non-stoichiometric OCMs for the CLWGS process tend to achieve higher conversions than those of traditional phase changing OCMs such as iron oxide under similar process conditions.

To develop such a methodology, a theory was proposed stating that the δ-pO_2 relationship of an ideal non-stoichiometric OCM should match exactly the gradient of the WGS gas phase thermodynamic curve of conversions vs. log pO_2. This is because a certain degree of conversion is possible at each chemical potential according to the WGS thermodynamics, and so any oxygen exchange potential existing outside of the range dictated by the thermodynamics will essentially be unusable; an ideal optimal non-stoichiometric OCM should be distributed so as to match the gradient of the thermodynamic conversion vs. log pO_2 curve as closely as possible per step change in log pO_2.

Having more oxygen capacity in the non-stoichiometric OCM at a thermodynamically active range of chemical potentials is favourable from an economic standpoint since less mass of material would be required for the same moles of oxygen, and this work has highlighted the importance of understanding the impact that the δ-pO_2 relationship has on the actual usable oxygen capacity of the non-stoichiometric OCM dictated by the WGS thermodynamic equilibria. Based on the theory for an ideal non-stoichiometric OCM, several promising prospective non-stoichiometric OCMs from the literature were identified, and the ideal δ-pO_2 relationship was used as a benchmark to compare the non-stoichiometric OCMs against. The materials CZ82 and LSFM6473 were identified from this procedure as having higher usable oxygen capacity than LSF641, which was a non-stoichiometric OCM that earlier work by Metcalfe et al (2019) had shown could

achieve stable high conversions, but suffered from limited oxygen capacity due to the occurrence of a limiting plateau in the δ-pO_2 relationship of the material in the thermodynamically active range of chemical potentials for WGS at 1093 K.

A 1-dimensional pseudo-homogenous reactor model was utilised to verify the theory for the optimal non-stoichiometric OCM for a CLWGS packed bed reactor system, and the effect on the conversions and product quality was investigated for different midpoints and gradients of the δ-pO_2 relationship of a hypothetical non-stoichiometric OCM.

The δ-pO_2 relationship for the OCM LSFM6473, which has previously not been investigated in the literature, was determined via TGA experiments. It was found that the doping of 1/3 proportion of Mn onto the B-site of LSF641 resulted in a significantly altered shape to the δ-pO_2 relationship, with the elimination of the limiting plateau that was seen with no Mn doping. This was due to the presence of Mn4+ cations in the δ≈0.2 reduced state for LSFM6473. Through comparison with the ideal OCM benchmark it was predicted that in a reactor this material could achieve high conversions at longer feed durations than LSF641 before having to switch half cycles. This increase was not directly derived from the presence of the Mn4+ cations, but from the shift in the shape of the δ-pO_2 curve combined with the elimination of the plateau which allows it to approach more closely the shape of the ideal non-stoichiometric OCM benchmark δ-pO_2 curve.

Further work was carried out using an in-situ x-ray diffraction technique to probe the changes in the lattice parameter of LSFM6473 at operating temperatures and determine its stability during cycling. The material was found to conform to a single phase cubic structure at operating temperatures, and the lattice parameter tended to return to the same values at each point after a whole cycle, suggesting reproducible conversions and good material stability. The thermal and chemical expansivities for LSFM6473 were determined from the in-situ data. While the chemical expansivity was only probed at a limited number of chemical potentials, the results suggested a non-linear relationship with δ, with the increase in the chemical expansivity becoming less with increasing values of δ. The thermal expansivity was found to be equal to 6.327×10^{-5} A/K and 6.118×10^{-5} A/K under buffer gas ratios of 1:20 and 20:1 CO_2 to CO, while a slightly higher value of 9.422×10^{-5} A/K was found when using the buffer gas ratio of 1:5 CO_2 to

CO. Since this falls in between the chemical potentials for 1:20 and 20:1 buffer gas ratios, it is inconclusive whether this is simply due to a large uncertainty or a genuine feature of the OCM.

By making use of the δ-pO_2 relationship and the thermochemical expansivities for LSFM6473 which were both determined in this work, the changes in oxygen non-stoichiometry for LSFM6473 during cycling could be determined along the length of the reactor bed and compared to the values determined from the computational model. Using this method, the largest δ change in the OCM was determined to be 0.15, between the CO and H_2O feed inlets during reduction and oxidation. Due to the large changes in oxygen content for the material, the in-situ x-ray diffraction technique was able to accurately track the changes in the value of δ along the bed

The performance of LSFM6473 and CZ82 was also investigated under different process parameters in a working packed bed reactor. Both materials successfully outperformed LSF641 as predicted by the ideal non-stoichiometric OCM theory, being able to be cycled at longer feed durations and higher flowrates and achieve comparable conversions to LSF641. With both LSFM6473 and CZ82, it was found that increasing the half cycle duration was not equivalent to extending the length of the profile from a shorter feed duration but instead resulted in a lowering of the product quality.

A long term cycling investigation for LSFM6473 for over 450 cycles using 3 minute feed durations was also carried out, with no noticeable drop in conversions or product quality detected. The lack of additional peaks in XRD diffraction scans for the reduced end of the bed also confirmed that the material was stable during cycling, and points towards the potential viability of the material for industrial scale-up.

Careful consideration of the performance of an OCM for a chemical looping system for hydrogen production is critical, as a material must be selected with minimal tendency for deactivation and with high oxygen capacity in order to decrease operational costs of replacing the OCM. This thesis demonstrated a methodology for selecting non-stoichiometric OCMs, starting from thermodynamic principles and eventually testing suitable non-stoichiometric OCMs in a working packed bed reactor. A theory for an

optimal non-stoichiometric OCM in a thermodynamically limited system was proposed and used to select suitable materials from the literature. According to this theory, a non-stoichiometric OCM should be used as this can overcome the thermodynamic limitations associated with phase changing materials, and the theory for an ideal non-stoichiometric OCM was proposed which states that the material should have a δ-pO_2 relationship that matches the gradient of the gas phase thermodynamic conversion vs. pO_2 relationship. This theory was proven using both modelling and experimental approaches. The selected materials LSFM6473 and CZ82 both demonstrated improved cycling performance in comparison to LSF641 as predicted from the theory. The use of LSFM6473 in larger scale experiments was found to be viable, with results for over 450 cycles of 3 minute feed durations with no noticeable sign of material degradation and steady conversions. Ultimately these results add to the growing body of work that suggests that the CLWGS process could be used in an industrial capacity as a full or partial replacement for SMR technology, along the path to a more environmentally friendly future for the hydrogen production industry.

8.2 Possible future work

In this work, a theory for an ideal non-stoichiometric OCM δ-pO_2 relationship was explained both theoretically, as well as via a reactor model simulation. Experimental investigation of the δ-pO_2 relationship for real non-stoichiometric OCMs also confirmed this theory, and improved performance with longer feed durations before having to switch half cycles was confirmed using a packed integral reactor. In this respect, a method of determining the δ-pO_2 relationship of a material from first principles by use of density functional theory may be an interesting area of future research. With such knowledge, the appropriate elemental compositions and doping ratios of a promising material may be identified in a more methodical manner and then compared with the optimal benchmark theory presented in this thesis, ultimately speeding up the discovery of new materials. For example work by Emery et al (2017) presented a large dataset of 5329 cubic and distorted perovskites including information on the oxygen vacancy formation energy. Of these perovskites, 395 are predicted to be thermodynamically stable and thus may represent promising avenues for future research. Such a line of

work would enable more rapid discovery and testing of potential new non-stoichiometric OCMs for the CLWGS process.

As the material LSFM6473 was previously not investigated in the literature, the δ-pO_2 data was determined only via this work. In the future, additional work may involve further investigations with TGA over a wider range of pO_2s, as well as methods such as coulometric titration that may yield a better understanding of the oxygen on-stoichiometry in the pO_2 range which the TGA could not measure and independently corroborate the results in this work, as well as with different doping ratios of Mn on the B-site.

Another interesting avenue of research is to investigate the potential performance implications of using a reactor bed consisting of segments of multiple different OCMs along its length. In particular, various configurations could be investigated making use of a more niche material such as LSFM6473, LSF641 or CZ82 at the reducing end of the bed to ensure stability and high conversions combined with a cheap abundant OCM such as iron oxide to carry most of the oxygen capacity at the less reducing segments of the bed. The thermodynamic model that was used in this thesis, along with the ideal non-stoichiometric OCM theory could developed to understand the implications of such a system. The main advantage of this system would be the economic benefit of being able to use a cheap and abundant OCM such as iron oxide, while having to use less of the expensive novel materials in the bed to potentially achieve high conversions and product quality close to that of a system with exclusively a non-stoichiometric OCM.

An important limitation of this work is its focus only on carbon monoxide as the reducing agent in the chemical looping process. While carbon monoxide is an ideal gas to use for laboratory investigations, on an industrial scale its use is not likely to be feasible, with the use of methane from natural gas being the more common solution. The theory for the ideal non-stoichiometric OCM in this thesis only applies to a system which is thermodynamically limited, which is not true for methane. In addition to considering kinetic limitations and side-reactions, the large endothermic heat of reaction when the OCM is reduced via oxidation of methane results in an energy deficit in two-step chemical looping systems with the water-gas shift reaction. In this respect, further work

needs to be carried out to more closely investigate the kinetics of the reactions with methane, as well as alternative reactor systems such as the three-step TRCL system to be able to achieve auto-thermal operation.

References

Adánez, Juan & Abad, Alberto & García-Labiano, F. & Gayán, Pilar & de Diego, Luis. (2012). Progress in Chemical-Looping Combustion and Reforming Technologies. Fuel and Energy Abstracts. 38. 10.1016/j.pecs.2011.09.001.

Alamsari, Bayu & Torii, Shuichi & Trianto, Azis & Bindar, Yazid. (2011). Heat and Mass Transfer in Reduction Zone of Sponge Iron Reactor. ISRN Mechanical Engineering. 2011. 10.5402/2011/324659.

Alvarado, Kyle & García Martínez, Juan B. & Matassa, Silvio & Egbejimba, Joseph & Denkenberger, David. (2020). Food in space from hydrogen oxidizing bacteria. Acta Astronautica. 180. 10.1016/j.actaastro.2020.12.009.

American Elements. Product Datasheet: Manganese(III) oxide. https://www.americanelements.com/manganese-iii-oxide-1317-34-6. Accessed 18th August 2020.

Andersson, Joakim & Grönkvist, Stefan. (2019). Large-scale storage of hydrogen. International Journal of Hydrogen Energy. 44. 11901-11919. 10.1016/j.ijhydene.2019.03.063.

Aroutiounian, V. & Arakelyan, V. & Shahnazaryan, Gohar. (2005). Metal oxide photoelectrodes for hydrogen generation using solar radiation-driven water splitting. Solar Energy. 78. 581-592. 10.1016/j.solener.2004.02.002.

Ashik, U.P.M & Viswan, Anchu & Kudo, Shinji & Hayashi, Jun-ichiro. (2018). Nanomaterials as Catalysts. 10.1016/B978-0-08-101971-9.00003-X.

Atimtay, Aysel. (2001). Cleaner energy production with integrated gasification combined cycle systems and use of metal oxide sorbents for H2S cleanup from coal gas. Clean Prod. Proc.. 2. 197-208. 10.1007/PL00011306.

Balat, Havva & Kırtay, Elif. (2010). Hydrogen from biomass – Present scenario and future prospects. International Journal of Hydrogen Energy. 35. 7416-7426. 10.1016/j.ijhydene.2010.04.137.

Balthasar, W. (1984). Hydrogen Production and Technology: Today, Tomorrow and Beyond. International Journal of Hydrogen Energy. 9. 649-668. 10.1016/0360-3199(84)90263-5.

Basu, Prabir & Cheng, L.. (2000). An Analysis of Loop Seal Operations in a Circulating Fluidized Bed. Chemical Engineering Research & Design. 78. 991-998. 10.1205/026387600528102.

Basu, Prabir. (2006). Combustion and Gasification in Fluidized Beds. 10.1201/9781420005158.

Bellona. (2019). Steel and emissions: How can we break the link? https://bellona.org/news/ccs/2019-03-is-steel-stealing-our-future#_edn1. Accessed 28th February 2021.

Benamira, Messaoud & Thommy, Léonard & Moser, F. & Joubert, O & Caldes, Maria. (2014). New anode materials for IT-SOFC derived from the electrolyte BaIn0.3Ti0.7O2.85 by lanthanum and manganese doping. Solid State Ionics. 265. 38–45. 10.1016/j.ssi.2014.07.006.

Bhatia, Suresh & Perlmutter, D.. (1980). A Random Pore Model for Fluid-Solid Reactions: I. Isothermal, Kinetic Control. AIChE Journal. 26. 379 - 386. 10.1002/aic.690260308.

Biniwale, Rajesh & Mizuno, Akira & Ichikawa, Masaru. (2004). Hydrogen production by reforming of iso-octane using spray-pulsed injection and effect of non-thermal plasma. Applied Catalysis A: General. 276. 169-177. 10.1016/j.apcata.2004.08.003.

Bishop, S. & Marrocchelli, Dario & Chatzichristodoulou, C. & Perry, N. & Mogensen, Mogens & Harry, Tuller & Wachsman, E.. (2014). Chemical Expansion: Implications for Electrochemical Energy Storage and Conversion Devices. Annual Review of Materials Research. 44. 205-239. 10.1146/annurev-matsci-070813-113329.

Bleeker, M.F. & Kersten, Sascha & Veringa, H.J.. (2007). Pure hydrogen from pyrolysis oil using the steam-iron process. Catalysis Today. 127. 278-290. 10.1016/j.cattod.2007.04.011.

Bleeker, M.F. & Kersten, Sascha & Veringa, H.J.. (2007). Pure hydrogen from pyrolysis oil using the steam-iron process. Catalysis Today. 127. 278-290. 10.1016/j.cattod.2007.04.011.

Bleeker, Mariken & Gorter, Sander & Kersten, Sascha & van der Ham, Louis & Berg, Henk & Veringa, Hubert. (2010). Hydrogen production from pyrolysis oil using the steam-iron process: A process design study. Clean Technologies and Environmental Policy. 12. 125-135. 10.1007/s10098-009-0237-0.

Bohn, C. & Cleeton, J. & Müller, C. & Chuang, S. & Scott, S. & Dennis, J.. (2010). Stabilizing Iron Oxide Used in Cycles of Reduction and Oxidation for Hydrogen Production. Energy & Fuels. 24. 10.1021/ef100199f.

Bohn, C. & Cleeton, J. & Müller, C. & Davidson, J. & Hayhurst, Allan & Scott, S. & Dennis, J.. (2010). The kinetics of the reduction of iron oxide by carbon monoxide mixed with carbon dioxide. AIChE Journal. 56. 1016 - 1029. 10.1002/aic.12084.

Bohn, Christopher & Muller, C.R. & Cleeton, Jason & Hayhurst, Allan & Davidson, John & Scott, Stuart & Dennis, John. (2008). Production of Very Pure Hydrogen with Simultaneous Capture of Carbon Dioxide using the Redox Reactions of Iron Oxides in Packed Beds. Industrial and Engineering Chemistry Research. 47. 10.1021/ie800335j.

Bromberg, Lev & Cohn, D.R & Rabinovich, Alexander & Alekseev, N.. (1999). Plasma catalytic reforming of methane. International Journal of Hydrogen Energy. 24. 1131-1137. 10.1016/S0360-3199(98)00178-5.

Callaghan, Caitlin. (2006). Kinetics and Catalysis of the Water-Gas-Shift Reaction: A Microkinetic and Graph Theoretic Approach. PhD thesis at Worcester Polytechnic Institute.

Cheng, Zhuo & Qin, Lang & Fan, Jonathan & Fan, Liang-Shih. (2018). New Insight into the Development of Oxygen Carrier Materials for Chemical Looping Systems. Engineering. 4. 10.1016/j.eng.2018.05.002.

Chiesa, Paolo & Lozza, Giovanni & Malandrino, Alberto & Romano, Matteo & Piccolo, Vincenzo. (2008). Three-reactors chemical looping process for hydrogen production. International Journal of Hydrogen Energy. 33. 2233-2245. 10.1016/j.ijhydene.2008.02.032.

Chisholm, Greig & Cronin, Leroy. (2016). Hydrogen From Water Electrolysis. 10.1016/B978-0-12-803440-8.00016-6.

Cho, Paul & Mattisson, Tobias & Lyngfelt, Anders. (2004). Comparison of iron-, nickel-, copper- and manganese-based oxygen carriers for chemical-looping combustion. Fuel. 83. 1215-1225. 10.1016/j.fuel.2003.11.013.

Cleeton, J. & Bohn, C. & Müller, C.R. & Dennis, J. & Scott, S.A.. (2009). Clean hydrogen production and electricity from coal via chemical looping: Identifying a suitable operating regime. International Journal of Hydrogen Energy. 34. 1-12. 10.1016/j.ijhydene.2008.08.069.

Coelho, Alan. (2020). TOPAS, TOPAS-Academic Technical Reference Version 7. http://www.topas-academic.net/Technical_Reference.pdf. Accessed 4th December 2020

Corbella, Beatriz & de Diego, Luis & García-Labiano, F. & Adánez, Juan & Palacios, José. (2006). Performance in a Fixed-Bed Reactor of Titania-Supported Nickel Oxide as Oxygen Carriers for the Chemical-Looping Combustion of Methane in Multicycle Tests. Industrial & Engineering Chemistry Research. 45. 157-165. 10.1021/ie050756c.

Corbella, Beatriz & de Diego, Luis & García-Labiano, F. & Adánez, Juan & Palaciost, José. (2005). Characterization Study and Five-Cycle Tests in a Fixed-Bed Reactor of Titania-Supported Nickel Oxide as Oxygen Carriers for the Chemical-Looping Combustion of Methane. Environmental science & technology. 39. 5796-803. 10.1021/es048015a.

Dawood, Furat. (2020). Hydrogen production for energy: An overview. International Journal of Hydrogen Energy. 45. 3847-3869. 10.1016/j.ijhydene.2019.12.059.

de Diego, Luis & García-Labiano, F. & Adánez, Juan & Gayán, Pilar & Abad, Alberto & Corbella, Beatriz & Palacios, Jose. (2004). Development of Cu-based oxygen carriers for chemical-looping combustion. Fuel. 83. 1749-1757. 10.1016/j.fuel.2004.03.003.

de Diego, Luis & García-Labiano, F. & Gayán, Pilar & Celaya Romeo, Javier & Palacios, José & Adánez, Juan. (2007). Operation of a 10 kWth chemical-looping combustor during 200 h with a CuO-Al2O3 oxygen carrier. Fuel. 86. 1036-1045. 10.1016/j.fuel.2006.10.004.

de Diego, Luis & Ortiz, María & García-Labiano, F. & Adánez, Juan & Abad, Alberto & Gayán, Pilar. (2009). Synthesis gas generation by chemical-looping reforming using a Ni-based oxygen carrier. Energy Procedia. 1. 3-10. 10.1016/j.egypro.2009.01.003.

de Leeuwe, Christopher & Hu, Wenting & Evans, John & von Stosch, Moritz & Metcalfe, Ian. (2021). Production of high purity H2 through chemical-looping water–gas shift at reforming temperatures – The importance of non-stoichiometric oxygen carriers. Chemical Engineering Journal. 423. 130174. 10.1016/j.cej.2021.130174.

de Leeuwe, Christopher & Papaioannou, Evangelos & Hu, Wenting & Evans, John & Ray, Brian & Metcalfe, Ian. (2020). Revisiting the thermal and chemical expansion and stability of La0.6Sr0.4FeO3. Journal of Solid State Chemistry. 293. 10.1016/j.jssc.2020.121838.

de Leeuwe, Christopher. (2019). Studies of a fixed bed chemical looping reactor for H_2 production by in-situ and operando x-ray and neutron diffraction. PhD thesis at Newcastle University.

De Vos, Yoran & Jacobs, Marijke & Van Der Voort, Pascal & Van Driessche, Isabel & Snijkers, Frans & Verberckmoes, An. (2020). Development of Stable Oxygen Carrier Materials for Chemical Looping Processes—A Review. Catalysts. 10. 926. 10.3390/catal10080926.

Dejoie, Catherine & Coduri, Mauro & Petitdemange, Sébastien & Giacobbe, Carlotta & Covacci, Ezio & Grimaldi, Olivier & Autran, Pierre-Olivier & Mogodi, Mashikoane & Šišak Jung, Dubravka & Fitch, Andy. (2018). Combining a nine-crystal multi-analyser stage

with a two-dimensional detector for high-resolution powder X-ray diffraction. Journal of Applied Crystallography. 51. 10.1107/S1600576718014589.

Demirci, Umit. (2018). About the Technological Readiness of the H2 Generation by Hydrolysis of B(−N)−H Compounds. Energy Technology. 6. 10.1002/ente.201700486.

Diglio, Giuseppe & Bareschino, Piero & Mancusi, Erasmo & Pepe, Francesco. (2015). Simulation of Hydrogen Production through Chemical Looping Reforming Process in a Packed-Bed Reactor. Chemical Engineering Research and Design. 105. 10.1016/j.cherd.2015.11.013.

Diglio, Giuseppe & Bareschino, Piero & Solimene, Roberto & Mancusi, Erasmo & Pepe, Francesco & Salatino, Piero. (2016). Numerical simulation of hydrogen production by chemical looping reforming in a dual fluidized bed reactor. Powder Technology. 316. 10.1016/j.powtec.2016.12.051.

DoITPoMS interactive Ellingham diagram (2022), University of Cambridge online resource. https://www.doitpoms.ac.uk/tlplib/ellingham_diagrams/interactive.php. Accessed 25th February 2022.

Dönitz, W. & Erdle, E.. (1985). High-temperature electrolysis of water vapor—status of development and perspectives for application. International Journal of Hydrogen Energy. 10. 291–295. 10.1016/0360-3199(85)90181-8.

Drift, Bram & Boerrigter, H. (2006). Synthesis gas from biomass for fuels and chemicals.

Duduković, Milorad. (2009). Frontiers in Reactor Engineering. Science (New York, N.Y.). 325. 698-701. 10.1126/science.1174274.

Dueso, Cristina & Thompson, Claire & Metcalfe, Ian. (2015). High-stability, high-capacity oxygen carriers: Iron oxide-perovskite composite materials for hydrogen production by chemical looping. Applied Energy. 5. 10.1016/j.apenergy.2015.05.062.

E4Tech. (2009). Review of Technologies for Gasification of Biomass and Wastes. http://www.ecolateral.org/gasificationnnfc090609.pdf. Accessed 22nd October 2020.

Ebnesajjad, S.. (2011). Handbook of Adhesives and Surface Preparation. 10.1016/C2010-0-65918-9.

El-Nagar, Raghda & Ghanem, Alaa. (2019). Syngas Production, Properties, and Its Importance. Sustainable Alternative Syngas Fuel. Ghenai, Chaouki & Inayat Abrar. IntechOpen. doi: 10.5772/intechopen.89379. https://www.intechopen.com/books/sustainable-alternative-syngas-fuel/syngas-production-properties-and-its-importance. Accessed 11th January 2021.

El-Shafie, Mostafa Ibrahim & Kambara, Shinji & Hayakawa, Yukio. (2019). Hydrogen Production Technologies Overview. Journal of Power and Energy Engineering. 7. 107-154. 10.4236/jpee.2019.71007.

Emery, Antoine & Wolverton, Chris. (2017). High-Throughput DFT calculations of formation energy, stability and oxygen vacancy formation energy of ABO3 perovskites. Scientific Data. 4. 170153. 10.1038/sdata.2017.153.

Feng, Hai & Arai, Masao & Matsushita, Yoshitaka & Tsujimoto, Yoshihiro & Yuan, Yahua & Sathish, C I & He, Jianfeng & Tanaka, Masahiko & Yamaura, Kazunari. (2014). High-pressure synthesis, crystal structure and magnetic properties of double perovskite oxide Ba2CuOsO6. Journal of Solid State Chemistry. 217. 10.1016/j.jssc.2014.05.007.

Fertman, Elena & Syrkin, E.s & Lykah, V. & Desnenko, V. & Beznosov, A. & Pal-Val, Pavel & Pal-Val, L.N. & Fedorchenko, A. & Khalyavin, D. & Feher, A.. (2015). Structural phase transition in La2/3Ba1/3MnO3 perovskite: Elastic, magnetic, and lattice anomalies and microscopic mechanism. AIP Advances. 5. 077189. 10.1063/1.4928075.

Fierro, J.L.G.. (2005). Metal Oxides: Chemistry and Applications. Gas Sensors Based on Semiconducting Metal Oxides. 683-738. 10.1201/9781420028126.

Flamos, Alexandros & Georgallis, Panikos & Doukas, H. & Psarras, John. (2011). Using Biomass to Achieve European Union Energy Targets—A Review of Biomass Status, Potential, and Supporting Policies. International Journal of Green Energy. 8. 411-428. 10.1080/15435075.2011.576292.

Forero, Carmen Rosa & Gayán, Pilar & de Diego, Luis & Abad, A. & García-Labiano, F. & Adánez, Juan. (2009). Syngas combustion in a 500 Wth Chemical-Looping Combustion system using an impregnated Cu-based oxygen carrier. Fuel Processing Technology. 90. 1471-1479. 10.1016/j.fuproc.2009.07.001.

Forero, Carmen Rosa & Gayán, Pilar & García-Labiano, F. & de Diego, Luis & Abad, A. & Adánez, Juan. (2010). Effect of gas composition in Chemical-Looping Combustion with copper-based oxygen carriers: Fate of sulphur. International Journal of Greenhouse Gas Control. 4. 762-770. 10.1016/j.ijggc.2010.04.002.

Franca, Rafael & Thursfield, Alan & Metcalfe, Ian. (2012). La0.6Sr0.4Co0.2Fe0.8O3−δ microtubular membranes for hydrogen production from water splitting. Journal of Membrane Science. 389. 173–181. 10.1016/j.memsci.2011.10.027.

Fremaux, Sylvain & Beheshti, Mohsen & Ghassemi, Hojat & Shahsavan Markadeh, Rasoul. (2014). An experimental study on hydrogen-rich gas production via steam gasification of biomass in a research-scale fluidized bed. Energy Conversion and Management. 91. 10.1016/j.enconman.2014.12.048.

Funk, James. (2001). Thermochemical hydrogen production: Past and present. International Journal of Hydrogen Energy. 26. 185-190. 10.1016/S0360-3199(00)00062-8.

García-Labiano, F. & de Diego, Luis & Adánez, Juan & Abad, Alberto & Gayán, Pilar. (2005). Temperature variations in the oxygen carrier particles during, their reduction and oxidation in a chemical-looping combustion system. Chemical Engineering Science. 60. 851-862. 10.1016/j.ces.2004.09.049.

García-Labiano, F. & de Diego, Luis & Gayán, Pilar & Adánez, Juan & Abad, Alberto & Dueso, Cristina. (2012). Effect of Fuel Gas Composition in Chemical-Looping Combustion with Ni-Based Oxygen Carriers. 1. Fate of Sulfur. Industrial & Engineering Chemistry Research. 48. 2499-2508. 10.1021/ie801332z.

Gayen, Pralay & Sankarasubramanian, Shrihari & Ramani, Vijay. (2020). Fuel and oxygen harvesting from Martian regolithic brine. Proceedings of the National Academy of Sciences. 117. 202008613. 10.1073/pnas.2008613117.

Georgakis, Christos & Chang, C.W. & Szekely, J.. (1979). A Changing Grain Size Model for Gas-Solid Reactions. Chemical Engineering Science. 34. 1072–1075. 10.1016/0009-2509(79)80012-3.

Go, Kangseok & Son, Sung & Kim, Sang & Kang, Kyoung-Soo & Park, Chu. (2009). Hydrogen production from two-step steam methane reforming in a fluidized bed reactor. International Journal of Hydrogen Energy. 34. 1301-1309. 10.1016/j.ijhydene.2008.11.062.

Gokon, Nobuyuki & Yawata, Takehiro & Bellan, Selvan & Kodama, Tatsuya & Cho, Hyunseok. (2019). Thermochemical behavior of perovskite oxides based on LaxSr1-x(Mn, Fe, Co)O3-δ and BaySr1-yCoO3-δ redox system for thermochemical energy storage at high temperatures. Energy. 171. 10.1016/j.energy.2019.01.081.

Goldschmidt, V.. (1926). Die Gesetze der Krystallochemie. Naturwissenschaften. 14. 477-485. 10.1007/BF01507527.

Guiochon, Georges & Felinger, Attila & Shirazi, Dean. (2006). Fundamentals of Preparative and Nonlinear Chromatography. Academic Press

Gupta, Puneet & Velazquez-Vargas, Luis & Fan, Liang-Shih. (2007). Syngas Redox (SGR) Process to Produce Hydrogen from Coal Derived Syngas. Energy & Fuels. 21. 10.1021/ef060512k.

Gupta, Sapna & Mahapatra, Manoj. (2015). Lanthanum chromite based perovskites for oxygen transport membrane. Materials Science and Engineering: R: Reports. 90. 10.1016/j.mser.2015.01.001.

H2stations. Press release. (2020). https://www.h2stations.org/press-pelease-10-years-evaluation-of-hydrogen-refuelling-infrastructure/. Accessed 28th February 2021.

H2stations. Press release. (2021). https://www.h2stations.org/press-release-2021-record-number-of-newly-opened-hydrogen-refeulling-stations-in-2020/. Accessed 28th February 2021.

Hacker, Viktor & Faleschini, Gottfried & Fuchs, Heidrun & Fankhauser, Robert & Simader, Guenter & Ghaemi, Mehdi & Spreitz, Birgit & Friedrich, Kurt. (1998). Usage of biomass gas for fuel cells by the SIR process. Journal of Power Sources. 71. 226-230. 10.1016/S0378-7753(97)02718-3.

Hacker, Viktor & Fankhauser, Robert & Faleschini, Gottfried & Fuchs, Heidrun & Friedrich, Kurt & Muhr, Michael & Kordesch, Karl. (2000). Hydrogen production by steam-iron process. Journal of Power Sources. 86. 531-535. 10.1016/S0378-7753(99)00458-9.

Hadi, Abdul & Mat, Ramli & Somderam, Sathoshini & Abd Aziz, Azharin & Mohamed, Amri. (2018). Hydrogen Sulfide Adsorption by Zinc Oxide-Impregnated Zeolite (Synthesized from Malaysian Kaolin) for Biogas Desulfurization. Journal of Industrial and Engineering Chemistry. 65. 10.1016/j.jiec.2018.05.003.

Haider, Syed Kumail & Azimi, Golnar & Duan, Lunbo & Anthony, Edward & Patchigolla, Kumar & Oakey, John & Leion, Henrik & Mattisson, T. & Lyngfelt, Anders. (2016). Enhancing properties of iron and manganese ores as oxygen carriers for chemical looping processes by dry impregnation. Applied Energy. 163. 41-50. 10.1016/j.apenergy.2015.10.142.

Hanson UK. (2021). Collaboration on green hydrogen research. https://www.hanson.co.uk/en/news-and-events/green-hydrogen-research. Accessed 28th February 2021.

He, Fang & Chen, Jing & Liu, Shuai & Huang, Zhen & Wei, Guoqiang & Wang, Guixia & Cao, Yan & Zhao, Kun. (2019). La1-xSrxFeO3 perovskite-type oxides for chemical-looping steam methane reforming: Identification of the surface elements and redox cyclic performance. International Journal of Hydrogen Energy. 44. 10.1016/j.ijhydene.2019.03.002.

He, Fang & Li, Xinai & Zhao, Kun & Huang, Zhen & Wei, Guoqiang & Li, Haibin. (2013). The use of La1−xSrxFeO3 perovskite-type oxides as oxygen carriers in chemical-looping reforming of methane. Fuel. 108. 465–473. 10.1016/j.fuel.2012.11.035.

Heidebrecht, P. & Sundmacher, Kai. (2009). Thermodynamic analysis of a cyclic water gas-shift reactor (CWGSR) for hydrogen production. Chemical Engineering Science, v.64, 5057-5065 (2009). 64. 10.1016/j.ces.2009.08.011.

Heidebrecht, Peter & Hertel, Christoph & Sundmacher, Kai. (2008). Conceptual Analysis of a Cyclic Water Gas Shift Reactor. International Journal of Chemical Reactor Engineering. 6. 10.2202/1542-6580.1495.

Hertel, Christoph & Heidebrecht, Peter & Sundmacher, Kai. (2012). Experimental quantification and modelling of reaction zones in a cyclic watergas shift reactor. Fuel and Energy Abstracts. 37. 10.1016/j.ijhydene.2011.10.085.

Hiden Analytical. (2016). Hiden QGA - Quantitative Gas Analysis System. Company Technical Information. https://www.hidenanalytical.com/wp-content/uploads/2016/06/QGA_Widescreen_webversion-4.pdf. Accessed 23rd October 2020

Hiden Analytical. (2016). Quadrupole Mass Spectrometry Concepts, Mass Spectrometers for Residual Gas Analysis. Company Technical Information. https://www.hidenanalytical.com/wp-content/uploads/2016/08/Mass_spec_concepts_Widescreen.pdf. Accessed 23rd October 2020

Holladay, Jamie & Hu, Jhen-Jia & King, D.L. & Wang, Y.. (2009). An Overview of Hydrogen Production Technologies. Catalysis Today. 139. 244-260. 10.1016/j.cattod.2008.08.039.

Hossain, Mohammad & Lasa, H.. (2010). Reduction and oxidation kinetics of Co-Ni/Al2O3 oxygen carrier involved in a chemical looping combustion process. Chemical Engineering Science. 65. 10.1016/j.ces.2009.01.059.

Hosseini, Seyed Ehsan & Butler, Brayden. (2019). An Overview of Development and Challenges in Hydrogen Powered Vehicles. International Journal of Green Energy. 10.1080/15435075.2019.1685999.

IEA. (2021). World Energy Outlook 2021, IEA, Paris. https://www.iea.org/reports/world-energy-outlook-2021. Accessed 21st March 2022.

IEA. (2018). Technology Roadmap - Low-Carbon Transition in the Cement Industry. https://www.iea.org/reports/technology-roadmap-low-carbon-transition-in-the-cement-industry. Accessed 28th February 2021.

IEA. (2019). The Future of Hydrogen. https://www.iea.org/reports/the-future-of-hydrogen. Accessed 28th February 2021.

Imtiaz, Qasim & Kurlov, Alexey & Rupp, Jennifer & Müller, Christoph. (2015). Highly Efficient Oxygen-Storage Material with Intrinsic Coke Resistance for Chemical Looping Combustion-Based CO2 Capture (ChemSusChem 12/2015). ChemSusChem. 8. 10.1002/cssc.201403426.

Ishihara, Tatsumi. (2009). Perovskite Oxide for Solid Oxide Fuel Cells. 10.1007/978-0-387-77708-5.

Jerndal, E. & Mattisson, T. & Lyngfelt, Anders. (2006). Thermal Analysis of Chemical-Looping Combustion. Chemical Engineering Research and Design. 84. 795-806. 10.1205/cherd05020.

Jiang, San & Wang, Wei. (2005). Sintering and Grain Growth of (La,Sr)MnO3 Electrodes of Solid Oxide Fuel Cells Under Polarization. Solid State Ionics. 176. 1185-1191. 10.1016/j.ssi.2005.02.013.

Jin, Hongguang & Okamoto, Toshihiro & Ishida, Masaru. (1998). Development of a Novel Chemical-Looping Combustion: Synthesis of a Looping Material with a Double Metal Oxide of CoO−NiO. Energy & Fuels. 12. 1272-1277. 10.1021/ef980080g.

Jin, Hongguang & Okamoto, Toshihiro & Ishida, Masaru. (1999). Development of a Novel Chemical-Looping Combustion: Synthesis of a Solid Looping Material of NiO/NiAl2O4. Industrial & Engineering Chemistry Research. 38. 126-132. 10.1021/ie9803265.

Kadier, Abudukeremu & Simayi, Yibadatihan & Abdeshahian, Peyman & Azman, Nadia Farhana & Kuppam, Chandrasekhar & Kalil, Mohd. (2016). A comprehensive review of microbial electrolysis cells (MEC) reactor designs and configurations for sustainable hydrogen gas production. Alexandria Engineering Journal. 55. 427-443. 10.1016/j.aej.2015.10.008.

Kammer Hansen, Kent & Skou, E.. (2005). LSFM perovskites as cathodes for the electrochemical reduction of NO. Solid State Ionics. 176. 915-920. 10.1016/j.ssi.2004.12.006.

Kang, Kyoung-Soo & Kim, Chang-Hee & Bae, Ki-Kwang & Cho, Won-Chul & Kim, Sung-Hyun & Park, Chu. (2010). Oxygen-carrier selection and thermal analysis of the chemical-looping process for hydrogen production. International Journal of Hydrogen Energy. 35. 12246-12254. 10.1016/j.ijhydene.2010.08.043.

Kaspar, J. & Fornasiero, Paolo & Balducci, G. & Monte, R. & Hickey, Neal & Sergo, Valter. (2003). Effect of ZrO2 content on textural and structural properties of CeO2-ZrO2 solid solutions made by citrate complexation route. Inorganica Chimica Acta. 349. 217-226. 10.1016/S0020-1693(03)00034-3.

Khan, Mohammed & Shamim, Tariq. (2017). Thermodynamic screening of suitable oxygen carriers for a three reactor chemical looping reforming system. International Journal of Hydrogen Energy. 42. 10.1016/j.ijhydene.2017.05.037.

Kierzkowska, Agnieszka & Bohn, C. & Scott, S. & Cleeton, J. & Dennis, J. & Müller, C.. (2010). Development of Iron Oxide Carriers for Chemical Looping Combustion Using Sol−Gel. Industrial & Engineering Chemistry Research. 49. 10.1021/ie100046f.

Kim, Hye-Lim & Kim, Shin & Lee, Kyu-Hyung & Lee, Hong-Lim & Lee, Ki-Tae. (2014). Oxygen ion conduction in barium doped LaInO3 perovskite oxides. Journal of Power Sources. 267. 723–730. 10.1016/j.jpowsour.2014.06.006.

Kim, Jeongdong & Park, Jinwoo & Qi, Meng & Lee, Inkyu & Moon, Il. (2021). Process Integration of an Autothermal Reforming Hydrogen Production System with Cryogenic Air Separation and Carbon Dioxide Capture Using Liquefied Natural Gas Cold Energy. Industrial & Engineering Chemistry Research. 60. 10.1021/acs.iecr.0c06265.

Kim, Sung & Kim, Sang. (2002). Effects of particle properties on solids recycle in loop-seal of a circulating fluidized bed. Powder Technology. 124. 76-84. 10.1016/S0032-5910(01)00472-7.

Kittel, Charles. (1996). Introduction to Solid State Physics. 10.1119/1.1934457.

Kodama, T & Ohtake, H & Matsumoto, S & Aoki, A & Shimizu, T & Kitayama, Y. (2000). Thermochemical methane reforming using a reactive WO3/W redox system. Energy. 25. 411-425. 10.1016/S0360-5442(99)00084-5.

Koike, Makoto & Miyagawa, H. & Suzuoki, T. & Ogasawara, K.. (2012). Ammonia as a hydrogen energy carrier and its application to internal combustion engines. 10.1533/9780857094575.2.61.

Kol'ko, V. & Zyuzin, Dmitry & Sadykov, V. & Kriventsov, Vladimir & Moroz, E.. (2007). Structure of the mixed oxides Mex(Ce0.5Zr0.5)1−xOy (Me = Gd, Pr). Glass Physics and Chemistry. 33. 335-339. 10.1134/S1087659607040050.

Koroneos, Christopher & Dompros, Aris & Roumbas, George & Moussiopoulos, Nicolas. (2004). Life cycle assessment of hydrogen fuel production process. International Journal of Hydrogen Energy. 29. 1443-1450. 10.1016/j.ijhydene.2004.01.016.

Kovacs, Kornel & Maróti, Gergely & Rákhely, Gábor. (2006). A novel approach for biohydrogen production. International Journal of Hydrogen Energy. 31. 1460-1468. 10.1016/j.ijhydene.2006.06.011.

Kuhn, M. & Bishop, S. & Rupp, J.L.M. & Harry, Tuller. (2013). Structural Characterization and Oxygen Nonstoichiometry of Ceria-Zirconia (Ce1−xZrxO2−δ) Solid Solutions. Acta Materialia. 61. 4277–4288. 10.1016/j.actamat.2013.04.001.

Kuhn, M. & Fukuda, Y. & Hashimoto, Shin-ichi & Sato, K. & Yashiro, Keiji & Mizusaki, Junichiro. (2012). Oxygen Nonstoichiometry and Thermo-Chemical Stability of Perovskite-Type La0.6Sr0.4Co1-yFeyO3-δ (y = 0, 0.2, 0.4, 0.5, 0.6, 0.8, 1) Materials. Journal of the Electrochemical Society. 160. F34-F42. 10.1149/2.050301jes.

Kuhn, M. & Hashimoto, Shin-ichi & Sato, K. & Yashiro, Keiji & Mizusaki, Junichiro. (2011). Oxygen Nonstoichiometry, Thermo-Chemical Stability and Lattice Expansion of La0.6Sr0.4FeO3−δ. Solid State Ionics. 195. 7-15. 10.1016/j.ssi.2011.05.013.

Kuhn, M. & Hashimoto, Shin-ichi & Sato, K. & Yashiro, Keiji & Mizusaki, Junichiro. (2013). Oxygen nonstoichiometry and thermo-chemical stability of La0.6Sr0.4CoO3−δ. Journal of Solid State Chemistry. 197. 38–45. 10.1016/j.jssc.2012.08.001.

Lamas, Diego & Fuentes, Rodolfo & Fabregas, Ismael & Rapp, M. & Lascalea, Gustavo & Casanova, J. & Walsöe de Reca, Noemi & Craievich, Aldo. (2005). Synchrotron X-ray diffraction study of the tetragonal–cubic phase boundary of nanocrystalline ZrO2 –CeO2 synthesized by a gel-combustion process. Journal of Applied Crystallography. 38. 867-873. 10.1107/S0021889805025343.

Lane, Howard. (1909). The Lane Hydrogen Producer. Flight.

Larring, Yngve & Braley, Carole & Pishahang, Mehdi & Andreassen, Kari & Bredesen, Rune. (2015). Evaluation of a Mixed Fe–Mn Oxide System for Chemical Looping Combustion. Energy & Fuels. 29. 150414155943002. 10.1021/acs.energyfuels.5b00048.

Lee, D.H.. (2015). Hydrogen production via the Kværner process and plasma reforming. 10.1016/B978-1-78242-361-4.00012-1.

Lehner, Markus & Tichler, Robert & Steinmüller, Horst & Koppe, Markus. (2014). Power-to-Gas: Technology and Business Models. 10.1007/978-3-319-03995-4.

Levenspiel, Octave. (1999). Chemical Reaction Engineering. 10.1021/ie990488g.

Lew, Sokyi & Jothimurugesan, Kandaswami & Flytzani-stephanopoulos, Maria. (1989). High Temperature H2S Removal from Fuel Gases by Regenerable Zinc Oxide-Titanium

Dioxide Sorbents. Industrial & Engineering Chemistry Research. 28. 10.1021/ie00089a006.

Li, Fanxing & Kim, Hyung & Sridhar, Deepak & Zeng, Liang & Chen, Joseph & Fan, Lik Sing. (2009). Syngas Chemical Looping Gasification Process: Oxygen Carrier Particle Selection and Performance. Energy and Fuels. 23. 10.1021/ef900236x.

Liu, Wen & Dennis, John & Scott, Stuart. (2012). The Effect of Addition of ZrO2 to Fe2O3 for Hydrogen Production by Chemical Looping. Industrial & Engineering Chemistry Research. 51. 16597–16609. 10.1021/ie302626x.

Liu, Yongzhuo & Gao, Minggang & Zhang, Xintao & Hu, Xiude & Guo, Qingjie. (2018). Characteristics of a CaSO4 composite oxygen carrier supported with an active material for in situ gasification chemical looping combustion of coal. RSC Advances. 8. 23372-23381. 10.1039/C8RA03425G.

Lopes Nunes Abreu dos Santos, Pedro & Nowak, Sophie & Lau-Truong, Stephanie & Blanchard, Juliette & Beaunier, Patricia & Rodrigues, José & Brayner, Roberta. (2019). Preparation of niobium-based oxygen carriers by polyol-mediated process and application to chemical-looping reforming. Journal of Nanoparticle Research. 21. 10.1007/s11051-019-4528-z.

Luciani, Giuseppina & Landi, Gianluca & Aronne, Antonio & Di Benedetto, Almerinda. (2018). Partial substitution of B cation in La0.6Sr0.4MnO3 perovskites: A promising strategy to improve the redox properties useful for solar thermochemical water and carbon dioxide splitting. Solar Energy. 171. 1-7. 10.1016/j.solener.2018.06.058.

Luo, Ming & Yi, Yang & Wang, Shuzhong & Wang, Zhuliang & Du, Min & Pan, Jianfeng & Wang, Qian. (2017). Review of hydrogen production using chemical-looping technology. Renewable and Sustainable Energy Reviews. 81. 10.1016/j.rser.2017.07.007.

Mah, Angel Xin Yee & Ho, Wai Shin & Bong, Cassendra & Hassim, Mimi & Liew, Peng Yen & Asli, Umi & Kamaruddin, Mohd & Chemmangattuvalappil, Nishanth. (2019). Review of hydrogen economy in Malaysia and its way forward. International Journal of Hydrogen Energy. 44. 10.1016/j.ijhydene.2019.01.077.

Markov, Alexey & Chesnokov, K. & Patrakeev, M. & Leonidov, I. & Chukin, A. & Leonidova, O. & Kozhevnikov, V.. (2015). Oxygen non-stoichiometry and mixed conductivity of La0.5Sr0.5Fe1−xMnxO3−δ. Journal of Solid State Electrochemistry. 20. 10.1007/s10008-015-3027-0.

Martin, M.. (2003). Materials in Thermodynamic Potential Gradients. The Journal of Chemical Thermodynamics. 75. 1291-1308. 10.1016/S0021-9614(03)00094-6.

Mattisson, Tobias & Johansson, Marcus & Lyngfelt, Anders. (2006). The use of NiO as an oxygen carrier in chemical-looping combustion. Fuel. 85. 736-747. 10.1016/j.fuel.2005.07.021.

Mattisson, Tobias & Lyngfelt, Anders & Cho, Paul. (2001). The use of iron oxide as an oxygen carrier in chemical-looping combustion of methane with inherent separation of CO2. Fuel. 80. 1953-1962. 10.1016/S0016-2361(01)00051-5.

Mattisson, Tobias & Lyngfelt, Anders. (2001). Applications of Chemical-Looping Combustion with Capture of CO2. Second Nordic Minisymposium on Carbon Dioxide Capture and Storage.

Meadowcroft, D. (2002). Some Properties of Strontium-Doped Lanthanum Chromite. Journal of Physics D: Applied Physics. 2. 1225. 10.1088/0022-3727/2/9/304.

Metcalfe, Ian & Ray, Brian & Dejoie, Catherine & Hu, Wenting & de Leeuwe, Christopher & Dueso, Cristina & García-García, Francisco & Mak, Cheuk-Man & Papaioannou, Evangelos & Thompson, Claire & Evans, John. (2019). Overcoming chemical equilibrium limitations using a thermodynamically reversible chemical reactor. Nature Chemistry. 11. 1. 10.1038/s41557-019-0273-2.

Miyamoto, Akira & Miura, Morimichi & Sakamoto, Kenji & Kamitomai, Shinji & Kosaki, Yukio & Murakami, Yuichi. (1984). Development of Germanium Oxide Media for the Production of Concentrated Hydrogen by the Steam-Iron Process. Industrial & Engineering Chemistry Product Research and Development. 23. 10.1021/i300015a028.

Miyaoka, Hiroki & Miyaoka, Hikaru & Ichikawa, Tomoyuki & Ichikawa, Takayuki & Kojima, Yoshitsugu. (2018). Highly purified hydrogen production from ammonia for PEM fuel cell. International Journal of Hydrogen Energy. 43. 10.1016/j.ijhydene.2018.06.065.

Mizusaki, Junichiro & Mori, Naoya & Takai, Hiroshi & Yonemura, Yuki & Minamiue, Hidehiro & Tagawa, Hiroaki & Dokiya, Masayuki & Inaba, Hideaki & Naraya, Kazunori & Sasamoto, Tadashi & Hashimoto, Takuya. (2000). Oxygen Non-Stoichiometry and Defect Equilibrium in the Perovskite-Type Oxides La1−xSrxMnO3+d. Solid State Ionics. 129. 163-177. 10.1016/S0167-2738(99)00323-9.

Mizusaki, Junichiro & Tagawa, Hiroaki & Naraya, Kazunori & Sasamoto, Tadashi. (1991). Non-Stoichiometry and Thermochemical Stability of the Perovskite-Type La1-xSrxMnO3-δ. Solid State Ionics. 49. 111-118. 10.1016/0167-2738(91)90076-N.

Mizusaki, Junichiro & Yamauchi, Shigeru & Fueki, Kazuo & Ishikawa, Akira. (1984). Nonstoichiometry of the Perovskite-Type Oxide La1−xSrxCrO3. Solid State Ionics. 12. 119-124. 10.1016/0167-2738(84)90138-3.

Mizusaki, Junichiro & Yonemura, Yuki & Kamata, Hiroyuki & Ohyama, Kouji & Mori, Naoya & Takai, Hiroshi & Tagawa, Hiroaki & Dokiya, Masayuki & Naraya, Kazunori & Sasamoto, Tadashi & Inaba, Hideaki & Hashimoto, Takuya. (2000). Electronic Conductivity, Seebeck Coefficient, Defect and Electronic Structure of Nonstoichiometric La1−xSrxMnO3. Solid State Ionics. 132. 167-180. 10.1016/S0167-2738(00)00662-7.

Mizusaki, Junichiro & Yoshihiro, Masafumi & Yamauchi, Shigeru & Fueki, Kazuo. (1985). Nonstoichiometry and Defect Structure of the Perovskite-Type Oxides La1−xSrxFeO3. Journal of Solid State Chemistry. 58. 257-266. 10.1016/0022-4596(85)90243-9.

Mondal, Kanchan & Lorethova, H. & Hippo, E. & Wiltowski, Tomasz & Lalvani, S.. (2004). Reduction of iron oxide in carbon monoxide atmosphere - Reaction controlled kinetics. Fuel Processing Technology. 86. 33-47. 10.1016/j.fuproc.2003.12.009.

Mori, Masashi & Hiei, Yoshiko & Yamamoto, Tohru. (2001). Thermal Expansion Control Technique of Sr-Doped Lanthanum Chromite Perovskites by B-Site Doping for High-

Temperature Solid Oxide Fuel Cell Separators. Journal of the American Ceramic Society. 84. 781 - 786. 10.1111/j.1151-2916.2001.tb00741.x.

Morison, Rachel. (2020). U.K.'s National Grid to Trial Gas Network With Hydrogen. https://www.bloomberg.com/news/articles/2020-11-30/u-k-s-national-grid-to-trial-gas-network-with-hydrogen. Accessed 21st December 2020.

Müller, C.R. & Bohn, C.D. & Song, Qilei & Scott, S. & Dennis, J.S.. (2011). The production of separate streams of pure hydrogen and carbon dioxide from coal via an iron-oxide redox cycle. Chemical Engineering Journal. 166. 1052-1060. 10.1016/j.cej.2010.11.067.

Muradov, N.. (1993). How to Produce Hydrogen from Fossil Fuels without CO2 Emission. International Journal of Hydrogen Energy. 18. 211-215. 10.1016/0360-3199(93)90021-2.

Muradov, N.. (2001). Catalysis of methane decomposition over elemental carbon. Catalysis Communications. 2. 89-94. 10.1016/S1566-7367(01)00013-9.

Murugan, Arul & Thursfield, Alan & Metcalfe, Ian. (2011). A chemical looping process for hydrogen production using iron-containing perovskites. Energy & Environmental Science. 4. 4639-4649. 10.1039/C1EE02142G.

Murugan, Arul. (2011). Iron-containing perovskite materials for stable hydrogen production by chemical looping water splitting. PhD thesis at Newcastle University.

Nalbandian, Lori & V.T, Zaspalis. (2015). Perovskites as Oxygen Carrier-Transport Materials for Hydrogen and Carbon Monoxide Production by Chemical Looping Processes. 10.1002/9783527686605.ch37.

National Center for Biotechnology Information. PubChem Compound Summary for CID 14801, Manganese dioxide. https://pubchem.ncbi.nlm.nih.gov/compound/Manganese-dioxide. Accessed 18th August 2020.

Nikolaidis, Pavlos & Poullikkas, Andreas. (2017). A comparative overview of hydrogen production processes. Renewable and Sustainable Energy Reviews. 67. 597-611. 10.1016/j.rser.2016.09.044.

Noorman, S. & Gallucci, Fausto & Annaland, M. & Kuipers, Hans. (2011). A theoretical investigation of CLC in packed beds. Part 1: Particle model. Chemical Engineering Journal. 167. 297-307. 10.1016/j.cej.2010.12.068.

Noorman, S. & Gallucci, Fausto & Annaland, M. & Kuipers, Hans. (2011). A theoretical investigation of CLC in packed beds. Part 2: Reactor model. Chemical Engineering Journal - CHEM ENG J. 167. 369-376. 10.1016/j.cej.2011.01.012.

Northern Gas Networks - H21 Leeds City Gate report. (2016). https://www.northerngasnetworks.co.uk/wp-content/uploads/2017/04/H21-Report-Interactive-PDF-July-2016.compressed.pdf. Accessed 21st December 2020.

Orhan, Mehmet & Dincer, Ibrahim & Naterer, G.. (2008). Cost analysis of a thermochemical Cu–Cl pilot plant for nuclear-based hydrogen production. International Journal of Hydrogen Energy. 33. 6006-6020. 10.1016/j.ijhydene.2008.05.038.

Otsuka, K & Kaburagi, T & Yamada, C & Takenaka, S. (2003). Chemical storage of hydrogen by modified iron oxides. Journal of Power Sources. 122. 111-121. 10.1016/S0378-7753(03)00398-7.

Otsuka, K & Yamada, C & Kaburagi, T & Takenaka, S. (2003). Hydrogen storage and production by redox of iron oxide for polymer electrolyte fuel cell vehicles. International Journal of Hydrogen Energy. 28. 335-342. 10.1016/S0360-3199(02)00070-8.

Otsuka, K. (1983). Hydrogen from water by reduced cerium oxide. Journal of Catalysis. 79. 493-496. 10.1016/0021-9517(83)90346-9.

Parisi, Daniel & Laborde, Miguel. (2004). Modelling of Counter Current Moving Bed Gas-Solid Reactor Used in Direct Reduction of Iron Ore. Chemical Engineering Journal. 104. 35-43. 10.1016/j.cej.2004.08.001.

Park, Jun & Levenspiel, Octave. (1977). The crackling core model for the multistep reaction of solid particles. Chemical Engineering Science. 32. 233–234. 10.1016/0009-2509(77)80110-3.

Parra, David & Valverde-Isorna, Luis & Pino, Fco & Patel, Martin. (2019). A review on the role, cost and value of hydrogen energy systems for deep decarbonisation. Renewable and Sustainable Energy Reviews. 101. 279-294. 10.1016/j.rser.2018.11.010.

Peña, Jose-Angel & Lorente, E. & Romero, E. & Herguido, Javier. (2006). Kinetic study of the redox process for storing hydrogen. Reduction stage. Catalysis Today. 116. 439-444. 10.1016/j.cattod.2006.05.068.

Pinsky, Roxanne & Sabharwall, Piyush & Hartvigsen, Jeremy & O'Brien, James. (2020). Comparative review of hydrogen production technologies for nuclear hybrid energy systems. Progress in Nuclear Energy. 123. 103317. 10.1016/j.pnucene.2020.103317.

Piotrowski, Krzysztof & Mondal, Kanchan & Lorethova, Hana & Stonawski, Lubor & Szymański, Tomasz & Wiltowski, Tomasz. (2005). Effect of Gas Composition on the Kinetics of Iron Oxide Reduction in a Hydrogen Production Process. International Journal of Hydrogen Energy. 30. 1543-1554. 10.1016/j.ijhydene.2004.10.013.

Pooler, Michael. (2020). Europe leads the way in the 'greening' of steel output. https://www.ft.com/content/b07c8a83-4b0c-4f96-8ff0-789c51b6e46b. Accessed 28th February 2021.

Quinelato, Antonio Luiz & Longo, Elson & Perazolli, L. & Varela, Jose. (2000). Effect of ceria content on the sintering of ZrO2 based ceramics synthesized from a polymeric precursor. Journal of the European Ceramic Society. 20. 1077-1084. 10.1016/S0955-2219(99)00269-1.

Rahimpour, M. R. & Nategh, M.. (2016). Hydrogen production from pyrolysis-derived bio-oil using membrane reactors. 10.1016/B978-0-08-100451-7.00016-5.

Reed, Homer & Berg, Clyde. (1953). Hydrogen Process. US Pat. 2635947.

Reuß, Markus & Grube, Thomas & Robinius, Martin & Preuster, Patrick & Wasserscheid, Peter & Stolten, Detlef. (2017). Seasonal storage and alternative carriers: A flexible hydrogen supply chain model. Applied Energy. 200. 290–302. 10.1016/j.apenergy.2017.05.050.

Rhodes, C. & Hutchings, Graham & Ward, A.. (1995). Water-gas shift reaction: Finding the mechanistic boundary. Catalysis Today. 23. 43-58. 10.1016/0920-5861(94)00135-O.

Rostrup-Nielsen, J.R & Rostrup-Nielsen, T. Large Scale Methanol Production from Natural Gas. Haldor Topsoe. http://www.topsoe.com/file/large-scale-methanol-production-natural-gas. Accessed 24th May 2018.

Rostrup-Nielsen, J.R. & Christiansen, Lars. (2011). Concepts in Synthesis Gas Manufacture.

Rumble, John. (2021). CRC Handbook of Chemistry and Physics 102nd Edition.

Rydén, Magnus & Lyngfelt, Anders & Mattisson, Tobias & Chen, De & Holmen, Anders & Bjørgum, Erlend. (2008). Novel oxygen-carrier materials for chemical-looping combustion and chemical-looping reforming; LaxSr1−xFeyCo1−yO3−δ perovskites and mixed-metal oxides of NiO, Fe2O3 and Mn3O4. International Journal of Greenhouse Gas Control. 2. 21-36. 10.1016/S1750-5836(07)00107-7.

Rydén, Magnus & Lyngfelt, Anders & Mattisson, Tobias. (2011). Combined manganese/iron oxides as oxygen carrier for chemical looping combustion with oxygen uncoupling (CLOU) in a circulating fluidized bed reactor system. Energy Procedia. 4. 341-348. 10.1016/j.egypro.2011.01.060.

Ryu, H-J & Jin, G-T & Bae, D-H & Yi, C-K. (2004). Continuous operation of a 50 kWth chemical-looping combustor: long-term operation with Ni- and Co-based oxygen carrier particles. Proc 5th China-Korea Joint Workshop on Clean Energy Technology, Qingdao University, China

Ryu, H-J & Seo, Y & Jin, G-T. (2005). Development of chemical-looping combustion technology: Long-term operation of a 50 kWth chemical-looping combustor with Ni- and

Co-based oxygen carrier particles. In: Proc. of the Regional Symp on Chem Eng. Hanoi, Vietnam

Sekiguchi, Hidetoshi & Mori, Yoshihiro. (2003). Steam plasma reforming using microwave discharge. Thin Solid Films. 435. 44-48. 10.1016/S0040-6090(03)00379-1.

Shabani, Bahman & Hafttananian, Mohammad & Khamani, Shadi & Ramiar, Abas & Ranjbar, Ali. (2019). Poisoning of proton exchange membrane fuel cells by contaminants and impurities: Review of mechanisms, effects, and mitigation strategies. Journal of Power Sources. 427. 21-48. 10.1016/j.jpowsour.2019.03.097.

Shen, Laihong & Gao, Zhengping & Wu, Jiahua & Xiao, Jun. (2010). Sulfur behavior in chemical looping combustion with NiO/Al2O3 oxygen carrier. Combustion and Flame. 157. 853-863. 10.1016/ j.combustflame.2009.11.015.

Shen, Laihong & Wu, Jiahua & Gao, Zhengping & Xiao, Jun. (2010). Characterization of chemical looping combustion of coal in a 1 kWth reactor with a nickel-based oxygen carrier. Combustion and Flame. 157. 934-942. 10.1016/j.combustflame.2009.10.009.

Shulman, Alexander & Cleverstam, Erik & Mattisson, Tobias & Lyngfelt, Anders. (2009). Manganese/Iron, Manganese/Nickel, and Manganese/Silicon Oxides Used in Chemical-Looping With Oxygen Uncoupling (CLOU) for Combustion of Methane. Energy & Fuels. 23. 10.1021/ef9005466.

Singh, Kalpana & Nowotny, Janusz & Thangadurai, Venkataraman. (2012). Amphoteric Oxide Semiconductors for Energy Conversion Device: A Tutorial Review. Chemical Society reviews. 42. 10.1039/c2cs35393h.

Słowiński, Grzegorz & Smoliński, Adam. (2016). Thermodynamic Feasibility of Pure Hydrogen Production and Storage in Iron and Germanium Based Double Chemical Looping Process. Journal of the Brazilian Chemical Society. 28. 10.21577/0103-5053.20160267.

Søgaard, Martin & Vang Hendriksen, Peter & Mogensen, Mogens. (2007). Oxygen Nonstoichiometry and Transport Properties of Strontium Substituted Lanthanum Ferrite. Journal of Solid State Chemistry. 180. 1489-1503. 10.1016/j.jssc.2007.02.012.

Sohn, Hong Yong & Szekely, J.. (1972). A Structural Model for Gas–Solid Reactions with a Moving Boundary—III. Chemical Engineering Science. 27. 763–778. 10.1016/0009-2509(72)85011-5.

Sohn, Hong Yong & Szekely, J.. (1973). A structural model for gas—solid reactions with a moving boundary—IV. Langmuir—Hinshelwood kinetics. Chemical Engineering Science. 28. 1169-1177. 10.1016/0009-2509(73)85026-2.

Son, Sung & Go, Kangseok & Kim, Sang. (2008). Thermogravimetric Analysis of Copper Oxide for Chemical-Looping Hydrogen Generation. Industrial & Engineering Chemistry Research. 48. 10.1021/ie800174c.

Spallina, Vincenzo & Marinello, B. & Gallucci, Fausto & Romano, Matteo & Annaland, M.. (2017). Chemical looping reforming in packed-bed reactors: Modelling, experimental validation and large-scale reactor design. Fuel Processing Technology. 156. 156-170. 10.1016/j.fuproc.2016.10.014.

Spath, Pamela & Mann, Margaret. (2000). Life cycle assessment of hydrogen production via natural gas steam reforming. https://www.osti.gov/servlets/purl/764485. Accessed 4th October 2020.

Speight, J.G.. (2015). Gasification processes for syngas and hydrogen production. 10.1016/B978-0-85709-802-3.00006-0.

Sreedhar, Inkollu & Agarwal, Bhawana & Goyal, Priyanka & Agarwal, Ankita. (2020). An overview of degradation in solid oxide fuel cells-potential clean power sources. Journal of Solid State Electrochemistry. 24. 10.1007/s10008-020-04584-4.

Svoboda, K. & Siewiorek, A. & Baxter, D. & Rogut, Jan & Punčochář, M.. (2007). Thermodynamic possibilities of pure hydrogen production by chromium, nickel and

manganese-based chemical looping process at lower temperatures. Chemical Papers-Slovak Academy of Sciences. 61. 110-120. 10.2478/s11696-007-0007-6.

Svoboda, Karel & Siewiorek, A. & Baxter, David & Rogut, Jan & Pohořelý, Michael. (2008). Thermodynamic Possibilities and Constraints for Pure Hydrogen Production by a Nickel and Cobalt-Based Chemical Looping Process at Lower Temperatures. Energy Conversion and Management. 49. 221-231. 10.1016/j.enconman.2007.06.036.

Swamy, Varghese & Dubrovinskaya, NA & Dubrovinsky, Leonid. (1999). High Temperature X-Ray Diffraction of Yttria to Melting Point. Journal of Materials Research. 14. 456 - 459. 10.1557/JMR.1999.0065.

Takenaka, Sakae & Kaburagi, Tomohiro & Yamada, Chisa & Nomura, Kiyoshi & Otsuka, Kiyoshi. (2004). Storage and supply of hydrogen by means of the redox of the iron oxides modified with Mo and Rh species. Journal of Catalysis. 228. 66–74. 10.1016/j.jcat.2004.08.027.

Taylor, D.. (1984). Thermal expansion data: III Sesquioxides, M2O3, with the corundum and the A-, B- and C-M2O3 structures.. Transactions & Journal of the British Ceramic Society. 83. 92-98.

ten Elshof, Andre & Lankhorst, M. & Bouwmeester, Henny. (1997). Oxygen Exchange and Diffusion Coefficients of Strontium-Doped Lanthanum Ferrites by Electrical Conductivity Relaxation. Journal of The Electrochemical Society. 144. 1060-1066. 10.1149/1.1837531.

Teraoka, Y. & Shimokawa, Hironobu & Kang, Ch & Kusaba, H. & Sasaki, K.. (2006). Fe-Based Perovskite-Type Oxides as Excellent Oxygen-Permeable and Reduction-Tolerant Materials. Solid State Ionics. 177. 2245-2248. 10.1016/j.ssi.2006.05.037.

Thursfield, Alan & Murugan, Arul & Franca, Rafa & Metcalfe, Ian. (2012). ChemInform Abstract: Chemical Looping and Oxygen Permeable Ceramic Membranes for Hydrogen Production. Energy & Environmental Science. 5. 7421-7459. 10.1039/C2EE03470K.

Tian, Hanjing & Chaudhari, Karuna & Simonyi, Thomas & Poston, James & Liu, Tengfei & Sanders, Tom & Veser, Götz & Siriwardane, Ranjani. (2008). Chemical-looping Combustion of Coal-derived Synthesis Gas Over Copper Oxide Oxygen Carriers. Energy & Fuels. 22. 10.1021/ef800438x.

Triyono, Djoko & Kafa, C & Laysandra, H.. (2018). Effect of Sr-substitution on the Structural and Dielectric Properties of LaFeO3 Perovskite Materials. Journal of Advanced Dielectrics. 8. 10.1142/S2010135X18500364.

Tyrer-Tomkinson. MASsoft Professional Version 7, Training Manual. https://hideninc.com/tech/MASsoft-V7-Training-Manual.pdf. Accessed 23rd October 2020

U.S. Geological Survey. (2013). Metal prices in the United States through 2010: U.S. Geological Survey Scientific Investigations Report 2012–5188, 204 p., http://pubs.usgs.gov/sir/2012/5188. Accessed 25th July 2019.

Urasaki, Kohei & Tanimoto, Naoshi & Hayashi, Taito & Sekine, Yasushi & Kikuchi, Eiichi & Matsukata, Masahiko. (2005). Hydrogen production via steam-iron reaction using iron oxide modified with very small amounts of palladium and zirconia. Applied Catalysis A: General. 288. 143-. 10.1016/j.apcata.2005.04.023.

Vasala, Sami & Yamauchi, Hisao & Karppinen, Maarit. (2014). Synthesis, Crystal Structure and Magnetic Properties of a New B-Site Ordered Double Perovskite Sr2CuIrO6. Journal of Solid State Chemistry. 220. 28. 10.1016/j.jssc.2014.08.008.

Verma, A. & Jindal, Vijay. (2009). Lattice Constant of Cubic Perovskites. Journal of Alloys and Compounds. 485. 514-518. 10.1016/j.jallcom.2009.06.001.

Villafan-Vidales, Heidi & Abanades, Stephane & Montiel-González, Moises & Romero-Paredes-Rubio, Hernando. (2016). Carbo- and methanothermal reduction of tungsten trioxide into metallic tungsten for thermochemical production of solar fuels. Energy Technol. 5. 692 – 702. 10.1002/ente.201600455.

Voitic, Gernot & Nestl, Stephan & Malli, Karin & Wagner, Julian & Bitschnau, Brigitte & Mautner, Franz & Hacker, Viktor. (2016). High purity pressurised hydrogen production from syngas by the steam-iron process. RSC Advances. 6. 10.1039/C6RA06134F.

Wallner, Thomas & Lohse-Busch, Hennning & Gurski, Stephen & Duoba, Mike & Thiel, Wolfgang & Martin, Dieter & Korn, Thomas. (2008). Fuel economy and emission evaluation of BMW Hydrogen 7 Mono-Fuel demonstration vehicles. International Journal of Hydrogen Energy. 33. 7607-7618. 10.1016/j.ijhydene.2008.08.067.

Wang, Baowen & Yan, Rong & Lee, Dong & Liang, David & Zheng, Ying & Zhao, Haibo & Zheng, Chuguang. (2008). Thermodynamic Investigation of Carbon Deposition and Sulfur Evolution in Chemical Looping Combustion with Syngas. Energy & Fuels. 22. 10.1021/ef7005673.

Wenzel, Marcus & Rihko-Struckmann, Liisa & Sundmacher, Kai. (2016). Thermodynamic Analysis and Optimization of RWGS Processes for Solar Syngas Production from CO2. AIChE Journal. 63. 10.1002/aic.15445.

World Steel Association. (2020). World Steel in Figures. https://www.worldsteel.org/en/dam/jcr:f7982217-cfde-4fdc-8ba0-795ed807f513/World%2520Steel%2520in%2520Figures%25202020i.pdf. Accessed 28th February 2021.

Wu, Yi-Ning & Quan, Wen & Zhu, Jia-Ni & Ding, Jie & Ren, Nan-Qi & Liu, Bing-Feng. (2016). Best mode for photo-fermentation hydrogen production: The semi-continuous operation. International Journal of Hydrogen Energy. 41. 10.1016/j.ijhydene.2016.05.182.

Yang, Jing-biao & Cai, Ningsheng & Li, Zhen-shan. (2008). Hydrogen Production from the Steam−Iron Process with Direct Reduction of Iron Oxide by Chemical Looping Combustion of Coal Char. Energy & Fuels. 22. 10.1021/ef800014r.

Yoo, H.-I. (2019). Demystification of Mizusaki's α-factor for the positively-deviated defect behavior of hyperstoichiometric oxides. ECI oral presentation.

Yüzbasi, Nur Sena & Kierzkowska, Agnieszka & Müller, Christoph. (2017). Development of Fe2O3-based, Al2O3-stabilized Oxygen Carriers using Sol-gel Technique for H2 Production via Chemical Looping. Energy Procedia. 114. 436-445. 10.1016/j.egypro.2017.03.1186.

Zafar, Qamar & Abad, Alberto & Mattisson, Tobias & Gevert, Borje & Strand, Michael. (2007). Reduction and oxidation kinetics of Mn3O4/Mg–ZrO2 oxygen carrier particles for chemical-looping combustion. Chemical Engineering Science. 62. 6556-6567. 10.1016/j.ces.2007.07.011.

Zafar, Qamar & Mattisson, Tobias & Gevert, Borje. (2005). Integrated hydrogen and power production with CO2 capture using chemical-looping reforming - redox reactivity of particles of CuO, Mn2O3, NiO, and Fe2O3 using SiO2 as a support. Ind Eng Chem Res. 44, 3485–3496. 10.1021/ie048978i

Zeng, Kai & Zhang, Dongke. (2010). Recent progress in alkaline water electrolysis for hydrogen production and applications. Progress in Energy and Combustion Science. 36. 307-326. 10.1016/j.pecs.2009.11.002.

Zeng, Liang & He, Feng & Li, Fanxing & Fan, Liang-Shih. (2012). Coal-Direct Chemical Looping Gasification for Hydrogen Production: Reactor Modeling and Process Simulation. Energy & Fuels. 26. 3680–3690. 10.1021/ef3003685.

Zhang, Zili. (2014). The Effect of Sulfur on Chemical Looping Combustion with Iron Oxides. PhD thesis at Imperial College London.

Zhou, Gong & Shah, Parag & Kim, Taeyoon & Fornasiero, Paolo & Gorte, Raymond. (2007). Oxidation entropies and enthalpies of ceria-zirconia solid solutions. Catalysis Today. 123. 86-93. 10.1016/j.cattod.2007.01.013.

Zhou, Zhiquan & Han, Lu & Bollas, George. (2015). Model-assisted analysis of fluidized bed chemical-looping reactors. Chemical Engineering Science. 134. 619-631. 10.1016/j.ces.2015.05.037.

Zhu, H.Y. & Hirata, T.. (1992). Coloration in ceria-doped zirconia induced by reduction heat treatments. Solid State Communications. 84. 527-529. 10.1016/0038-1098(92)90183-A.